Single-Vector Aiding of an IMU for CubeSat Attitude Determination

A THESIS

SUBMITTED TO THE FACULTY OF THE

UNIVERSITY OF MINNESOTA

BY

Kail P Laughlin

IN PARTIAL FULFILLMENT OF THE REQUIREMENTS

FOR THE DEGREE OF

MASTER OF SCIENCE

Advisor: **Demoz Gebre-Egziabher**

July 2020

Acknowledgements

I would like to extend my heartfelt gratitude to my advisor, Professor Demoz Gebre-Egziabher for his constant support throughout my time with the Aerospace Engineering & Mechanics department. His unwavering belief in my capabilities as an engineer motivated me to be my best self at all times. Whenever I felt disheartened or unsure, Professor Gebre was always there to remind me that I was following the right path. No matter the choice, he made sure to support my decisions (even if he did think a PhD would have suited me better). I know that I would not be the engineer I am today without him.

I would like to thank Vibhor Bageshwar for teaching me about stochastic observability and always finding the time to talk. Most of all, I want to thank him for consistently treating me with respect and for sharing his wisdom surrounding what it means to be an engineer. His input was a necessary but not sufficient condition for the timely completion of my thesis.

I would like to thank Professor Ryan Caverly for always having the time to discuss whatever was on my mind, for giving me the opportunity to help him teach the complexities of spacecraft attitude determination and control, and for teaching me the *right* way to code.

I would like to thank Thanasi Pantazides for tolerating my incessant questions regarding hardware, IMUs, my writing, and pretty much any and all things CubeSat related. Oh, and for always holding the door open for me.

I would like to thank Jordan Hoyt, Liam Elke, Kerry Sun, and the entire AEM Systems Lab for me keeping me sane by letting me annoy them day in and day out.

I would like to thank Mike Rogge, Keegan Bunker, Abram Voss, and the UMN Small Satellite Research Lab's ADCS team for having my back and always laughing with me (or at me).

I would like to thank Jasmin Goh and Dharsyan Paramaswaran for sticking with me through both my degrees and somehow not disowning me.

I would like to thank Kyle Houser and Robert Halverson for showing me what it means to be a leader. Surprisingly not as easy as I thought.

I would like to thank Whitney Moore for giving an annoying Freshman a job, letting him barge into her office at all times of the day, and for guiding him through his college career.

I would like to thank Rachel Anderson, for shaping me into the man I am today.

Dedication

To Mom & Dad

For teaching me that nothing worth doing

is ever easy

Abstract

Kail P Laughlin

Words: 256

This thesis examines CubeSat attitude determination using the Earth's magnetic field (EMF) vector aiding a low-cost IMU. CubeSats provide relatively cost-effective methods of performing scientific research in orbital environments. However, to adequately perform this research, knowledge of the CubeSat's orientation in 3D space (attitude) is often required. To that end, the design of a reliable attitude determination (AD) system on-board a CubeSat is a critical aspect for many mission designers. As a primary goal of CubeSat design is to ensure science objectives are met while minimizing, cost, mass, and volume, this thesis investigates a minimal sensor approach to CubeSat AD. Specifically, an inertial based AD scheme reliant on the use of an inertial measurement unit (IMU) aided only by vector measurements of the Earth's magnetic field (EMF) is developed. An extended Kalman filter (EKF) approach to recursively estimate the attitude on-orbit using an IMU and a three-axis magnetometer (TAM) is detailed. Additionally, we describe a test to assess the stochastic observability of the EKF developed. We present simulation results showcasing the performance of the AD system for multiple orbital inclinations and initial attitude errors. Moreover, we discuss conditions in which the EMF vector can and cannot be effectively utilized as the sole aiding measurement, and we evaluate the stochastic observability of the linearized discrete time system. We extend the AD system discussed here to two current University of Minnesota Small Satellite Research Lab CubeSat designs: IMPRESS and EXACT. We describe future work for the implementation of the AD system and potential improvements to the EKF design.

Table of Contents

List of Tables

List of Figures

List of Abbreviations

AD	Attitude Determination
ADCS	Attitude Determination and Control System
CMG	Control Moment Gyros
COM	Center of Mass
CONOPS	Concept of Operations
COTS	Commercial Off-The-Shelf
CS	Control System
CSS	Coarse Sun Sensor
DCM	Direction Cosine Matrix
DSS	Digital Sun Sensor
EKF	Extended Kalman Filter
EMF	Earth Magnetic Field
EXACT	Experiment for X-ray Navigation, Characterization and Timing
GM	Gauss-Markov
GPS	Global Positioning System
HyCUBE	Hypersonic Configurable Unit Ballistic Experiment
IGRF	International Geomagnetic Reference Field
IMPRESS	IMpulsive Phase Rapid Energetic Solar Spectrometer
IMU	Inertial Measurement Unit
INS	Inertial Navigation Systems
IRB	In-Run Bias
ISS	International Space Station
KF	Kalman Filter
MEMS	Micro Electrical-Mechanical Systems
pdf	Probability Density Function
PDF	Probability Distribution Function
QP	Quadratic Program
RV	Random Variable
RWA	Reaction Wheel Assemblies
SAA	Small Angle Assumption
SOCRATES	Signal Opportunity CubeSat Ranging And Timing Experiment
STD	Standard Deviation
TDOA	Time Difference of Arrival
VMA	Vector Matching Algorithm

WMM	World Magnetic Model
XNAV	X-ray Navigation

List of Notation

$(\cdot)^T$	Vector or matrix transpose
$(\cdot)^\times$	Vector cross product or skew symmetric matrix operator
$(\cdot)^{-1}$	Vector or matrix inverse
$(\cdot)^\dagger$	Matrix pseudoinverse
$(\cdot)_m$	Measured quantity of $(\cdot)$
$\widehat{(\cdot)}$	Estimated value of $(\cdot)$
$\sigma_{max}(\cdot)$	Maximum singular value of $(\cdot)$
$\otimes$	Quaternion multiplier
$\Omega(\cdot)$	Left quaternion operator
$\mathrm{B}(\cdot)$	Right quaternion operator
$P(X)$	Probability of random variable X
$F_X(X)$	Probability distribution function of random variable X
$f_X(x)$	Probability density function of random process X
$E\{(\cdot)\}$	Expected value of $(\cdot)$
σ_X	Standard deviation of random process X
$\boldsymbol{\mathcal{F}_S}$	Spacecraft body frame
$\boldsymbol{\mathcal{F}_{\widehat{S}}}$	Estimated spacecraft body frame
$\boldsymbol{\mathcal{F}_g}$	IMU frame
$\boldsymbol{\mathcal{F}_N}$	NED frame
$\boldsymbol{\mathcal{F}_{EF}}$	ECEF frame
$\boldsymbol{\mathcal{F}_E}$	ECI frame
n_1	Payload normal axis
S^i	i^{th} basis vector of spacecraft body frame
g^i	i^{th} basis vector of IMU frame
N^i	i^{th} basis vector of NED frame
EF^i	i^{th} basis vector of ECEF frame
E^i	i^{th} basis vector of ECI frame
$\bar{v}^E$	Vector represented in the ECI frame
$\bar{v}^S$	Vector represented in the spacecraft body frame
ϵ	Knowledge error between true CubeSat detector axis and estimate detector axis
Δ	Control error between true CubeSat detector axis and estimate detector axis

R_3	3-Rotation matrix
R_2	2-Rotation matrix
R_1	1-Rotation matrix
C_{SE}	Direction cosine matrix that transforms a vector represented in $\boldsymbol{\mathcal{F}_E}$ to a vector represented in $\boldsymbol{\mathcal{F}_S}$
ψ	Yaw angle, 3-2-1 Euler angles
θ	Pitch angle, 3-2-1 Euler angles
ϕ	Roll angle, 3-2-1 Euler angles
Ψ_{321}	3×1 array of 3-2-1 Euler angles representing the attitude between $\boldsymbol{\mathcal{F}_S}$ and $\boldsymbol{\mathcal{F}_E}$
q_{SE}	Attitude quaternion that maps a vector in $\boldsymbol{\mathcal{F}_E}$ to a vector in $\boldsymbol{\mathcal{F}_S}$
q_0	Scalar component of a given attitude quaternion
$\bar{q}$	Vector component of a given attitude quaternion
θ_{eul}	Axis rotation angle specified by Euler's theorem
$\bar{e}$	Axis of rotation specified by Euler's theorem
$\bar{\omega}^{SE}$	Angular velocity vector of $\boldsymbol{\mathcal{F}_S}$ with respect to $\boldsymbol{\mathcal{F}_E}$
$\bar{\omega}_m^{SE}$	Measured angular velocity vector of $\boldsymbol{\mathcal{F}_S}$ with respect to $\boldsymbol{\mathcal{F}_E}$
$\bar{n}_g$	Gyro Gaussian additive white noise vector
$\bar{b}$	Gyro bias vector
$\bar{b}_0$	Constant turn on bias (null shift)
$\bar{b}_1$	In-run bias stability
τ_{GM}	Correlation time on Gauss-Markov process
SF	Matrix of scale factor errors
sf_{gi}	Scale factor on the i^{th} axis of the gyro
$\overline{sf}$	Vector of scale factors
F_k	Discrete time state mapping matrix
L_k	Discrete time noise mapping matrix
α, β, γ	Tuning parameters
H_k	Discrete time measurement matrix
Φ_k	State transition matrix
Γ_k	Linearized discrete time noise mapping
Q_k	Discrete time process noise covariance matrix
$Q_{w,k}$	Modified discrete time process noise covariance matrix
R_k	Discrete time measurement noise covariance matrix
P	State covariance matrix

P^-	*A priori* state covariance matrix
P^+	*A posteriori* state covariance matrix
K_k	Discrete time Kalman gain matrix
$\bar{w}_k$	Discrete time process noise vector
$\bar{v}_k$	Discrete time measurement noise vector
$\bar{x}_k$	Discrete time state vector
$\hat{\bar{x}}_k^-$	*A priori* state estimate
$\hat{\bar{x}}_k^+$	*A posteriori* state estimate
$\bar{y}_k$	Discrete time state measurement
σ_{sf}	Standard deviation on gyro scale factor process noise
σ_{IRB}	Standard deviation of gyro in-run bias stability process noise
σ_b	Standard deviation on the additive noise in the gyro in-run bias process
σ_g	Standard deviation on the gyro output noise
σ_{mag}	Standard deviation on the magnetometer output noise
κ	Matrix condition number
$\delta\bar{z}^S$	Extended Kalman filter measurement error vector
$\delta\bar{x}$	Error state vector
$\delta\bar{b}_g$	Gyro bias error vector
$\delta\bar{q}_{S\hat{S}}$	Quaternion error vector between estimate body frame $\mathcal{F}_{\hat{S}}$ and true body frame $\mathcal{F}_S$
$\delta\overline{sf}$	Scale factor error vector
$\delta\bar{\omega}^{SE}$	Angular velocity error vector
$\delta\psi$	Yaw error, 3-2-1 Euler angles
$\delta\theta$	Pitch error, 3-2-1 Euler angles
$\delta\phi$	Roll error, 3-2-1 Euler angles
$\bar{m}^m$	EMF vector represented in magnetometer sensor frame
$\bar{b}_m^{hi}$	Magnetometer hard iron biases
$\bar{n}_m$	Magnetometer output noise vector
$C_{sf,m}$	Matrix of magnetometer scale factor errors
C_{si}	Matrix of magnetometer soft iron biases
$\mathcal{O}_k$	Deterministic observability matrix
Λ_k	Stochastic observability Riccati matrix
$\bar{Q}_k$	Stochastic observability Riccati matrix

I_S	Moment of inertia tensor of CubeSat, principal axes
i	Orbital inclination

1 Introduction

1.1 Motivation

CubeSats provide a cost-effective, standardized platform for the development and application of space-science focused missions and research [1]. Within the past decade, the CubeSat architecture has been adopted and used widely as a testbed by many research institutions and universities [2] [3] [4], due to accessibility and relative ease of use. As the use of this architecture expands, so do the developments of the integrated systems on-board the CubeSat. Typically, these systems consist of the scientific payload coupled with Commercial Off-The-Shelf (COTS) [5] [6] sensors, actuators, and avionics required to ensure proper mission objectives are achieved on-orbit [7]. Effectively designing subsystems while simultaneously minimizing mass and cost of each subsystem is often the main design challenge that is faced by university-based researchers. One such subsystem, the Attitude Determination and Control System (ADCS), is generally one of the more massive and costly subsystems as it can include multiple COTS sensors and actuators [7]. To this end, optimizing the ADCS for low mass and cost is a key trade study within the design of CubeSats.

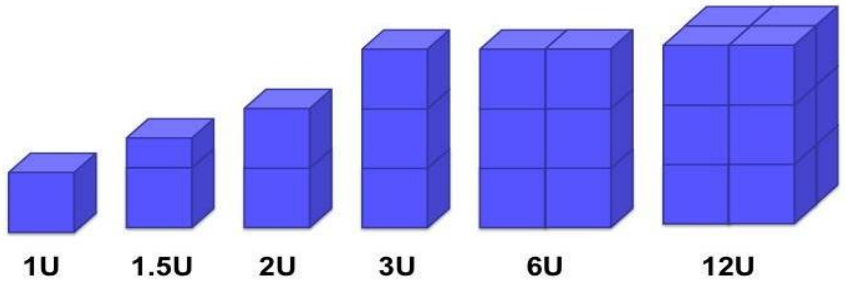

Figure 1.1 Standard CubeSat designs based around the 1U form factor [1].

The ADCS can be split into two components: (1) attitude determination (AD) and (2) the control system (CS). AD is responsible for accurately determining an estimate of how the spacecraft is oriented in 3-D space, while the CS is responsible for changing that orientation to a desired setpoint. This change in orientation is often coined as *slew,* and the speed at which the maneuver occurs is given as *slew rate* [8]. While not all CubeSats require active control, many need some form of attitude knowledge to collect and resolve scientific data. Additionally, the accuracy required of this data coupled with operational slew rates drive the choice of hardware used within the system. A list of common ADCS hardware (not specific to CubeSats) is given in Table 1.1.

Table 1.1 Common ADCS Hardware

AD Hardware	**CS Hardware**
Sun Sensors	Thrusters
Star Trackers	Magnetorquers
Magnetometers	Reaction Wheel Assemblies (RWA)
Inertial Measurement Unit (IMU)	Control Moment Gyros (CMGs)

This thesis focuses solely on the AD portion of the ADCS, specifically in the development of a minimal sensor approach to determining a CubeSat's attitude. The approach developed here will be utilized on two upcoming CubeSat missions, IMPRESS and EXACT, currently being developed by the University of Minnesota's Small Satellite Research Lab. A description of each of these missions is given in the following sections.

1.1.1 IMPRESS

IMPRESS (IMpulsive Phase Rapid Energetic Solar Spectrometer) is a 3U CubeSat with a sun-pointed spectrometer payload used to characterize hard X-ray emission from solar flares with high rate capability and high timing precision. IMPRESS is expected to launch in early 2022 and will measure solar flares in the rising phase of Solar Cycle 25, investigating the processes by which flares accelerate particles to high energies.

Primary scientific objectives are (1) to investigate flare electron timescales by measuring short ($<$2 second) spikes in hard X-ray time profiles; (2) to investigate electron beaming in solar flares via stereoscopic hard X-ray directivity measurements; (3) in collaboration with new space-based instruments, to provide a complete assessment of flare-accelerated electron distributions from thermal to non-thermal energies; (4) to develop and demonstrate a high-energy radiation detector that can measure a vast range of brightness's in solar flares, precipitating electron microbursts, and other astrophysical bursts without pileup or saturation.

A Concept of Operations (CONOPS) diagram for can be seen in Figure 1.2. IMPRESS begins its mission with deployment via a standard Poly-Picosatellite Orbital Deployer (P-POD) ((1) in Figure 1.2). After P-POD ejection, IMPRESS will go through a start-sequence including any detumbling required ((2) in Figure 1.2), followed by deployment of its solar panels ((3) in Figure 1.2). Radio link and sub-system powerup will also begin at this time. An attitude estimate required for solar observation will be obtained over the course of multiple orbits (more information given in Chapter 3). After an estimate is obtained, solar science will

begin ((4) in Figure 1.2), with periodic data downlinking occurring over the mission lifecycle ((5) in Figure 1.2).

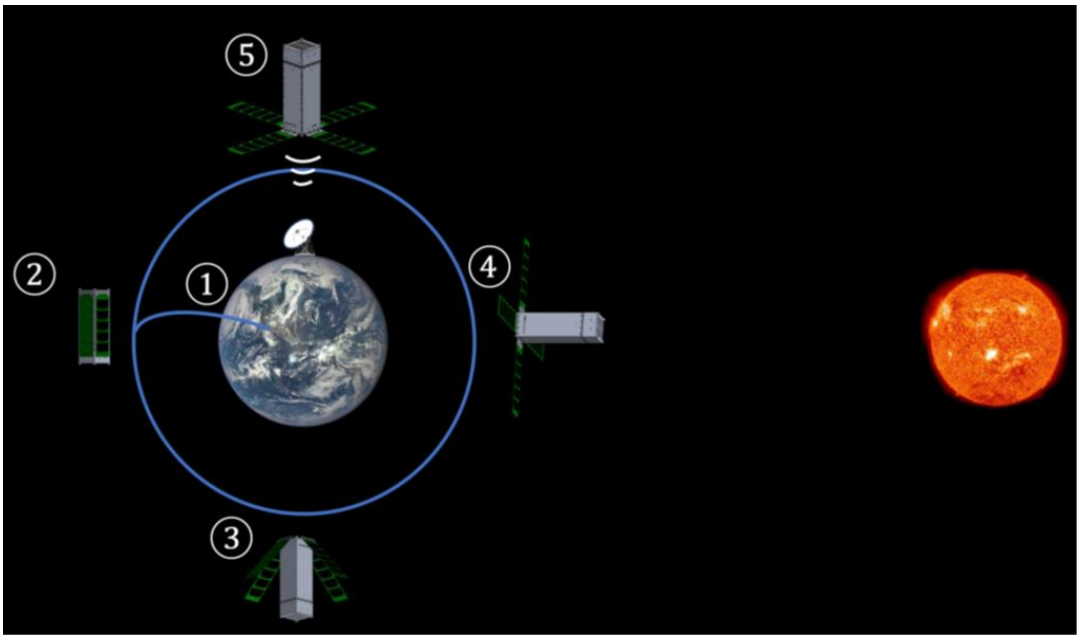

Figure 1.2 IMPRESS CONOPS.

Once IMPRESS is in its primary mission attitude, the sun vector will be kept within a cone of half-angle of 25°. This requirement is discussed further in section 1.2. So long as the attitude is maintained within this cone, no control is implemented.

1.1.2 EXACT

EXACT (Experiment for X-ray Navigation, Characterization and Timing) is an identical CubeSat to IMPRESS. However, instead of pointing at the sun it will point at the Crab Pulsar within the Crab Nebula. The same payload on IMPRESS will be used, in this case, to observe x-ray emissions from the Crab

Pulsar. Its primary mission will be to test and validate new techniques for time-synchronization across spacecraft. Specifically, this will be used to help develop and validate a version of X-ray navigation (XNAV) technology. A secondary mission of EXACT will be to measure X-ray photon energies and arrival times to study electron acceleration in solar flares, similar to IMPRESS.

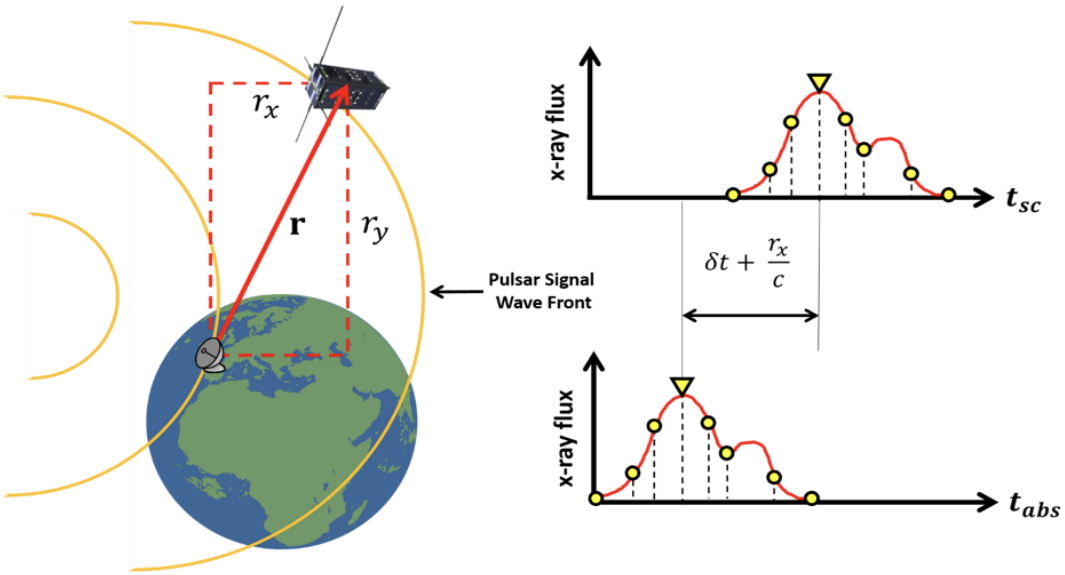

Figure 1.3 EXACT time synchronization experiment.

Primary mission objectives of EXACT are (1) to accurately time tag incoming photons from astrophysical signals in order to get accurate Time Difference of Arrival (TDOA) information for use in XNAV calculations; (2) to validate the performance of a simple, inexpensive XNAV sensor; and (3) to measure its position in orbit so as to provide a reference for TDOA ranging measurements. Secondary scientific objectives are also present and are akin to the primary solar science objectives of IMPRESS.

The time synchronization experiment conducted by EXACT is given in Figure 1.3. TDOA ranging measurements are created by differencing the X-ray fluxes seen at ground stations and on-orbit. For the secondary scientific mission, the CONOPS follows that of IMPRESS given in Figure 1.2.

1.2 Problem Statement

As the nominal operational conditions for IMPRESS and EXACT require accurate pointing, an active ADCS is required. Specifically, IMPRESS and EXACT require celestial body of interest (sun, pulsar) pointing. As such, the primary problem is to develop an AD algorithm that meets the AD requirements of each mission.

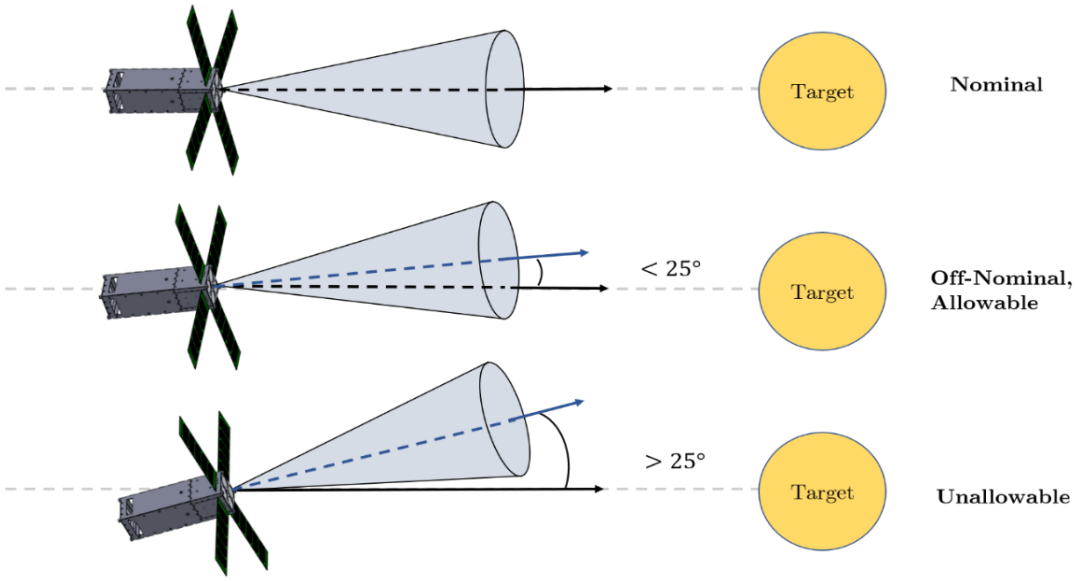

Figure 1.4 IMPRESS & EXACT pointing requirements. The target in the case of IMPRESS is the sun. In the case of EXACT, it is the Crab Pulsar.

Science objectives mandate that the payload of IMPRESS and EXACT be pointed within a half cone of $25°$ as seen in Figure 1.4. This $25°$ error requirement is split up into two components: knowledge error (given as ϵ) and control error (given as Δ). Knowledge error is error attributed to the AD portion of the ADCS, whereas control error is attributed to the CS portion. The combination of these two errors make up the total angular error allowed in the ADCS, which must remain less than $25°$ for science objectives to be met. Specifically, derived requirements specify that $\epsilon \leq 10°$ and $\Delta \leq 15°$ for both missions. This problem statement can be rephrased as follows: Based upon the pointing requirements of IMPRESS and EXACT, the problem is to provide an AD solution with $\epsilon \leq 10°$ during the mission lifespan.

1.3 Thesis Contribution

The primary goals of this thesis are to:

- Analyze the performance of an attitude determination (AD) system based on aiding a low-quality inertial measurement unit (IMU) with a single-vector measurement of the Earth's magnetic field (EMF).
- Analyze the observability of the AD system based on the use of the IMU and EMF vector measurements.

1.4 Thesis Organization

In Chapter 2, we provide an overview of attitude determination. Specifically, we discuss attitude reference frames and parameterizations in addition to the choice of notation used. Common AD schemes are described.

In Chapter 3, we discuss the concept of vector matching and how it can be used as an aiding measurement. For an inertial sensor based AD system, we develop an EKF structure that utilizes the EMF. We emphasize the types of sensors selected for use in this system along with their noise characteristics. Derivations of measurement models for each sensor in addition to the dynamics of the system are provided. The general vector matching algorithm (VMA) used in this work is outlined, and the factors that affect VMA convergence and performance are discussed.

In Chapter 4, we briefly discuss the concept of state observability. Specifically, we discuss two types of observability: Deterministic observability and stochastic observability. We elaborate upon a comprehensive test to verify both metrics and mention the usefulness of such a test.

In Chapter 5, we showcase a set of simulations utilizing the models developed in Chapter 3, and highlight conditions in which the VMA successfully estimates the attitude of the CubeSat. We provide analysis of the results, with discussion on the drawbacks of the simulation environment as well as cases in which the developed VMA does not converge.

In Chapter 6, we present conclusions based upon the models developed, their use in simulation, and their applicability to IMPRESS, EXACT. We present the current design of the ADCS structure for each mission and elaborate upon the system architecture. We also perform first approximation analysis of the UMN's HyCUBE (Hypersonic Configurable Unit Ballistic Experiment) CubeSat ADCS, currently in development. We conclude the thesis with a list of future work and additional developments to the EKF algorithm.

2 Attitude Determination Fundamentals

2.1 Introduction

Attitude Determination (AD) is the practice of estimating the orientation (attitude) of a rigid body in 3-D space with respect to some fixed reference frame [8]. By no means a trivial task, AD is only a subset of the broader problem of estimating the attitude of a rigid body and then changing that attitude to desired orientation. This process is often referred to as attitude determination and control, otherwise known as the ADCS on-board a flight vehicle. While the ADCS is an important system, this thesis will focus solely on the AD component.

AD from vector measurements (the so-called Wahba's Problem, discussed in Section 2.5, posed in 1965 [9]) has been studied extensively for the last 60 years. The problem states that given multiple vector measurements in the spacecraft body frame and their known equivalents in an inertial (non-moving) frame, one can estimate the attitude of the spacecraft in a least squares sense. Practical solutions to this problem began to be developed in the late 1960's and 70's with multiple methods such as QUEST and TRIAD [8] [10]. Alternative approaches, such as the Kalman filter, also began to be implemented throughout the 70's and 80's [11], and continue to be prominent in practice [12] [13] [14]. Due to its broad applicability and relatively easy interpretation, the Kalman filter has become one of the primary methods of state estimation, and is used extensively in many applications [15] [16].

Within the scope of this thesis, the Kalman filter (and the extended Kalman filter) serve as the basis for the AD scheme developed. However, to accurately describe and develop this scheme, general knowledge of AD and the methods used on-orbit for real-time determination must be discussed. To this end, this chapter

discusses what reference frames are, how attitude is parameterized within reference frames, and the notation commonly used to describe attitude. Inertial sensor or rate gyroscope based AD is highlighted, with focus placed on the inherent difficulties in utilizing only inertial AD. We conclude the chapter with a discussion of inertial aiding techniques, and the sensors utilized within them.

2.2 Reference Frames

A reference frame is a cartesian coordinate system that consists of a set of three orthonormal basis vectors [8]. Reference frames often contain physical points that allow us to quantify the position of an object with respect to the reference frame itself. In terms of AD, there are numerous reference frames that can be utilized. A description of many (but not all) of these reference frames follows. It is assumed that each frame mentioned below is a right-handed coordinate system.

2.2.1 Spacecraft Body Frame

The spacecraft body frame is denoted by $\boldsymbol{\mathcal{F}_S}$ and has a basis of $\{S^1\ S^2\ S^3\}$. The origin of the body frame is assumed to be located at the center of mass (COM) of the spacecraft, with its basis vectors aligned with the principal moments of inertia axes of the spacecraft itself. The convention we adopt is to align the positive S^3 axis along the normal axis as the scientific payload, n_1, as seen in Figure 2.1. This convention is chosen to allow for the payload normal axis to align with a principle inertia axis of the satellite. It is important to note that $\boldsymbol{\mathcal{F}_S}$ is affixed to the spacecraft, and thus any rotation seen in the frame is equivalent to the rotation seen by the spacecraft.

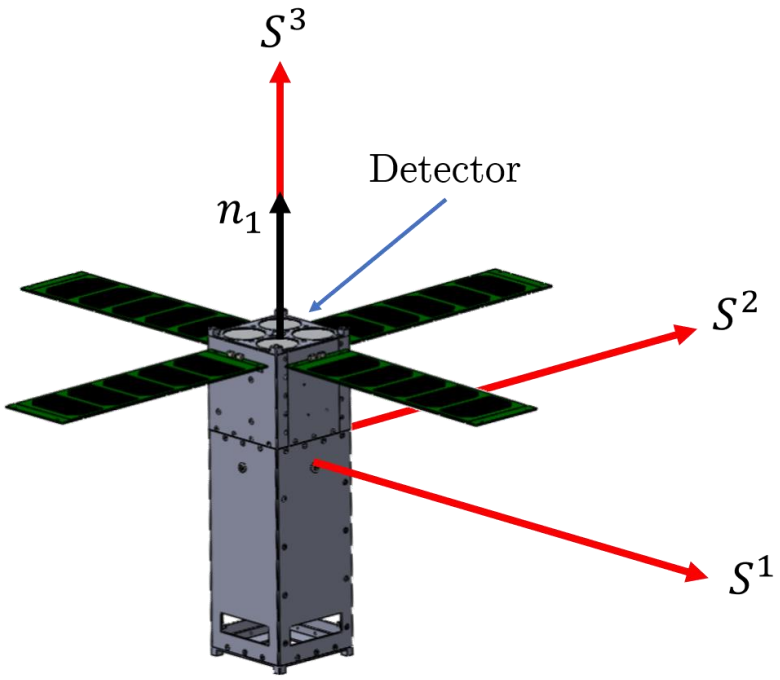

Figure 2.1 Spacecraft body frame.

2.2.2 IMU Frame

The IMU (Inertial Measurement Unit) frame is denoted by $\boldsymbol{\mathcal{F}_g}$ and has the basis of $\{g^1\ g^2\ g^3\}$. It is defined as the right-handed axes affixed to IMU sensor aboard the spacecraft, with origin located at the COM of the sensor. This sensor provides rotational rate information and is an important aspect of inertial sensor based AD, discussed later in this chapter. In the cases where $\boldsymbol{\mathcal{F}_S}$ and $\boldsymbol{\mathcal{F}_g}$ are not aligned, IMU outputs must be rotated and translated from $\boldsymbol{\mathcal{F}_g}$ to $\boldsymbol{\mathcal{F}_S}$. For example, if the IMU outputs a positive angular rate of $\omega_{g3} = 2°/s$ in the g^3 direction, but is aligned such that g^3 is parallel and opposite of S^2 as seen in Figure 2.2, then the angular rate seen by the body frame is actually $\omega_{S2} = -2°/s$. Thus, some angular rotation between frames is required. If $\boldsymbol{\mathcal{F}_S}$ and $\boldsymbol{\mathcal{F}_g}$ are aligned, then no rotational

correction must be made. The $\boldsymbol{\mathcal{F}_g}$ frame is useful as it allows sensors to be aligned in ways that are more practical for hardware implementation, so long as the attitude between $\boldsymbol{\mathcal{F}_g}$ and $\boldsymbol{\mathcal{F}_S}$ is known. While not necessarily aligned, it is assumed that $\boldsymbol{\mathcal{F}_g}$ is fixed with respect to $\boldsymbol{\mathcal{F}_S}$.

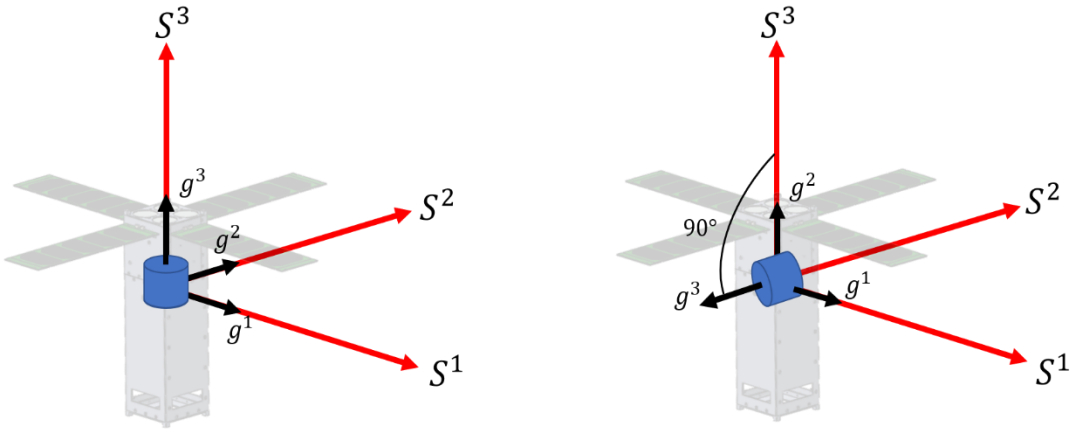

Figure 2.2 IMU frame with respect to spacecraft body frame, aligned (left) and unaligned (right) cases. The IMU is the cylindrical shape to which $\{g^1\ g^2\ g^3\}$ *are affixed.*

2.2.3 North-East-Down (NED) Frame

The north-east-down frame (NED) is a reference frame used within inertial navigation applications and is often referred to as the navigation frame. It is denoted by $\boldsymbol{\mathcal{F}_N}$ and has the basis of $\{N^1\ N^2\ N^3\}$. The origin of the frame is located at the COM of the spacecraft, similar to $\boldsymbol{\mathcal{F}_S}$. The north-east-down naming is derived from the fact that N^1 points positive North, N^2 points positive East, and N^3 points positive down towards the center of the Earth. This is conveyed in Figure 2.3.

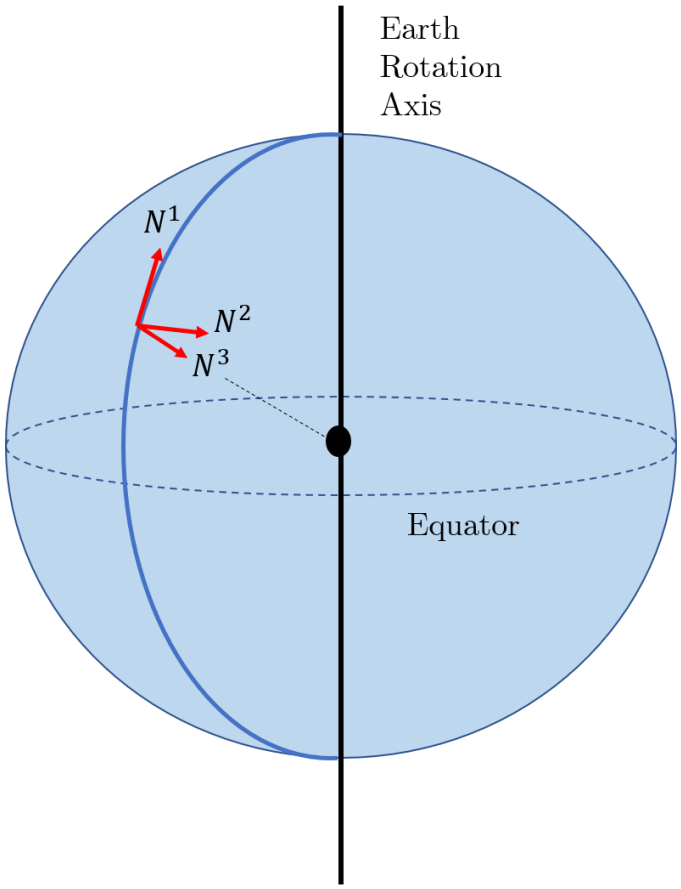

Figure 2.3 NED frame.

2.2.4 Earth Centered Earth Fixed (ECEF) Frame

The Earth Centered Earth Fixed (ECEF) frame is given by $\boldsymbol{\mathcal{F}_{EF}}$ and has the basis of $\{EF^1\ EF^2\ EF^3\}$. The origin of the frame is located at the center of the Earth. EF^1 points to the intersection of the prime meridian and the equator, EF^3 is parallel to Earth's axis of rotation with the positive direction pointing to Earth's North Pole, and EF^2 completes the orthogonal frame as seen in Figure 2.4. Spacecraft position is often measured in latitude, longitude, and altitude ($\phi, \lambda,$ and h respectively) when using the ECEF frame.

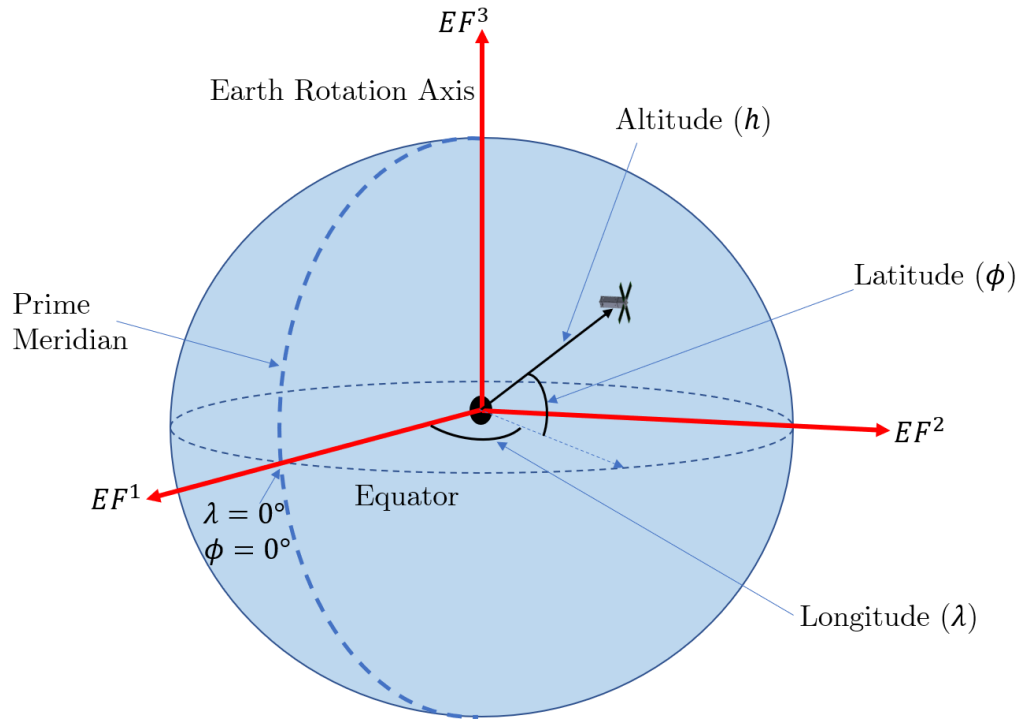

Figure 2.4 ECEF frame.

2.2.5 Earth Centered Inertial (ECI) Frame

The Earth Centered Inertial (ECI) frame is given by $\boldsymbol{\mathcal{F}_E}$ and has the basis of $\{E^1\ E^2\ E^3\}$. The origin of this frame is located at the center of the Earth, similar to $\boldsymbol{\mathcal{F}_{EF}}$. In the instance of the ECI frame, the E^1 basis vector is defined to be pointing along the line drawn by the vernal equinox on January 1, 2000 at 12:00 Terrestrial Time [17]. The E^3 direction is aligned with the Earth's rotation axis and is positive in the direction of the North pole. The E^2 direction completes the orthogonal system. This ECI frame is often referred to as the J2000 ECI frame [17]. A visual representation of this is given in Figure 2.5. Contrary to all previous frames listed, the ECI frame is considered an inertial frame and is fixed in space, as shown graphically in Figure 2.6. At every instant, $\{E^1\ E^2\ E^3\}$ are pointed in the same direction in inertial space.

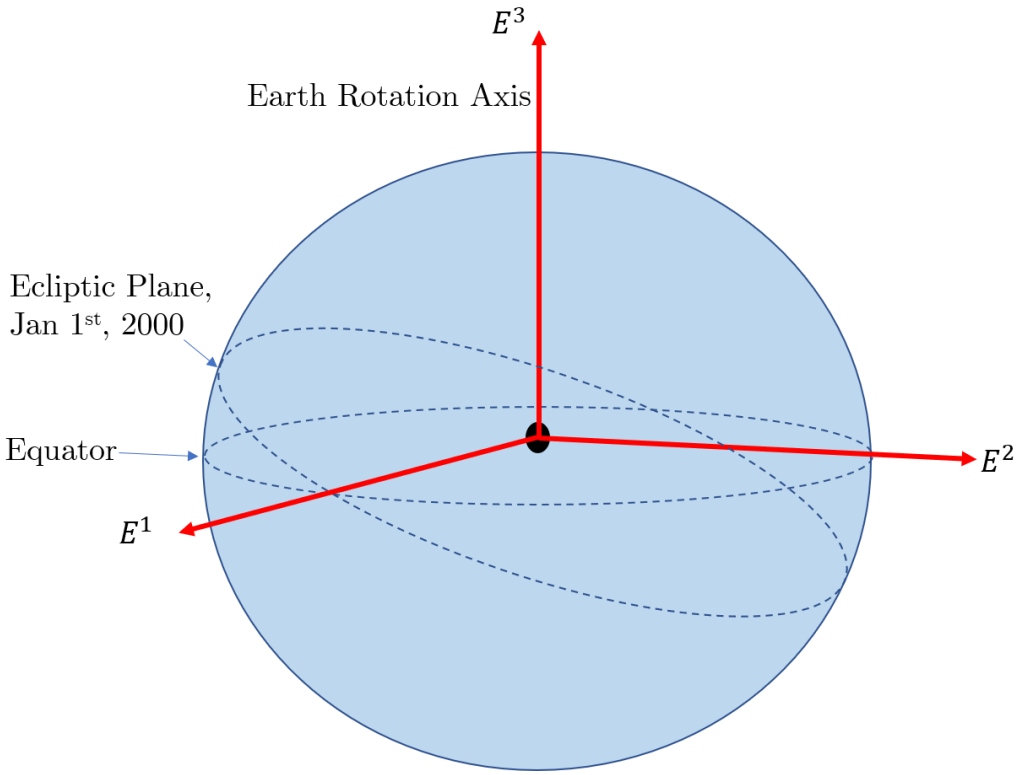

Figure 2.5 ECI frame.

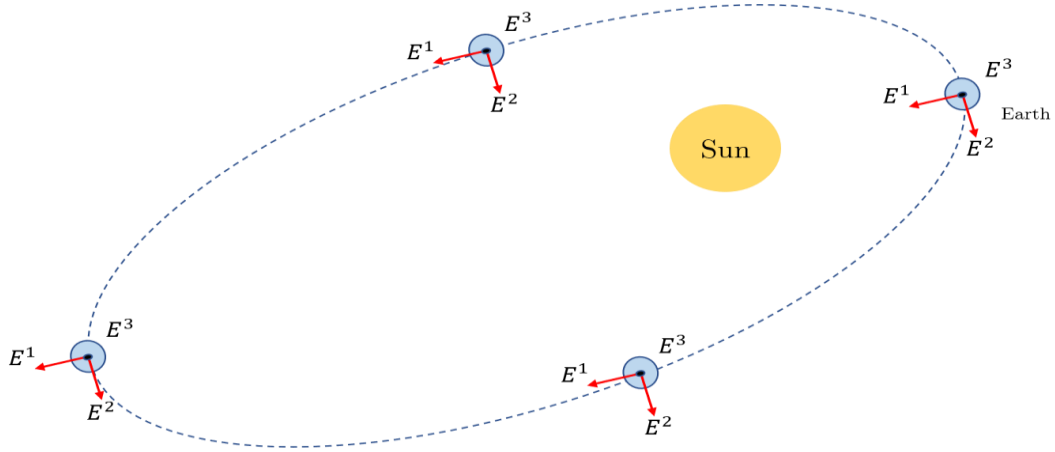

Figure 2.6 ECI frame in solar orbit.

2.2.6 Reference Frames Used in This Work

We will focus on three of the reference frames listed previously: The Spacecraft body frame ($\mathcal{F}_S$), IMU frame ($\mathcal{F}_g$), and the Earth centered inertial frame

($\boldsymbol{\mathcal{F}_E}$). The spacecraft frame is used as a body fixed frame required for AD, which is discussed further in the following sections. The IMU frame is selected to allow flexibility in hardware implementation, and to allow for rotations from the IMU sensor output frame to the spacecraft body frame. The ECI frame is selected as an inertial frame relative to which Newton's laws are valid (specifically applied to the dynamic relations seen in Chapter 3). Figure 2.7 shows how the frames are related to each other. As shown, $\boldsymbol{\mathcal{F}_S}$ can rotate in 3-D space, while $\boldsymbol{\mathcal{F}_E}$ is inertially fixed.

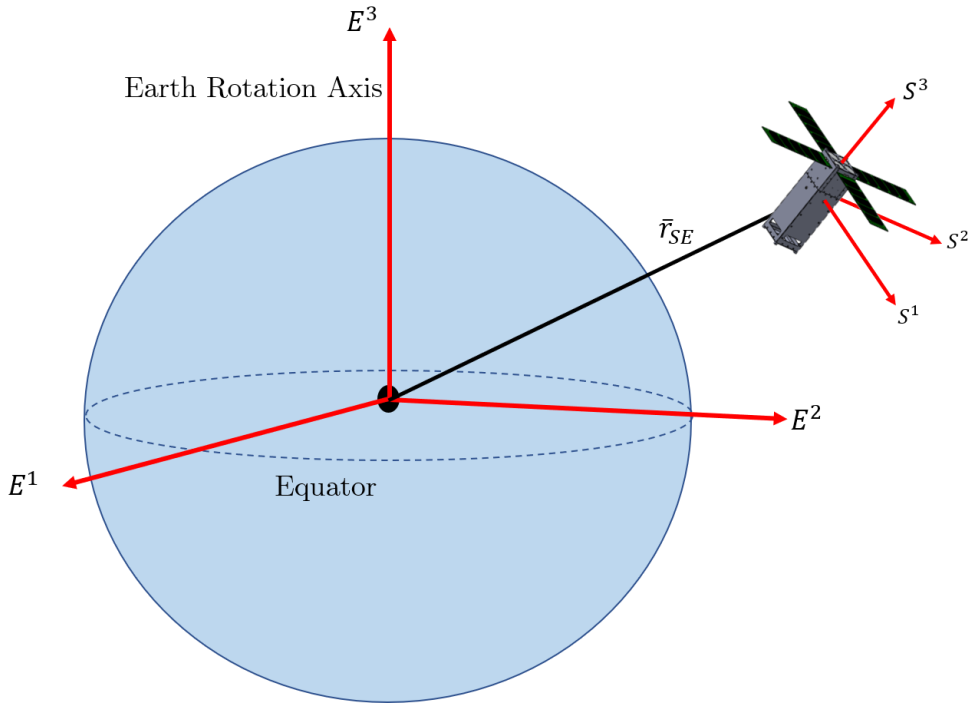

Figure 2.7 $\boldsymbol{\mathcal{F}_S}$ shown with relation to $\boldsymbol{\mathcal{F}_E}$.

2.3 Attitude Parameterizations

To quantify the attitude of a CubeSat, a selection of at least two reference frames must be made. We select an inertial frame and the other to be some frame

attached to the body of the CubeSat itself. Auxiliary frames between these two may be used, however for the purposes of this section, it will be assumed that only a body frame and inertial frame are selected. As mentioned in the previous section, we choose the ECI frame ($\boldsymbol{\mathcal{F}_E}$) as our inertial frame and the spacecraft body frame ($\boldsymbol{\mathcal{F}_S}$) as the body frame.

With these selections, the attitude of a CubeSat can be defined as the angular orientation of $\boldsymbol{\mathcal{F}_S}$ relative to $\boldsymbol{\mathcal{F}_E}$. How to quantify and parameterize this angular orientation is dependent upon the user and the application. Three useful attitude parameterizations will be covered in the following section: Direction Cosine Matrices (DCMs), 3-2-1 Euler Angles, and Quaternions.

2.3.1 Direction Cosine Matrices (DCMs)

Consider two frames, $\boldsymbol{\mathcal{F}_S}$ and $\boldsymbol{\mathcal{F}_E}$, initially aligned so that their individual basis vectors match, as seen in Figure 2.8. A vector, $\bar{v}$, can also be represented in both frames, and is given by the blue arrow in Figure 2.8. In this specific instance, the vector represented in $\boldsymbol{\mathcal{F}_S}$ denoted by $\bar{v}^S$ and the vector represented in $\boldsymbol{\mathcal{F}_E}$ denoted by $\bar{v}^E$ are equivalent such that

$$\bar{v}^S = \bar{v}^E \tag{2.1}$$

with both vectors being equivalent to $\bar{v}$. Now consider the scenario in which we rotate $\mathcal{F}_S$ about its 3-axis by an angle ψ, as seen in Figure 2.9. In this instance, Equation (2.1) no longer holds, as the bases of each frame are no longer aligned.

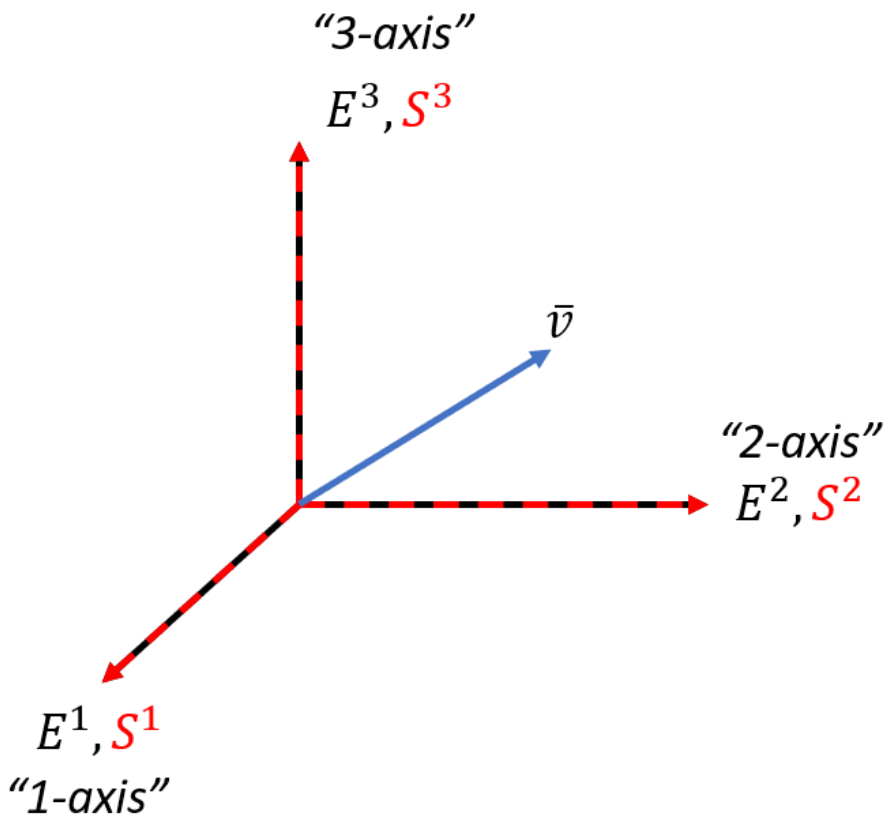

Figure 2.8 $\boldsymbol{\mathcal{F}_S}$ aligned with $\boldsymbol{\mathcal{F}_E}$ with common vector $\bar{v}$.

For the general case where rotation occurs about all three axes, the rotation can be quantified by a direction cosine matrix (DCM) between the two frames such that

$$\bar{v}^S = C_{SE}\bar{v}^E \tag{2.2}$$

where C_{SE} is the 3×3 DCM that transforms a vector represented in $\boldsymbol{\mathcal{F}_E}$ to a vector represented in $\boldsymbol{\mathcal{F}_S}$. The subscripts on C_{SE} denote the frames of interest, with the starting frame as the right-most subscript, and the ending frame as the left-most subscript. We will maintain this convention throughout this thesis.

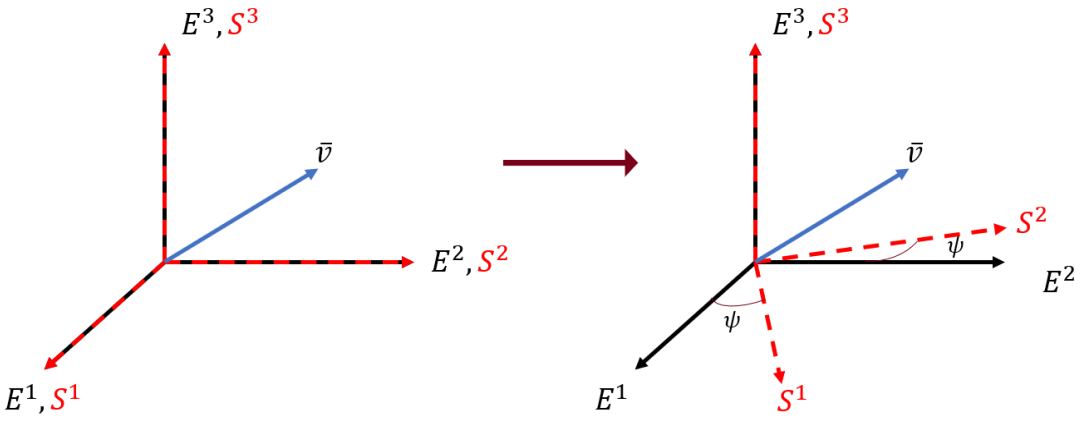

Figure 2.9 $\mathcal{F}_S$ *rotated from* $\mathcal{F}_E$ *by* ψ.

The DCM is made up of sines and cosines of the angles between each frame's basis vectors (hence the name), and is given by

$$C_{SE} = \begin{bmatrix} c_{11} & c_{12} & c_{13} \\ c_{21} & c_{22} & c_{23} \\ c_{31} & c_{32} & c_{33} \end{bmatrix} \tag{2.3}$$

where the columns of the DCM represent the unit vectors of the ending frame's basis axes projected along the starting frame's basis axes [18]. Specifically, the element in the i^{th} row and the j^{th} column is the cosine of the angle between the i axis of the starting frame and the j axis of the ending frame.

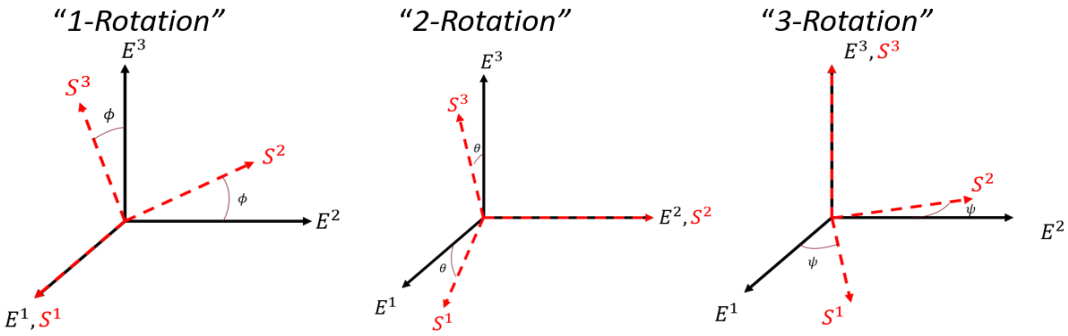

Figure 2.10 Common axes rotations.

The DCM for the rotation shown in Figure 2.9 can be given by

$$C_{SE} = R_3 = \begin{bmatrix} cos\psi & sin\psi & 0 \\ -sin\psi & cos\psi & 0 \\ 0 & 0 & 1 \end{bmatrix} \tag{2.4}$$

where R_3 is known as a *3-Rotation*. While this is an extremely useful matrix, it is only applicable for single rotations that occur about the 3-axis of the starting frame. In the instances of rotations about the 1 and 2 axes, different DCMs must be formulated. The matrices for these specific rotations are given below as

$$R_1 = \begin{bmatrix} 1 & 0 & 0 \\ 0 & cos\phi & sin\phi \\ 0 & -sin\phi & cos\phi \end{bmatrix} \tag{2.5}$$

$$R_2 = \begin{bmatrix} cos\theta & 0 & -sin\theta \\ 0 & 1 & 0 \\ sin\theta & 0 & cos\theta \end{bmatrix} \tag{2.6}$$

$$R_3 = \begin{bmatrix} cos\psi & sin\psi & 0 \\ -sin\psi & cos\psi & 0 \\ 0 & 0 & 1 \end{bmatrix} \tag{2.4}$$

where the angles of ϕ, θ, and ψ correspond to the angles seen in Figure 2.10, with R_1 being a *1-Rotation*, R_2 being a *2-Rotation*, and R_3 being a *3-Rotation*.

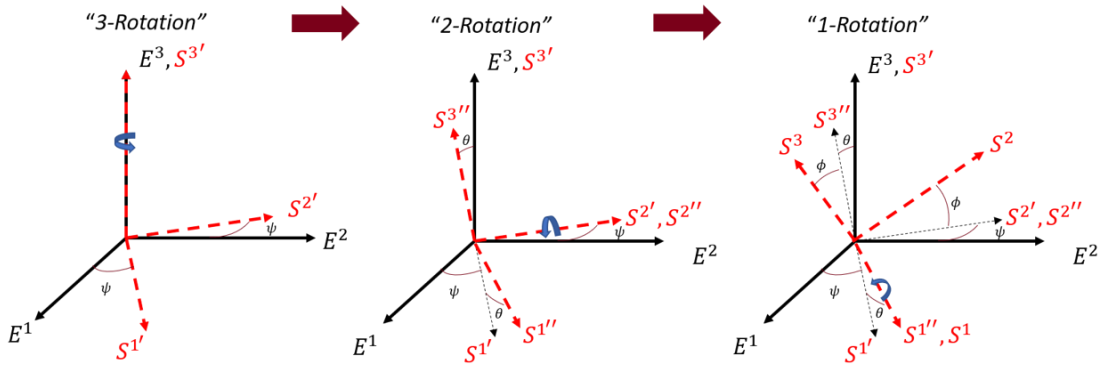

Figure 2.11 Euler angle rotation sequence (3-2-1).

The DCMs seen in Equations (2.4) - (2.6) are only useful for simple rotations about a single axis. In reality, frame rotations are rarely this simple. Fortunately, any complex rotation can be treated as a sequence of the simple rotations given by Equations (2.4) - (2.6). For example, any orientation can be obtained by what is commonly known as a "3-2-1" rotation sequence, often labeled as the "yaw-pitch-roll" rotation sequence [19]. A graphical representation of this is seen in Figure 2.11. Mathematically, this is given by multiplying R_3, R_2, and R_1 seen in Equations (2.4) – (2.6) in sequence as

$$C_{SE} = R_{321} = R_1 R_2 R_3$$

$$= \begin{bmatrix} cos\theta cos\psi & -cos\theta sin\psi & sin\theta \\ sin\phi sin\theta cos\psi + cos\phi sin\psi & -sin\phi sin\theta sin\psi + cos\phi cos\psi & -sin\phi cos\theta \\ -cos\phi sin\theta cos\psi + sin\phi sin\psi & cos\phi sin\theta sin\psi + sin\phi cos\psi & cos\phi cos\theta \end{bmatrix} \quad (2.7)$$

where the angles ψ, θ, and ϕ are the angles for the 3, 2, and 1 rotations, respectively. Note that the sequence of multiplication seen in Equation (2.7) is opposite the sequence of rotations.

C_{SE} is the DCM that maps a vector in the inertial frame $\boldsymbol{\mathcal{F}_E}$ to the spacecraft frame $\boldsymbol{\mathcal{F}_S}$, and as such is a valid attitude parameterization. Specifically, we can

completely represent the orientation of our CubeSat if C_{SE} is known. While C_{SE} is a unique matrix, the sequence of rotations used are not. C_{SE} could have also been obtained through "1-2-3", "3-2-3", "2-3-2", or multiple other rotation sequences. This implies that the angles ψ, θ, and ϕ, along with the sequence of rotation, are not unique. This is important to note when discussing further parameterizations, such as Euler Angles.

2.3.2 Euler Angles (3-2-1 Sequence)

Euler angles are another method of parameterizing attitude and are useful due to their relatively intuitive nature. Euler angles consist of three angles: ψ, known as yaw, θ, known as pitch, and ϕ, known as roll. Euler angles themselves are also the three specific angles that can be used to make up the DCM as seen in Equation (2.7) and Figure 2.11.

This orientation of one frame relative to another can be obtained through multiple rotation sequences, as discussed in the previous section. To elaborate on Euler angles, a specific rotation sequence must be defined. For the remainder of this thesis, it will be assumed that any Euler angles being discussed are of the 3-2-1 or yaw-pitch-roll rotation sequence. The set of 3-2-1 Euler angles, Ψ_{SE}, that map a vector in $\boldsymbol{\mathcal{F}_E}$ to a vector in $\boldsymbol{\mathcal{F}_S}$ can be defined as

$$\Psi_{\mathrm{SE}} = \begin{bmatrix} \psi \\ \theta \\ \phi \end{bmatrix} \tag{2.8}$$

given in radians or degrees. In this instance, the Euler angles represent a roadmap of rotations that can be used to get to $\boldsymbol{\mathcal{F}_S}$ from $\boldsymbol{\mathcal{F}_E}$, as seen in Figure 2.12, and is useful for visualizing the attitude of an object.

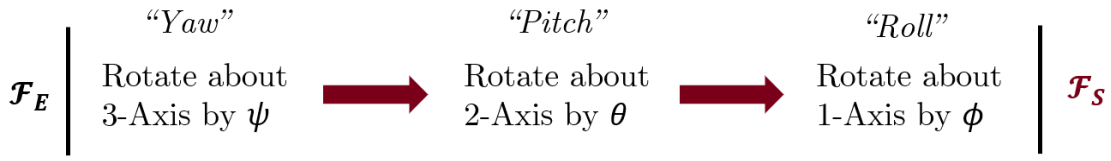

Figure 2.12 Rotation sequence roadmap for 3-2-1 Euler angle sequence.

While Euler angles are useful for visualization, they can be challenging in numerical implementation. Specifically, for the 3-2-1 sequence at $\theta = 90°$, a numerical singularity occurs within the kinematic equations of motion for Euler angles. This singularity is commonly known as "gimbal lock" [20].

2.3.3 Quaternions

Quaternions are a widely used alternative to Euler angles, as they do not have a kinematic singularity and can be relatively easy to implement numerically. The downside to quaternion implementation is their inherent abstract formulation, which can be difficult to visualize. In practice, quaternions are often used to propagate the attitude dynamics of a system and are then converted to Euler angles for visual representation.

The attitude quaternion can be thought of as an extension of Euler's rotational theorem, which states that any relative orientation between two frames can be described by a single rotation, θ_{eul}, about a fixed vector, $\bar{e}$ [8], as seen in Figure 2.13. While there are multiple definitions of a quaternion, we will define it as a 4×1 matrix, consisting of a scalar and vector component. That is,

$$q_{SE} = \begin{bmatrix} q_0 \\ \bar{q} \end{bmatrix} = \begin{bmatrix} q_0 \\ q_1 \\ q_2 \\ q_3 \end{bmatrix} \tag{2.9}$$

where q_{SE} is the attitude quaternion that describes the attitude of $\boldsymbol{\mathcal{F}_S}$ with respect to $\boldsymbol{\mathcal{F}_E}$. Note that the scalar component is given by q_0, whereas the vector component is given by $\bar{q}$. Additionally, according to Euler's theorem, a quaternion can be defined such that

$$q_{SE} = \begin{bmatrix} q_0 \\ \bar{q} \end{bmatrix} = \begin{bmatrix} \cos\left(\frac{\theta_{eul}}{2}\right) \\ \|\bar{e}\| \cdot sin\left(\frac{\theta_{eul}}{2}\right) \end{bmatrix} \tag{2.10}$$

where $\|\bar{e}\|$ is a normalized rotational axis and θ_{eul} is the angle of rotation about that axis.

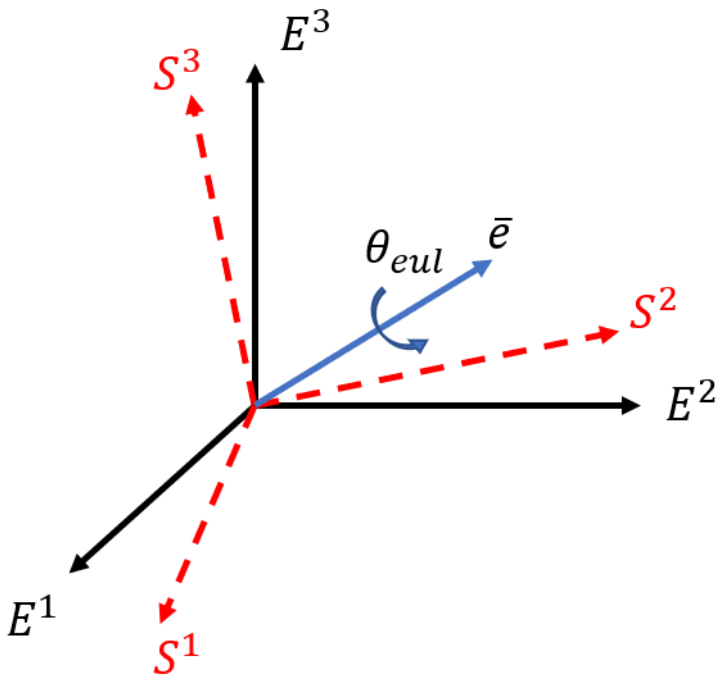

Figure 2.13 Visual representation of Euler's Theorem.

While DCMs and Euler angles will be utilized within this work, much of the numerical analysis contained within the AD algorithms will be performed using

quaternions. To this end, a description of a few key mathematical concepts of quaternions will be discussed further. For detailed information on quaternion mathematics and uses, see [21]. The reader is advised to be careful when utilizing quaternions, as the location of the scalar component, q_0, can vary depending on the quaternion definition used. In general, quaternion implementation, their mathematics, and their meaning can vary depending on the convention used. The sections below assume the convention specified in Equation (2.9).

2.3.3.1 Quaternion Norm

The norm of a quaternion is given by

$$|q| = \sqrt{q_0^2 + q_1^2 + q_2^2 + q_3^2} \tag{2.11}$$

and is required to be equal to 1 to be a valid attitude representation. Specifically, $|q| = 1$. To ensure this constraint is met in computation where sensor error or numerical roundoff can yield quaternions where $|q| \neq 1$, a quaternion can be normalized by dividing by its norm such that

$$q_{normalized} = \frac{q}{|q|} \tag{2.12}$$

where $q_{normalized}$ represents a valid unit attitude quaternion.

2.3.3.2 Quaternion Conjugate

The conjugate of a quaternion is given by

$$q^* = \begin{bmatrix} q_0 \\ -\bar{q} \end{bmatrix} = \begin{bmatrix} q_0 \\ -q_1 \\ -q_2 \\ -q_3 \end{bmatrix} \tag{2.13}$$

where we have inverted the vector portion, $\bar{q}$.

2.3.3.3 Quaternion Inverse

The inverse of a quaternion is given by

$$q^{-1} = \frac{q^*}{|q|} \tag{2.14}$$

If the quaternion is a unit quaternion, then the inverse is equivalent to the conjugate such that $q^{-1} = q^*$.

2.3.3.3 Quaternion Multiplication

The product of two quaternions q and p is defined as

$$q \otimes p = \begin{bmatrix} p_0 q_0 - \bar{p} \cdot \bar{q} \\ p_0 \bar{q} + q_0 \bar{p} + \bar{p} \times \bar{q} \end{bmatrix} \tag{2.15}$$

where $(\cdot)$ is the dot product operator and $(\times)$ is the cross-product operator. The resultant of the product of two quaternions is also a quaternion. As there is a cross product within Equation (2.15), the quaternion product is not commutative, implying

$$q \otimes p \neq p \otimes q \tag{2.16}$$

However, the quaternion product is associative such that

$$(q \otimes p) \otimes r = p \otimes (p \otimes r) \tag{2.17}$$

where q, p, and r are all quaternions.

2.3.4 Overview of Notation & Frame Transformations

The general overview and notation of transforming a vector from one frame to another, given by the attitude parameterizations above, is discussed below.

2.3.4.1 DCM Frame Transformations

A vector given in frame $\boldsymbol{\mathcal{F}_E}$ denoted by $\bar{v}^E$ can be transformed to a vector given in $\boldsymbol{\mathcal{F}_S}$ via the DCM by

$$\bar{v}^S = C_{SE}\bar{v}^E \tag{2.2}$$

where C_{SE} denotes the 3×3 DCM between frames $\boldsymbol{\mathcal{F}_E}$ and $\boldsymbol{\mathcal{F}_S}$. We choose the convention such that the right subscript of C_{SE} indicates the starting frame and the left subscript indicates the ending frame.

2.3.4.2 Euler Angle Frame Transformations (3-2-1)

Like the frame transformation given by Equation (2.2), the transformation of a vector given in frame $\boldsymbol{\mathcal{F}_E}$ denoted by $\bar{v}^E$ to a vector given in $\boldsymbol{\mathcal{F}_S}$ via the 3-2-1 Euler angles is given by

$$\bar{v}^S = R_{321}\bar{v}^E \tag{2.18}$$

where R_{321} is the 3-2-1 Euler angle DCM given in Equation (2.7). In this instance, R_{321} is equivalent to C_{SE}.

2.3.4.3 Quaternion Frame Transformations

The quaternion representation of the transformation of a vector given in frame $\boldsymbol{\mathcal{F}_E}$ denoted by $\bar{v}^E$ to a vector given in $\boldsymbol{\mathcal{F}_S}$ is given as

$$\bar{v}^S = q_{SE} \otimes \begin{bmatrix} 0 \\ \bar{v}^E \end{bmatrix} \otimes q_{SE}^{-1} \tag{2.19}$$

where q_{SE} represents the quaternion representation of the attitude between $\boldsymbol{\mathcal{F}_E}$ and $\boldsymbol{\mathcal{F}_S}$. The $\otimes$ is the quaternion multiplier as defined in Equation (2.15). Similar to the DCM, we define the right subscript on q_{SE} to be the starting frame, and the left subscript to be the ending frame.

2.4 Inertial Based Attitude Determination

In general, no sensor exists to give a direct measurement of the Euler angles or quaternion. However, if the kinematics of the spacecraft are known, then attitude can be indirectly calculated.

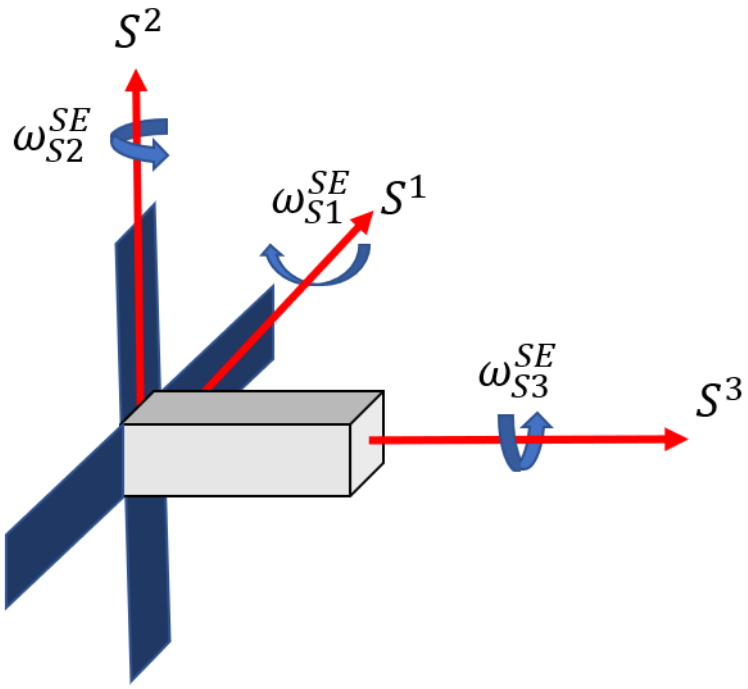

Figure 2.14 Angular rates of a spacecraft.

Consider the angular velocity vector of a spacecraft S in the body frame $\boldsymbol{\mathcal{F}_S}$ with respect to an inertial frame $\boldsymbol{\mathcal{F}_E}$ given by

$$\bar{\omega}^{SE} = \begin{bmatrix} \omega_{S1}^{SE} \\ \omega_{S2}^{SE} \\ \omega_{S3}^{SE} \end{bmatrix} \tag{2.20}$$

where ω_{S1}^{SE}, ω_{S2}^{SE}, and ω_{S3}^{SE} correspond to the angular velocities of each body axis (S^1, S^2, and S^3, respectively) in rad/s. The right superscript on $\bar{\omega}$ indicates the inertial frame and the left superscript indicates the selected body frame. A visual representation of this is given in Figure 2.14. While not derived here, it can be shown that the description of the angular velocity $\bar{\omega}^{SE}$ depends on the attitude parameterization used [8]. That is,

$$\bar{\omega}^{SE} = \bar{\omega}^{SE}\left(A, \dot{A}\right) \tag{2.21}$$

where A is a given attitude parameterization and $\dot{A}$ is the time rate of change of that parameterization. In the instance of the 3-2-1 Euler angle sequence, Equation (2.21) can be written as

$$\bar{\omega}^{SE} = \begin{bmatrix} \dot{\psi} - \dot{\phi}\sin\theta \\ \dot{\phi}\cos\theta\sin\psi + \dot{\theta}\cos\psi \\ \dot{\phi}\cos\theta\cos\psi - \dot{\theta}\sin\psi \end{bmatrix} \tag{2.22}$$

where $\dot{\psi}$, $\dot{\theta}$, and $\dot{\phi}$ represent the time rate of change of the 3-2-1 Euler angles. Rearranging Equation (2.22) [8], we have

$$\begin{bmatrix} \dot{\phi} \\ \dot{\theta} \\ \dot{\psi} \end{bmatrix} = \begin{bmatrix} 0 & \sec\theta\sin\psi & \sec\theta\cos\psi \\ 0 & \cos\psi & -\sin\psi \\ 1 & \tan\theta\sin\psi & \tan\theta\cos\psi \end{bmatrix} \bar{\omega}^{SE} \tag{2.23}$$

which solves for the rate of change of the 3-2-1 Euler angles given $\bar{\omega}^{SE}$ and an initial attitude. If utilizing quaternions, Equation (2.21) can be written as

$$\begin{bmatrix} 0 \\ \bar{\omega}^{SE} \end{bmatrix} = 2(\dot{q}_{SE} \otimes q_{SE}^{-1}) \tag{2.24}$$

where $\dot{q}_{SE}$ represents the time rate of change of the quaternion. Rearranging Equation (2.24) gives

$$\dot{q}_{SE} = \frac{1}{2}\begin{bmatrix} 0 \\ \bar{\omega}^{SE} \end{bmatrix} \otimes q_{SE} \tag{2.25}$$

which solves for the rate of change of q_{SE} given $\bar{\omega}^{SE}$ and an initial attitude quaternion. Fortunately, sensors exist to measure the angular velocity of a spacecraft. These are typically known as rate gyroscopes or "gyros" and are often components of IMUs.

2.4.1 Inertial AD with Noisy IMUs

All sensors have noise that can usually be characterized by a stochastic process (see Appendix A for a description of how we define stochastic processes). Ideally, an IMU's output will be equivalent to the true angular rates of the body, as given by

$$\bar{\omega}_m^{SE} = \bar{\omega}^{SE} \tag{2.26}$$

where $\bar{\omega}_m^{SE}$ is the measured angular rate vector. In reality, the IMU measurements will be corrupted by some form of noise. We typically treat this noise as a stochastic process that varies through time. As a first approximation, we can model this simplistically by including an additive noise term to the measurement model of Equation (2.26) such that

$$\bar{n}_g \sim N(0, \sigma_g^2)$$

$$\bar{\omega}_m^{SE} = \bar{\omega}^{SE} + \bar{n}_g \tag{2.27}$$

where $\bar{n}_g$ is some additive noise with zero mean and variance σ_g^2. Replacing $\bar{\omega}^{SE}$ with $\bar{\omega}_m^{SE}$ as defined above in Equation (2.27) will yield

$$\begin{bmatrix} \dot{\phi} \\ \dot{\theta} \\ \dot{\psi} \end{bmatrix}_m = \begin{bmatrix} 0 & \sec\theta_m \sin\psi_m & \sec\theta_m \cos\psi_m \\ 0 & \cos\psi_m & -\sin\psi_m \\ 1 & \tan\theta_m \sin\psi_m & \tan\theta_m \cos\psi_m \end{bmatrix} \bar{\omega}_m^{SE} \tag{2.28}$$

where $\left[\dot{\phi}\ \dot{\theta}\ \dot{\psi}\right]_m^T$ are the measured Euler angle rates of the vehicle and ϕ_m , θ_m, and ψ_m are the measured Euler angles. These measured angles are found by integrating the noisy Euler angle rates throughout time, which requires an integration of the random noise $\bar{n}_g$ that is attributed to angular rates of the body. This process will cause the noise levels to grow at each integration, eventually causing the measured Euler angles to drift from the true Euler angles.

For example, take Figure 2.15 which shows the yaw error, $\delta\psi$, between the true value of ψ and the value calculated by integrating measured angular rates from a consumer grade IMU (red line). After only $60\ s$ of measurements, the error has reached $13°$. An error in attitude this large is typically unacceptable in most practical ADCS applications.

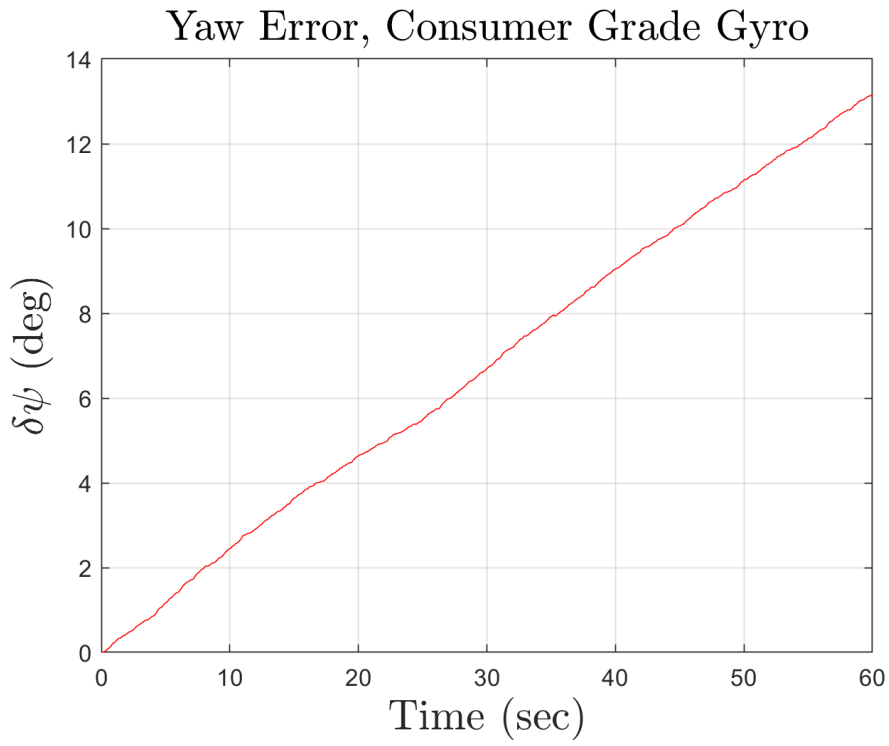

Figure 2.15 Yaw error propagation with noisy gyro.

2.4.2 Gyro Measurement Model

The drift rate or the slope of the red line in Figure 2.15 is dependent on the amount and types of noise in the gyro measurements. As such, it is important to properly characterize the noise on a rate gyro. While the nature of the noise within the measurement model shown in Equation (2.27) is simple, it is not accurate. Not only are gyro noise characteristics not purely additive, they are also sometimes functions of time. A more general and accurate model for a rate gyroscope can be given by

$$\bar{\omega}_m^{SE} = (1_3 + SF)\bar{\omega}^{SE} + \bar{b}(t) + \bar{n}_g \tag{2.29a}$$

$$\bar{b}(t) = \bar{b}_0 + \bar{b}_1(t) \tag{2.29b}$$

where SF reperesents a 3×3 diagonal matrix of scale factor errors, $\bar{b}(t)$ is a 3×1 bias vector that is a function of time, and $\bar{n}_g$ is a 3×1 vector of random, gaussian, additive white noise. These types of noise are discussed in the following sub sections. For a detailed description of IMU errors, see [22] [23]. Additionally, Appendix C overviews how to read IMU specification sheets and details how to quantify some of the following values.

2.4.2.1 Scale Factor Errors

A scale factor is a multiplicative error term. It is a multiplier on the true angular velocity that results in a scaled version being output from the sensor, with units typically being % or parts per million (ppm). For example, if there is a 20% scale factor error present on one axis of the rate gyro, a true angular velocity of $5°/s$ will result in $6\,°/s$ being output from the gyro ($(1 + 0.2)5°/s = 6\,°/s$). Scale factors can be represented in a 3×3 diagonal scale factor matrix SF that is given by

$$SF = \begin{bmatrix} sf_{g1} & 0 & 0 \\ 0 & sf_{g2} & 0 \\ 0 & 0 & sf_{g3} \end{bmatrix} \tag{2.30}$$

where sf_{g1}, sf_{g2}, and sf_{g3} represent the individual scale factors in each gyro axis. A graphical representation of scale factors is seen in Figure 2.16.

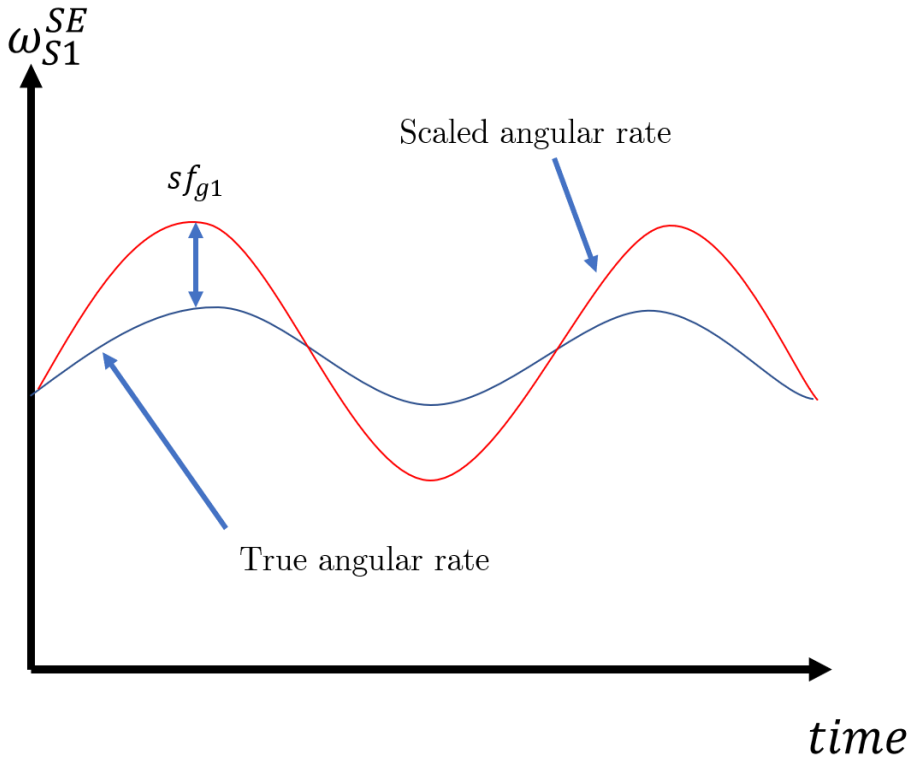

Figure 2.16 Scale factor errors.

2.4.3.2 Bias and White Noise

Two types of biases are modeled by Equation (2.29): Constant turn on bias (b_0) and in-run bias ($b_1(t)$). The constant turn on bias is present every time the rate gyro is turned on and may or may not be relatively constant throughout time. This bias is sometimes referred to as *bias repeatability* or *null-shift* and has the units of $°/s$ or rad/s. The in-run bias is not constant and is considered a correlated, colored noise process. It can change throughout the duration of sampling and often is modeled as a 1st order Gauss-Markov process with correlation time τ_{GM}. More discussion of this is held in Chapter 3. The in-run bias is sometimes referred to as *bias stability* and has the units of $°/hr$, typically. Inertial aiding systems often seek

to estimate these biases and calibrate the measurements as time goes on. A discussion of this will be included in Section 2.5.

The noise vector $\bar{n}_g$ is often treated as random white noise that is added to the gyro measurement. It is a Gaussian random variable, with zero-mean, and can be referred to as *output noise* or sometimes *angle random walk* (ARW). This term is arguably the simplest noise term and is purely additive. A visual representation of the biases and white noise can be seen in Figure 2.17. The in-run bias and white noise combine to add the sharp peaks and troughs seen in the red line in Figure 2.17, whereas the null-shift has pushed the red line itself above the true angular rate by some fixed amount.

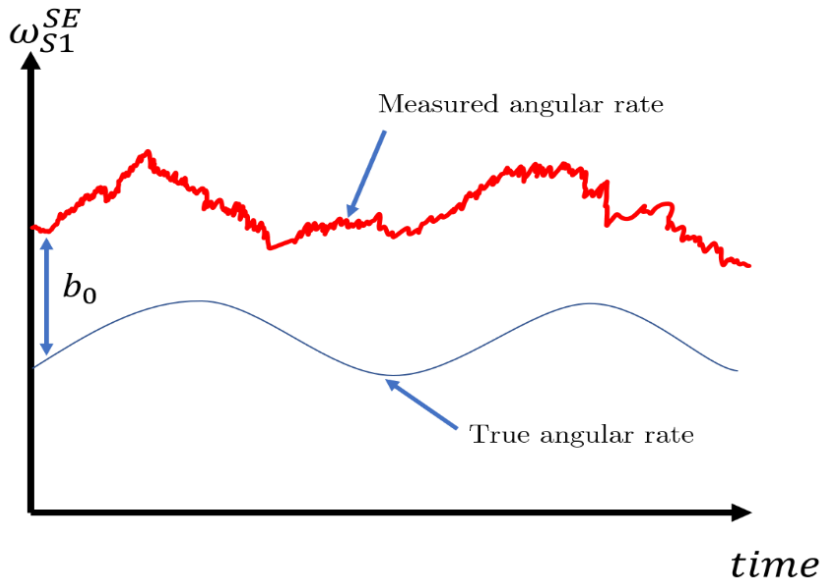

Figure 2.17 Bias and white noise errors.

2.5 Vector Matching & Aided Inertial AD

In most cases, as seen by Figure 2.15, sole use of a rate gyro in an IMU does not allow accurate AD. Instead, IMUs are often used in conjunction with additional sensors that supplement the IMU's inertial measurement with external measurements. The external measurements are independent of the integrated noise of the gyros and are used to calibrate the gyro measurement. This is performed by solving Wahba's Problem [9], and is sometimes referred to as vector matching.

Wahba's problem involves computing a least squares estimate of the DCM between two frames based upon a set of vector measurements in one frame and the same set of vectors known in another frame. Specifically, if the spacecraft frame $\boldsymbol{\mathcal{F}_S}$ and ECI frame $\boldsymbol{\mathcal{F}_E}$ are used with a common origin, then Wahba's problem is:

Given a set of $\boldsymbol{n}$ *vectors* $\{\bar{u}_{m,1}^S, \bar{u}_{m,2}^S, \dots, \bar{u}_{m,n}^S\}$ *measured in* $\boldsymbol{\mathcal{F}_S}$ *and the same set of vectors known in* $\boldsymbol{\mathcal{F}_E}$, $\{\bar{u}_1^E, \bar{u}_2^E, \dots, \bar{u}_n^E\}$, *compute the DCM that minimizes the cost function*

$$J = \sum_{i=2}^{n} \left\| \bar{u}_i^S - C_{SE} \bar{u}_i^E \right\|^2 \tag{2.31}$$

where C_{SE} *is constructed using the attitude quaternion that is subject to the quaternion norm constraint given by Equation (2.11) such that*

$$|q_{SE}| = \sqrt{q_0^2 + q_1^2 + q_2^2 + q_3^2} = 1 \tag{2.32}$$

where q_{SE} *is the attitude quaternion that represents the attitude between* $\boldsymbol{\mathcal{F}_E}$ *and* $\boldsymbol{\mathcal{F}_S}$.

A unique solution to Wahba's problem requires at least two, non-collinear, non-zero sets of vectors be measured and known. This implies that if two sensors on board a spacecraft can provide two non-collinear measurements, and a knowledge of what those measurements should be in an inertial frame is also stored on board, then an estimate of the attitude can be determined.

2.5.1 Aiding Sensors

There are many sensors that can be used to solve Wahba's problem. Below is a list of some common sensors for spacecraft applications. For detailed description of these and additional sensors, see Chapter 4 of [8].

2.5.1.1 Three-axis Magnetometer (TAM)

A three-axis magnetometer (TAM) is used to obtain a measurement of the Earth's Magnetic Field (EMF) vector seen in the $\boldsymbol{\mathcal{F}_S}$ frame at a given instance in time. In most cases the magnetometers used in spacecraft are small, lightweight, and inexpensive. However, if being used in an AD vector matching scheme, a well-modeled magnetic field is required. This requires the storage of the International Geomagnetic Reference Field (IGRF) [24] or World Magnetic Model (WMM) [25] on board the spacecraft, in addition to position knowledge typically obtained from a GPS. Furthermore, this restricts the use to low-Earth orbits, as the EMF is not well modeled beyond altitudes of $600\ km$.

While TAMs are very useful, they are also susceptible to high amounts of noise, due to external magnetic fields created from ferromagnetic materials, payloads, wiring, or actuators. In many applications, these external magnetic fields are removed by placing the TAM on a boom far away from the rest of the hardware

or electrical components of the spacecraft. However, as CubeSats are already constrained on mass and size, a TAM cannot be adequately separated from the remainder of the electrical components within the main structure. Thus, a real-time calibration technique must be used on-orbit to remove any external magnetic fields.

2.5.1.2 Sun Sensors

Sun sensors provide a measurement of the unit direction vector towards the sun. There are two types of sun sensors, coarse sun sensors (CSSs) and fine or digital sun sensors (DSSs). The CSS is typically made up of a single or multiple photocells or photodiodes, whose electric current outputs are directly proportional to the intensity of light that falls on them. DSSs are more intricate and can be made up of multiple slits with photosensitive material behind them. Both CSSs and DSSs are susceptible to albedo or any additional light that may be found in the field of view of the sensor itself, which can cause relatively large error stacking [8]. In optimal conditions, the CSS will have an angular resolution error $\leq 3°$, whereas the DSS will have angular resolution error of $1°$ or less. Sun sensors are a useful sensor for AD but do not always provide an effective measurement (i.e. when the Earth eclipses the sun).

2.5.1.3 Star Trackers

Star trackers are essentially digital cameras that calculate the unit direction vector to a given star based upon an internal star map stored onboard the spacecraft, similar to sun sensors. Star trackers also provide vector measurements to multiple star systems, allowing the use of only a single star tracker for a complete attitude solution. While star trackers are useful and very accurate, they can be

highly susceptible to external noise, such as albedo light, and can be extremely expensive ($\sim\$100{,}000$), which causes them to be unsuitable for small scale applications such as CubeSats. Moreover, they can often be very power hungry and massive [8].

2.5.2 AD State Filtering

So far, two methods of AD have been discussed: (1) using a rate gyro in an IMU to propagate the dynamics of the vehicle and (2) using aiding sensors to solve Wahba's problem. While the use of an IMU is simple, it cannot be the sole sensor as the noise propagation that occurs causes the attitude estimate to drift. Conversely, using only aiding sensors can be expensive and inefficient, and requires consistent measurement of external phenomena such as the sun's position vector. Additionally, no guarantees have been made on the quality of either method's estimate of the attitude, as all sensors have some form of noise.

In practice, *both* IMU and aiding sensors can be used together. Specifically, an AD system can combine or blend IMU and aiding sensor measurements to create an "optimal" (the definition of optimality can vary) estimate of the spacecraft's attitude, along with some metric of the quality of the estimate itself. The algorithm that blends the measurements together is often denoted as a filter, estimator, or observer [26]. A specific filter that is often used in estimating the attitude of a spacecraft is the Extended Kalman Filter (EKF), which is a non-linear extension of the general Kalman Filter (KF). EKFs are extremely useful in state estimation, as they combine sensor measurements with a stochastic system based around the dynamic and measurement models of the system itself. This allows both an estimate and a statistical metric, such as variance, of that estimate to be propagated

throughout time based upon a characterization of the noise within the system. Detailed information and derivation of both the KF and the EKF can be found in Appendix B. It is suggested that the reader familiarizes themselves with the general EKF before proceeding to Chapter 3.

2.6 Summary

Within this chapter, the concepts related to attitude determination (AD) were detailed. Focus was placed on the description of common reference frames used within spacecraft AD, along with the selected reference frames used within this thesis. Three attitude parameterizations, direction cosine matrices (DCMs), Euler angles, and quaternions, were discussed. The choice of quaternion as the main attitude parameterization was motivated, and useful quaternion mathematics and properties were highlighted.

Inertial based AD using rate gyroscopes within an inertial measurement unit (IMU) was described, along with the inherent problems that come with using an IMU as the sole AD sensor. A common gyroscope error model was shown, and the types of errors found within this model were explained. Attitude drift due to IMU noise was briefly discussed.

The description of IMU drift caused by noise motivated the discussion of inertially aided systems, specifically in the instance of vector matching or solving Wahba's problem. Common aiding sensors, such as three axis magnetometers (TAMs), sun sensor, and star trackers, were briefly described. State estimation and filtering, motivated by the blending of aiding and IMU sensor outputs, was

introduced. Specifically, the concept of Kalman filters (KFs) and extended Kalman filters (EKFs) (as shown in [26]) was briefly discussed.

3 Magnetometer-Based Single Vector Attitude Determination

3.1 Introduction

As seen in Chapter 2, the attitude of a spacecraft can be determined by using angular rate measurements from an IMU, external vector measurements used to solve Wahba's problem [9], or a combination of the two (filtering) [6] [8] [26]. However, within the framework of CubeSats, the architectures of these AD techniques are generally limited in cost, mass, and volume, necessitating the general use of commercial off-the-shelf (COTS) parts [5] [6]. For example, the choice of IMU can be limited to be of consumer grade [27] by cost and is often a micro electrical-mechanical system (MEMS) device to minimize volume and mass. Unfortunately, consumer grade IMUs are typically plagued by noisy sensor measurements [28], and prolonged use can cause attitude estimates to drift as seen by Figure 2.15. Conversely, the sole use of external sensors can be infeasible as the phenomena that these sensors measure is not always readily available (such as sun and star vector measurements). This can reduce the frequency of accurate AD solutions obtained which can limit science objectives and mission performance. Moreover, external vector measurements can require multiple expensive and massive sensors that are still prone to some form of noise corruption.

Current AD architectures typically solve for attitude in two ways: (1) by solving Wahba's problem analytically, using external vector measurements and recursive solvers such as QUEST, and (2) by blending external vector measurements with noisy inertial rates from an IMU in a filter format. In the first method, no state kinematics are included and as such no gyro measurement is

required. In the second method, a gyro is included to smooth estimates and to allow for an AD solution in the event that no aiding sensor measurements are available. Generally, mission requirements on the accuracy and estimate convergence speed, coupled with expected CubeSat operating conditions, can affect the choice of which scheme to use.

Within the past decade, multiple AD systems have been developed for CubeSat use. In [29], an attitude determination module is designed that uses sun vector measurements and a star tracker to obtain an attitude solution through time. While no gyros are included within this scheme, [29] posits that an IMU can be easily incorporated. As seen by the Cat-2 mission in [30], QUEST is utilized in combination with a low-pass filter to provide an attitude estimate in the absence of gyros, or in a low-power configuration. This option uses two vector measurements obtained via a TAM and 6 coarse photodiodes. Within [31], Wahba's problem is solved via a singular value decomposition (SVD) method. Angular rates themselves are estimated via an extended Kalman filter (EKF) architecture to refine the attitude estimates throughout time.

While not including a rate gyro may reduce the fault modes within an AD scheme, as posited by [32], it does not allow for AD solutions in environments where external measurements are not readily available (i.e. Earth eclipse of the sun). As such, many current CubeSat AD architectures rely on the use of filters to blend inertial gyro measurements with external reference measurements. During the Cat-2 mission [29], when gyroscope readings are available, a multiplicative extended Kalman filter (MEKF) is used to fuse kinematics with the dual vector measurements in a filtering methodology. Similarly, in [33], the same MEKF is used to estimate attitude on orbit using a TAM and a sun sensor. Within [34], a

hybrid attitude determination approach is performed, utilizing multiple sensors and an EKF to estimate the attitude on-orbit. Additionally, the QUEST algorithm is implemented prior to EKF use to ensure that attitude estimates do not diverge. As seen in [35], a similar approach is taken, utilizing both QUEST and an EKF during different flight conditions to obtain an attitude solution.

While the use of the EKF is common, it is not without its limitations. Namely, the linearization of the state dynamics and measurements does not preserve problem constraints, which can lead to estimate divergence. To mitigate this, some AD architectures have used the unscented Kalman filter (UKF). Within [6], a UKF is used to propagate 13 sigma points of the satellite attitude kinematics through time, blending estimates with measurements from a TAM and a sun sensor. In [36], a similar UKF architecture is developed, with the inclusion of robustness characteristics that reject external perturbations to the measurement models. While the UKF maintains problem constraints by not performing a linearization at each time update, it requires more computational power to solve for each sigma point. Moreover, as state vectors increase in size, computation time increases drastically. To reduce computation time, implementation of fast unscented Kalman filters are proposed in [37]. However, within this use, attitude is parameterized via Euler angles, resulting in a kinematic singularity dependent upon the system dynamics.

Within [38] [39] [40], more novel techniques are used to determine the attitude of a spacecraft. In [38], the attitude of a CubeSat is determined via processing the angles-of-arrival and angles-of-departure of communications measurements from a formation of flying CubeSats. Reference [39] shows that CubeSat orbit and attitude determination are performed by optical tracking of

pulsing LEDs on-board a CubeSat in flight. Within [40], the attitude of a spinning bob is estimated by assuming the angular moment vector is fixed in inertial space, and utilizing a TAM to supply external measurement information to determine the nutation angle of the vehicle.

As shown above, there are multiple ways to solve for the attitude of a CubeSat. The goal of this chapter is to expand upon the AD method shown in [41], in which a MEKF was used with a TAM as the sole aiding sensor. Specifically, this chapter discusses the Earth's magnetic field as a measurement vector and develops CubeSat dynamic and measurement models that are used within an EKF architecture. This EKF is also used to calibrate the gyroscope on-orbit by estimating the attitude of the CubeSat in addition to gyroscope errors as defined in Chapter 2. Focus is given to details associated with understanding the selection of noise covariance models used within the EKF.

3.2 Earth Magnetic Field as a Measurement Vector

In many applications, the Earth's magnetic field (EMF) vector is used as one of the vector measurements required for a solution to Wahba's problem [33] [30] [42]. However, the AD solution developed in this chapter focuses on using the EMF vector as the sole aiding measurement. To accurately describe this methodology, we need to discuss the EMF and its characteristics.

The EMF is a 3-D natural phenomenon that is always present around the Earth. Depending on the proximity to Earth's surface, the EMF can resemble a magnetic dipole as seen in the top image of Figure 3.1. However, as altitude above the surface increases, the EMF reduces in strength by a $1/r^3$ falloff [8] and can vary greatly depending on solar phenomena. As such, the EMF is generally well

modeled up to $600\,km$ above the Earth's surface [24] but uncertain at higher altitudes. This limits EMF use as an attitude aiding measurement to Low-Earth-Orbit (LEO).

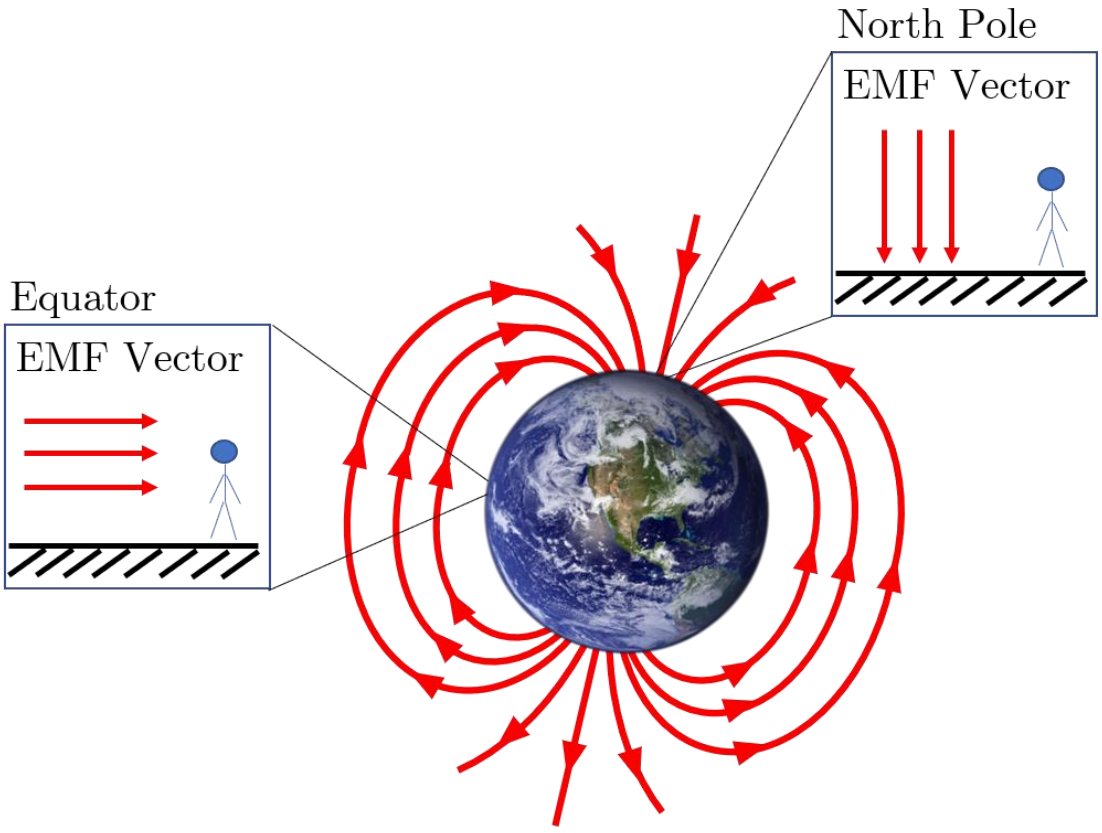

Figure 3.1 Simplistic visualization of the Earth magnetic field (EMF).

A measurement of the EMF vector can change in magnitude and direction depending upon where on the Earth's surface it is being measured. Consider the simplistic EMF seen in Figure 3.1. A measurement of the EMF vector at any point along the equator will be horizontal with respect to the Earth's surface and will be pointing towards the North pole. Now consider an EMF vector measurement at the North pole itself. The vector measurement will be pointing directly downwards

into the Earth's surface. As we move North from the equator, the local EMF vector's direction will change as a function of how fast we are travelling and the altitude at which we make these vector measurements. For example, consider the 2D case shown in Figure 3.2. If three vehicles make an initial EMF vector measurement at t_0 at position x_0, then travel North and then make another EMF measurement at time t_1, there will be some angular difference between the initial and current EMF vectors denoted by γ. For a given $\Delta t = t_1 - t_0$, the size of γ is generally dependent on the speed of the vehicles themselves.

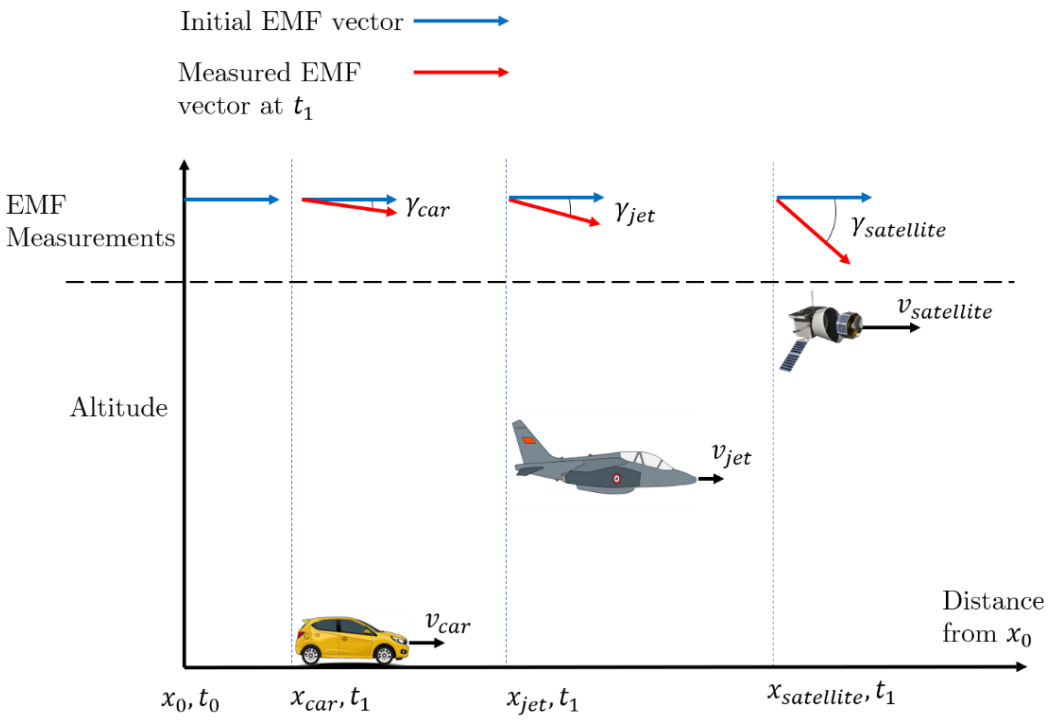

Figure 3.2 Difference between EMF measurements based on vehicle speeds.

In many applications, such as the one shown in [42], the EMF vector remains relatively constant. However, in satellite applications, the EMF vector can change

by large amounts over short periods of times due to the orbital nature of the vehicle. We can utilize this fact to help solve for the attitude. Recall that a requirement of Wahba's problem is to have two noncollinear vector measurements to resolve the attitude of a vehicle unambiguously. However, in this chapter we will try to answer the following question:

If we have knowledge of some initial EMF vector at an initial time, and have travelled a sufficient distance such that another EMF vector measurement is significantly different than the initial measurement, can we utilize these two vector measurements to solve Wahba's problem?

Stated differently, does the EMF vector vary enough with time to be used as the sole AD aiding vector measurement? This question is the backbone of the AD solution presented in [41] and elaborated upon in this thesis. In the CubeSat case, the answer is dependent upon four parameters:

- The speed and altitude of the CubeSat
- The rotational rates of the CubeSat
- The inclination of the CubeSat's orbit
- The frequency at which measurements occur

The remainder of this chapter focuses on developing the dynamic and measurement models required to utilize this AD scheme in an EKF framework based on single-vector EMF measurements. A discussion of simulation results and the importance of the above parameters is given in Chapter 5.

3.3 EKF Architecture

As attitude dynamics of a spacecraft in orbit are inherently non-linear [8], we choose to use an EKF architecture for estimating the attitude. The goal of the EKF developed will be to iteratively estimate the attitude quaternion, q_{SE}, in addition to scale factor and bias errors present on the gyroscope, thereby calibrating the gyroscope in-flight.

Recall that the EKF linearizes the state dynamics about the optimal state trajectory at each time step. As such, the EKF is estimating the deviations of the state vector about this optimal trajectory, denoted by $\delta\bar{x}$. In the instance of our filter, the state error vector can be given by

$$\delta\bar{x} = \bar{x} - \hat{\bar{x}} = \begin{bmatrix} \delta\bar{q}_{S\hat{S}}^T & \delta\bar{b}_g^T & \delta\overline{sf}^T \end{bmatrix}^T \tag{3.1}$$

where $\delta\bar{q}_{S\hat{S}}$, $\delta\bar{b}_g$, and $\delta\overline{sf}$ represent the errors between the true and estimated state values. To estimate these parameters, the EKF will require the development of sensor models, a dynamic or time update model, and a measurement model. This section formulates the linearized error-state version of these required models based upon the use of a three-axis rate gyroscope, or "gyro", and a three-axis magnetometer (TAM). For more details on the general EKF, see Appendix B.

3.3.1 Sensor Models

3.3.1.1 Gyro Measurement Model

A gyro measures the angular velocity of the body it is attached to with respect to some inertial frame, as seen in Chapter 2. In general, a gyro measurement is corrupted by multiple errors that must be accounted for within its measurement

model. A model for a gyro measuring angular rates between a body frame $\boldsymbol{\mathcal{F}_S}$ and inertial frame $\boldsymbol{\mathcal{F}_E}$ can be given by

$$C_{Sg}\bar{\omega}_m^{gE}(t) = \left(1_3 + SF(t)\right)\left(\bar{\omega}^{SE}(t)\right) + C_{Sg}\left(\bar{b}_g(t) + \bar{n}_g(t)\right) \tag{3.2}$$

where $\bar{\omega}_m^{gE}$ is the 3×1 angular velocity measured in the gyro frame, $\bar{\omega}^{SE}$ is the true angular velocity in the body frame, $\bar{b}_g(t)$ is the time varying bias vector, and $\bar{n}_g$ is the additive wideband noise vector. $SF(t)$ represents a matrix of slowly time varying scale factor errors such that

$$SF(t) = \begin{bmatrix} sf_{g1}(t) & 0 & 0 \\ 0 & sf_{g2}(t) & 0 \\ 0 & 0 & sf_{g3}(t) \end{bmatrix} \tag{3.3}$$

where sf_g represent scale factors in each axis of the gyro measurement, resolved in the gyro frame $\boldsymbol{\mathcal{F}_g}$. C_{Sg} is the 3×3 DCM that represents any rotation between the gyro frame and the body frame. In the instance where the gyro frame axes are perfectly aligned with the body frame axes, this matrix is the identity matrix 1_3 Similarly, $SF = 0_3$ when there are no scale factor errors present.

A single scale factor error is assumed to vary via a random walk process modeled as follows:

$$\dot{sf}(t) = n_{sf}(t) \tag{3.4a}$$

$$E\{n_{sf}(t)\} = 0 \tag{3.4b}$$

$$E\{n_{sf}(t)n_{sf}(\tau)^T\} = \sigma_{sf}^2\delta(t-\tau) \tag{3.4c}$$

where σ_{sf} is the standard deviation of the scale factor white noise and $\delta(t-\tau)$ is the Dirac delta function.

The time varying bias can be modeled as

$$\bar{b}_g(t) = \bar{b}_{g,0} + \bar{b}_{g,1}(t) \tag{3.5}$$

where $\bar{b}_{g,0}$ represents a constant null-shift bias vector and $\bar{b}_{g,1}(t)$ represents a time varying colored noise process, or bias drift rate. The bias drift rate is often modeled as a 1st order Gauss-Markov (GM) correlated process. In the instance of a single axis gyro, the GM process is given by:

$$\dot{b_g}(t) = \dot{b_{g,1}}(t) = -\frac{1}{\tau_{GM}} b_{g,1}(t) + n_g^b(t) \tag{3.6a}$$

$$E\{b_{g,1}(t)\} = 0 \tag{3.6b}$$

$$E\{b_{g,1}(t) b_{g,1}(\tau_{GM})^T\} = \sigma_{IRB}^2 \exp\left[-\frac{t}{\tau_{GM}}\right] \tag{3.6c}$$

$$Q_{b_{g,1}} = \frac{2\sigma_{IRB}^2}{\tau_{GM}} \tag{3.6d}$$

where σ_{IRB} refers to the standard deviation of the correlated process $b_{g,1}$, τ_{GM} is the correlation time of process $b_{g,1}$, n_g^b is the driving process noise, and $Q_{b_{g,1}}$ is the power spectral density of n_g^b. Consistent with literature in inertial navigation, we refer to the standard deviation of this process as σ_{IRB} where IRB stands In-Run bias. The driving process noise n_g^b is modeled as a zero-mean, Gaussian, white noise process such that

$$E\{n_g^b(t)\} = 0 \tag{3.7a}$$

$$E\{n_g^b(t) n_g^b(\tau)^T\} = \sigma_b^2 \delta(t - \tau) \tag{3.7b}$$

where σ_b is the standard deviation of the driving process noise n_g^b.

The additive white noise (also known as wideband or output noise) vector given by $\bar{n}_g$ can be represented by a zero-mean, Gaussian, white noise process. This is given for a single gyro by

$$E\{n_g(t)\} = 0 \tag{3.8a}$$

$$E\{n_g(t)n_g(\tau)^T\} = \sigma_g^2\delta(t-\tau) \tag{3.8b}$$

where σ_g stands for the standard deviation of process $\bar{n}_g$. This standard deviation corresponds to the angular random walk (ARW, in $rad/\sqrt{sec}$) term often listed on specifications sheets.

The estimated value of the measured angular velocity can be given by taking the expectation of Equation (3.2) such that

$$E\{C_{Sg}\bar{\omega}_m^{gE}(t)\} = E\{(1_3 + SF(t))(\bar{\omega}^{SE}(t) + C_{Sg}(\bar{b}_g(t) + \bar{n}_g(t)))\}$$

$$C_{Sg}\bar{\omega}_m^{gE}(t) = \left(1_3 + \widehat{SF}(t)\right)\hat{\bar{\omega}}^{SE}(t) + C_{Sg}\hat{\bar{b}}_g(t)$$

$$\hat{\bar{\omega}}^{SE}(t) = \left(1_3 + \widehat{SF}(t)\right)^{-1} C_{Sg}\left(\bar{\omega}_m^{gE}(t) - \hat{\bar{b}}_g(t)\right) \tag{3.9a}$$

with the true angular velocity given by

$$\bar{\omega}^{SE}(t) = \left(1_3 + SF(t)\right)^{-1} C_{Sg}\left(\bar{\omega}_m^{gE}(t) - \bar{b}_g(t) - \bar{n}_g(t)\right) \tag{3.9b}$$

where $\hat{\bar{\omega}}^{SE}$ is the estimate of the angular velocity, $\hat{\bar{b}}_g(t)$ is the estimate of the gyro bias vector, and $\left(1_3 + \widehat{SF}(t)\right)^{-1}$ is the inverse matrix of the estimated scale factors of the form

$$\left(1_3 + \widehat{SF}(t)\right)^{-1} = \begin{bmatrix} 1 + \widehat{sf}_{g1}(t) & 0 & 0 \\ 0 & 1 + \widehat{sf}_{g2}(t) & 0 \\ 0 & 0 & 1 + \widehat{sf}_{g3}(t) \end{bmatrix}^{-1}$$

$$\left(1_3 + \widehat{SF}(t)\right)^{-1} \approx \left(1_3 - \widehat{SF}(t)\right) = \begin{bmatrix} 1 - \widehat{sf}_{g1}(t) & 0 & 0 \\ 0 & 1 - \widehat{sf}_{g2}(t) & 0 \\ 0 & 0 & 1 - \widehat{sf}_{g3}(t) \end{bmatrix} \quad (3.10)$$

where we assume $\widehat{sf}(t)$ are sufficiently small. As both C_{Sg} and $\bar{\omega}_m^{gE}$ are deterministic (known) parameters, their expected values are simply the values themselves.

The difference between the true and estimated angular velocity can be obtained by substituting Equation (3.2) into Equation (3.9) and simplifying such that

$$\delta\bar{\omega}^{SE}(t) = \bar{\omega}^{SE}(t) - \hat{\bar{\omega}}^{SE}(t)$$

$$= \left(1_3 - SF(t)\right)C_{Sg}\bar{\omega}_m^{gE} - \left(1_3 - SF(t)\right)C_{Sg}\bar{b}_g(t) - \left(1_3 - SF(t)\right)C_{Sg}\bar{n}_g$$
$$- \left(1_3 - \widehat{SF}(t)\right)C_{Sg}\bar{\omega}_m^{gE} + \left(1_3 - \widehat{SF}(t)\right)C_{Sg}\hat{\bar{b}}_g(t)$$

$$= -\delta SF(t)C_{Sg} - C_{Sg}\delta\bar{b}_g(t) + \left(\delta SF(t) + \widehat{SF}(t)\right)C_{Sg}\left(\delta\bar{b}_g(t) + \hat{\bar{b}}_g(t)\right)$$
$$- \widehat{SF}(t)C_{Sg}\hat{\bar{b}}(t) - C_{Sg}\bar{n}_g + \left(\delta SF(t) + \widehat{SF}(t)\right)C_{Sg}\bar{n}_g(t)$$

$$= -\delta SF(t)C_{Sg}\bar{\omega}_m^{gE} - C_{Sg}\delta\bar{b}_g(t) + \delta SF(t)C_{Sg}\delta\bar{b}_g(t) + \delta SF(t)C_{Sg}\hat{\bar{b}}_g(t)$$
$$+ \widehat{SF}(t)C_{Sg}\delta\bar{b}_g(t) + \widehat{SF}(t)C_{Sg}\hat{\bar{b}}_g(t) - \widehat{SF}(t)C_{Sg}\hat{\bar{b}}_g(t) - C_{Sg}\bar{n}_g(t)$$
$$+ \delta SF(t)C_{Sg}\bar{n}_g(t) + \widehat{SF}(t)C_{Sg}\bar{n}_g(t)$$

$$\delta\bar{\omega}^{SE}(t) = -diag\left(C_{Sg}\left(\bar{\omega}_m^{gE}(t) - \hat{\bar{b}}_g(t)\right)\right)\delta\overline{sf}(t) - \left(1_3 - \widehat{SF}(t)\right)C_{Sg}\delta\bar{b}_g(t)$$
$$- \left(1_3 - \widehat{SF}(t)\right)C_{Sg}\bar{n}_g(t) \quad (3.11a)$$

where we have assumed that higher order terms are negligible. The error values of the states can be given by

$$\delta SF(t) = SF(t) - \widehat{SF}(t) \quad (3.11b)$$

$$\delta\bar{b}_g(t) = \bar{b}_g(t) - \hat{\bar{b}}_g(t) = \bar{b}_{g,1}(t) \tag{3.11c}$$

with the differential matrix of scale factors given by

$$\delta SF(t) = diag\left(\delta\overline{sf}(t)\right) \tag{3.12a}$$

$$\delta\overline{sf}(t) = \begin{bmatrix} \delta sf_{g1}(t) \\ \delta sf_{g2}(t) \\ \delta sf_{g3}(t) \end{bmatrix} \tag{3.12b}$$

The rate of change of a single scale factor differential can be obtained by subtracting the expected value of Equation (3.4a) from itself such that

$$\dot{\widehat{sf}}(t) = E\{\dot{sf}(t)\} = 0 \tag{3.13a}$$

$$\delta\dot{sf}(t) = \dot{sf}(t) - \dot{\widehat{sf}}(t) = n_{sf}(t) \tag{3.13b}$$

with vector representation given as

$$\delta\dot{\overline{sf}}(t) = \bar{n}_{sf}(t) \tag{3.14}$$

The rate of change of $\delta\bar{b}_g$ can similarly be determined by taking the derivative with respect to time of Equation (3.11c)

$$\dot{\hat{\bar{b}}}_g(t) = E\left\{\dot{\bar{b}}_g(t)\right\} = 0 \tag{3.15}$$

with

$$\delta\dot{\bar{b}}_g(t) = \frac{d}{dt}\left(\bar{b}_g(t)\right) - \frac{d}{dt}\left(\hat{\bar{b}}_g(t)\right) \tag{3.16a}$$

$$\delta\dot{\bar{b}}_g(t) = -\frac{1}{\tau_{GM}}\bar{b}_{g,1}(t) + \bar{n}_g^b(t) = -\frac{1}{\tau_{GM}}\delta\bar{b}_g(t) + \bar{n}_g^b(t) \tag{3.16b}$$

where we have made use of the fact that $\bar{b}_{g,1}(t) = \delta\bar{b}_g(t)$ and noted that the expected value of $\dot{\bar{b}}_g$ is 0.

3.3.1.2 Magnetometer Measurement Model

A magnetometer measures the local magnetic field surrounding the body it is attached to, as discussed in Chapter 2. A measurement model for the magnetometer can be given by [43]

$$C_{Sm}\bar{m}_m^m(t) = C_{sf,m}(t)C_{si}(t)\left(\bar{m}^S(t) + \bar{b}_m^{hi}(t) + \bar{n}_m(t)\right) \tag{3.17}$$

where C_{Sm} is the 3×3 DCM that represents any rotation between the magnetometer frame and the spacecraft body frame, $\bar{m}_m^m$ is the measured magnetic field vector in the magnetometer frame, $\bar{m}^S$ is the true magnetic field vector in the body frame, $C_{sf,m}$ is the 3×3 diagonal matrix of magnetometer scale factor errors such that

$$C_{sf,m}(t) = \begin{bmatrix} 1 + sf_{m1}(t) & 0 & 0 \\ 0 & 1 + sf_{m2}(t) & 0 \\ 0 & 0 & 1 + sf_{m3}(t) \end{bmatrix} \tag{3.18}$$

similar to the gyroscope scale factor matrix SF. The 3×3 matrix denoted by C_{si} is a matrix of "soft-iron" biases due to external fluctuations in the magnetic field, $\bar{b}_m^{hi}$ is the vector of "hard-iron" biases due to the residual magnetic field caused by the spacecraft's electronic components, and $\bar{n}_m$ is additive gaussian, zero-mean white noise to the magnetometer measurements. For the purpose of this thesis, it is assumed that all magnetometer measurements have be calibrated such that there are no soft-iron, hard-iron, or scale factor errors present. Additionally, it is assumed that the magnetometer is perfectly aligned with the body frame. This simplifies Equation (3.17) into

$$\bar{m}_m^S = \bar{m}^S + \bar{n}_m(t) \tag{3.19a}$$

$$E\{\bar{n}_m(t)\} = 0 \tag{3.19b}$$

$$E\{\bar{n}_m(t)\bar{n}_m(\tau)^T\} = \sigma_{mag}^2\delta(t-\tau) \tag{3.19c}$$

where σ_{mag} is the standard deviation of the wideband magnetometer output noise. The scenarios in which Equation (3.19) is an accurate representation are discussed further in Chapter 6.

3.3.2 EKF Time Update

3.3.2.1 Attitude Kinematics Equations

The attitude of the system is parameterized via the 4×1 quaternion and can be propagated through time such that

$$q_{SE}(t) = \begin{bmatrix} q_0(t) \\ \bar{q}(t) \end{bmatrix} = \begin{bmatrix} q_0(t) \\ q_1(t) \\ q_2(t) \\ q_3(t) \end{bmatrix} \tag{3.20a}$$

$$\dot{q}_{SE}(t) = \frac{1}{2}\begin{bmatrix} 0 \\ \bar{\omega}^{SE}(t) \end{bmatrix} \otimes q_{SE}(t) \tag{3.20b}$$

$$\dot{q}_{SE}(t) = \frac{1}{2}\begin{bmatrix} 0 & -\bar{\omega}^{SE,T}(t) \\ \bar{\omega}^{SE}(t) & -\bar{\omega}^{SE,\times}(t) \end{bmatrix} q_{SE}(t) = \frac{1}{2}\Omega\big(\bar{\omega}^{SE}(t)\big)q_{SE}(t) \tag{3.20c}$$

where $\bar{\omega}^{SE,T}$ refers to the 1×3 transpose of the angular velocity vector and $\bar{\omega}^{SE,\times}$ is the skew symmetric matrix of $\bar{\omega}^{SE}$. The additional equation of Equation (3.20c) is defined as it is useful for derivation and removes the use of quaternion multiplication [44]. For the remainder of this chapter, we will neglect the inclusion of (t) to ease notation. Note that depending on convention used, these equations will be slightly different.

We assume that a multiplication of two quaternions, q_{gS} and q_{SE}, follows the convention suggested by the multiplication of two DCMs

$$C_{gE}(q_{gE}) = C_{gS}\big(q_{gS}\big)C_{SE}(q_{SE}) = C_{gE}\big(q_{gS} \otimes q_{SE}\big) \tag{3.21}$$

where C_{gE} represents the DCM from frame $\boldsymbol{\mathcal{F}_E}$ to frame $\boldsymbol{\mathcal{F}_g}$ that is parameterized by the multiplication of individual quaternions q_{gS} and q_{SE}. This represents an initial rotation to $\boldsymbol{\mathcal{F}_S}$ from $\boldsymbol{\mathcal{F}_E}$ parameterized by q_{SE} followed by another rotation from $\boldsymbol{\mathcal{F}_S}$ to $\boldsymbol{\mathcal{F}_g}$ parameterized by q_{gS}.

In the instance where a rotation between two frames is small, the quaternion and DCM parameterizations of this small angle assumption (SAA) are

$$q_{SAA} \sim \begin{bmatrix} 1 \\ \delta q_1 \\ \delta q_2 \\ \delta_{q3} \end{bmatrix} = \begin{bmatrix} 1 \\ \delta \bar{q} \end{bmatrix} = \delta q_{SAA} \tag{3.22a}$$

$$C_{SAA}(q_{SAA}) \sim 1_3 - 2\delta \bar{q}^{\times} \tag{3.22b}$$

where the scalar portion of the quaternion is approximately 1 and the vector portion resembles some small quaternion vector, denoted by $\delta \bar{q}$. The DCM of this small angle assumption, C_{SAA} parameterized by the small quaternion q_{SAA}, resembles the 3×3 identity matrix minus the skew symmetric matrix (denoted by $(\cdot)^{\times}$) of the small quaternion vector.

One of the goals of the EKF is to estimate the attitude of the vehicle, and thus estimate the quaternion between the inertial frame and the spacecraft frame. This estimate can be quantified by determining a quaternion between the inertial frame, $\boldsymbol{\mathcal{F}_E}$, and an estimate body frame, $\boldsymbol{\mathcal{F}_{\hat{S}}}$, denoted by $q_{\hat{S}E}$. The true quaternion can be related to the estimate quaternion via the following relationship [8]

$$q_{SE} = \delta q_{S\hat{S}} \otimes q_{\hat{S}E} \tag{3.23}$$

where the true quaternion q_{SE} is equivalent to the estimate quaternion, $q_{\hat{S}E}$, multiplied by some small "error" quaternion, $\delta q_{S\hat{S}}$. Graphically, this can be represented by Figure 3.3, in which the true attitude can be obtained by first

performing a rotation from $\boldsymbol{\mathcal{F}_E}$ to the estimate body frame $\boldsymbol{\mathcal{F}_{\hat{S}}}$, followed by a corrective rotation from the estimate body frame $\boldsymbol{\mathcal{F}_{\hat{S}}}$ to the true body frame $\boldsymbol{\mathcal{F}_S}$. This corrective rotation can be thought of as a small angular rotation about the estimated body frame.

The quaternion error can be obtained by rearranging Equation (3.23) to obtain the following

$$\delta q_{S\hat{S}} = q_{SE} \otimes q_{\hat{S}E}^{-1} = q_{SE} \otimes q_{E\hat{S}} \tag{3.24}$$

where the inverse of $q_{\hat{S}E}$ is equivalent to $q_{E\hat{S}}$ such that $q_{\hat{S}E}^{-1} = q_{E\hat{S}}$. As an aside, the quaternion notation used above allows for the interior subscripts of quaternion multiplication to be equivalent, resulting in a quaternion that is the parameterization of the attitude between the exterior subscripts of the multiplied quaternions. In general, it is a method to ensure the quaternion multiplication is correct.

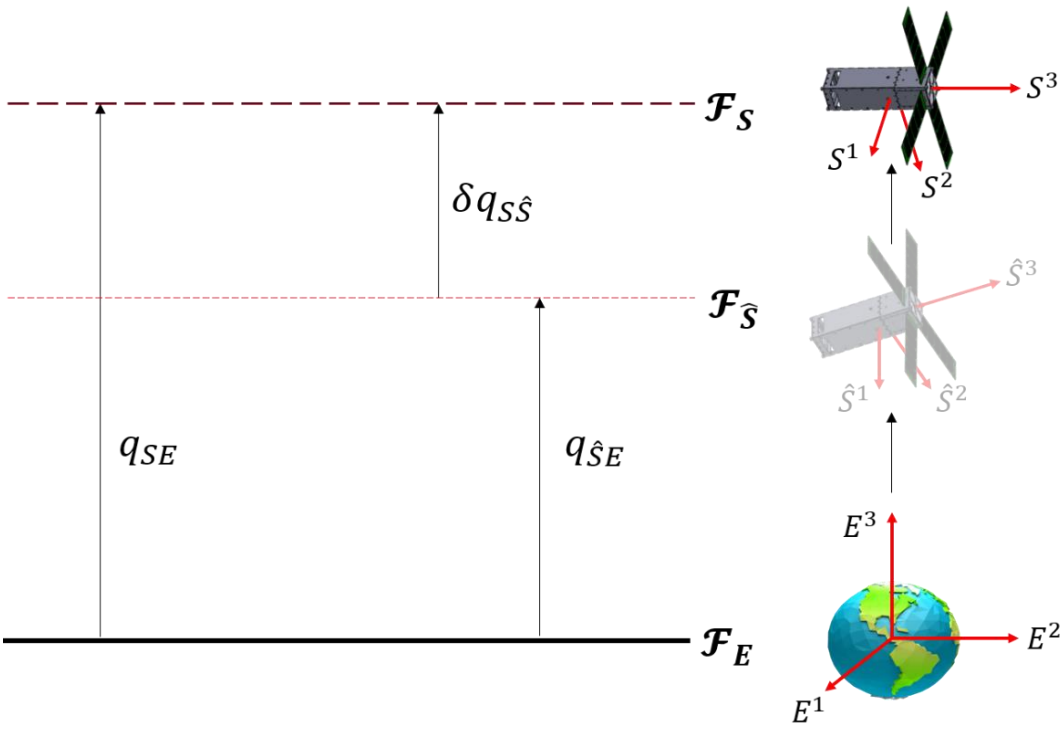

Figure 3.3 Visual representation of attitude quaternion multiplication.

The rate of change of the quaternion error $\delta q_{S\hat{S}}$, $\delta \dot{q}_{S\hat{S}}$, can be obtained by taking the time derivative of Equation (3.24) such that

$$\delta \dot{q}_{S\hat{S}} = q_{SE} \dot{\otimes} q_{\hat{S}E}^{-1} = \dot{q}_{SE} \otimes q_{\hat{S}E}^{-1} + q_{SE} \otimes \dot{q}_{\hat{S}E}^{-1} \tag{3.25}$$

The rate of change of the estimate quaternion is given by taking the expectation of Equation (3.20c)

$$\dot{q}_{\hat{S}E} = E\{\dot{q}_{SE}\} = E\left\{\frac{1}{2}\Omega(\bar{\omega}^{SE})q_{SE}\right\} = \frac{1}{2}\Omega(\hat{\bar{\omega}}^{SE})q_{\hat{S}E} \tag{3.26}$$

where its inverse can be shown to be [44]

$$\dot{q}_{\hat{S}E}^{-1} = q_{\hat{S}E}^{-1} \otimes -\frac{1}{2}\begin{bmatrix}0\\ \hat{\bar{\omega}}^{SE}\end{bmatrix} = -\frac{1}{2}\begin{bmatrix}0 & -\hat{\bar{\omega}}^{SE,T}\\ \hat{\bar{\omega}}^{SE,\times}\end{bmatrix} q_{\hat{S}E}^{-1} = -\frac{1}{2}\mathrm{B}(\hat{\bar{\omega}}^{SE})q_{\hat{S}E}^{-1} \tag{3.27}$$

Substituting Equations (3.27) and (3.20b) into Equation (3.25), the rate of change of the quaternion error is

$$\delta\dot{q}_{S\hat{S}} = \frac{1}{2}\begin{bmatrix}0\\ \bar{\omega}^{SE}\end{bmatrix} \otimes q_{SE} \otimes q_{\hat{S}E}^{-1} + q_{SE} \otimes q_{\hat{S}E}^{-1} \otimes -\frac{1}{2}\begin{bmatrix}0\\ \hat{\bar{\omega}}^{SE}\end{bmatrix} \tag{3.28}$$

where we have maintained the quaternion multiplication. Noting that $q_{SE} \otimes q_{\hat{S}E}^{-1} = \delta q_{S\hat{S}}$, we can simplify Equation (3.28) to be

$$\delta\dot{q}_{S\hat{S}} = \frac{1}{2}\begin{bmatrix}0\\ \bar{\omega}^{SE}\end{bmatrix} \otimes \delta q_{S\hat{S}} + \delta q_{S\hat{S}} \otimes -\frac{1}{2}\begin{bmatrix}0\\ \hat{\bar{\omega}}^{SE}\end{bmatrix} \tag{3.29}$$

Using the definitions of $\Omega(\cdot)$ and $\mathrm{B}(\cdot)$, Equation (3.29) can be further simplified to be

$$\delta\dot{q}_{S\hat{S}} = \frac{1}{2}\left(\Omega(\bar{\omega}^{SE}) - \mathrm{B}(\hat{\bar{\omega}}^{SE})\right)\delta q_{S\hat{S}} \tag{3.30}$$

where $\Omega(\bar{\omega}^{SE})$ and $\mathrm{B}(\hat{\bar{\omega}}^{SE})$ are defined in Equations (3.20c) and (3.27) respectively. At this point, we have reduced the quaternion error propagation to be a function of the estimated and truth angular velocities. If we define the difference between the true angular velocity and the estimate angular velocity as

$$\delta\bar{\omega}^{SE} = \bar{\omega}^{SE} - \hat{\bar{\omega}}^{SE} \tag{3.31}$$

similar to Equation (3.11a), then we can rewrite $\bar{\omega}^{SE}$ as

$$\bar{\omega}^{SE} = \delta\bar{\omega}^{SE} + \hat{\bar{\omega}}^{SE} \tag{3.32}$$

and substitute Equation (3.32) into Equation (3.30) and simplify to obtain

$$\delta\dot{q}_{S\hat{S}} = \frac{1}{2}\begin{bmatrix}0 & -\delta\bar{\omega}^{SE,T}\\ \delta\bar{\omega}^{SE} & -\delta\bar{\omega}^{SE,\times}\end{bmatrix}\delta q_{S\hat{S}} - \begin{bmatrix}0\\ \hat{\bar{\omega}}^{SE,\times}\end{bmatrix}\delta q_{S\hat{S}} \tag{3.33}$$

where we have not made any assumptions on the size of the angular rotation parameterized by $\delta\dot{q}_{S\hat{S}}$. Writing Equation (3.33) in terms of $\delta\dot{q}_{0,S\hat{S}}$ and $\delta\dot{\bar{q}}_{S\hat{S}}$, we have

$$\delta\dot{q}_{0,S\hat{S}} = -\frac{1}{2}\delta\bar{\omega}^{SE,T}\delta\bar{q}_{S\hat{S}} \tag{3.34a}$$

$$\delta\dot{\bar{q}}_{S\hat{S}} = \tfrac{1}{2}\left(\delta\bar{\omega}^{SE}\delta q_{0,S\hat{S}} - (\delta\bar{\omega}^{SE} + 2\widehat{\bar{\omega}}^{SE})^{\times}\delta\bar{q}_{S\hat{S}}\right) \tag{3.34b}$$

If we assume that the quaternion representation of $\delta\dot{q}_{S\hat{S}}$ denotes a small angle and that multiples of higher order terms are negligible, then the SAA can be invoked in the format of Equation (3.22a) such that the rate of change of the error quaternion can now be written as

$$\delta\dot{q}_{0,S\hat{S}} \approx 0 \tag{3.35a}$$

$$\delta\dot{\bar{q}}_{S\hat{S}} = \frac{1}{2}(\delta\bar{\omega}^{SE}) - \widehat{\bar{\omega}}^{SE,\times}\delta\bar{q}_{S\hat{S}} \tag{3.35b}$$

where

$$\widehat{\bar{\omega}}^{SE} = \left(1_3 - \widehat{SF}\right)C_{Sg}\left(\bar{\omega}_m^{gE} - \hat{\bar{b}}_g\right) \tag{3.9a}$$

$$\begin{aligned}\delta\bar{\omega}^{SE} = -diag\left(C_{Sg}\left(\bar{\omega}_m^{gE} - \hat{\bar{b}}_g\right)\right)\delta\overline{sf} - \left(1_3 - \widehat{SF}\right)C_{Sg}\delta\bar{b}_g \\ -\left(1_3 - \widehat{SF}(t)\right)C_{Sg}\bar{n}_g\end{aligned} \tag{3.11a}$$

with the assumption that the scale factors are sufficiently small. We note that the rate of change of the scalar component is considered to be negligible. The rate of change of the vector portion of the quaternion is a function of the array of scale factor differentials, δSF, the bias vector errors, $\delta\bar{b}_g$, measured angular velocity, $\bar{\omega}_m^{gE}$, and the estimated angular velocity $\widehat{\bar{\omega}}^{SE}$. The equations formulated within this section are grouped below for clarity.

$$\delta\dot{q}_{0,S\hat{S}} \approx 0 \tag{3.35a}$$

$$\delta\dot{\bar{q}}_{S\hat{S}} = \frac{1}{2}(\delta\bar{\omega}^{SE}) - \hat{\bar{\omega}}^{SE,\times}\delta\bar{q}_{S\hat{S}} \tag{3.35b}$$

$$\dot{q}_{\hat{S}E} = \frac{1}{2}\begin{bmatrix} 0 & -\hat{\bar{\omega}}^{SE,T} \\ \hat{\bar{\omega}}^{SE} & -\hat{\bar{\omega}}^{SE,\times} \end{bmatrix} q_{\hat{S}E} = \frac{1}{2}\Omega(\hat{\bar{\omega}}^{SE})q_{\hat{S}E} \tag{3.26}$$

$$\delta\dot{\bar{b}}_g = -\frac{1}{\tau_{GM}}\delta\bar{b}_g + \bar{n}_g^b \tag{3.16b}$$

$$\dot{\hat{\bar{b}}}_g = 0 \tag{3.15}$$

$$\delta\dot{\overline{sf}} = \bar{n}_{sf} \tag{3.14}$$

$$\dot{\hat{\overline{sf}}} = 0 \tag{3.13a}$$

with the estimated angular velocity given by

$$\hat{\bar{\omega}}^{SE} = \left(1_3 - \widehat{SF}\right)C_{Sg}\left(\bar{\omega}_m^{gE} - \hat{\bar{b}}_g\right) \tag{3.9}$$

and the inverse scale factor matrix as

$$\left(1_3 + \widehat{SF}\right)^{-1} \approx \left(1_3 - \widehat{SF}\right) = \begin{bmatrix} 1 - \widehat{sf}_{g1} & 0 & 0 \\ 0 & 1 - \widehat{sf}_{g2} & 0 \\ 0 & 0 & 1 - \widehat{sf}_{g3} \end{bmatrix} \tag{3.10}$$

3.3.2.2 State Error Covariance Propagation

To propagate the state covariance on the EKF estimate, the continuous time error state equations must be placed into state space format such that

$$\delta\dot{\bar{x}}(t) = F(t)\delta\bar{x}(t) + L(t)\bar{n}(t) \tag{3.36}$$

where

$$\delta\bar{x} = \begin{bmatrix} \delta\bar{q}_{S\hat{S}}^T & \delta\bar{b}_g^T & \delta\overline{sf}^{,T} \end{bmatrix}^T \tag{3.1}$$

with $F(t)$ and $L(t)$ representing the continuous time mapping matrices of the system. In the instance of our system, we assume that the cumulative process noise vector $\bar{n}$ is the input. Using the state error equations developed previously, Equation (3.36) can be expanded such that

$$\delta\dot{\bar{x}}(t) = \begin{bmatrix} -\widehat{\bar{\omega}}^{SE,\times} & -\frac{1}{2}(1_3 - \widehat{SF})C_{Sg} & \frac{1}{2}diag\left(C_{Sg}\left(\bar{\omega}_m^{gE} - \hat{\bar{b}}_g\right)\right) \\ 0_3 & -\frac{1}{\tau_{GM}}1_3 & 0_3 \\ 0_3 & 0_3 & 0_3 \end{bmatrix}\delta\bar{x}(t) + \begin{bmatrix} -\frac{1}{2}(1_3 - \widehat{SF})C_{Sg} & 0_3 & 0_3 \\ 0_3 & 1_3 & 0_3 \\ 0_3 & 0_3 & 1_3 \end{bmatrix}\begin{bmatrix} \bar{n}_g \\ \bar{n}_g^b \\ \bar{n}_{sf} \end{bmatrix} \tag{3.37}$$

where 0_3 represents a 3×3 matrix of zeros, and $\frac{1}{2}diag\left(C_{Sg}\left(\bar{\omega}_m^{gE} - \hat{\bar{b}}_g\right)\right)$ is a diagonalization of the 3×1 bias "corrected" angular velocity measurement. While the state propagation equation posed here is useful, it is for the continuous time case. In practice, implementation on hardware forces the system to be in discrete time. For the system given in Equation (3.36), the discrete form can be obtained via

$$\delta\bar{x}_k = \exp[F(t)(t_k - t_{k-1})]\delta\bar{x}_{k-1} + \int_{t_{k-1}}^{t_k} \exp[F(\tau)]L(\tau)\,\bar{n}(\tau)d\tau \tag{3.38}$$

where $t_k - t_{k-1}$ is the discrete time interval. This can be rewritten in the form of

$$\delta\bar{x}_k = \Phi_{k-1}\delta\bar{x}_{k-1} + \Gamma_{k-1}\bar{n}_{k-1} \tag{3.39}$$

where

$$\Phi_{k-1} = \exp[F(t)(t_k - t_{k-1})] \tag{3.40}$$

$$\Gamma_{k-1} = \int_{t_{k-1}}^{t_k} \exp[F(\tau)] d\tau L(t_{k-1}) \tag{3.41}$$

with the assumption that the noise vector $\bar{n}(t)$ is constant between the interval of (t_k, t_{k-1}).

With the above information, the state covariance update can be written as a modified form of Equation (B.25)

$$P_k^- = \Phi_{k-1} P_{k-1}^- \Phi_{k-1}^T + Q_{w,k-1} \tag{3.42}$$

with $Q_{w,k-1}$ representing the modified form of the process noise term in Equation (B.25) given by $L_{k-1} Q_{k-1} L_{k-1}^T$. This discretization can be obtained via [41]

$$Q_{w,k-1} = \int_{t_{k-1}}^{t_k} \Phi(t_{k-1}, \tau) L(\tau) Q_w(\tau) L^T(\tau) \Phi^T(t_{k-1}, \tau) d\tau \tag{3.43}$$

where $Q_w(t)$ is the continuous time process noise covariance matrix. This covariance matrix is often denoted as the power spectral density (PSD) matrix of the process noise vector. Within this work it is defined as the following 9×9 matrix

$$Q_w(t) = \begin{bmatrix} \sigma_{g1}^2 & 0 & 0 & 0 & 0 & 0 & 0 & 0 & 0 \\ 0 & \sigma_{g2}^2 & 0 & 0 & 0 & 0 & 0 & 0 & 0 \\ 0 & 0 & \sigma_{g3}^2 & 0 & 0 & 0 & 0 & 0 & 0 \\ 0 & 0 & 0 & \frac{2\sigma_{IRB,1}^2}{\tau_{GM}} & 0 & 0 & 0 & 0 & 0 \\ 0 & 0 & 0 & 0 & \frac{2\sigma_{IRB,2}^2}{\tau_{GM}} & 0 & 0 & 0 & 0 \\ 0 & 0 & 0 & 0 & 0 & \frac{2\sigma_{IRB,3}^2}{\tau_{GM}} & 0 & 0 & 0 \\ 0 & 0 & 0 & 0 & 0 & 0 & \sigma_{sf1}^2 & 0 & 0 \\ 0 & 0 & 0 & 0 & 0 & 0 & 0 & \sigma_{sf2}^2 & 0 \\ 0 & 0 & 0 & 0 & 0 & 0 & 0 & 0 & \sigma_{sf3}^2 \end{bmatrix} \tag{3.44a}$$

$$Q_w(t) = diag\left[\sigma_{g1}^2\ \sigma_{g2}^2\ \sigma_{g3}^2\ \frac{2\sigma_{IRB,1}^2}{\tau_{GM}}\ \frac{2\sigma_{IRB,2}^2}{\tau_{GM}}\ \frac{2\sigma_{IRB,3}^2}{\tau_{GM}}\ \sigma_{sf1}^2\ \sigma_{sf2}^2\ \sigma_{sf3}^2\right] \tag{3.44b}$$

where the continuous time process noise covariance matrix is formulated using the standard deviations on the output noise (given by ARW on spec sheets), in-run bias stability, and scale factor errors of the selected gyro of choice. While this matrix may seem straight forward, careful attention must be placed when selecting these parameters. The formulation of this matrix, along with the measurement noise covariance matrix, will be discussed in detail later within this section.

3.3.2.3 Time Update Equations

Given the above information, the time update equations can be used to discretely update the state such that

$$\widehat{SF}_{k-1} = diag\left(\widehat{\overline{sf}}_{k-1}\right) \tag{3.45a}$$

$$\hat{\bar{\omega}}_{k-1}^{SE} = \left(1_3 - \widehat{SF}_{k-1}\right)C_{Sg}\left(\bar{\omega}_{m,k-1}^{gE} - \hat{\bar{b}}_{g,k-1}\right) \tag{3.45b}$$

$$q_{\hat{S}E,k} = \exp\left[\frac{1}{2}\Omega(\hat{\bar{\omega}}_{k-1}^{SE})(t_k - t_{k-1})\right]q_{\hat{S}E,k-1} \tag{3.45c}$$

$$\hat{\bar{b}}_{g,k} = \hat{\bar{b}}_{g,k-1} \tag{3.45d}$$

$$\widehat{\overline{sf}}_k = \widehat{\overline{sf}}_{k-1} \tag{3.45e}$$

$$P_k^- = \Phi_{k-1}P_{k-1}\Phi_{k-1}^T + Q_{w,k-1} \tag{3.45f}$$

Note that the biases and the scale factors remain constant over time updates and are updated through the measurement portion of the EKF. Additionally, we use the estimated angular velocity, corrected by the current scale factor and bias estimates, to propagate the quaternion estimate at each time update. The estimates

of the states at this point can be considered the *a priori* state estimates that will eventually be corrected by a measurement update.

3.3.3 EKF Measurement Update

3.3.3.1 Measurement Model

Consider the quaternion error model posed by Equation (3.23)

$$q_{SE} = \delta q_{S\hat{S}} \otimes q_{\hat{S}E} \tag{3.23}$$

where the true quaternion is made up of a rotation from the inertial frame $\boldsymbol{\mathcal{F}_E}$ to the estimate spacecraft frame $\boldsymbol{\mathcal{F}_{\hat{S}}}$ followed by a correction rotation from the estimate spacecraft frame to the true spacecraft frame $\boldsymbol{\mathcal{F}_S}$, parameterized by $\delta q_{S\hat{S}}$. If we assume that [41]

- The position of the vehicle in the $\boldsymbol{\mathcal{F}_E}$ frame is known well (i.e. sufficiently small position errors are present)
- The quaternion estimation error can be modeled by $\delta q_{S\hat{S}}$
- The quaternion error modeled $\delta q_{S\hat{S}}$ is sufficiently small (i.e. we assume the SAA)

then we can rewrite Equation (3.23) in DCM format such that

$$C_{SE} = C_{S\hat{S}} C_{\hat{S}E} = \left[1_3 - 2\delta\bar{q}^{\times}_{S\hat{S}}\right] C_{\hat{S}E} \tag{3.46}$$

where C_{SE} is the 3×3 DCM that maps a representation of a vector in $\boldsymbol{\mathcal{F}_E}$ to a representation of the same vector in $\boldsymbol{\mathcal{F}_S}$. The DCM denoted by $C_{\hat{S}E}$ is the 3×3 DCM that maps a vector representation in $\boldsymbol{\mathcal{F}_E}$ to a representation in the estimated body frame $\boldsymbol{\mathcal{F}_{\hat{S}}}$.

Now consider the general case in which we have a 3×1 measured vector in the spacecraft body frame $\bar{u}_m^S$ and a known model of that vector in the inertial frame, $\bar{u}^E$. The relationship between these vectors can be given as

$$\bar{u}_m^S = C_{SE}\bar{u}^E \tag{3.47}$$

If we substitute Equation (3.46) into Equation (3.47), then Equation (3.47) becomes

$$\bar{u}_m^S = \left[1_3 - 2\delta\bar{q}_{S\hat{S}}^{\times}\right]C_{\hat{S}E}\bar{u}^E \tag{3.48a}$$

$$\bar{u}_m^S = C_{\hat{S}E}\bar{u}^E - 2\delta\bar{q}_{S\hat{S}}^{\times}C_{\hat{S}E}\bar{u}^E \tag{3.48b}$$

where we can rearrange Equation (3.48b) to be

$$\delta\bar{z}^S = \bar{u}_m^S - \bar{u}^{\hat{S}} = -2\bar{u}^{\hat{S},\times}\delta\bar{q}_{S\hat{S}} \tag{3.49}$$

with $\bar{u}^{\hat{S}} = C_{\hat{S}E}\bar{u}^E$. The error between the measured vector in the true body frame $\boldsymbol{\mathcal{F}_S}$ and the modeled vector in the estimate body frame $\boldsymbol{\mathcal{F}_{\hat{S}}}$ is given by $\delta\bar{z}^S$, and is directly related to the error quaternion. Now, assuming that we have a set of n measurement vectors $\{\bar{u}_{m,1}^S, \bar{u}_{m,2}^S, \ldots, \bar{u}_{m,n}^S\}$ and their known equivalents in the inertial frame $\{\bar{u}_1^E, \bar{u}_2^E, \ldots, \bar{u}_n^E\}$, Equation (3.49) can be extended such that

$$\begin{bmatrix}\delta\bar{z}_1^S\\ \delta\bar{z}_2^S\\ \vdots\\ \delta\bar{z}_n^S\end{bmatrix} = \begin{bmatrix}-2(C_{\hat{S}E}\bar{u}_1^E)^{\times}\\ -2(C_{\hat{S}E}\bar{u}_2^E)^{\times}\\ \vdots\\ -2(C_{\hat{S}E}\bar{u}_n^E)^{\times}\end{bmatrix}\delta\bar{q}_{S\hat{S}} = H\delta\bar{q}_{S\hat{S}} \tag{3.50}$$

where H is the measurement matrix containing the measurement vectors modeled in the inertial frame mapped to the estimate body frame via $C_{\hat{S}E}$. Note that we could have obtained similar but different models based upon which frame we choose to linearize in, which is discussed in detail in [41]. Also note that Equation (3.50) allows for the inclusion of multiple measurement vectors, yet only one is required

at a given measurement update. This formulation allows for additional sensor measurements to be easily incorporated into the EKF scheme.

In this work, the measurement model takes the form of

$$\delta\bar{z}^S = H_{mag}\delta\bar{x} \tag{3.51a}$$

$$\delta\bar{z}^S = \bar{m}_m^S - \bar{m}_{modeled}^{\hat{S}} = [-2(C_{\hat{S}E}\bar{m}_{modeled}^E)^\times \ 0_3 \ 0_3]\delta\bar{x} \tag{3.51b}$$

with

$$\delta\bar{x} = \left[\delta\bar{q}_{S\hat{S}}^T \quad \delta\bar{b}_g^T \quad \delta\overline{sf}^{,T}\right]^T \tag{3.1}$$

where H_{mag} is a 3×9 matrix, $\bar{m}_m^S$ is the EMF measurement in the spacecraft body frame, and $\bar{m}_{modeled}^{\hat{S}}$ is the EMF vector modeled in the inertial frame mapped to the estimate body frame via the current estimate of the attitude, parameterized by DCM $C_{\hat{S}E}$. The inclusion of the 0_3 terms are to highlight that while both the gyro bias and scale factor errors are states, they are not directly measured by the TAM.

3.3.3.2 Measurement Update Equations

The EKF measurement utilizes the above measurement model iteratively such that

$$K_k = P_k^- H_{mag,k}^T\left(H_{mag,k}P_k^- H_{mag,k}^T + R_k\right)^{-1} \tag{3.52a}$$

$$P_k^+ = \left(1_9 - K_k H_{mag,k}\right)P_k^- \tag{3.52b}$$

$$\delta\bar{x}_k = K_k\delta\bar{z}^S \tag{3.52c}$$

$$\delta\bar{x}_k = \left[\delta\bar{q}_{S\hat{S},k}^T \ \ \delta\bar{b}_{g,k}^T \ \ \delta\overline{sf}_k^T\right]^T \tag{3.52d}$$

$$q_{\hat{S}E,k} = \begin{bmatrix} 1 \\ \delta\bar{q}_{S\hat{S},k} \end{bmatrix} \otimes q_{\hat{S}E,k-1} \tag{3.52e}$$

$$q_{\hat{S}E,k} = \frac{q_{\hat{S}E,k}}{\left|q_{\hat{S}E,k}\right|} \tag{3.52f}$$

$$\hat{\bar{b}}_{g,k} = \hat{\bar{b}}_{g,k-1} + \delta\bar{b}_{g,k} \tag{3.52g}$$

$$\widehat{\overline{sf}}_k = \widehat{\overline{sf}}_{k-1} + \delta\overline{sf}_k \tag{3.52h}$$

where K_k is the Kalman gain at the current timestep and R_k is the measurement noise covariance matrix. Note that the EKF here updates the measurements via a multiplication of the Kalman gain K and the $\delta\bar{z}^S$ value, as opposed to a corrective addition. The measurement noise covariance is a simpler model than the process noise covariance, and can be modeled as

$$R_k = diag\left[\sigma_{mag,1}^2 \;\; \sigma_{mag,2}^2 \;\; \sigma_{mag,3}^2\right] \tag{3.53}$$

where the matrix R_k is populated with the standard deviations of the magnetometer output noise in each axis. This value should maintain the same units as the measurement units.

At each measurement update, the EKF calculates the current error between the state trajectory and the estimates via Equation (3.52c). Note that after this error vector estimate is calculated, we utilize its individual components to update the quaternion, bias, and scale factor estimates through the above equations. The quaternion update also requires a re-normalization of the estimate, as seen by Equation (3.52f), to ensure it is a proper attitude quaternion with unit norm.

3.3.4 EKF Performance

3.3.4.1 Process Noise Covariance

The process noise covariance is used to quantify any uncertainties in how the dynamic model of the system is propagated. As the dynamics of our system are

propagated by noisy inertial measurements, the covariance matrix is comprised primarily of the noise characteristics of the rate gyro within the IMU. The process noise covariance matrix, denoted by $Q_w(t)$ as seen in Equation (3.44), is created by taking the noise characteristics of the gyro and implementing them into a matrix format. Specifically, $Q_w(t)$ is dependent upon three gyro parameters: The standard deviation of the output noise (or Noise Density/ARW), the standard deviation of the in-run bias stability, and the standard deviation on the scale factors. These values can generally be taken off a specification sheet for an IMU (see Appendix C).

The units on the covariance matrix should match with the units of the states themselves. These units should generally be in rad/s for the output noise and in-run bias stability standard deviations, and parts-per-million on the scale factor errors. However, the in-run bias stability is often given on spec sheets in $°/hr$, so a conversion before filter use must be implemented. Additionally, if noise density or ARW are being used instead of output noise, similar conversions must be made.

While spec sheets often give much needed information regarding the noise characteristics, many times important parameters (such as scale factors or correlation time) are neglected. With this in mind, a table covering the common ranges for these parameters based upon grade is shown in Table C.3. It should be noted that this table is created based upon the experiences of the author and can vary depending upon the hardware itself. To conclusively obtain results on the noise characteristics of a sensor, multiple hardware tests should be performed after purchase. Some of these tests are detailed within [23].

3.3.4.2 EKF convergence Speed & Tuning

Depending on the mission and requirements upon the AD system, the convergence speed of the EKF can be a critical design parameter. The convergence speed of the EKF architecture is dependent upon 4 factors

- Initial state covariance matrix, P_0^+
- Process noise covariance matrix, $Q_w(t)$
- Measurement noise covariance matrix, R_k
- Measurement update frequency

These are typically the trade spaces that an EKF designer works in. Specifically, $Q_w(t)$ and R_k are directly affected by the choice of sensor hardware and errors present in the system. Initial covariance is dependent upon on how accurate the starting estimate of the EKF, and is generally initialized large to represent high initial uncertainty (this can be problematic depending on the system, see [26] for more details). The measurement update frequency is dependent on the mission environment, payload, and sensors used. This is typically a less constraining factor than the covariance of the system.

In the experience of the author, EKF convergence speed is primarily affected by the condition number of $Q_w(t)$. Explicitly, this is defined as

$$\kappa_{Q_w} = \frac{\sigma_{max}\big(Q_w(t)\big)}{\sigma_{min}\big(Q_w(t)\big)} \tag{3.54}$$

where κ_{Q_w} is the condition number, $\sigma_{max}\big(Q_w(t)\big)$ and $\sigma_{min}\big(Q_w(t)\big)$ represent the maximum and minimum singular values, respectively, of the process noise covariance matrix $Q_w(t)$. The condition number is dependent upon the noise characteristics of the sensor, and depending on the size, can lead to poor

convergence speed. For example, consider the simple process noise matrix (excluding scale factors) given by

$$Q = diag[\sigma_g^2\ \sigma_g^2\ \sigma_g^2\ \frac{2\sigma_{IRB}^2}{\tau_{GM}}\ \frac{2\sigma_{IRB}^2}{\tau_{GM}}\ \frac{2\sigma_{IRB}^2}{\tau_{GM}}]$$

where $\sigma_g = 0.135°/s$, $\sigma_{IRB} = 2.5e^{-5}\ °/s$, $\tau_{GM} = 30\ s$. The condition number of this matrix is given as $\kappa_{Q_w} = 1.3e^5$. If we were to change the $\sigma_g = 0.005°/s$, then we can show that the condition number changes to be $\kappa_{Q_w} = 981$. This drastic change can generally signify changes in the convergence speed. Typically, it has been found that slower convergence speed is correlated with higher condition number, and faster convergence is correlated with lower condition number. Often this was dependent on the ratio of the output noise and the in-run bias stability.

To increase the convergence speed without changing sensor characteristics, a few methods can be implemented. One such method is the incorporation of tuning parameters into the noise mapping matrix $L(t)$ such that

$$L(t) = \begin{bmatrix} -\frac{1}{2}\alpha(1_3 - \widehat{SF})C_{Sg} & 0_3 & 0_3 \\ 0_3 & \beta 1_3 & 0_3 \\ 0_3 & 0_3 & \gamma 1_3 \end{bmatrix} \tag{3.55}$$

where α, β, and γ are the scalar tuning parameters [41]. These parameters control the closed loop estimator poles, and as such, the speed of the poles themselves. Tuning parameters are typically picked through trial and error approaches and can vary greatly depending on the problem in which they are used. As [41] mentions, the use of tuning parameters allows for the user to control the speed of the closed loop estimator poles. However, there is a trade-off between convergence speed and accuracy when using these parameters. As the tuning parameters are increased, the

EKF convergence time decreases while the estimate noise increases. Conversely, as the tuning parameters are decreased, EKF convergence time increases, while the estimate noise decreases. In terms of the condition number, the use of tuning parameters changes the condition number of the mapping matrix used in discretization, which is similar to directly changing the noise characteristics of the system itself by modifying the values contained within $Q_w(t)$.

An alternative to tuning is to over bound the covariance of the system. This involves placing larger values on the noise characteristics within $Q_w(t)$ than would be present on IMU measurements. In certain applications, this can be an easier and more intuitive approach to tuning but can also result in estimate covariance criteria not being met. In application, covariance over bounding can be directly performed by increasing the standard deviation on the in-run bias of the system.

In both instances of tuning and covariance over bounding, the system characteristics are being modified to enhance certain functionalities. While this is beneficial, we run the risk of losing physical interpretation of the system itself by modifying parameters. Care should be placed when using the tuning or overabounding technique.

3.3.4.3 Estimate Constraints

In some applications, there may be additional constraints on the filter states that are difficult to model within the EKF structure. For example, it may be known that physically, a state must lie within a certain range and cannot exceed a set boundary. However, it can be difficult to incorporate this knowledge into the derivation of the EKF itself. The general solution to this problem is known as constrained Kalman filtering.

Assume that the state estimate satisfies some equality constraint $D\bar{x} = \bar{d}$ or some inequality constraint $D\bar{x} \leq \bar{d}$ where D is a known matrix and $\bar{d}$ is a known vector. The incorporation of this state constraint can be performed in multiple ways [26] [45] [46]. One such technique is the Maximum Probability Method shown in [45]. The constrained Kalman filter can be derived by finding a new estimate, $\tilde{x}$, such that

$$\min_{\tilde{x}}(\tilde{x} - \bar{\bar{x}})^T P^{-1}(\tilde{x} - \bar{\bar{x}}) \tag{3.56}$$

$$such\ that\ D\tilde{x} \leq \bar{d}$$

If this minimization is performed after the measurement update of the EKF, then the unconstrained state estimate $\bar{\bar{x}} = \hat{\bar{x}}_k^+$, and Equation (3.56) can be expanded to be (neglecting constant terms)

$$\min_{\tilde{x}}\left(\tilde{x}^T P^{-1}\tilde{x} - 2\hat{\bar{x}}_k^{+,T} P^{-1}\tilde{x}\right) such\ that\ D\tilde{x} \leq \bar{d} \tag{3.57}$$

This minimization is often known as a quadratic program (QP) and can be solved multiple ways. The solution to the above QP will produce an $\tilde{x}$ that is a new constrained version of the original state $\hat{\bar{x}}_k^+$. In essence, the solution to Equation (3.57) is now another update used within the EKF and places the states under constraints specified by the inequality relationship of $D\tilde{x} \leq \bar{d}$. While a new constrained covariance can also be determined, it is theorized that the any new or updated covariance will be equivalent or smaller than that of the unconstrained case [45]. As such, by not updating the covariance, we are maintaining a "worst-case" covariance, and saving computational power.

3.3.5 Vector Matching Algorithm

The filter developed within this chapter is initialized with some initial state estimate and an initial covariance estimate. The relative size of the initial covariance is large to indicate uncertainty in the initial state estimate. During time updates, the kinematic equations propagate the kinematics of the system at the gyro sampling frequency rate. The gyro measurement of the angular velocity is corrected based upon the bias and scale factors estimated at the last measurement update. When a measurement update occurs, the EKF calculates an error state vector between the current nominal trajectory and the current estimate of the state and utilizes that to correct the state estimate. To maintain the quaternion unit constraint, the new estimate of the quaternion is renormalized. Measurement corrections occur at the magnetometer sampling frequency and are dependent upon sensor availability. The complete EKF architecture, referred to from here on as "Vector Matching Algorithm" or VMA, is summarized below.

Initialization

$$q_{\hat{S}E,0} = E\{q_{SE,0}\} \tag{3.58}$$

$$\hat{\bar{b}}_{g,0} = E\{\bar{b}_{g,0}\} \tag{3.59}$$

$$\widehat{\overline{sf}_0} = E\{\overline{sf}_0\} \tag{3.60}$$

$$P_0^+ = E\{\delta\bar{x}_0\delta\bar{x}_0^T\} \tag{3.61}$$

Time Update

$$\widehat{SF}_{k-1} = diag\left(\widehat{\overline{sf}}_{k-1}\right) \tag{3.45a}$$

$$\hat{\bar{\omega}}_{k-1}^{SE} = \left(1_3 - \widehat{SF}_{k-1}\right)C_{Sg}\left(\bar{\omega}_{m,k-1}^{gE} - \hat{\bar{b}}_{g,k-1}\right) \tag{3.45b}$$

$$q_{\hat{S}E,k} = \exp\left[\frac{1}{2}\Omega(\hat{\bar{\omega}}_{k-1}^{SE})(t_k - t_{k-1})\right] q_{\hat{S}E,k-1} \tag{3.45c}$$

$$\hat{\bar{b}}_{g,k} = \hat{\bar{b}}_{g,k-1} \tag{3.45d}$$

$$\widehat{\overline{sf}}_k = \widehat{\overline{sf}}_{k-1} \tag{3.45e}$$

$$P_k^- = \Phi_{k-1} P_{k-1} \Phi_{k-1}^T + Q_{w,k-1} \tag{3.45f}$$

Measurement Update

$$K_k = P_k^- H_{mag,k}^T \left(H_{mag,k} P_k^- H_{mag,k}^T + R_k\right)^{-1} \tag{3.52a}$$

$$P_k^+ = \left(1_9 - K_k H_{mag,k}\right) P_k^- \tag{3.52b}$$

$$\delta\bar{x}_k = K_k \delta\bar{z}^S \tag{3.52c}$$

$$\delta\bar{x}_k = \begin{bmatrix} \delta\bar{q}_{S\hat{S},k}^T & \delta\bar{b}_{g,k}^T & \delta\overline{sf}_k^T \end{bmatrix}^T \tag{3.52d}$$

$$q_{\hat{S}E,k} = \begin{bmatrix} 1 \\ \delta\bar{q}_{S\hat{S},k} \end{bmatrix} \otimes q_{\hat{S}E,k-1} \tag{3.52e}$$

$$q_{\hat{S}E,k} = \frac{q_{\hat{S}E,k}}{\left|q_{\hat{S}E,k}\right|} \tag{3.52f}$$

$$\hat{\bar{b}}_{g,k} = \hat{\bar{b}}_{g,k-1} + \delta\bar{b}_{g,k} \tag{3.52g}$$

$$\widehat{\overline{sf}}_k = \widehat{\overline{sf}}_{k-1} + \delta\overline{sf}_k \tag{3.52h}$$

3.4 Summary

Within this chapter, we stated the benefits of developing a minimal sensor approach to determining the attitude of a CubeSat. Current schemes for CubeSat AD were discussed, highlighting the consistent use of multiple sensors to provide a dual-vector approach to solving Wahba's problem. Research around the use of the

EMF vector as the sole aiding sensor was mentioned, with a discussion of the benefits regarding this AD architecture.

The EMF was explained, in addition to how it varies as a function of location, time, and velocity. It was posited that this phenomenon could be taken advantage of by CubeSats as a varying measurement vector used within an EKF framework. Situations in which this may be a viable AD solution, specifically pertaining to the kinematics of a CubeSat in flight, were mentioned and briefly discussed.

An EKF architecture utilizing a three-axis rate gyroscope and a three-axis magnetometer (TAM) was developed, based on previous work in [41]. A gyro sensor error model, containing scale factor, bias, and white noise errors was derived. The magnetometer model and noise characteristics were briefly described. The attitude kinematic equations, parameterized by the quaternion, were developed, and error state vector equations for the EKF states of interest were formulated.

A vector matching measurement model, based on the use of the EMF field as the sole measurement, was derived with the quaternion attitude kinematic error. The combination of this model and the attitude kinematic error equations developed was used to formulate an EKF based vector matching algorithm (VMA). General notes on the design parameters, such as sensor noise covariance models, were discussed, with an emphasis placed on the pitfalls of poorly designed covariance matrices. Additional techniques for increasing EKF convergence speed, such as parameter tuning and state constraints, were briefly mentioned.

4 State Observability

The VMA developed in Chapter 3 has the capability to estimate three different states: The attitude quaternion error, gyro biases, and gyro scale factor errors. However, at this point we have not made any claims about the *quality* of those estimates, and the performance of the VMA itself. Specifically, we have no guarantee that the VMA will accurately estimate the states as designed or remain stable throughout time. To make this claim, we need to develop additional metrics dependent upon the system matrices and how they interact with each other. A metric that will help us address the accuracy problem, in part, is the concept of observability. Observability can be separated into two types: Deterministic observability and stochastic observability. This brief chapter will discuss each of these metrics and how they are useful. Additionally, a comprehensive test for the state observability of a system is showcased.

4.1 Deterministic Observability

Consider the linear, discrete time, stochastic system given by

$$x_k = \Phi_{k-1} x_{k-1} + \Gamma_{k-1} w_{k-1} \tag{4.1a}$$

$$z_k = H_k x_k + v_k \tag{4.1b}$$

In the framework of our EKF, deterministic observability is a system property that is dependent on the state mapping matrix Φ_k and measurement matrix H_k. As defined in [26], deterministic observability is

Definition 4.1 *A discrete-time system is observable if for any initial state* $\boldsymbol{x_0}$ *and some final time k the initial state* $\boldsymbol{x_0}$ *can be uniquely determined by knowledge of the input* $\boldsymbol{u_i}$ *and output* $\boldsymbol{y_i}$ *for all* $\boldsymbol{i \in [0, k]}$.

Concisely, a system is deterministically observable at some time instant if we can determine the initial state from knowledge of the inputs and outputs to the system at each timestep. With regards to the EKF, a deterministically observable system implies a system where all that all measured states can be *influenced* and corrected during the measurement update. If the system is deterministically unobservable, then at least one state is not being influenced by the measurement vector and is being estimated open-loop [47].

A test of whether a system is deterministically observable can be obtained by recursively evaluating the observability Gramian, $\mathcal{O}_N^T\mathcal{O}_N$, defined as [47]

$$\mathcal{O}_N^T\mathcal{O}_N = H_0^T H_0 + \sum_{k=1}^{N} \Phi_{k-1,0}^T H_k^T H_k \Phi_{k-1,0} \tag{4.2}$$

where N is finite number of measurement, H_k is the measurement matrix at time k, and $\Phi_{k-1,0}$ is the state transition matrix from time 0 to time $k-1$, defined as

$$\Phi_{k-1,0} = \Phi_{k-1}\Phi_{k-2} \dots \Phi_0 \tag{4.3}$$

The value $\mathcal{O}_N$ represents the observability matrix created from measurements up to measurement N, defined as

$$\mathcal{O}_N = \begin{bmatrix} H_0 \\ H_1\Phi_0 \\ \vdots \\ H_N\Phi_{N-1,0} \end{bmatrix} \tag{4.4}$$

Deterministic observability can be determined by checking that $\mathcal{O}_N^T\mathcal{O}_N$ has full rank. That is, if

$$\rho(\mathcal{O}_N^T\mathcal{O}_N) = n \tag{4.5}$$

where n is the number of states within the system, then the system is deterministically observable. By fulfilling the full rank requirement, we are stating that each state can be influenced at the measurement update.

4.2 Stochastic Observability

While deterministic observability is a useful metric, it does not incorporate noise within the system or initial state covariance. Additionally, Φ_k and H_k may contain external noise, potentially contaminating the rank calculation. In the deterministic observability sense, sensor characteristics given by the noise matrices $Q_{w,k}$, R_k, and initial state covariance P_0, are not incorporated. Thus, while a system may be deterministically observable, the state covariance of the system may grow unbounded throughout time, implying uncertainty on the filter estimates. As such, deterministic observability is a necessary, but not sufficient, condition for ensuring the state estimate covariances are bounded.

Stochastic observability can be defined as follows [47]

Definition 4.2 *The system in Equation (4.1) is stochastically observable if there exists a finite time t_N such that the state covariance matrix is bounded or less than a predefined threshold value, T_v, in the sense that*

$$\sigma_{max}(P_k) < T_v \qquad t_k \geq t_N \tag{4.6}$$

Where $T_v, t_N < \infty$ and $\sigma_{max}(\cdot)$ refers to the largest singular value of the matrix $(\cdot)$.

Concisely, the definition states that if the state covariance is bounded by some fixed amount at a finite time, then the system is considered to be stochastically observable. If a system is stochastically unobservable, then it is implied that at least one state has unbounded covariance that will grow throughout time.

A test to determine the stochastic observability of the system is adapted from [47] and summarized below. For details on the specific equations used in addition to proofs, see [47].

Consider the system of Equation (4.1) and assume the initial covariance is selected such that

$$P_0 = \alpha 1_n \qquad \alpha \in \mathcal{R}, \alpha > 0 \tag{4.7}$$

where 1_n is the $n \times n$ identity matrix and α is some scalar quantity. The covariance propagation equation (discrete Riccati equation) can be written in the following form:

$$P_k = \alpha \Lambda_k + \bar{Q}_k + \Delta_k(\alpha^{-1}) \tag{4.8}$$

where three terms are present: Λ_k, $\bar{Q}_k$, and Δ_k. If it can be shown that Λ_k, $\bar{Q}_k$, and Δ_k remain constant or go to zero as a function of time, then P_k will also remain constant or go to zero as a function of time. As such, the test involves determining the size of each term at the measurement update.

Under the conditions posed above, if the maximum singular value of Λ_k is equal to zero such that

$$\sigma_{max}(\Lambda_j) = 0 \tag{4.9}$$

where $j < \infty$, then it can be shown that $\sigma_{max}(\Lambda_k) = 0$ for all $k \geq j$. Given this result, the covariance propagation equation can be reduced to

$$P_k = \bar{Q}_k + \Delta_k(\alpha^{-1}) \tag{4.10}$$

In the instances in which the scalar $\alpha \to \infty$, Equation (4.10) reduces further [47] to

$$P_k = \bar{Q}_k \tag{4.11}$$

which highlights that the covariance is now only a function of the term $\bar{Q}_k$ at each measurement update. To determine if the covariance is bounded, we must determine the value of $\bar{Q}_k$ at each measurement. If we can show that

$$\sigma_{max}(\bar{Q}_k) \leq T_v \tag{4.12}$$

where T_v is some threshold value, then we can show the covariance is similarly bounded. The checks provided by Equations (4.9) and (4.12) give a test to assess the stochastic observability of the system.

4.3 Observability Test

The combined observability test of the system can be performed via the following set of steps:

At each measurement update:

1. Compute the observability gramian $\mathcal{O}_N^T\mathcal{O}_n$ and check its rank, using the current state transition matrix $\Phi_{k-1,0}$ and the current measurement matrix H_k via

$$\mathcal{O}_N^T\mathcal{O}_N = H_0^T H_0 + \sum_{k=1}^{N} \Phi_{k-1,0}^T H_k^T H_k \Phi_{k-1,0} \tag{4.2}$$

1.1. *If* $\rho(\mathcal{O}_N^T\mathcal{O}_N) = n$

→ *Deterministically Observable*

1.1.1. Calculate Λ_k as defined in [47] and compute maximum singular value

1.1.2. Calculate $\bar{Q}_k$ as defined in [47] and compute its maximum singular value

1.1.3. *If* $\sigma_{max}(\Lambda_k) = 0$ *and* $\sigma_{max}(\bar{Q}_k) \leq T_v$

→ *Stochastically Observable*

1.1.4. *If* $\sigma_{max}(\Lambda_k) \neq 0$ *or* $\sigma_{max}(\bar{Q}_k) \geq T_v$

$\rightarrow$ ***Stochastically Unobservable***

1.2. *If* $\rho(\mathcal{O}_N^T \mathcal{O}_N) \neq n$

$\rightarrow$ ***Deterministically Unobservable***

$\rightarrow$ ***Stochastically Unobservable***

Note that deterministic observability is a necessary, but not sufficient condition to determine the state observability of the system, whereas stochastic observability is a sufficient condition for state observability of the system.

As stated in [47], the test developed above is useful because it can highlight requirements for the restructuring of the system. For example, the condition stated by Equation (4.12) implies that increases to P_k due to the system matrices of Γ_k, Q_k, Φ_k, and $\bar{Q}_k$ are offset due to corrections and contributions from H_k and R_k. Thus, a failure of this test suggests different system parameters (such as sensor hardware, sampling frequencies, noise characteristics) may be required. A passing of this test implies that the state covariance will be bounded throughout some time interval.

4.4 Summary

This chapter discussed the concept of state observability via two metrics: Deterministic observability and stochastic observability. We briefly discussed the value of knowing state observability and posed its usefulness as a metric to determine VMA performance. We described the individual parameters that are used in testing the observability of a system, and then posed a comprehensive observability test that can be used to validate state observability.

5 VMA Trade Studies

5.1 Introduction

This chapter evaluates multiple flight conditions of IMPRESS and EXACT using the VMA developed in Chapter 3. Specifically, the VMA is tested by changing the orbital inclination, angular rates, and gyro errors present at each run. The simulation structure, orbital conditions, CubeSat inertia parameters, sensors used, and noise characteristics are discussed. Focus is placed on describing how noise is simulated within the system and how we choose to model the individual error statistics. A comprehensive discussion of each simulation scenario will be presented, showcasing the convergence speed and estimation accuracy of the states of interest. Additionally, the stochastic observability of the system is verified via the test discussed in Chapter 4.

5.2 Simulation Parameters & Structure

The goal of the simulation is to evaluate the effect of certain noise characteristics, orbital conditions, and angular rates of the CubeSat on the attitude solution obtained by the VMA. This is done by varying the types of noise present on gyro data, initial angular velocity, and orbital inclination while holding other parameters constant. Orbital inclination is specifically varied to analyze the rate of change of the EMF vector (see Figure 3.1 Simplistic visualization of the Earth magnetic field (EMF). Note that no control policies are added to these simulation studies.

Currently, no designs on IMPRESS or EXACT have been finalized, and as such, no inertia tensor has been determined. To this end, we maintain a constant

principle axes inertia tensor for these simulations based upon heritage flight information of SOCRATES (Signal Opportunity CubeSat Ranging And Timing Experiment), the UMN's previous CubeSat. We choose this tensor as SOCRATES was a 3U CubeSat, which is the expected size of each of the upcoming mission's CubeSats. While this is a valid first approximation, it is expected that each mission will have varying inertia tensors as more developments occur, and any future simulation studies should incorporate these developments. Additionally, note that the choice of the principal axis inertia causes oscillatory precession and nutation in the ω_{S1}^{SE} and ω_{S2}^{SE} axes, with constant spin in the ω_{S3}^{SE} axis, as no control is implemented to damp out angular rates.

As IMPRESS and EXACT are expected to be deployed from the International Space Station (ISS), an orbital parameter baseline can be determined. These constant parameters, along with their chosen values, are given in Table 5.1 and Table 5.2.

Table 5.1 Common-orbital parameters for all simulations

Orbital Parameter	Value	Description
LLA_0	$[0.11°\quad 174°\quad 401\,km]$	Initial Latitude, Longitude, Altitude
$\bar{v}_0^E$	$[0\quad 4.9\quad 5.8]\,km/s$	Initial Velocity in ECI frame
T	$93\,min$	Orbital Period
e	0.001	Orbital Eccentricity
ω	$0°$	Argument of Perigee
RA	$0°$	Right Ascension
t_{per}	$0\,s$	Time of Perigee Passage

Table 5.2 Common spacecraft parameters for all simulations

Spacecraft Parameter	Value	Description
m_s	$3.33\ kg$	Spacecraft Mass
I_S	$\begin{bmatrix} 0.0508 & 0 & 0 \\ 0 & 0.0508 & 0 \\ 0 & 0 & 0.0252 \end{bmatrix} kg * m^2$	Spacecraft Inertia Tensor
f_{IMU}	$10\ Hz$	Gyro Sampling Frequency
f_{TAM}	$0.1\ Hz$	Magnetometer Sampling Frequency
σ_{IRB}	$5.1°/hr$	Gyro In-Run Bias Stability STD
σ_g	$0.135\ °/s$	Gyro Wideband Noise
σ_{BR}	$0.2°/s$	Gyro Bias Repeatability STD
σ_{sf}	$200\ ppm$	Gyro Scale Factor Noise STD
τ_{GM}	$300\ s$	Gyro Correlation Time
σ_{mag}	$1\ mGauss$	Magnetometer Output Noise STD

The simulations were run in MATLAB by creating truth data via a continuous time integration of the spacecraft attitude dynamics equations (detailed description can be seen in Chapter 3 of [8]) using ODE45 with a J2 perturbation of $J2 = 1.0826E^{-3}$. No control policies or external torques were implemented within the simulation. As the desired gyro sample rate for the mission is $10\ Hz$, the step size of ODE45 was selected to be 0.1 seconds to match this gyro sample rate. The outputs of ODE45 were the CubeSat's true state, consisting of the position and velocity in ECI, CubeSat angular velocity between ECI frame $\boldsymbol{\mathcal{F}_E}$ and spacecraft

body frame $\boldsymbol{\mathcal{F}_S}$, and attitude quaternion from $\boldsymbol{\mathcal{F}_E}$ to $\boldsymbol{\mathcal{F}_S}$. This is shown in block diagram format in Figure 5.1.

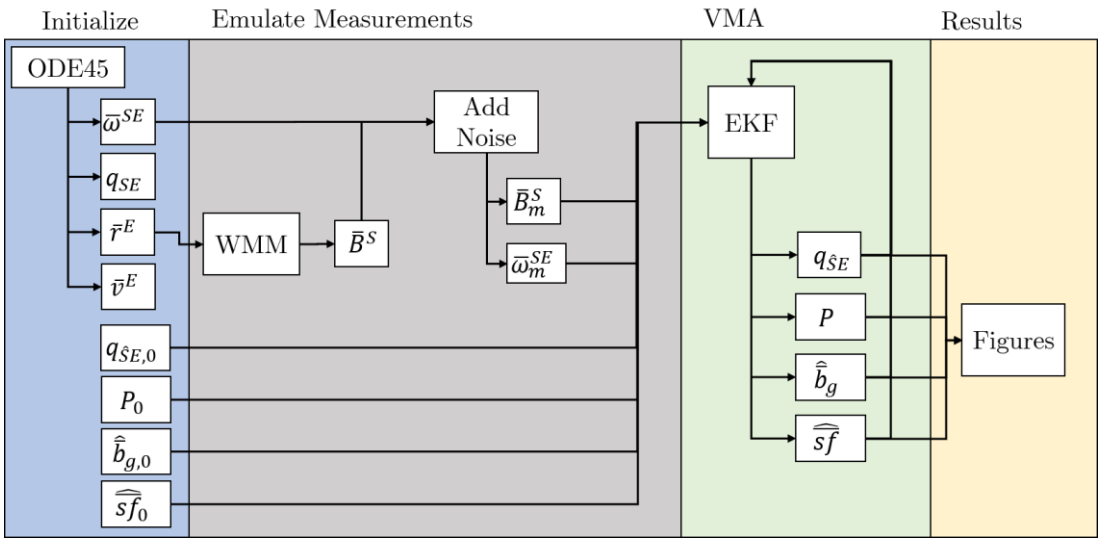

Figure 5.1 Simulation Block Diagram

The position vector was input into an WMM EMF model to obtain the magnetic field vector in ECI coordinates at every instant of the simulation. Angular velocity and magnetometer data were corrupted using the noise parameters denoted in Table 5.2 to give a noisy angular velocity and magnetometer vectors that were treated as sensor measurement vectors throughout the timeframe of the simulation. Note that sensor parameters seen in Table 5.2 were chosen based off of the ADIS16488 IMU/TAM, which is the current IMU/TAM selection for both IMPRESS and EXACT. Additionally, magnetometer noise used in the simulation, σ_{mag}, was five times larger than the expected TAM output noise as seen on the ADIS16488 spec sheet. This was done to try and partially accommodate for a lack of TAM calibration in the simulation.

After data corruption, the measurement vectors were input into the VMA EKF and ran through a simulation time frame of 5 orbits, or approximately 8 hours. The VMA was performed with tuning parameters on the noise mapping matrix given by $\alpha = 1, \beta = 5$, and $\gamma = 1$.

As no external torques were input into the system, the angular velocity was allowed to oscillate throughout time. Based upon the inertia parameters stated in Table 5.2, this caused the angular velocity about the S^3 axis of the spacecraft to remain constant over the simulation timeframe. This will be important with regards to scale factor estimation which will be discussed in the following sections.

In the scenarios in which scale factors were estimated, a constrained optimization took place in the form of Equation (3.57). Specifically, we solved the quadratic program (QP) [45]

$$\min_{\tilde{x}_{sf}} \left({\tilde{x}_{sf}}^T P_{sf}^{-1} \tilde{x}_{sf} - 2\hat{\tilde{x}}_{k,sf}^{+,T} P_{sf}^{-1} \tilde{x}_{sf} \right) \tag{5.1}$$

$$subject\ to \quad \left(0.95 - \left(1_3 + \widehat{SF}_{k-1}\right)\right) \leq \hat{\tilde{x}}_{k,sf} \leq \left(1.05 - \left(1_3 + \widehat{SF}_{k-1}\right)\right)$$

where $\tilde{x}_{sf}$ is the constrained scale factor estimate, $\hat{\tilde{x}}_{k,sf}^{+}$ is the *a posteriori* unconstrained scale factor estimate after the measurement update, P_{sf} is the 3×3 covariance matrix of the scale factor estimates, and $\widehat{SF}_{k-1}$ is the scale factor matrix given by the previous scale factor estimates. This constraint forces the total scale factor term given by $\left(1_3 + \widehat{SF}_k\right)$ to remain between the values of 0.95 and 1.05. This is a reasonable assumption as most gyroscope scale factor errors lie within this range. Note that in Equation (5.1) only scale factor estimates are constrained. As stated in Chapter 3, the covariance can be updated, however we took the

conservative approach and did not update them. This QP was solved utilizing MATLAB's `quadprog()` function.

In every simulation, we assess the convergence of the EKF through the error Euler angles and the knowledge error, ϵ. Recall that IMPRESS and EXACT require that ϵ be below $10°$ for science objectives to be met. As the normal vector to the detector face lies along the S^3 axis of the body spacecraft frame (see Figure 2.1), this requirement can be met by ensuring that the angular error between the estimated 3-axis, $\hat{S}^3$, and the true 3-axis, S^3, remains below $10°$. This angular error can be formulated mathematically by the following

$$\epsilon = \cos^{-1}\left(C_{S\hat{S}}^{3,3}\right) * \frac{180}{\pi} \tag{5.2}$$

where $C_{S\hat{S}}^{3,3}$ is the (3,3) element of the error DCM representing the attitude between the true and estimate body frames, $\boldsymbol{\mathcal{F}_S}$ and $\boldsymbol{\mathcal{F}_{\hat{S}}}$. Additionally, we would like to also determine some value of covariance for the given angular error ϵ. This can be determined using the covariance law [48]

$$P_\epsilon = G_\epsilon P_q G_\epsilon^T \tag{5.3}$$

where P_q is the 3×3 covariance matrix on the quaternion error $\delta\bar{q}_{S\hat{S}}$, P_ϵ is the scalar covariance on ϵ, and G_ϵ is the Jacobian of ϵ with respect to $\delta\bar{q}_{S\hat{S}}$ such that

$$G_\epsilon = \left[\frac{\partial\epsilon}{\partial q_1} \;\; \frac{\partial\epsilon}{\partial q_2} \;\; \frac{\partial\epsilon}{\partial q_3}\right] \tag{5.4}$$

Similarly, an expression for the 3-2-1 Euler angles can also be obtained such that

$$P_\Psi = G_\Psi P_q G_\Psi^T \tag{5.5}$$

where P_Ψ is the 3×3 covariance matrix on the 3-2-1 Euler angles and G_Ψ is given by

$$G_{\Psi} = \begin{bmatrix} \frac{\partial \psi}{\partial q_1} & \frac{\partial \psi}{\partial q_2} & \frac{\partial \psi}{\partial q_3} \\ \frac{\partial \theta}{\partial q_1} & \frac{\partial \theta}{\partial q_2} & \frac{\partial \theta}{\partial q_3} \\ \frac{\partial \phi}{\partial q_1} & \frac{\partial \phi}{\partial q_2} & \frac{\partial \phi}{\partial q_3} \end{bmatrix} \tag{5.6}$$

It should be noted that the covariances obtained using Equations (5.4) and (5.6) are determined under the assumption that $\delta q_{S\hat{S}}$ is small such that Equation (3.21a) holds.

5.3 Simulation Scenarios

For IMPRESS and EXACT, cases based around a combination of differing orbital inclinations and spacecraft angular rates were tested. Additionally, the inclusion of scale factor errors within the gyroscope model was also simulated for each of these conditions.

Simulations on the convergence of the VMA EKF estimate were tested with 30 Monte Carlo runs, each with a period of 5 orbits. In each run, the simulated noise characteristics and initial EKF estimates were varied. Specifically, the attitude quaternion was not constrained, the in-run bias was randomized based upon the characteristics given in Table 5.2, and the bias repeatability was randomized to be within the range of $-0.4°/s \leq b_0 \leq 0.4°/s$.

For each simulation, two sets of results are presented: results in which scale factor errors were not added into the noise of the system (i.e. no scale factor errors are present in the noise itself), and results in which scale factor errors were included and estimated. In instances where scale factor errors were included and estimated, scale factors were randomized to be within the range of $-50000\,ppm \leq \overline{sf} \leq 50000\,ppm$. Unfortunately, the case where scale factor errors were present within

the system noise but not estimated, was neglected due to time constraints. The author acknowledges that this case study is important and should be included within any future work for completeness.

Angular velocity was varied over three cases: a "tumbling" scenario with angular velocities expected after deployment, a nominal spin stabilized scenario, and a low angular velocity scenario. Orbital inclination was also varied between discrete values of $88°$, $50°$, and $2°$. The combinations of these values provide 9 unique test cases that each had 30 Monte Carlo runs over 5 orbits. The initial covariance was given as

$$P_0 = diag\left[0.3^2\ 0.3^2\ 0.3^2\ \left(0.5\frac{^\circ}{s}\right)^2\ \left(0.5\frac{^\circ}{s}\right)^2\ \left(0.5\frac{^\circ}{s}\right)^2\right] \tag{5.7}$$

$$P_0 = diag\left[0.3^2\ 0.3^2\ 0.3^2\ \left(0.5\frac{^\circ}{s}\right)^2\ \left(0.5\frac{^\circ}{s}\right)^2\ \left(0.5\frac{^\circ}{s}\right)^2\ (0.05)^2\ (0.05)^2\ (0.05)^2\right] \tag{5.8}$$

where Equation (5.7) is the initial covariance for scenarios in which scale factors were not included, and Equation (5.8) is for the cases when they were included and estimated. These initial covariances were selected as a form of "worst-case" expected on the states themselves but were chosen somewhat arbitrarily.

The state observability test as defined in Chapter 4 was performed for each run. It was verified that each run was deterministically observable via the observability Gramian rank calculation given by Equation (4.2). Stochastic observability was tested via the $\sigma_{max}(\Lambda_k)$ and $\sigma_{max}(\bar{Q}_k)$ metrics of Equations (4.9) and (4.12), respectively, with the results presented for each simulation run. Based upon the values of these metrics at each time step, in addition to the general trend

of $\sigma_{max}(\bar{Q}_k)$, we state whether or not the system was considered stochastically observable.

For each simulation, the figures presented showcase 6 out of 30 Monte Carlo runs of the VMA over a period of 5 orbits. While it was verified that each Monte Carlo run presented similar phenomena, only 6 are displayed to for clarity. State attitude estimates parameterized by the 3-2-1 Euler angles, and values for $\delta\bar{b}_g$ and $\delta\overline{sf}$ (when included) are given by the red lines. One STD (1σ) bounds on each of the state estimates are given by the blue dashed lines within the figures. Stochastic observability tests are also given, with the stochastic observability metrics of $\sigma_{max}(\Lambda_k)$ and $\sigma_{max}(\bar{Q}_k)$ being shown. Each of these plots also showcase 6 out of 30 Monte Carlo runs.

5.3.1 High Inclination-orbit, "Tumble" Angular Velocity

Table 5.3 Simulation 1 Parameters

Parameter	Value	Description
$\bar{\omega}_0^{SE}$	$[1.15 \quad -2.86 \quad 1.71]^T \, °/s$	Initial Angular Velocity
i	$88°$	Orbital Inclination
Ψ_{321}	$[0° \quad 80° \quad 0°]^T$	Initial 3-2-1 Euler Angles
$q_{SE,0}$	$[0.667 \quad 0 \quad -0.745 \quad 0]^T$	True Initial Attitude Quaternion
$\bar{b}_0$	$-0.4°/s \leq b_0 \leq 0.4°/s$	Constant Bias Error
$\overline{sf}$	$-50000 \, ppm \leq \overline{sf} \leq 50000 \, ppm$	Scale Factor Errors

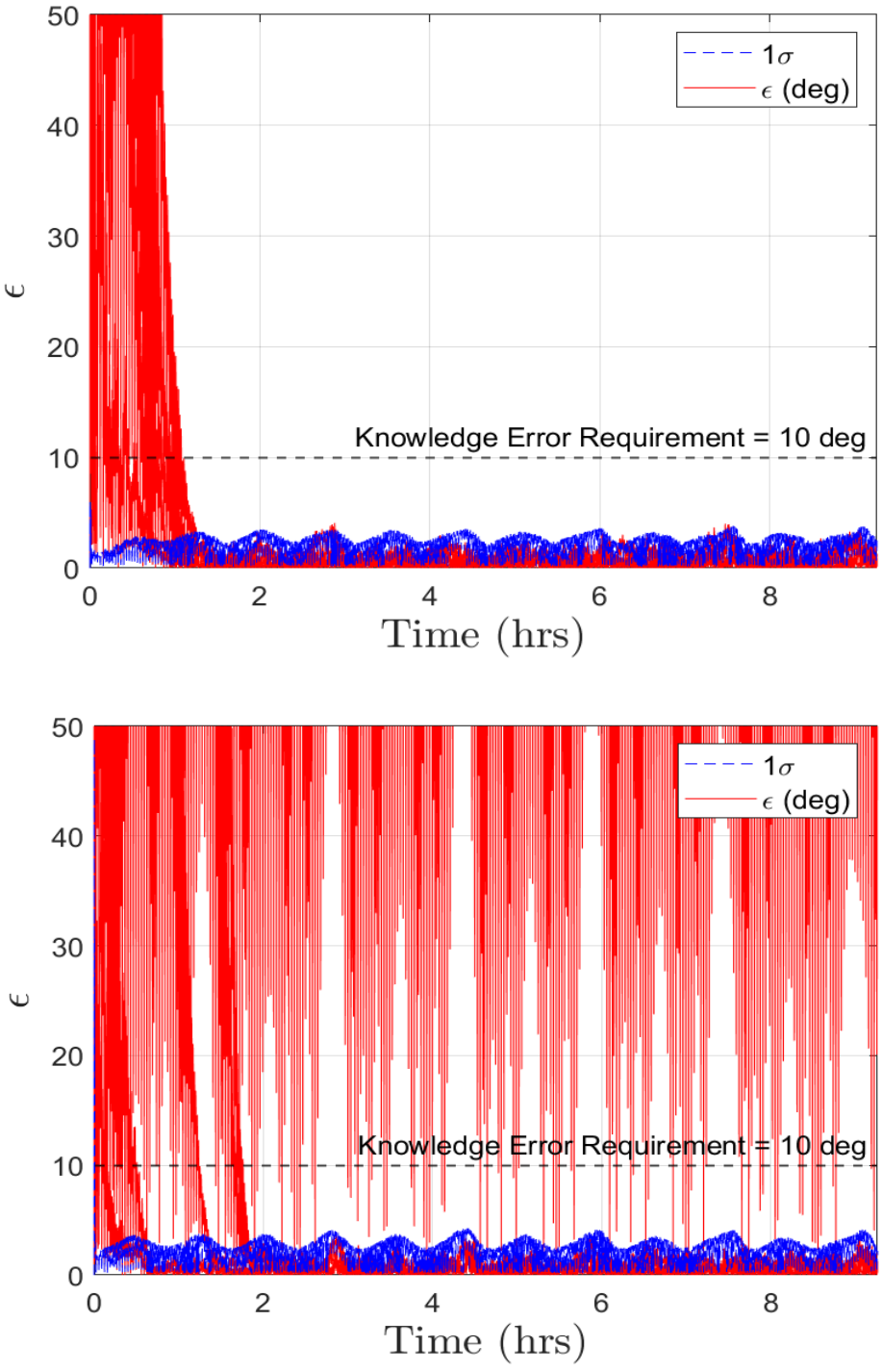

Figure 5.2 Pointing error ϵ history for high inclination, high $\bar{\omega}$ with no scale factor errors (top) and with scale factor errors (bottom).

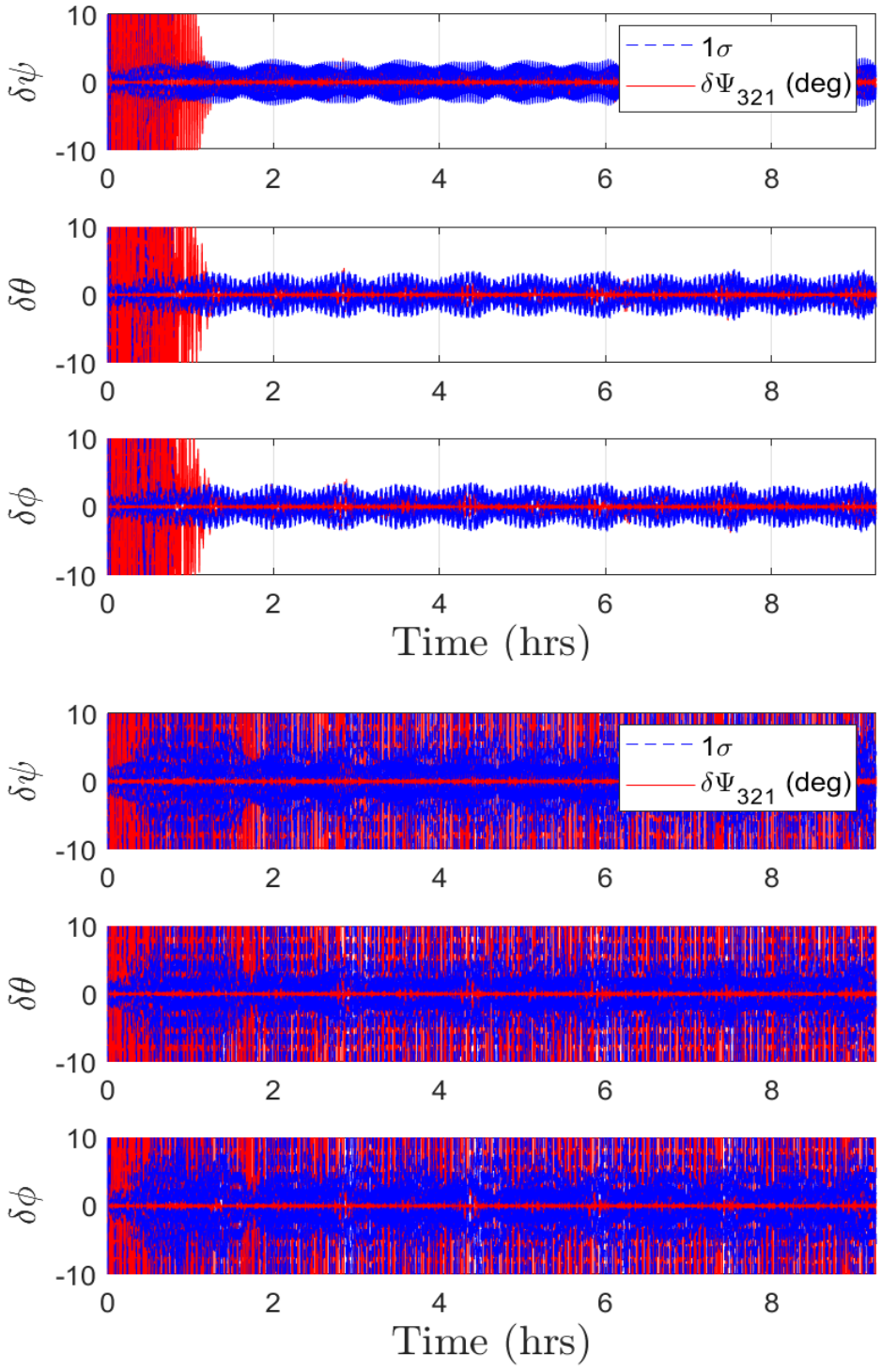

Figure 5.3 Euler angle error $\delta\Psi_{321}$ history for high inclination, high $\bar{\omega}$ with no scale factor errors (top) and with scale factor errors (bottom).

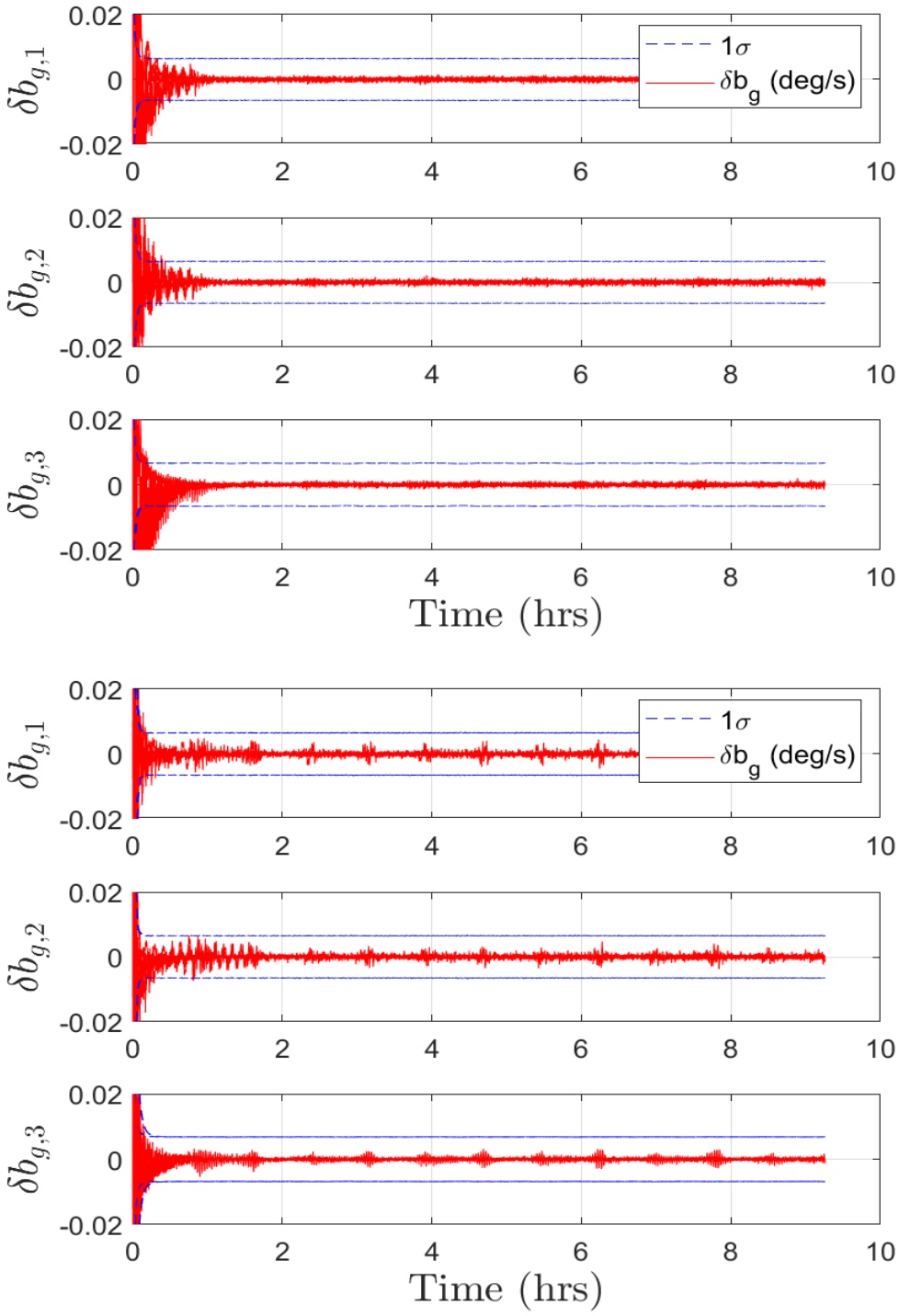

Figure 5.4 IMU bias error δb_g history for high inclination, high $\bar{\omega}$, with no scale factor errors (top) and with scale factor errors (bottom).

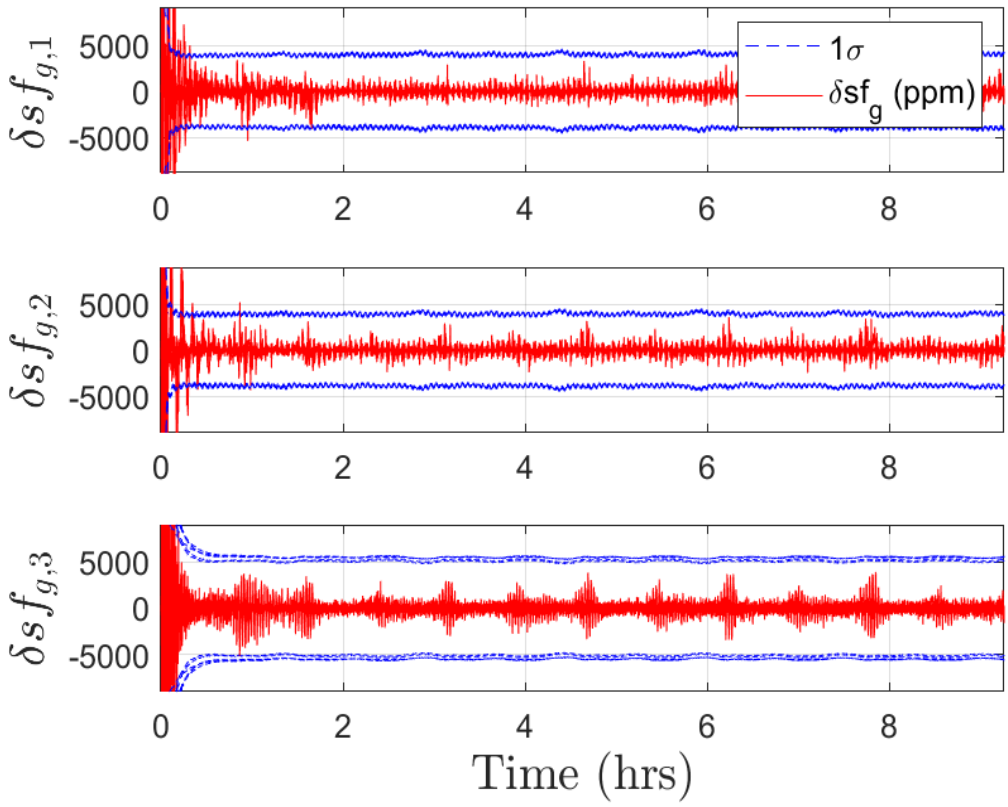

Figure 5.5 IMU scale factor error δsf_g for high inclination, high $\bar{\omega}$ for cases where scale factors are included.

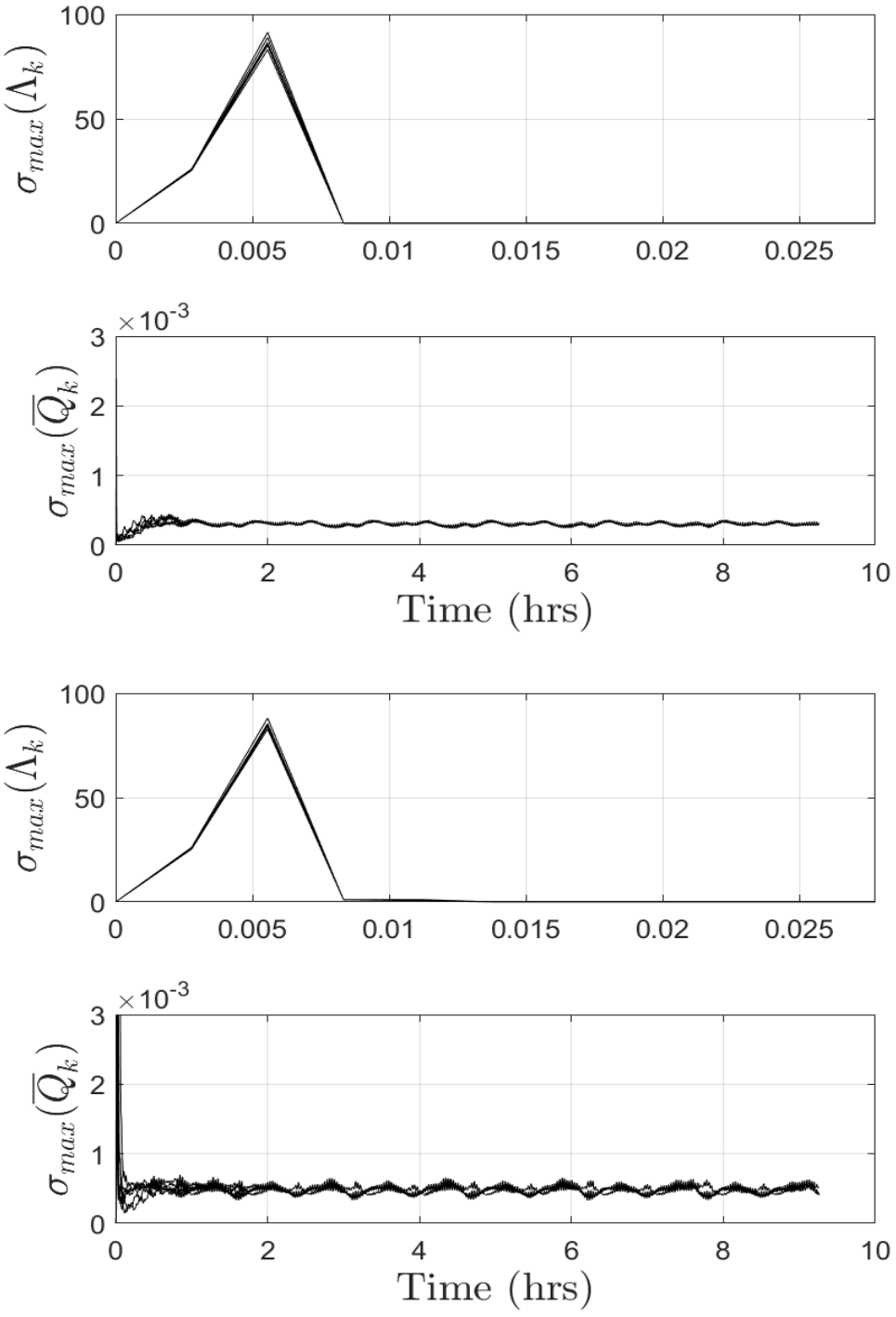

Figure 5.6 Stochastic observability metrics for high inclination, high $\overline{\omega}$ with no scale factor errors (top) and with scale factor errors (bottom).

In Figure 5.2 the angular error ϵ between S^3 and $\hat{S}^3$ axes as defined by Equation (5.2) is given for a high $\bar{\omega}^{SE}$ scenario at an orbital inclination of $i = 88°$. The top plot showcases ϵ when no scale factor errors are included within the noise of the system, with the bottom plot being for scenarios in which scale factor errors are included and estimated. With no scale factors, the ϵ estimate converges to below a 1σ of $4.5°$ within one and half hours. When scale factors are included and estimated, half of the runs converge to below a 1σ of $5.5°$ within one and a half hours, while the other half diverge and oscillate at a higher value of ϵ. Additionally, the ϵ covariance bound has slightly sharper peaks in the instance with scale factors than the no scale factor case. A similar phenomenon can be seen in the Euler angle plots of Figure 5.3.

In Figure 5.4, the bias state estimation errors are presented. The 1σ bound on the bias errors are approximately $0.007°/s$, with estimates converging to below that bound within half an hour of initialization. This is similar in the scale factor case of the bottom plot, however there is a noticeable increase in estimate convergence that occurs in a little under 2 hours. Moreover, there appears to be some form of oscillation within the bias estimates throughout the simulation timeframe that cause spikes to occur periodically. In the instance of the scale factor estimation errors seen in Figure 5.5, we see estimates converging to below a 1σ bound of $5000\ ppm$ within half an hour. Similar to the bias estimates, the scale factors appear to be oscillating throughout the simulation time frame with no real steady state values being obtained.

The results of a stochastic observability test of the system are presented in Figure 5.6 with the two metrics of $\sigma_{max}(\Lambda_k)$ and $\sigma_{max}(\bar{Q}_k)$ for each scenario presented. In both instances of scale factor inclusion, the value of $\sigma_{max}(\Lambda_k)$ peaks

at the 2nd measurement update at 20 seconds with a value of 86, and then begins to reduce to 0 in the following measurements. However, the rate at which this convergence happens is slightly slower when scale factors are included, reducing to zero at the 5th measurement as opposed to the 3rd in the no scale factor case. In either instance, this implies that the state covariance is no longer a function of the initial state covariance, P_0, after 5 measurement updates.

The $\sigma_{max}(\bar{Q}_k)$ plots within Figure 5.6 showcase the second metric of the stochastic observability test. In the instance where no scale factors are included, the value of $\sigma_{max}(\bar{Q}_k)$ seems to converge to an oscillatory trend near one and a half hours. This mimics the oscillation seen in state covariance of the Euler angle estimates of Figure 5.3. When scale factor errors are included, the values of $\sigma_{max}(\bar{Q}_k)$ seem to be more oscillatory and less uniform. Additionally, the steady state values appear to be larger when scale factors are included. However, as both instances of $\sigma_{max}(\bar{Q}_k)$ appear to be bounded, the values of $\sigma_{max}(\Lambda_k)$ and $\sigma_{max}(\bar{Q}_k)$ imply that the system is stochastically observable for both cases of scale factor inclusion.

5.3.2 High Inclination-orbit, Spin Stabilized Angular Velocity

Table 5.4 Simulation 2 Parameters

Parameter	Value	Description
$\bar{\omega}_0^{SE}$	$[0 \quad 0 \quad 0.57]^T \, °/s$	Initial Angular Velocity
i	$88°$	Orbital Inclination
Ψ_{321}	$[0° \quad 80° \quad 0°]^T$	Initial 3-2-1 Euler Angles
$q_{SE,0}$	$[0.667 \quad 0 \quad -0.745 \quad 0]^T$	True Initial Attitude Quaternion
$\bar{b}_0$	$-0.4°/s \leq b_0 \leq 0.4°/s$	Constant Bias Error
$\overline{sf}$	$-50000 \, ppm \leq \overline{sf} \leq 50000 \, ppm$	Scale Factor Errors

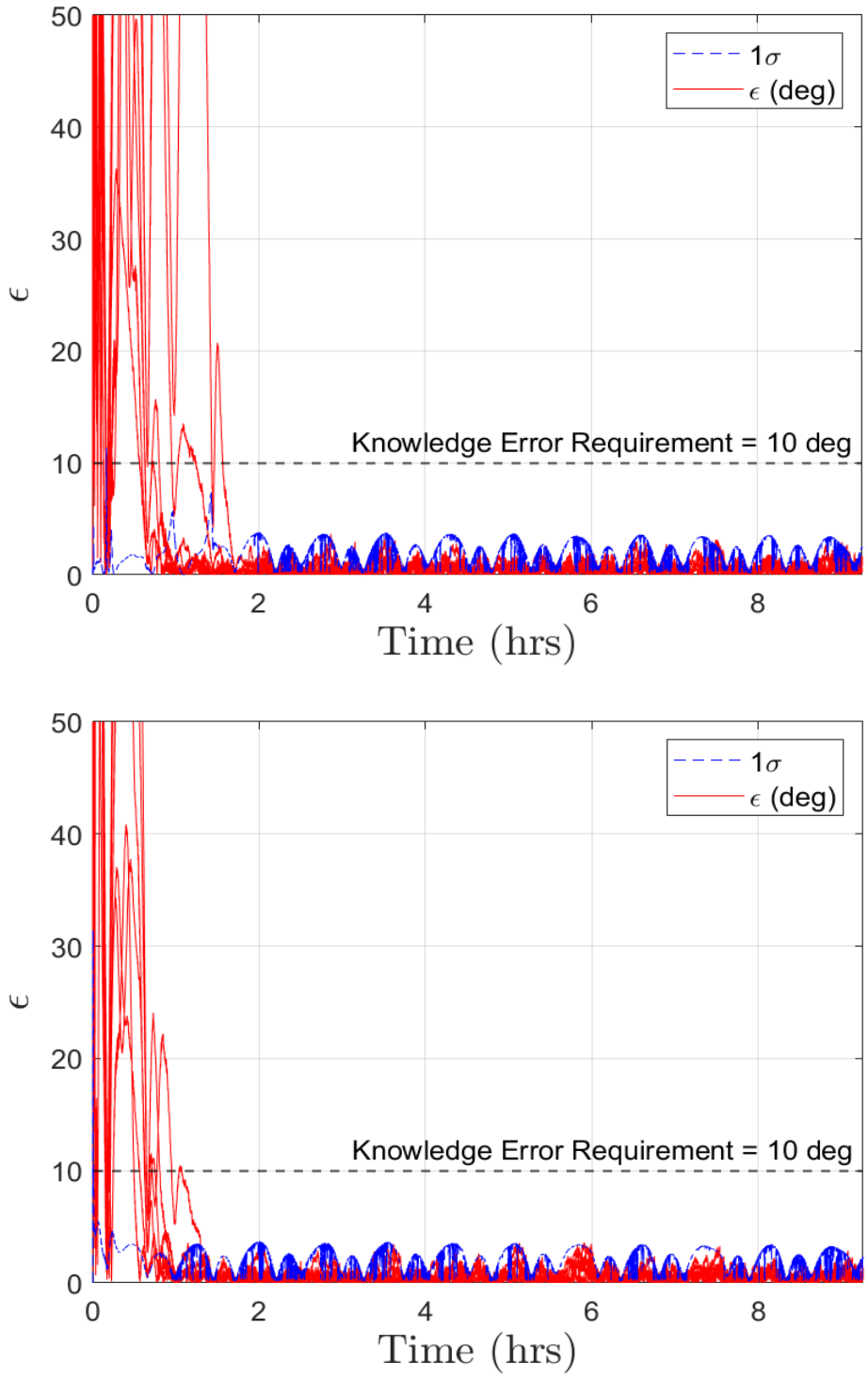

Figure 5.7 Pointing error ϵ history for high inclination, spin $\bar{\omega}$ with no scale factor errors (top) and with scale factor errors (bottom)

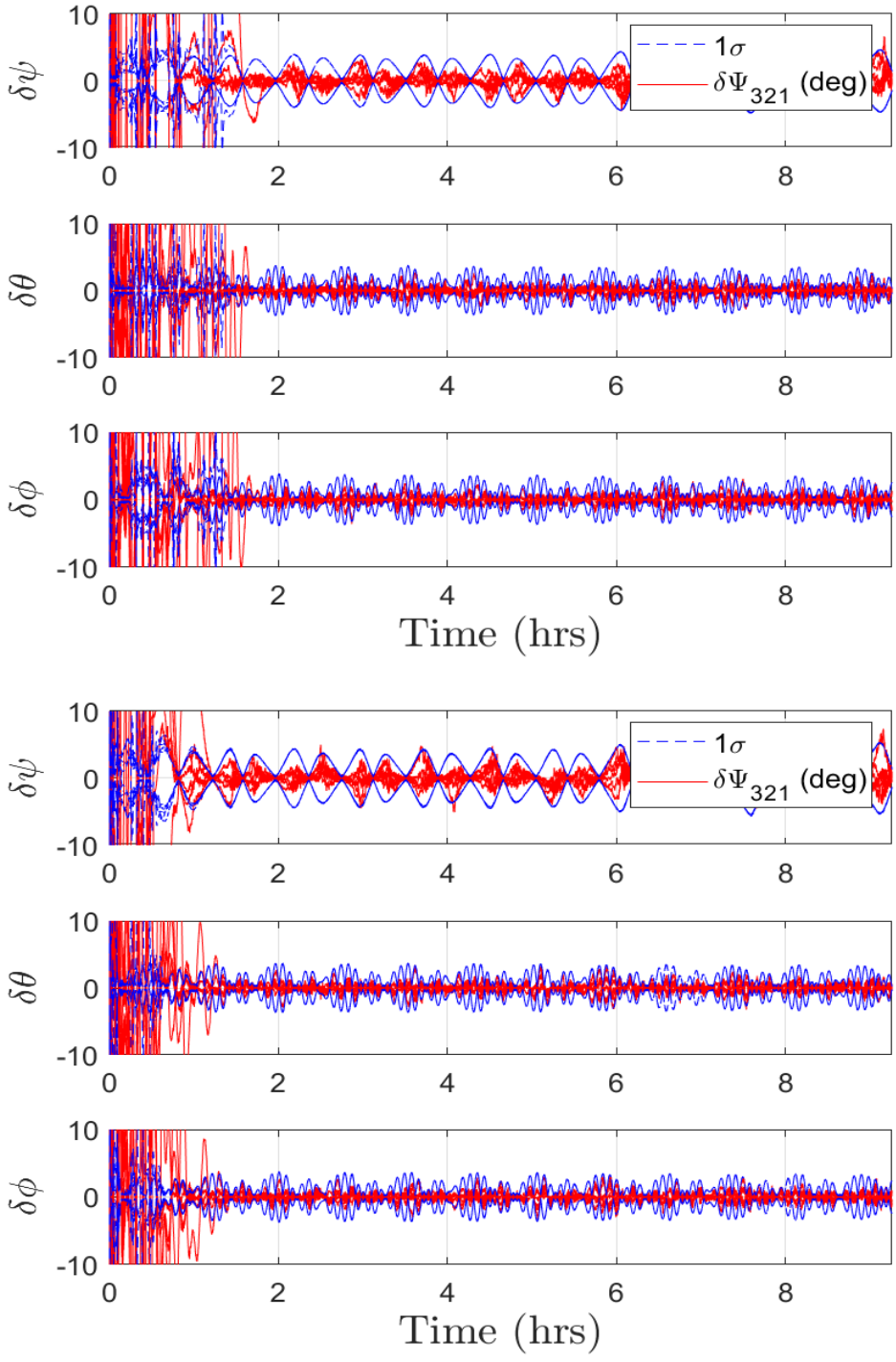

Figure 5.8 Euler angle error $\delta\Psi_{321}$ history for high inclination, spin $\bar{\omega}$ with no scale factor errors (top) and with scale factor errors (bottom).

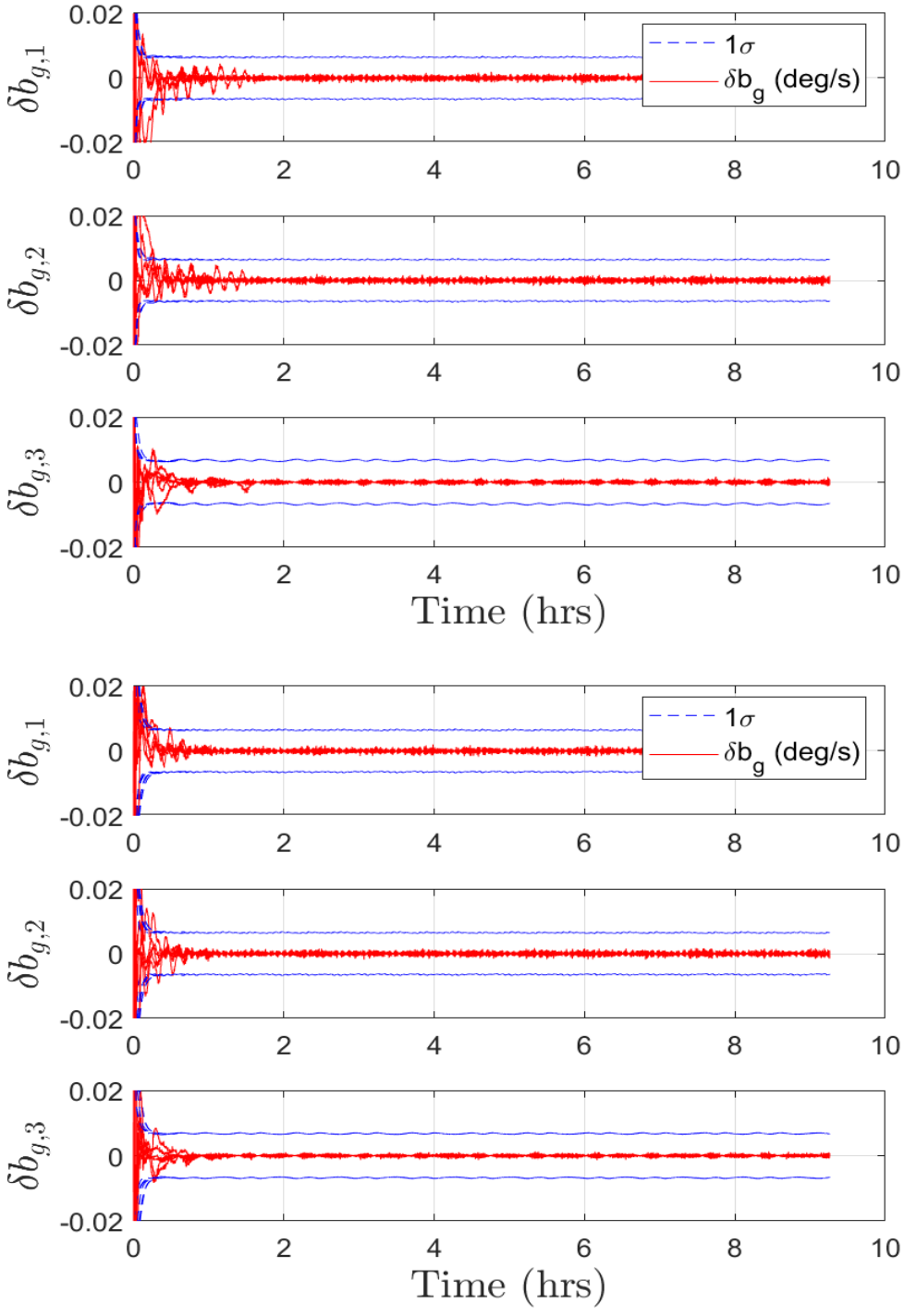

Figure 5.9 IMU bias error δb_g history for high inclination, spin $\bar{\omega}$ with no scale factor errors (top) and with scale factor errors (bottom).

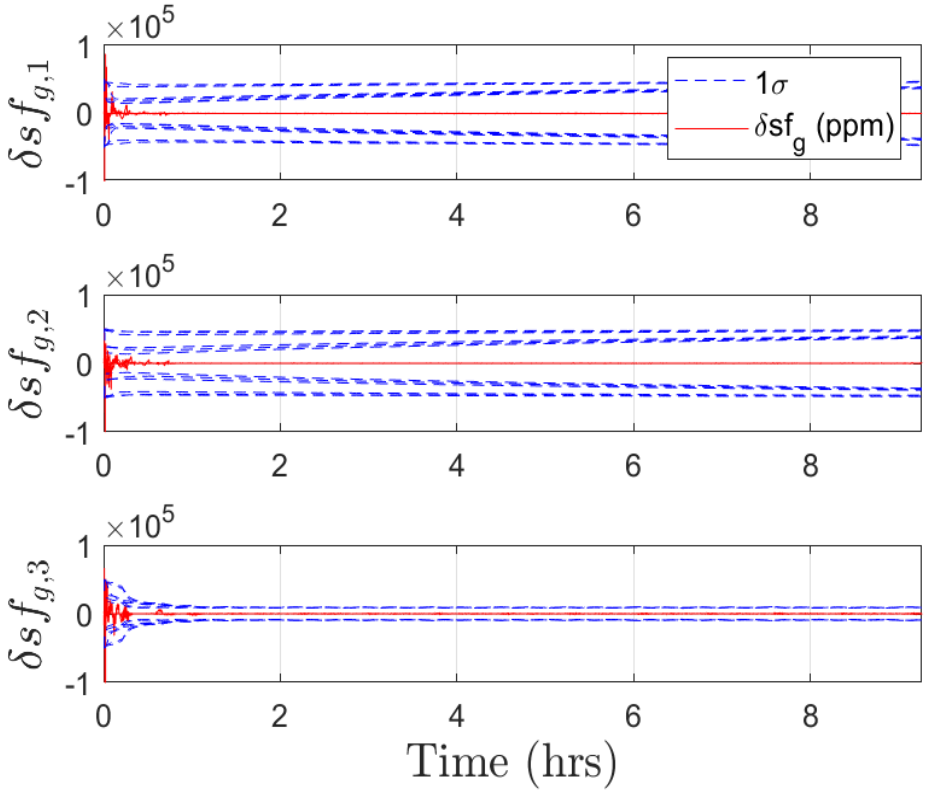

Figure 5.10 IMU scale factor error δsf_g for high inclination, spin $\bar{\omega}$ for cases where scale factors are included.

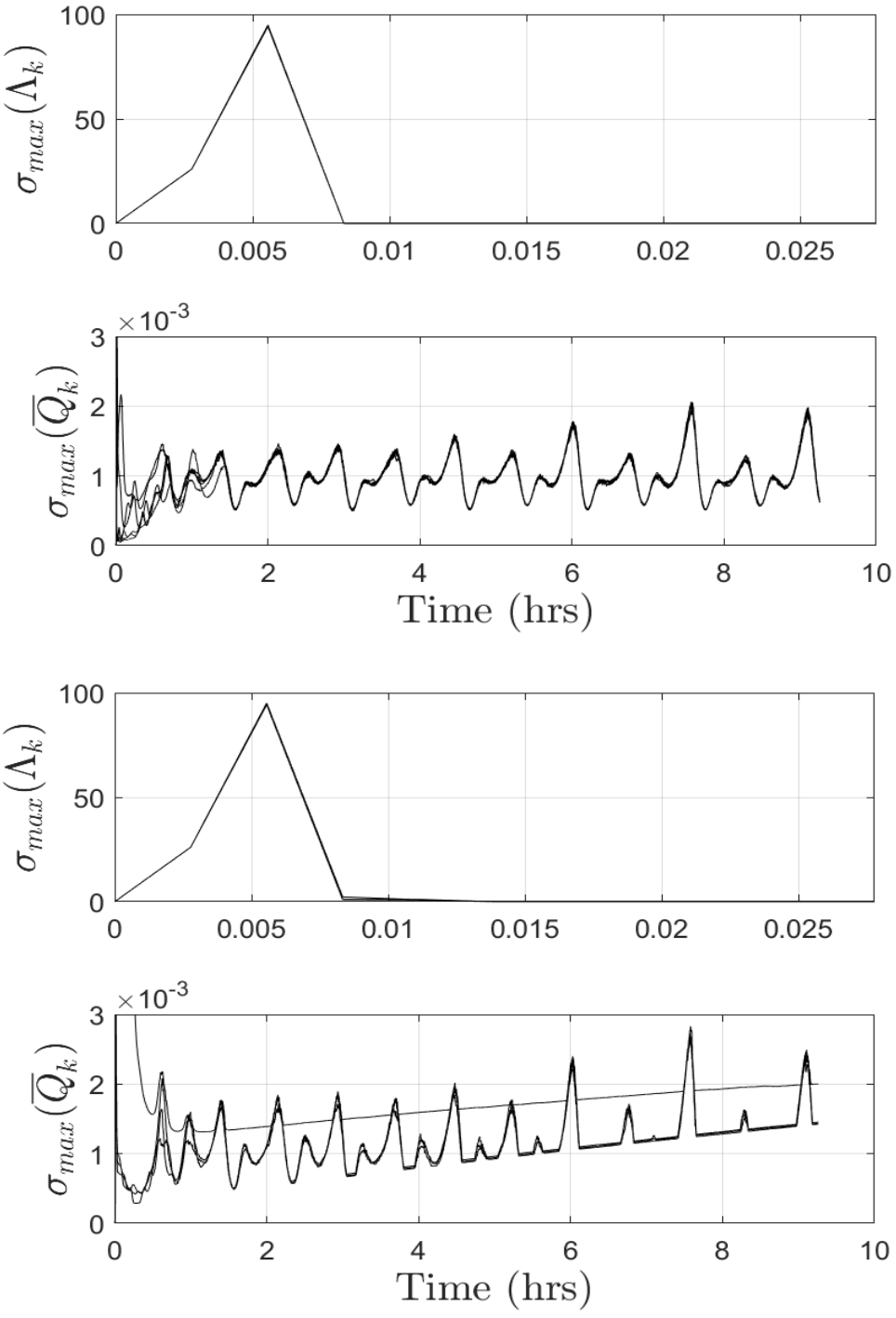

Figure 5.11 Stochastic observability metrics for high inclination, spin $\overline{\omega}$ with no scale factor errors (top) and with scale factor errors (bottom).

In Figure 5.7 the angular error ϵ is given for a spin stabilized $\bar{\omega}^{SE}$ scenario at an orbital inclination of $i = 88°$. In both cases of scale factor inclusion, the ϵ estimate converges to below a 1σ of $5°$ within one and half to two hours. A similar phenomenon is shown in the Euler angle plots of Figure 5.8. In this figure, it is clearly seen that the covariance on the $\delta\psi$ estimates have less oscillation frequency than those of $\delta\phi$ and $\delta\theta$. Additionally, it appears that the attitude estimates given by the red lines in both Figure 5.7 and Figure 5.8 are larger in the instance when scale factor errors are included.

In Figure 5.9, the bias state estimation errors are presented. Similar to the high $\bar{\omega}^{SE}$ case, the 1σ bound on the bias errors are approximately $0.006°/s$, with estimates converging to below that bound in less than a half hour of initialization. In each case of scale factor inclusion, the bias estimates maintain relatively similar convergence trend, no longer oscillating in the manner of Figure 5.4 and converging to relatively steady values in about two hours.

In the instance of the scale factor estimation errors seen in Figure 5.10, we see each axis estimate converging to a steady state value within half an hour. However, in the S^1 and S^2 axes, the covariance appears to be noticeably different for each run. Moreover, some covariance bounds appear to be growing throughout time in these axes. This is due to the lack of angular velocity in the S^1 and S^2 axes, causing the respective scale factors to be unobservable. The S^3 axis of the scale factor estimates has a lower covariance bound that appears to be constant. In the S^1 and S^2 axis, the upper bounds on the covariance appear to be nearing $45000\,ppm$, whereas the covariance on the S^3 is bounded near $8500\,ppm$.

The results of a stochastic observability test of the system are presented in Figure 5.11. Similar to the high $\bar{\omega}^{SE}$ case, the values of $\sigma_{max}(\Lambda_k)$ for both scale factor cases peak at the 2nd measurement update, and then begin to reduce to 0 in the following measurements, with slightly different rates. As with Figure 5.6, this implies that the state covariance is no longer a function of the initial state covariance, P_0.

The value of $\sigma_{max}(\bar{Q}_k)$ can be seen in the lower sub-plots of Figure 5.11. When no scale factors are included, the value of $\sigma_{max}(\bar{Q}_k)$ converges to an oscillatory behavior in about two hours. Noticeable peaks and troughs in the value of $\sigma_{max}(\bar{Q}_k)$ are present throughout the simulation time frame. While the peaks seem to be increasing after four hours, the troughs stay at a relatively consistent level. Additionally, the peaks begin to reduce again after 8 hours. This trend is assumed to be due to the varying EMF vector throughout the orbit, and not due to unbounded growth in covariance. As such, the no scale factor case is considered stochastically observable.

In the instance where scale factors are included, the plot of $\sigma_{max}(\bar{Q}_k)$ has significant differences from the no scale factor case. Firstly, the general value of $\sigma_{max}(\bar{Q}_k)$ is larger than that of the prior case, indicated higher amounts of noise in the system. Secondly, trends are less uniform, and after three hours, the troughs of the plot disappear and are replaced by a growing trend line. This can be attributed to the growing covariance on the scale factor estimates in the S^1 and S^2 axes. As the peaks of the plot appear to follow the same pattern as the no scale factor instance, we treat this linear growth as failure to the stochastic observability test, indicating this simulation scenario is stochastically unobservable. Detailed discussion of this trend can be found at the end of this chapter.

5.3.3 High Inclination-orbit, Low Angular Velocity

Table 5.5 Simulation 3 Parameters

Parameter	Value	Description
$\bar{\omega}_0^{SE}$	$[0 \quad 0 \quad 0.057]^T \, °/s$	Initial Angular Velocity
i	$88°$	Orbital Inclination
Ψ_{321}	$[0° \quad 80° \quad 0°]^T$	Initial 3-2-1 Euler Angles
$q_{SE,0}$	$[0.667 \quad 0 \quad -0.745 \quad 0]^T$	True Initial Attitude Quaternion
$\bar{b}_0$	$-0.4°/s \leq b_0 \leq 0.4°/s$	Constant Bias Error
$\overline{sf}$	$-50000 \, ppm \leq \overline{sf} \leq 50000 \, ppm$	Scale Factor Errors

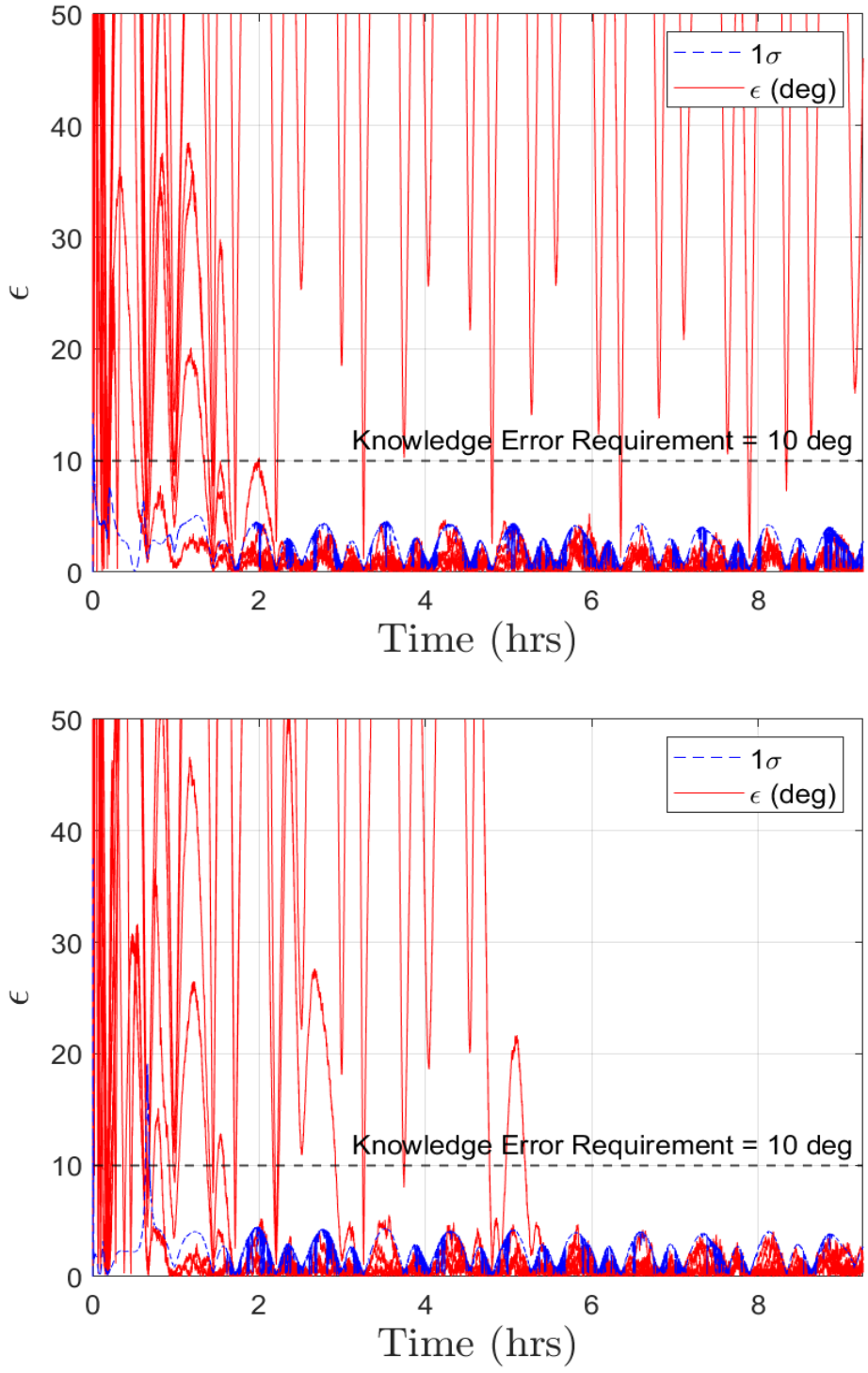

Figure 5.12 Pointing error ϵ history for high inclination, low $\bar{\omega}$ with no scale factor errors (top) and with scale factor errors (bottom)

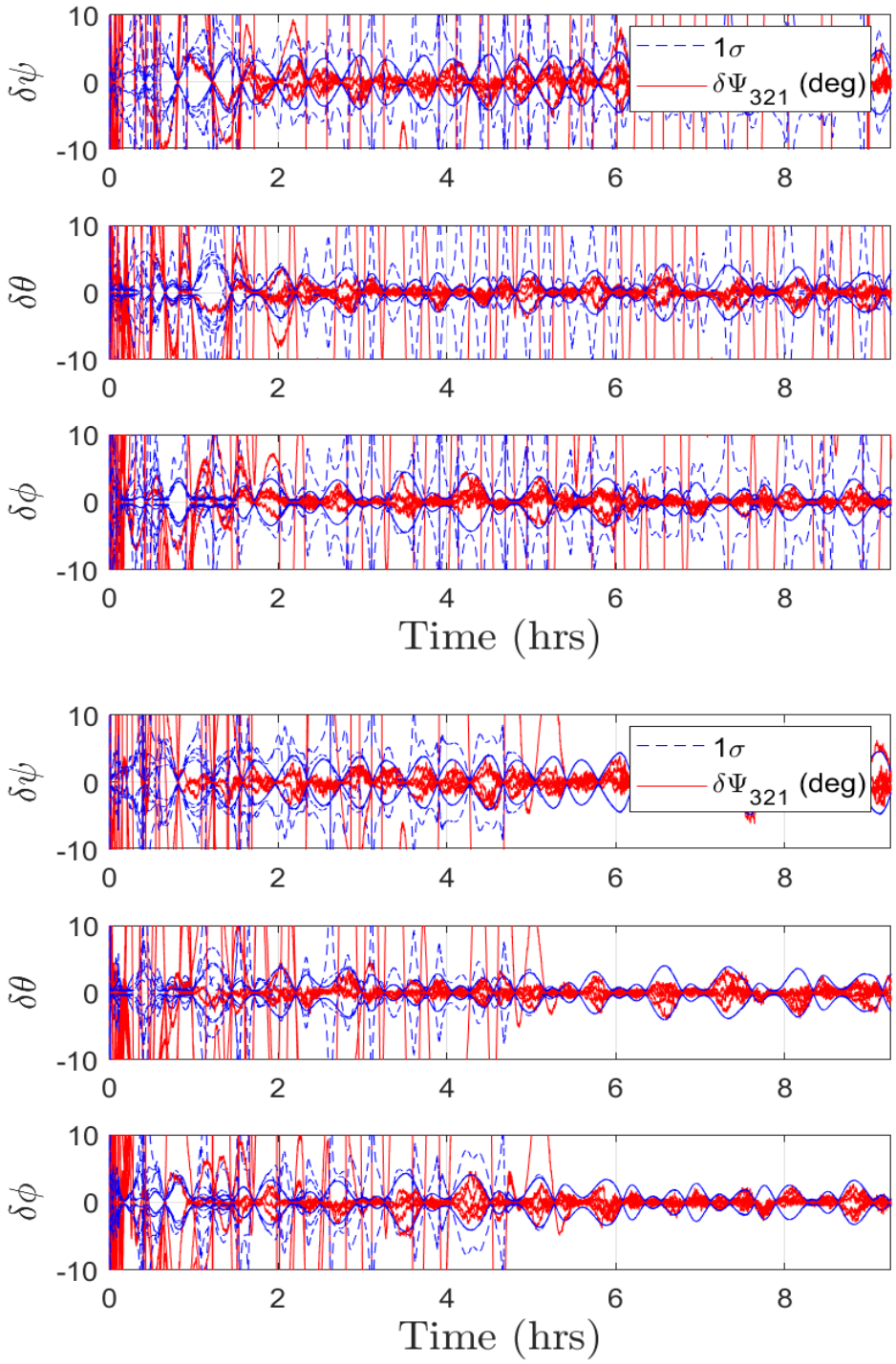

Figure 5.13 Euler angle error $\delta\Psi_{321}$ history for high inclination, low $\bar{\omega}$ with no scale factor errors (top) and with scale factor errors (bottom).

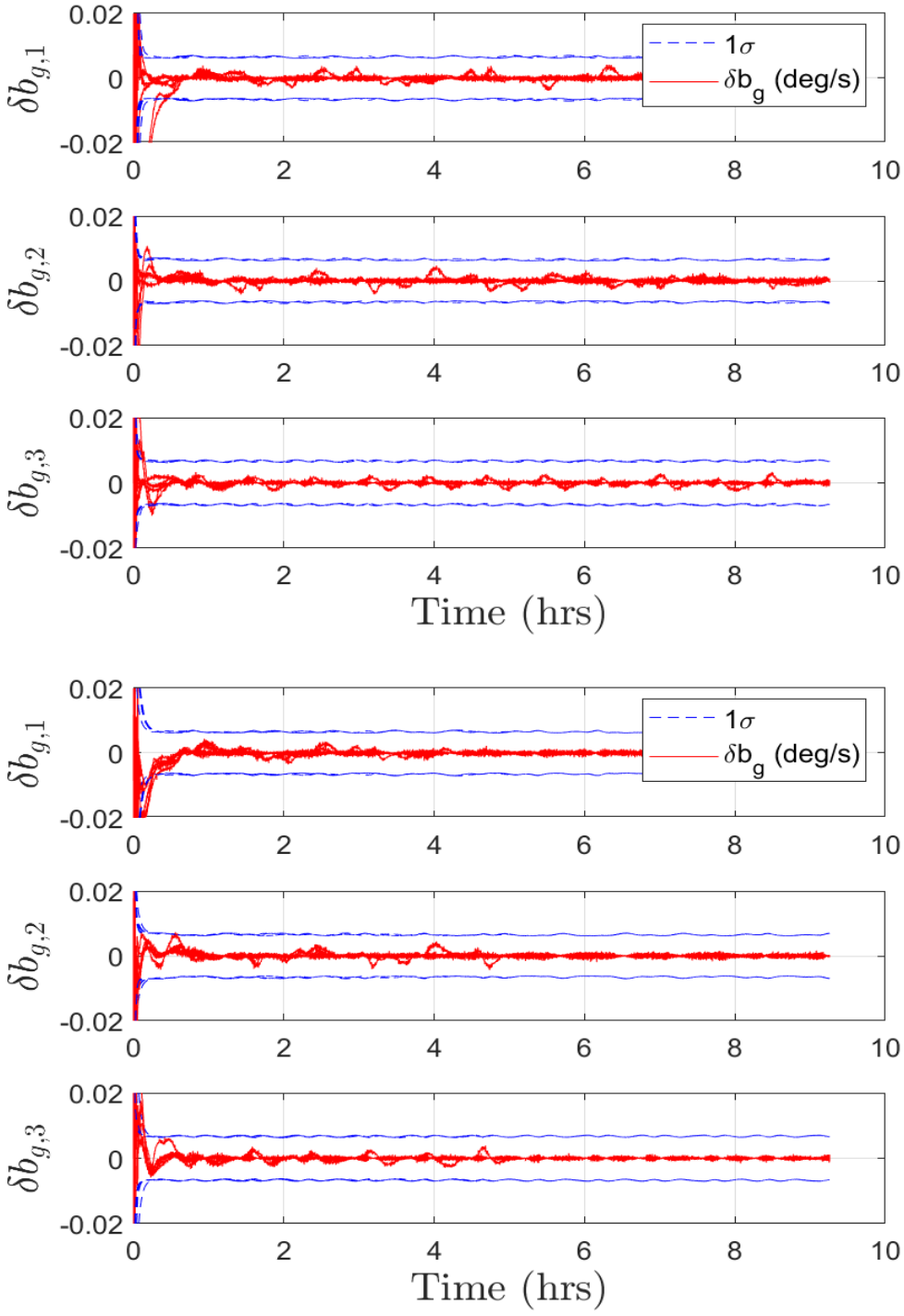

Figure 5.14 IMU bias error δb_g history for high inclination, low $\bar{\omega}$ with no scale factor errors (top) and with scale factor errors (bottom).

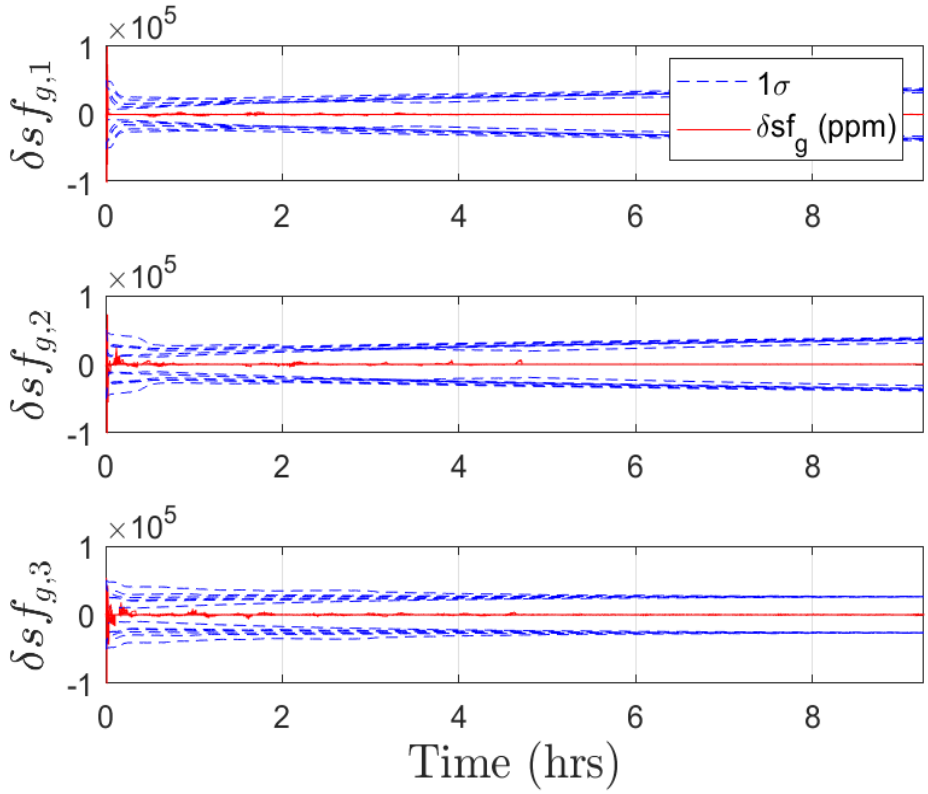

Figure 5.15 IMU scale factor error δsf_g for high inclination, low $\bar{\omega}$ for cases where scale factors are included.

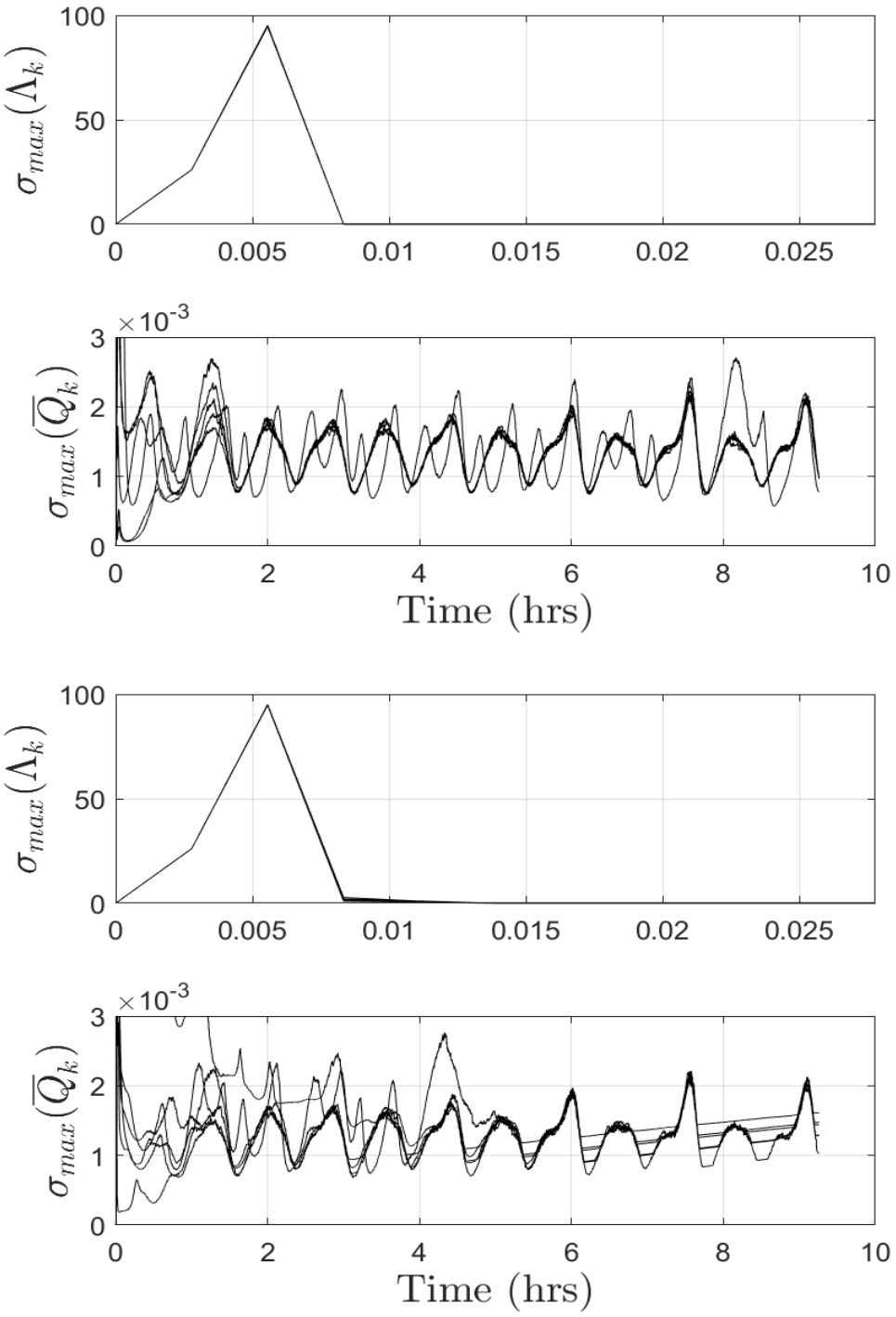

Figure 5.16 Stochastic observability metrics for high inclination, low $\overline{\omega}$ with no scale factor errors (top) and with scale factor errors (bottom).

Figure 5.12 showcases the VMA convergence for the low $\bar{\omega}^{SE}$ case. When no scale factor errors are present within the noise of the system, a 5 out of 6 Monte Carlo runs converge to below a 1σ bound of $5°$ in a little over two hours. The remaining plot does not converge within simulation timeframe and appears to be oscillating with large amplitude. When scale factor estimates are included, 6 out of 6 runs converge to below a 1σ bound of $5°$ within five and half hours of initialization. A similar phenomenon is shown in the Euler angle plots of Figure 5.13.

The bias estimation errors are shown in Figure 5.14. Similar to both the high and spin stabilized $\bar{\omega}^{SE}$ cases, the 1σ bound on the bias errors are approximately $0.007°/s$, with estimates converging to below that bound in less than a half hour of initialization. A noticeable difference is that the bias covariance in Figure 5.14 appears slightly oscillatory when compared to Figure 5.4 and Figure 5.9. Bias estimates do not appear to converge to a steady state value in the no scale factor case, instead oscillating throughout the simulation time frame. In the scale factor case, the bias estimates seem to converge to a steady estimate after about five and half hours.

In the instance of the scale factor estimation errors of Figure 5.15, we see each axis estimate converging below the 1σ bounds almost immediately. Covariance estimates on the S^1 and S^2 axes are climbing throughout the simulation time, while the covariance estimate in the S^3 axis converges to a steady bound of 20000 ppm. This is a noticeable increase when compared to the covariance in the S^3 axis as seen by Figure 5.10.

The results of a stochastic observability test are given in Figure 5.16. Similar to both the high and spin stabilized $\bar{\omega}^{SE}$ cases, the value of $\sigma_{max}(\Lambda_k)$ peaks at 20 seconds, and then begins to limit to zero afterwards. The value of $\sigma_{max}(\bar{Q}_k)$ in the instance where no scale factors are included appears to have a lower frequency of oscillation than the higher $\bar{\omega}^{SE}$ cases. Additionally, one of the trends does not match the others, which is due to the lone estimate that has not converged. In the case where scale factor errors are included, the values of $\sigma_{max}(\bar{Q}_k)$ begin to follow the same trend at about five and half hours. Moreover, a linear slope appears near the troughs of the trend, similar to the cases of scale factor inclusion for the spin stabilized $\bar{\omega}^{SE}$ case. Due to this trend, we treat this simulation scenario as stochastically unobservable.

5.3.4 Mid Inclination-orbit, "Tumble" Angular Velocity

Table 5.6 Simulation 4 Parameters

Parameter	Value	Description
$\bar{\omega}_0^{SE}$	$[1.15 \quad -2.86 \quad 1.71]^T \, °/s$	Initial Angular Velocity
i	$50°$	Orbital Inclination
Ψ_{321}	$[0° \quad 80° \quad 0°]^T$	Initial 3-2-1 Euler Angles
$q_{SE,0}$	$[0.667 \quad 0 \quad -0.745 \quad 0]^T$	True Initial Attitude Quaternion
$\bar{b}_0$	$-0.4°/s \leq b_0 \leq 0.4°/s$	Constant Bias Error
$\overline{sf}$	$-50000\, ppm \leq \overline{sf} \leq 50000\, ppm$	Scale Factor Errors

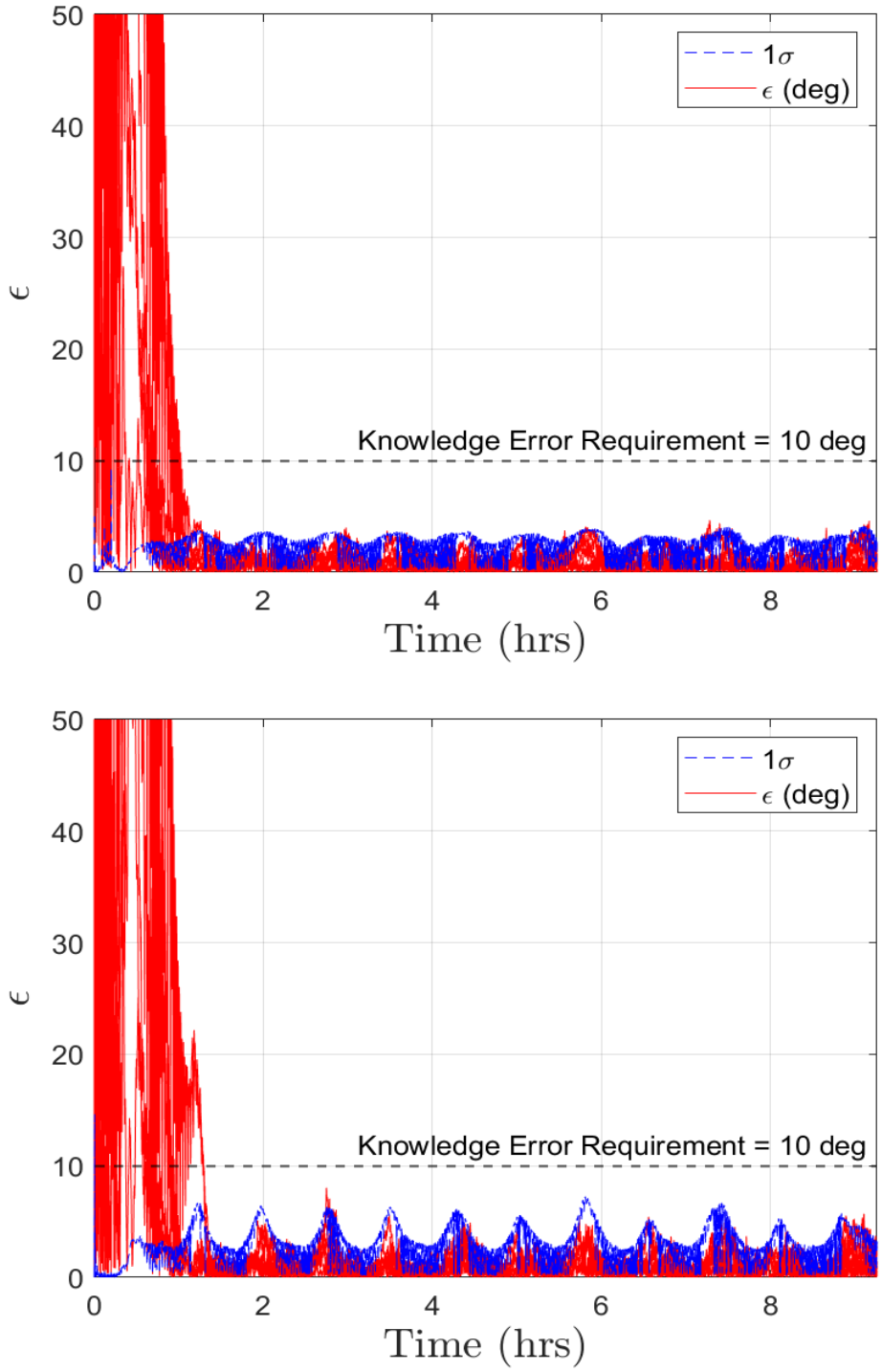

Figure 5.17 Pointing error ϵ history for mid inclination, high $\bar{\omega}$ with no scale factor errors (top) and with scale factor errors (bottom)

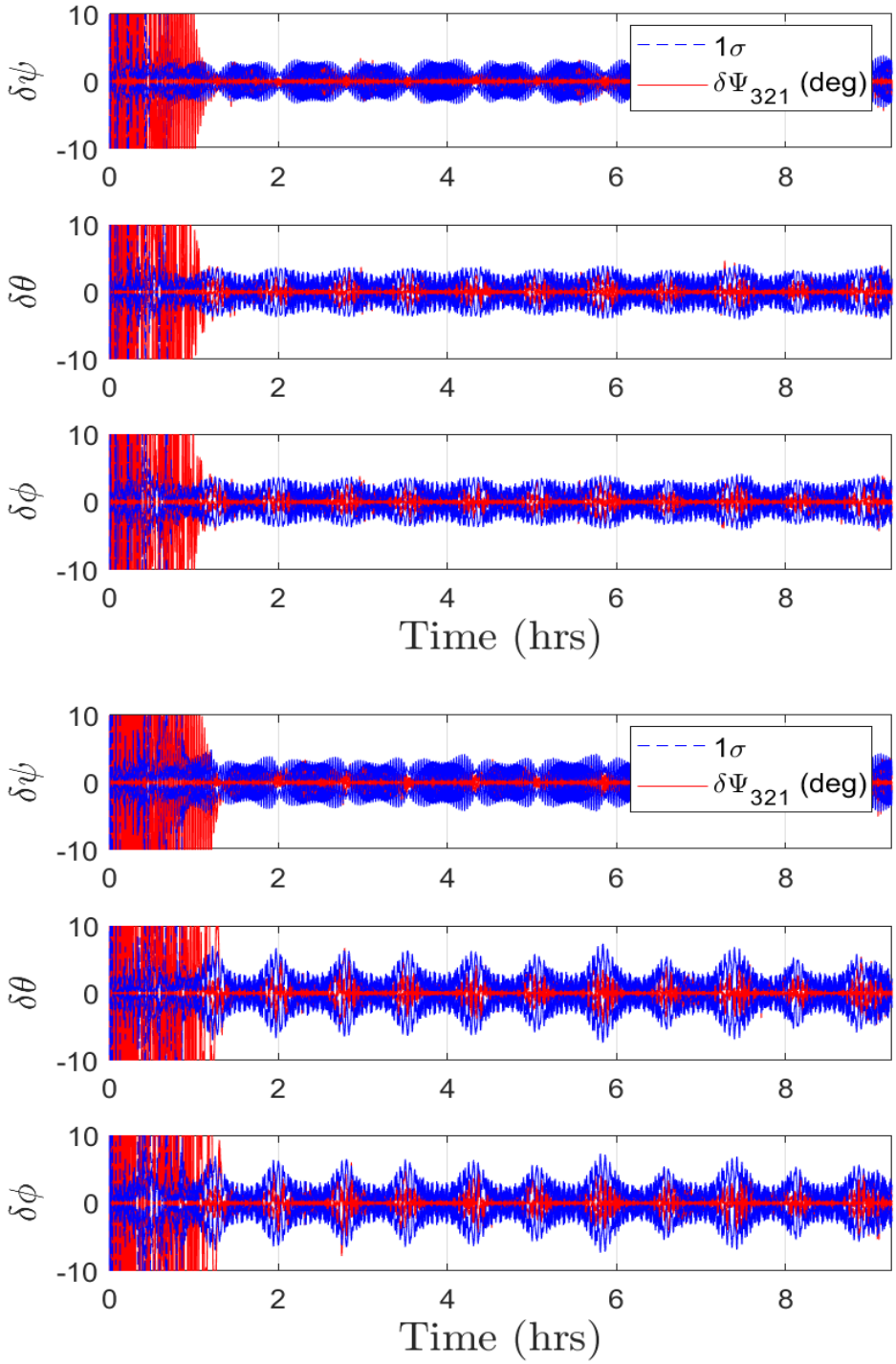

Figure 5.18 Euler angle error $\delta\Psi_{321}$ history for mid inclination, high $\bar{\omega}$ with no scale factor errors (top) and with scale factor errors (bottom).

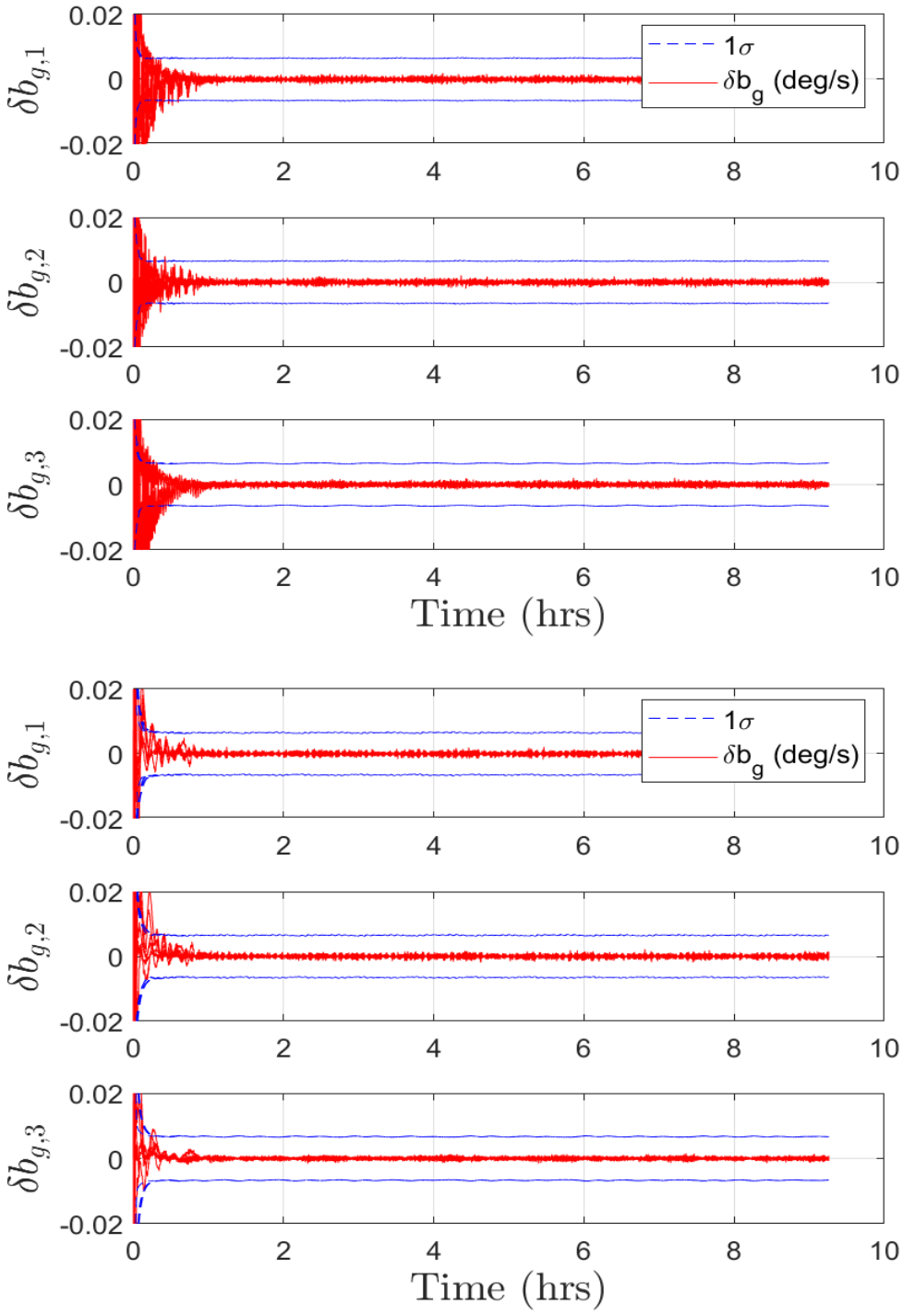

Figure 5.19 IMU bias error δb_g history for mid inclination, high $\bar{\omega}$ with no scale factor errors (top) and with scale factor errors (bottom).

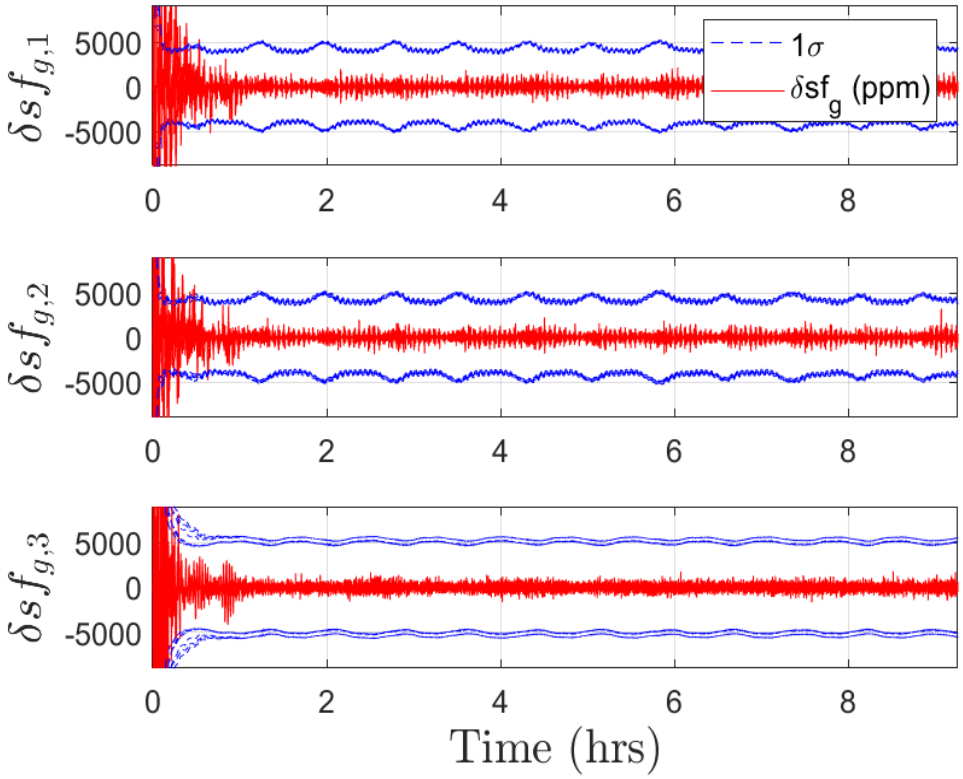

Figure 5.20 IMU scale factor error δsf_g for mid inclination, high $\bar{\omega}$ for cases where scale factors are included.

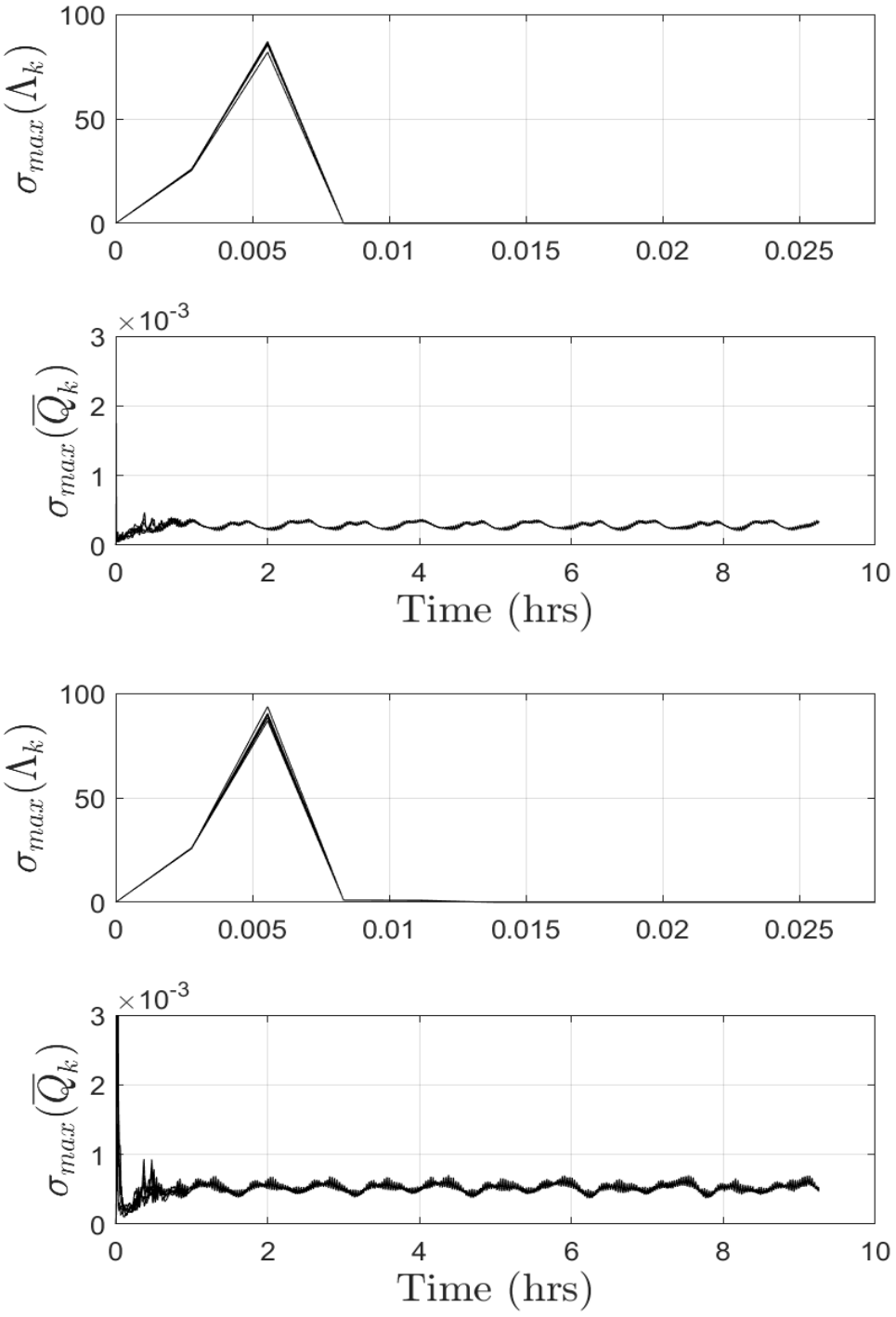

Figure 5.21 Stochastic observability metrics for mid inclination, high $\overline{\omega}$ with no scale factor errors (top) and with scale factor errors (bottom).

In Figure 5.17 the angular error ϵ between S^3 and $\hat{S}^3$ axes as defined by Equation (5.2) is given for a high $\bar{\omega}^{SE}$ scenario at an orbital inclination of $i = 50°$. The top plot showcases ϵ when no scale factor errors are included within the noise of the system, with the bottom plot being for scenarios in which scale factor errors are included and estimated. With no scale factors, the ϵ estimate converges to below a 1σ of $4.5°$ within one and half hours. When scale factors are included and estimated, the ϵ estimate converges to below a 1σ of $5° - 7°$ within one and a half hours. Specifically, noticeable periodic peaks with amplitude of approximately $7°$ are present in the covariance for the scale factors. A similar phenomenon is seen in the Euler angle plots of Figure 5.18

In Figure 5.19, the bias state estimation errors are presented. The 1σ bound on the bias errors are approximately $0.007°/s$, with estimates converging to below that bound within half an hour of initialization. In both instances of scale factor inclusion, it appears that steady state estimates are reached in approximately one hour after initialization. In the instance of the scale factor estimation errors seen in Figure 5.20, we see estimates converging to below a 1σ bound of $5000\ ppm$ within half an hour. Similar to the bias estimates, the scale factors reach steady state estimation values after about one hour.

The results of a stochastic observability test of the system are presented in Figure 5.21 with the two metrics of $\sigma_{max}(\Lambda_k)$ and $\sigma_{max}(\bar{Q}_k)$ for each scenario presented. In both instances of scale factor inclusion, the value of $\sigma_{max}(\Lambda_k)$ peaks at the 2nd measurement update at 20 seconds with a value of 86, and then begins to reduce to 0 in the following measurements, similar to the high inclination cases. This implies that the state covariance is no longer a function of the initial state covariance, P_0, after 5 measurement updates.

The $\sigma_{max}(\bar{Q}_k)$ plots within Figure 5.21 showcase the second metric of the stochastic observability test. In both instances of scale factor inclusion, the value of $\sigma_{max}(\bar{Q}_k)$ seems to converge to an oscillatory trend near one hour. This mimics the oscillation seen in state covariance of the Euler angle estimates of Figure 5.18. When scale factor errors are included, the values of $\sigma_{max}(\bar{Q}_k)$ seem to a slightly larger amplitude in oscillation. Additionally, the steady state values appear to be larger when scale factors are included. However, as both instances of $\sigma_{max}(\bar{Q}_k)$ appear to be bounded, the values of $\sigma_{max}(\Lambda_k)$ and $\sigma_{max}(\bar{Q}_k)$ imply that the system is stochastically observable for both cases of scale factor inclusion.

5.3.5 Mid Inclination-orbit, Spin Stabilized Angular Velocity

Table 5.7 Simulation 5 Parameters

Parameter	Value	Description
$\bar{\omega}_0^{SE}$	$[0 \quad 0 \quad 0.57]^T \, °/s$	Initial Angular Velocity
i	$50°$	Orbital Inclination
Ψ_{321}	$[0° \quad 80° \quad 0°]^T$	Initial 3-2-1 Euler Angles
$q_{SE,0}$	$[0.667 \quad 0 \quad -0.745 \quad 0]^T$	True Initial Attitude Quaternion
$\bar{b}_0$	$-0.4°/s \leq b_0 \leq 0.4°/s$	Constant Bias Error
$\overline{sf}$	$-50000 \, ppm \leq \overline{sf} \leq 50000 \, ppm$	Scale Factor Errors

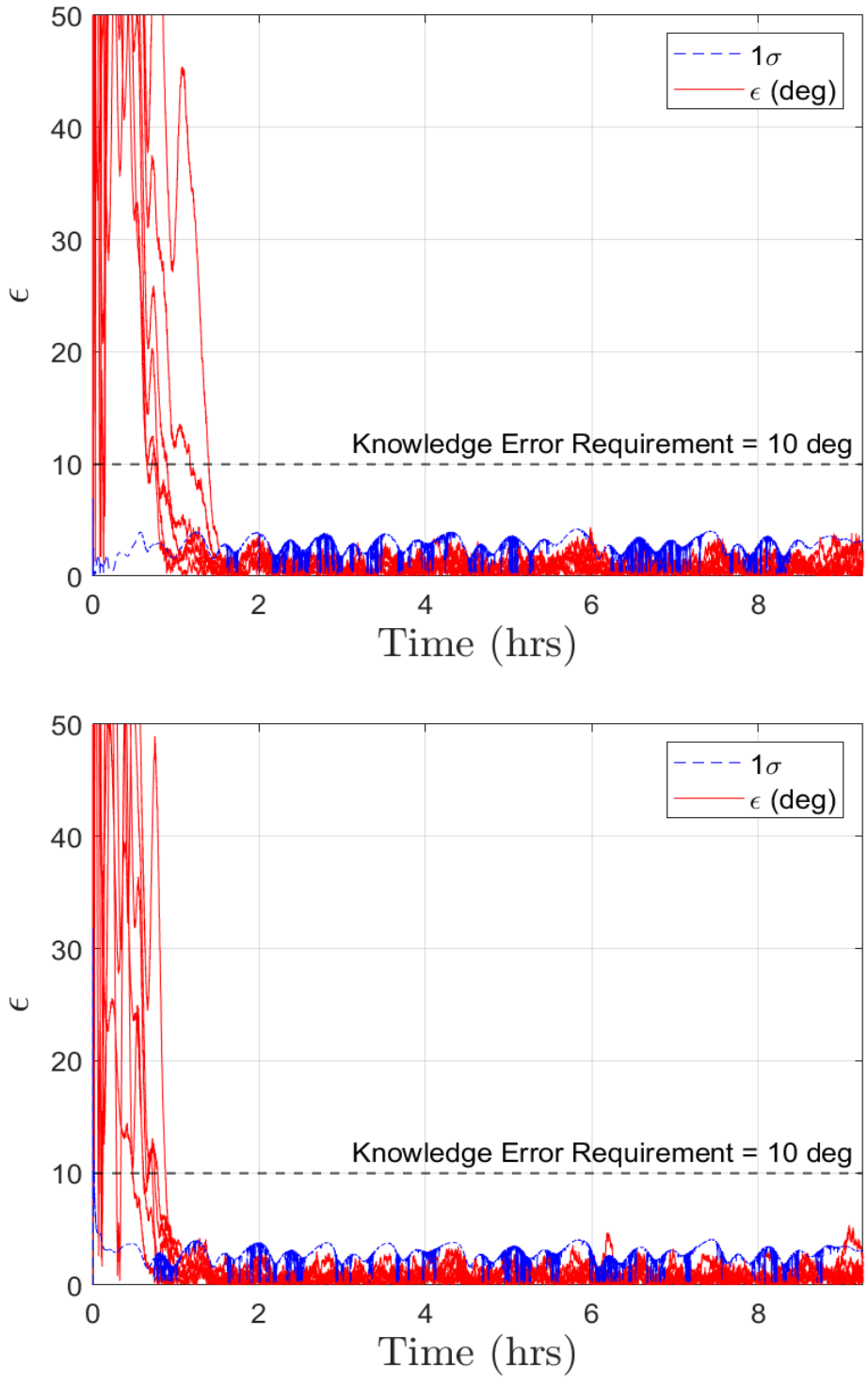

Figure 5.22 Pointing error ϵ history for mid inclination, spin $\bar{\omega}$ with no scale factor errors (top) and with scale factor errors (bottom).

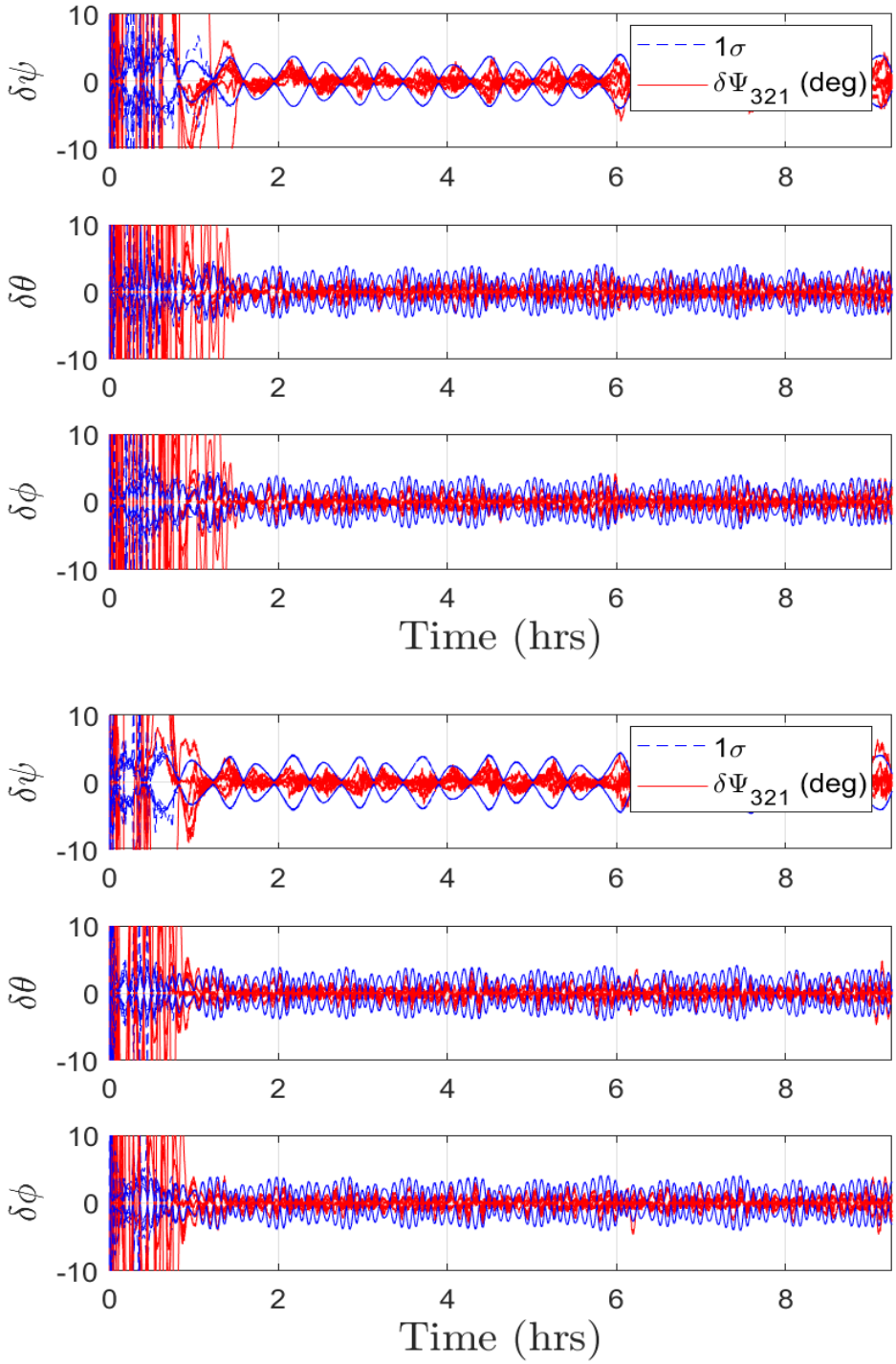

Figure 5.23 Euler angle error $\delta\Psi_{321}$ history for mid inclination, spin $\bar{\omega}$ with no scale factor errors (top) and with scale factor errors (bottom).

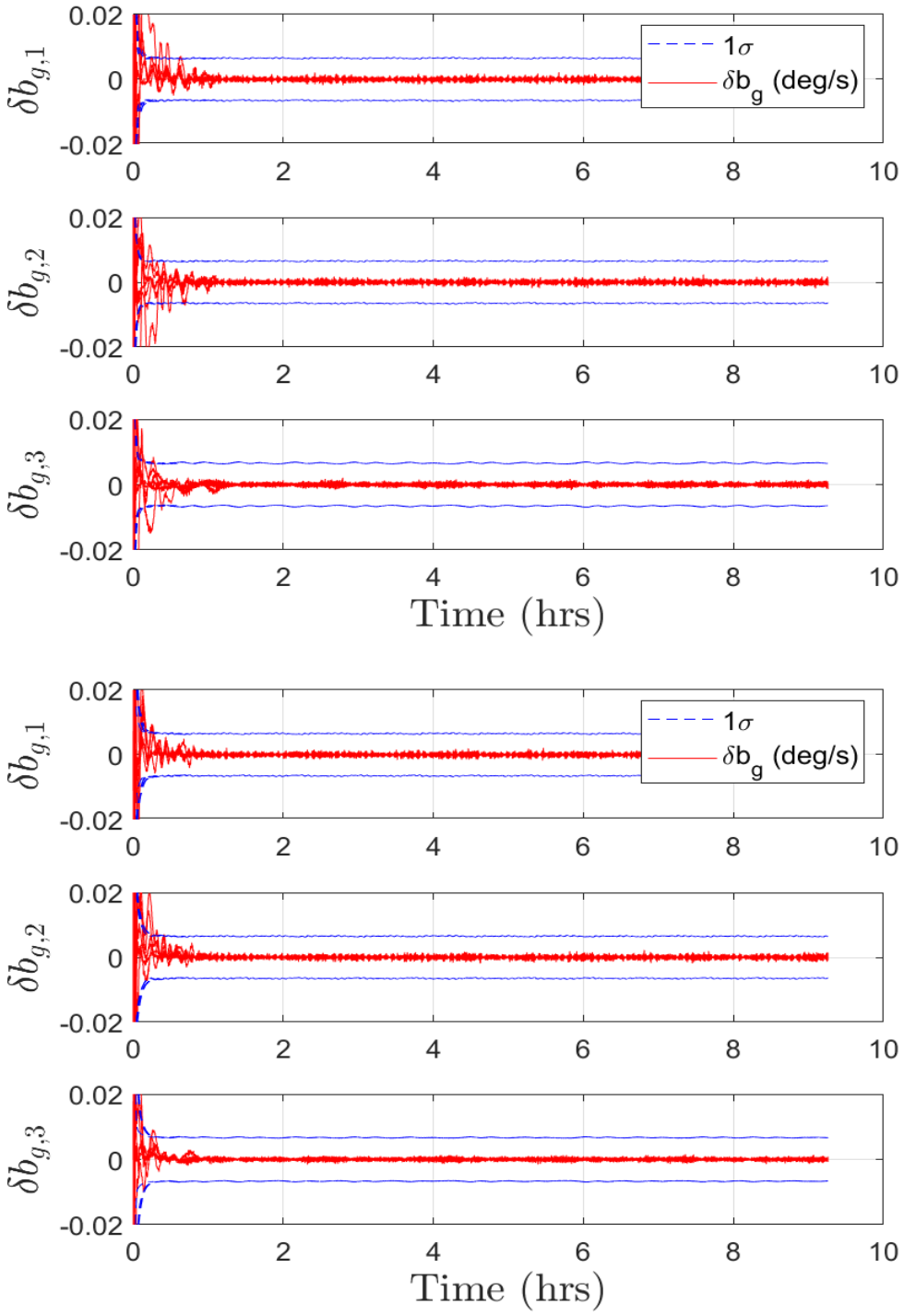

Figure 5.24 IMU bias error δb_g history for mid inclination, spin $\bar{\omega}$ with no scale factor errors (top) and with scale factor errors (bottom).

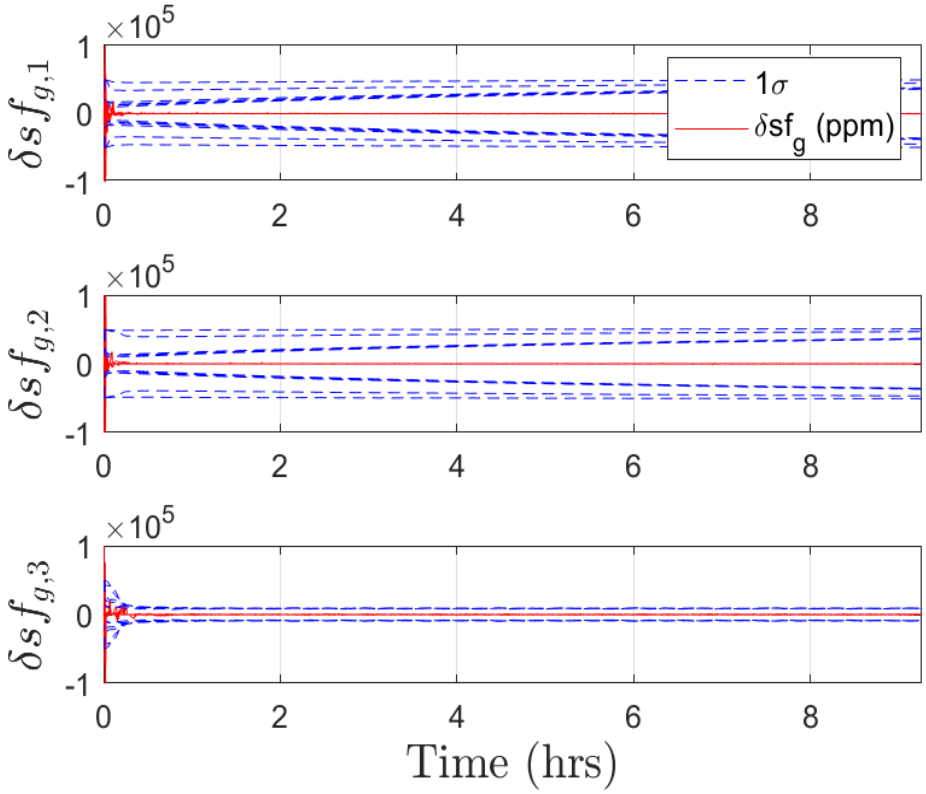

Figure 5.25 IMU scale factor error δsf_g for mid inclination, spin $\bar{\omega}$ for cases where scale factors are included.

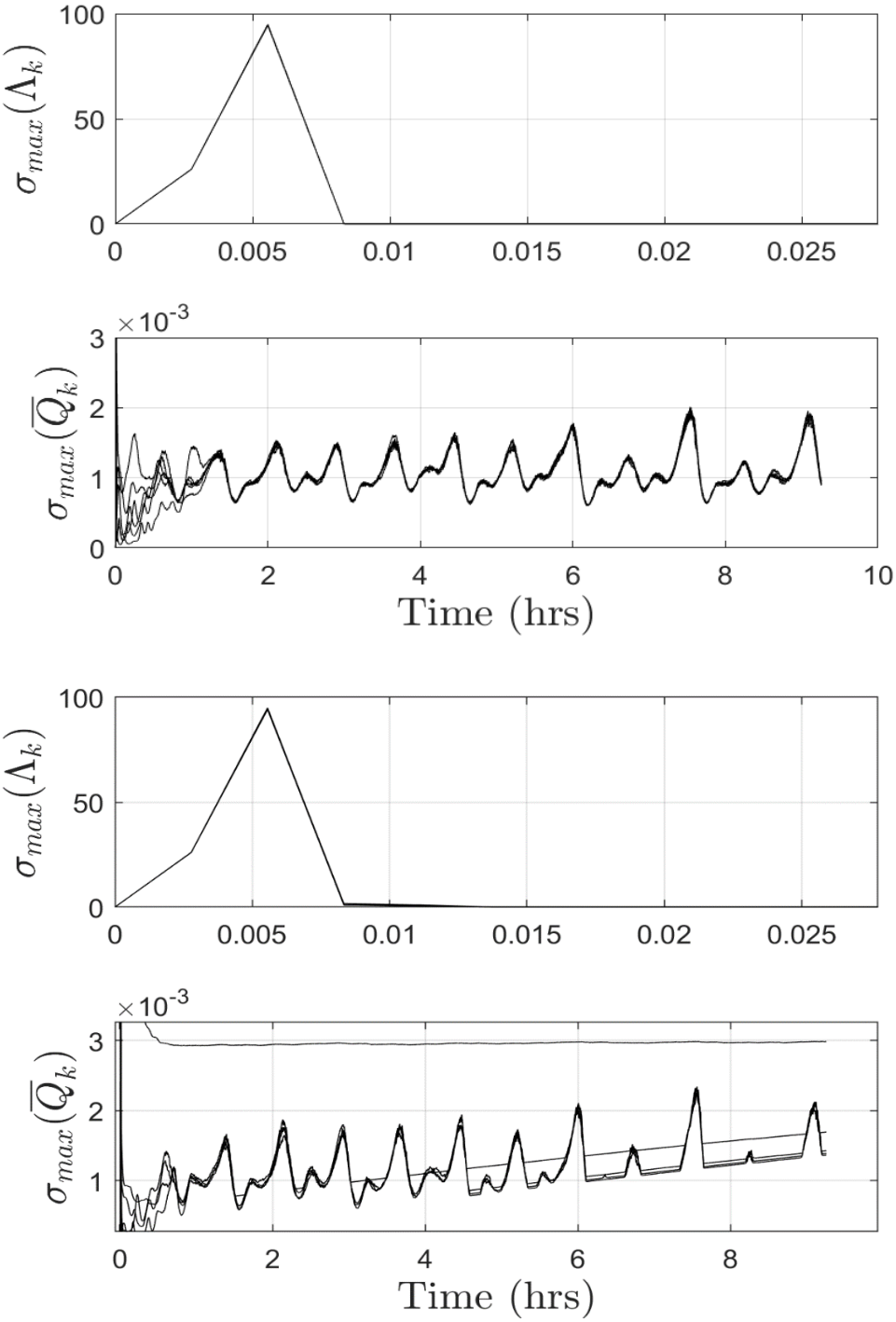

Figure 5.26 Stochastic observability metrics for mid inclination, spin $\overline{\omega}$ with no scale factor errors (top) and with scale factor errors (bottom).

In Figure 5.22 the angular error ϵ is given for a spin stabilized $\bar{\omega}^{SE}$ scenario at an orbital inclination of $i = 50°$. In both cases of scale factor inclusion, the ϵ estimate converges to below a 1σ of $5°$ within one and half to two hours. A similar phenomenon is shown in the Euler angle plots of Figure 5.23. In this figure, it is clearly seen that the covariance on the $\delta\psi$ estimates have less oscillation frequency than those of $\delta\phi$ and $\delta\theta$. Attitude estimates in both Figure 5.22 and Figure 5.23 are of similar scale as opposed to the high inclination spin case seen in Figure 5.7 and Figure 5.8.

In Figure 5.24, the bias state estimation errors are presented. Similar to the high $\bar{\omega}^{SE}$ case, the 1σ bound on the bias errors are approximately $0.006°/s$, with estimates converging to below that bound in less than a half hour of initialization. In each case of scale factor inclusion, the bias estimates maintain relatively similar convergence trend, converging to relatively steady values in about one and a half hours.

In the instance of the scale factor estimation errors seen in Figure 5.25, we see each axis estimate converging to a steady state value within half an hour. However, in the S^1 and S^2 axes, the covariance appears to be noticeably different for each run. Moreover, some covariance bounds appear to be growing throughout time in these axes. This is due to the lack of angular velocity in the S^1 and S^2 axes, causing the respective scale factors to be unobservable. The S^3 axis of the scale factor estimates has a lower covariance bound that appears to be constant. In the S^1 and S^2 axis, the upper bounds on the covariance appear to be nearing $45000\,ppm$, whereas the covariance on the S^3 is bounded near $8500\,ppm$.

The results of a stochastic observability test of the system are presented in Figure 5.26. Similar to the high $\bar{\omega}^{SE}$ case, the values of $\sigma_{max}(\Lambda_k)$ for both scale factor cases peak at the 2nd measurement update, and then begin to reduce to 0 in the following measurements, with slightly different rates, implying that the state covariance is no longer a function of the initial state covariance, P_0.

The value of $\sigma_{max}(\bar{Q}_k)$ can be seen in the lower sub-plots of Figure 5.26. When no scale factors are included, the value of $\sigma_{max}(\bar{Q}_k)$ converges to an oscillatory behavior in about one and a half hours. Noticeable peaks and troughs in the value of $\sigma_{max}(\bar{Q}_k)$ are present throughout the simulation time frame. While the peaks seem to be increasing after five hours, the troughs stay at a relatively consistent level. Additionally, the peaks begin to reduce again after 8 hours. This trend is assumed to be due to the varying EMF vector throughout the orbit, and not due to unbounded growth in covariance. As such, the no scale factor case is considered stochastically observable.

In the instance where scale factors are included, the plot of $\sigma_{max}(\bar{Q}_k)$ has significant differences from the no scale factor case. Firstly, the general value of $\sigma_{max}(\bar{Q}_k)$ is larger than that of the prior case, indicated higher amounts of noise in the system. Secondly, trends are less uniform, with a single trend line that remains flat at the top of the $\sigma_{max}(\bar{Q}_k)$ plot. After one and a half hours, some troughs of the plot begin to disappear and are replaced by a growing trend line. This can be attributed to the growing covariance on the scale factor estimates in the S^1 and S^2 axes. As the peaks of the plot appear to follow the same pattern as the no scale factor instance, we treat this linear growth as failure to the stochastic observability test, indicating this simulation scenario is stochastically unobservable.

5.3.6 Mid Inclination-orbit, Low Angular Velocity

Table 5.8 Simulation 6 Parameters

Parameter	Value	Description
$\bar{\omega}_0^{SE}$	$[0 \quad 0 \quad 0.057]^T \, °/s$	Initial Angular Velocity
i	$50°$	Orbital Inclination
Ψ_{321}	$[0° \quad 80° \quad 0°]^T$	Initial 3-2-1 Euler Angles
$q_{SE,0}$	$[0.667 \quad 0 \quad -0.745 \quad 0]^T$	True Initial Attitude Quaternion
$\bar{b}_0$	$-0.4°/s \leq b_0 \leq 0.4°/s$	Constant Bias Error
$\overline{sf}$	$-50000 \, ppm \leq \overline{sf} \leq 50000 \, ppm$	Scale Factor Errors

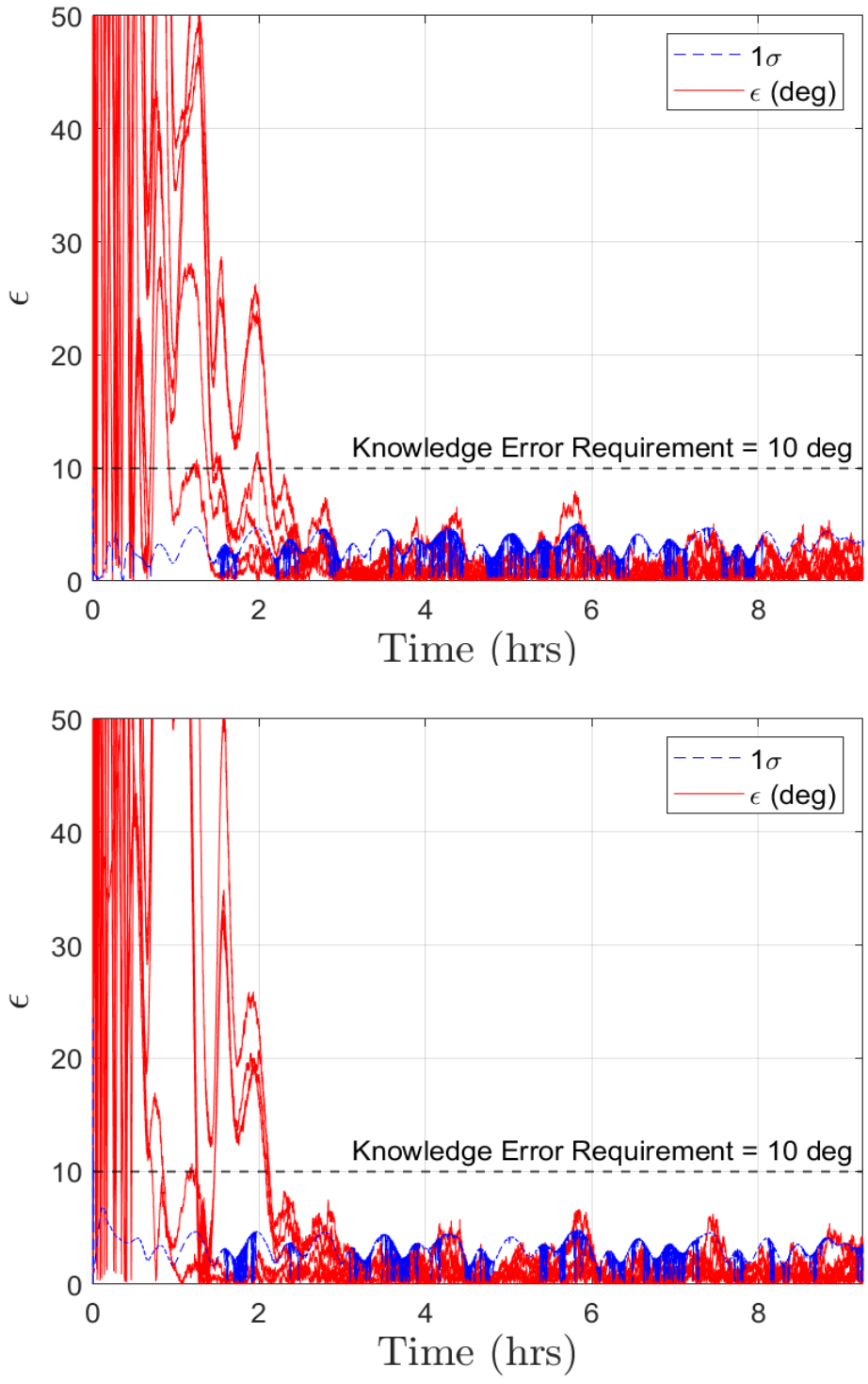

Figure 5.27 Pointing error ϵ history for mid inclination, low $\bar{\omega}$ with no scale factor errors (top) and with scale factor errors (bottom).

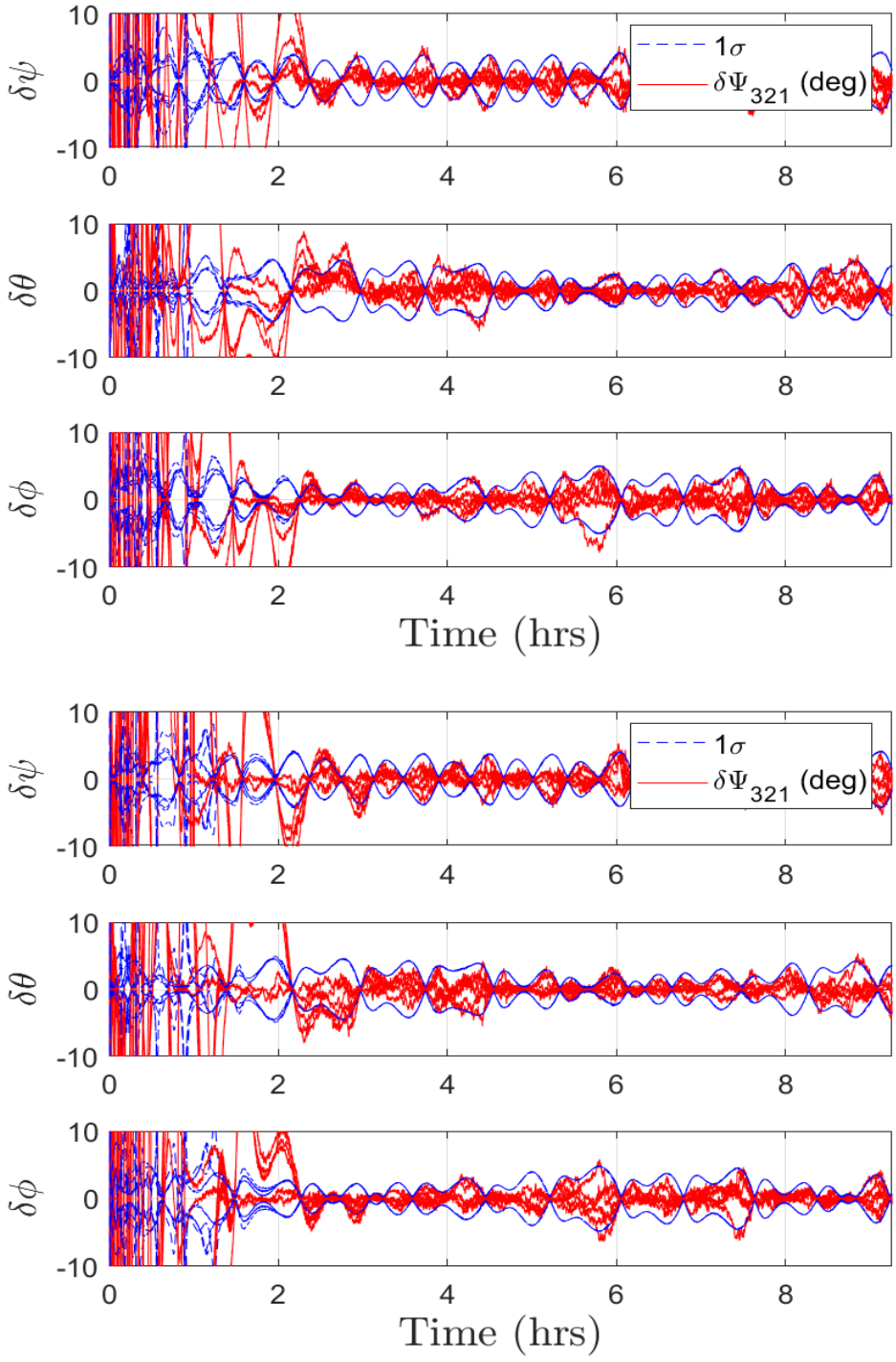

Figure 5.28 Euler angle error $\delta\Psi_{321}$ history for mid inclination, low $\bar{\omega}$ with no scale factor errors (top) and with scale factor errors (bottom).

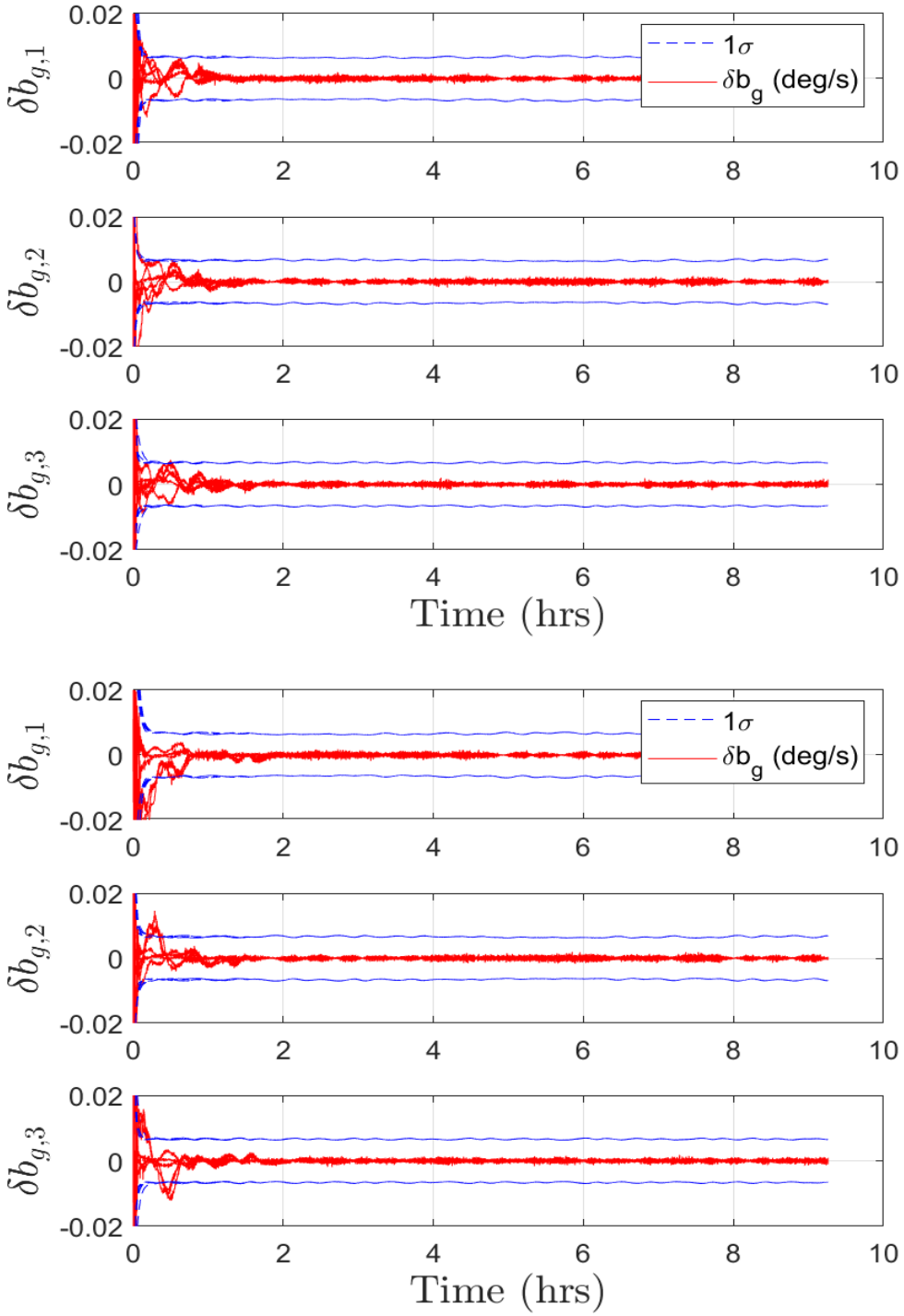

Figure 5.29 IMU bias error δb_g history for mid inclination, low $\bar{\omega}$, with no scale factor errors (top) and with scale factor errors (bottom).

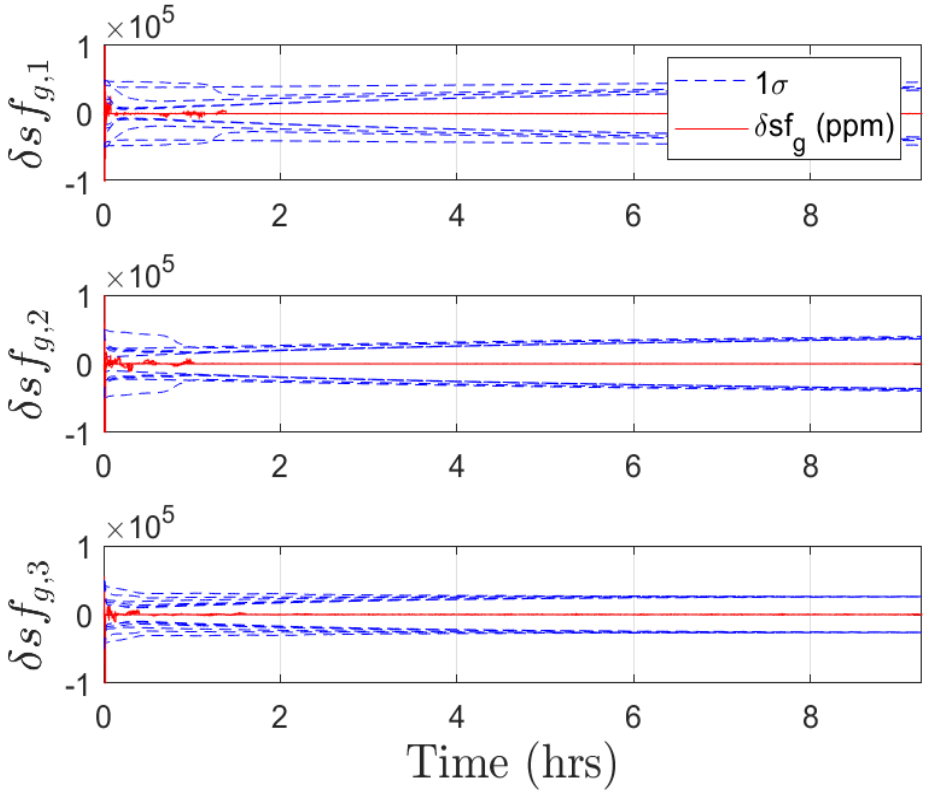

Figure 5.30 IMU scale factor error δsf_g for mid inclination, low $\bar{\omega}$ for cases where scale factors are included.

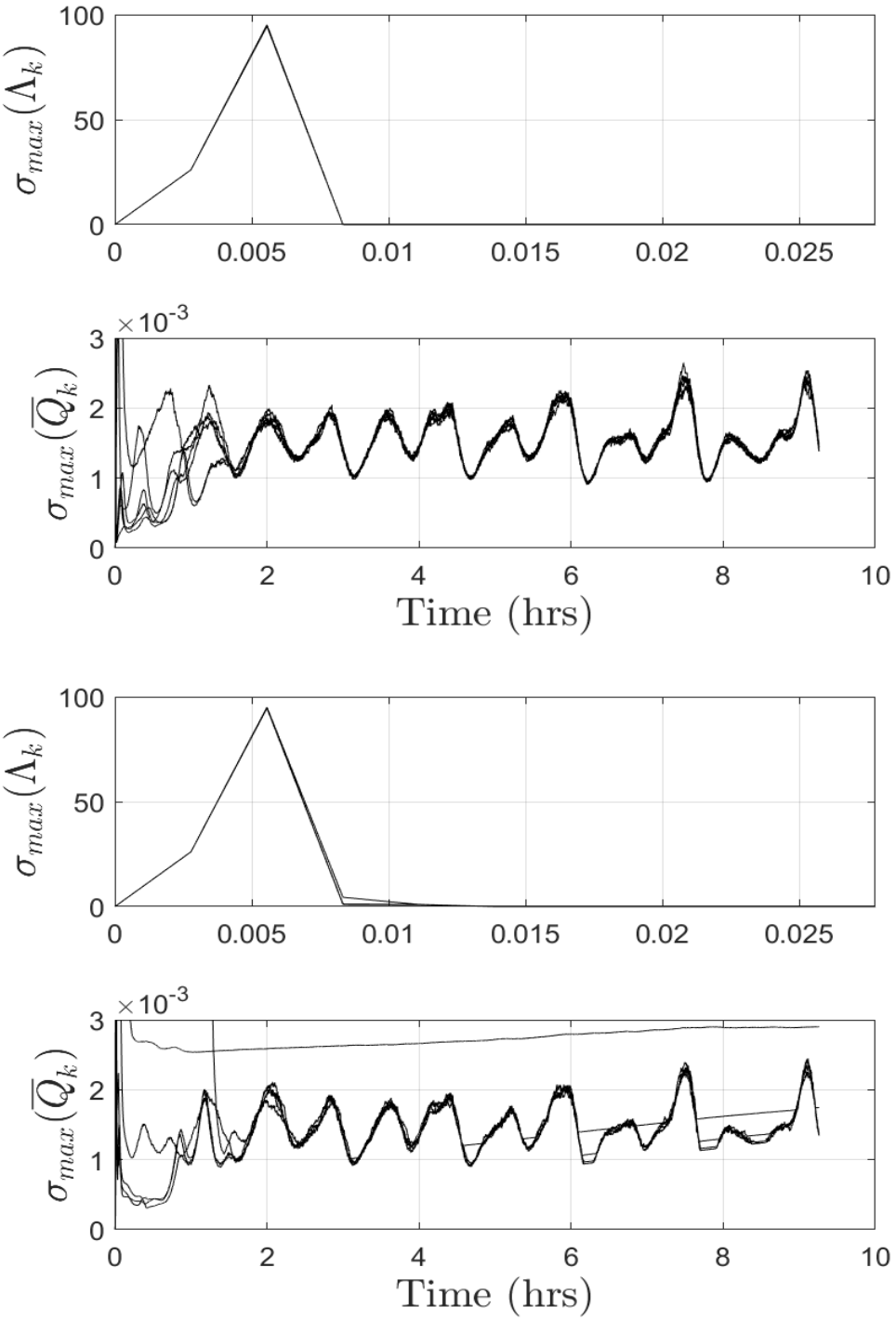

Figure 5.31 Stochastic observability metrics for mid inclination, low $\overline{\omega}$ with no scale factor errors (top) and with scale factor errors (bottom).

Figure 5.27 showcases the VMA convergence for the low $\bar{\omega}^{SE}$ case. When no scale factor errors are present within the noise of the system, all runs converge to be below or close to below a 1σ bound of $6°$ in a little over two hours. This is slightly better than the scenario presented by the high inclination case of Figure 5.12. When scale factor estimates are included, all runs converge to below or close to below a 1σ bound of $6°$ within two and half hours of initialization. A similar phenomenon is shown in the Euler angle plots of Figure 5.28. General estimates on the attitude parameters of ϵ and Euler angles are less steady in this low $\bar{\omega}^{SE}$ case as opposed to the higher $\bar{\omega}^{SE}$ cases.

The bias estimation errors are shown in Figure 5.29. Similar to both the high and spin stabilized $\bar{\omega}^{SE}$ cases, the 1σ bound on the bias errors are approximately $0.007°/s$, with estimates converging to below that bound in less than a half hour of initialization. A noticeable difference is that the bias covariance in Figure 5.29 appears slightly oscillatory when compared to Figure 5.19 and Figure 5.24. In both cases, the bias estimates seem to converge to a steady estimate after about two hours.

In the instance of the scale factor estimation errors of Figure 5.30, we see each axis estimate converging below the 1σ bounds almost immediately. Covariance estimates on the S^1 and S^2 axes are climbing throughout the simulation time, while the covariance estimate in the S^3 axis converges to a steady bound of 20000 ppm. This is a noticeable increase when compared to the covariance in the S^3 axis as seen by Figure 5.25.

The results of a stochastic observability test are given in Figure 5.31. Similar to both the high and spin stabilized $\bar{\omega}^{SE}$ cases, the value of $\sigma_{max}(\Lambda_k)$ peaks at 20

seconds, and then begins to limit to zero afterwards. The value of $\sigma_{max}(\bar{Q}_k)$ appears to have a lower frequency of oscillation than the higher $\bar{\omega}^{SE}$ cases. In the case where scale factor errors are included, the values of $\sigma_{max}(\bar{Q}_k)$ begin to have a linear slope near the troughs of the trend after 4 hours, similar to the cases of scale factor inclusion for the spin stabilized $\bar{\omega}^{SE}$ case. Due to this trend, we treat this simulation scenario as stochastically unobservable.

5.3.7 Low Inclination-orbit, "Tumble" Angular Velocity

Table 5.9 Simulation 7 Parameters

Parameter	Value	Description
$\bar{\omega}_0^{SE}$	$[1.15 \quad -2.86 \quad 1.71]^T \, °/s$	Initial Angular Velocity
i	$2°$	Orbital Inclination
Ψ_{321}	$[0° \quad 80° \quad 0°]^T$	Initial 3-2-1 Euler Angles
$q_{SE,0}$	$[0.667 \quad 0 \quad -0.745 \quad 0]^T$	True Initial Attitude Quaternion
$\bar{b}_0$	$-0.4°/s \leq b_0 \leq 0.4°/s$	Constant Bias Error
$\overline{sf}$	$-50000\, ppm \leq \overline{sf} \leq 50000\, ppm$	Scale Factor Errors

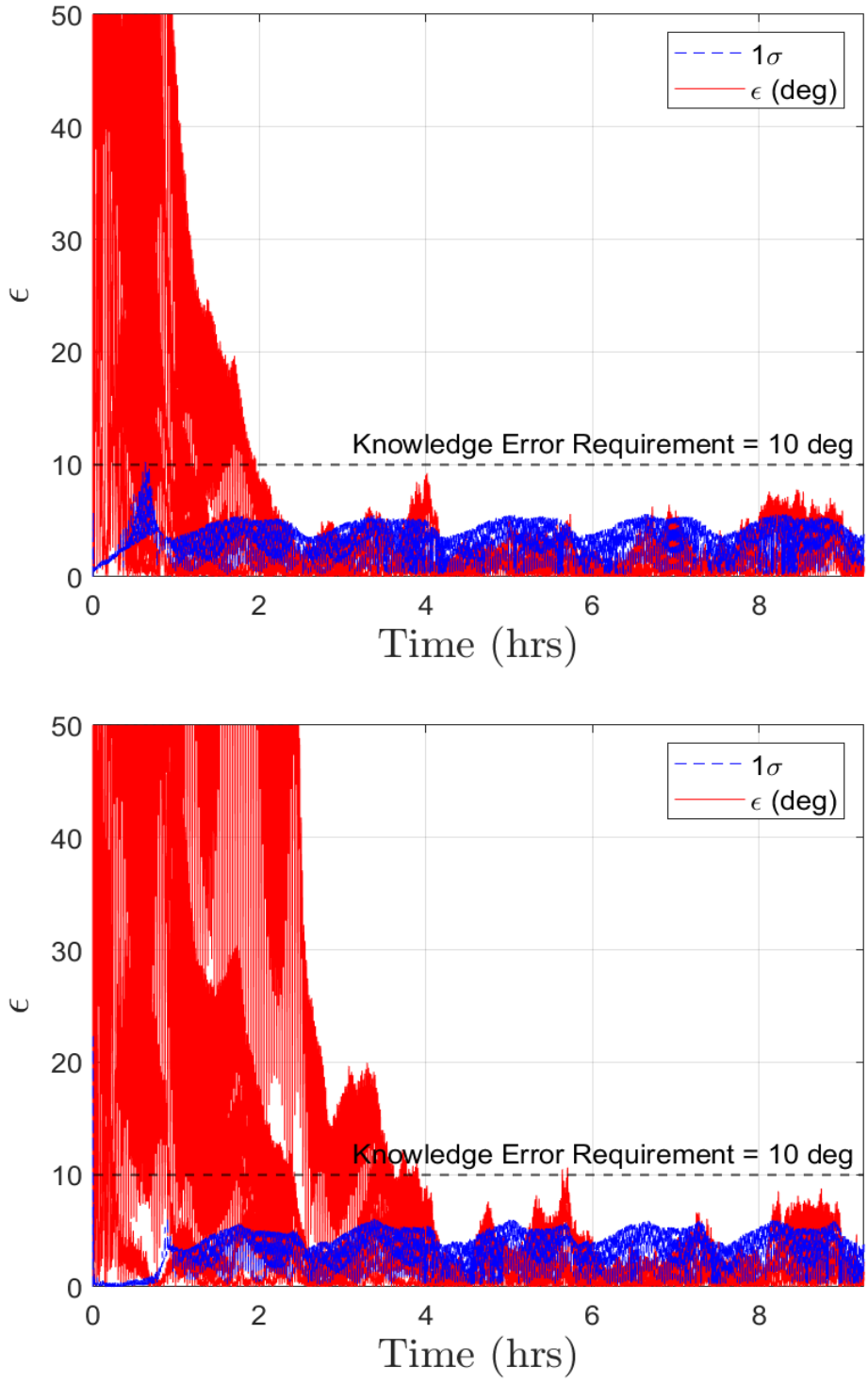

Figure 5.32 Pointing error ϵ history for low inclination, High $\bar{\omega}$ with no scale factor errors (top) and with scale factor errors (bottom).

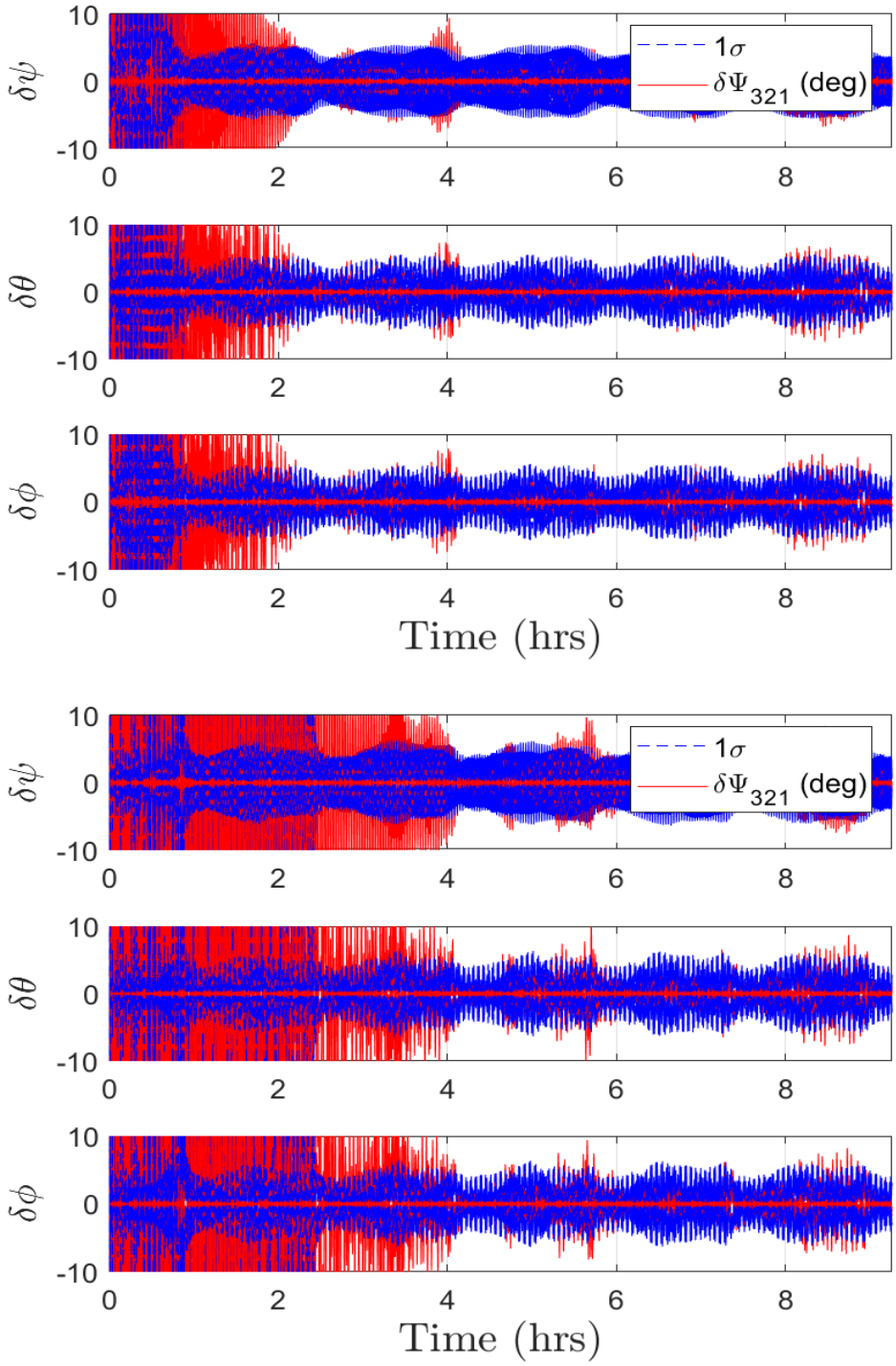

Figure 5.33 Euler angle error $\delta\Psi_{321}$ history for low inclination, high $\bar{\omega}$ with no scale factor errors (top) and with scale factor errors (bottom).

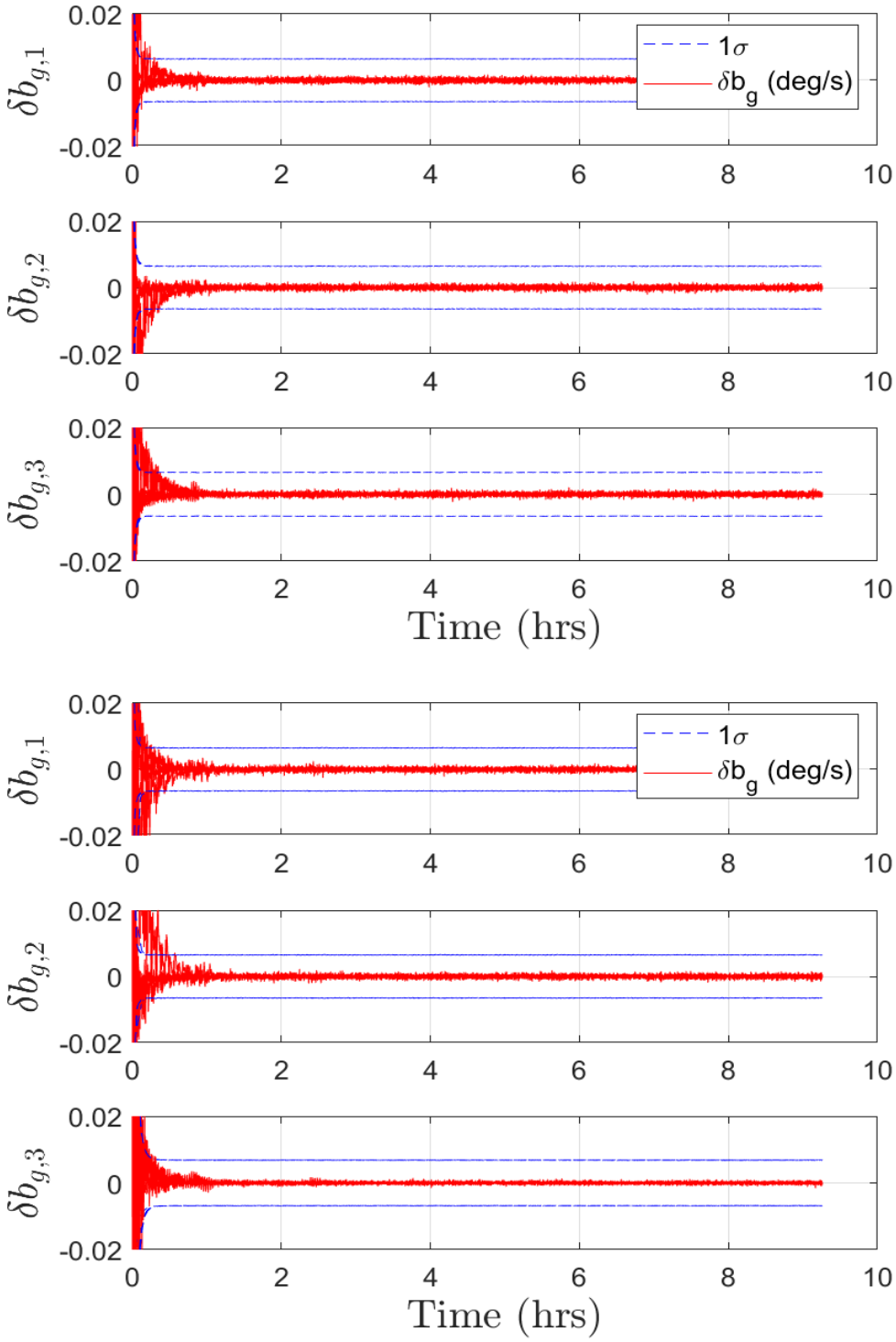

Figure 5.34 IMU bias error δb_g history for low inclination, high $\bar{\omega}$ with no scale factor errors (top) and with scale factor errors (bottom).

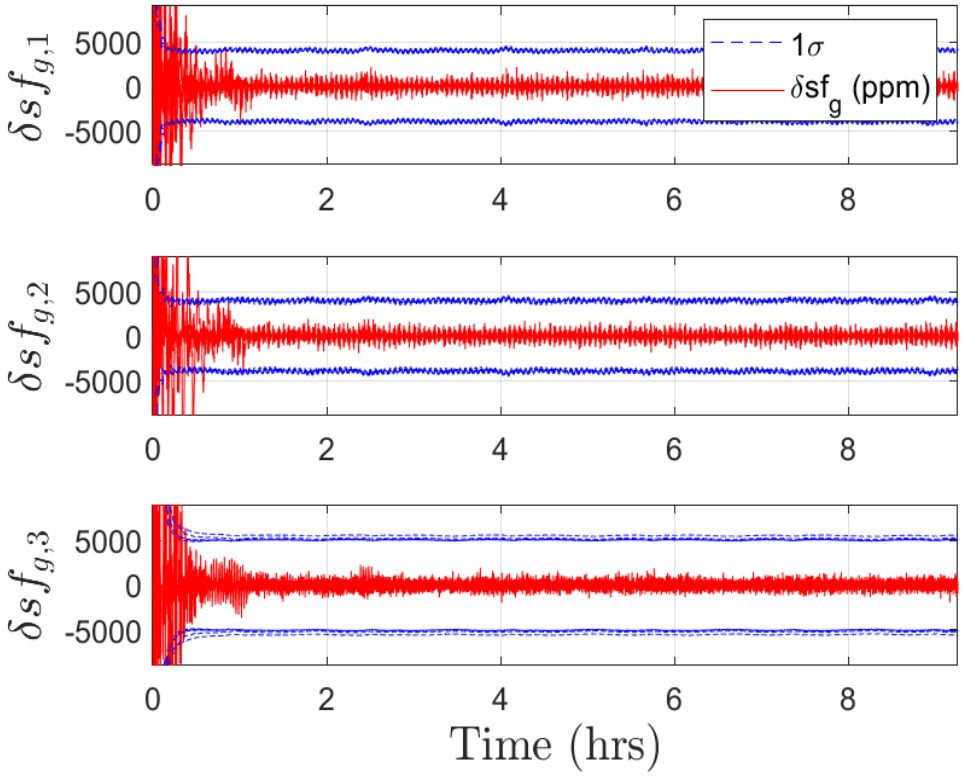

Figure 5.35 IMU scale factor error δsf_g for low inclination, high $\bar{\omega}$ for cases where scale factors are included.

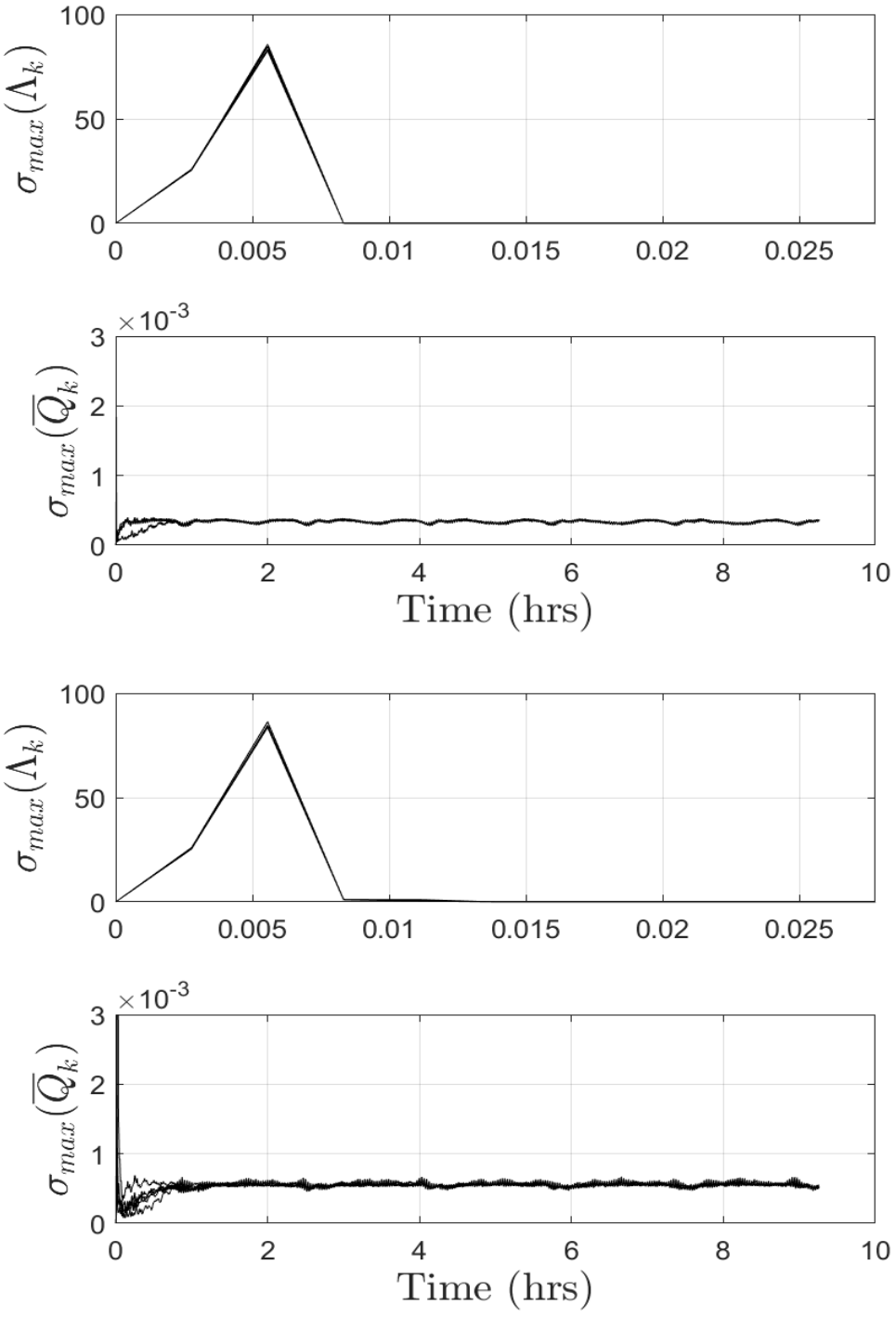

Figure 5.36 Stochastic observability metrics for low inclination, high $\overline{\omega}$ with no scale factor errors (top) and with scale factor errors (bottom).

In Figure 5.32 the angular error ϵ between S^3 and $\hat{S}^3$ axes as defined by Equation (5.2) is given for a high $\bar{\omega}^{SE}$ scenario at an orbital inclination of $i = 2°$. The top plot showcases ϵ when no scale factor errors are included within the noise of the system, with the bottom plot being for scenarios in which scale factor errors are included and estimated. With no scale factors, the ϵ estimate converges to below or near a 1σ of $6°$ in a little over two hours. When scale factors are included and estimated, the ϵ estimate converges to below a 1σ of $6° - 7°$ in a little over four hours. Contrary to the covariance of the previous simulation scenarios, the covariance seen in Figure 5.32 has less difference between its peak and trough amplitudes. Moreover, the state estimates seem to exceed the covariance bounds more frequently than the higher inclination scenarios. A similar phenomenon is seen in the Euler angle plots of Figure 5.33.

In Figure 5.34, the bias state estimation errors are presented. The 1σ bound on the bias errors are approximately $0.007°/s$, with estimates converging to below that bound within half an hour of initialization. In both instances of scale factor inclusion, it appears that steady state estimates are reached in approximately one hour after initialization. In the instance of the scale factor estimation errors seen in Figure 5.35, we see estimates converging to below a 1σ bound of $5000\ ppm$ within half an hour. Similar to the bias estimates, the scale factors reach steady state estimation values after about one hour.

The results of a stochastic observability test of the system are presented in Figure 5.36 with the two metrics of $\sigma_{max}(\Lambda_k)$ and $\sigma_{max}(\bar{Q}_k)$ for each scenario presented. In both instances of scale factor inclusion, the value of $\sigma_{max}(\Lambda_k)$ peaks at the 2nd measurement update at 20 seconds with a value of 86, and then begins to reduce to 0 in the following measurements, similar to the high inclination cases.

This implies that the state covariance is no longer a function of the initial state covariance, P_0, after 5 measurement updates.

The $\sigma_{max}(\bar{Q}_k)$ plots within Figure 5.36 showcase the second metric of the stochastic observability test. In both instances of scale factor inclusion, the value of $\sigma_{max}(\bar{Q}_k)$ seems to converge to an oscillatory trend near one hour. This mimics the oscillation seen in state covariance of the Euler angle estimates of Figure 5.33. When scale factor errors are included, the values of $\sigma_{max}(\bar{Q}_k)$ seem to a slightly larger amplitude in oscillation. Additionally, the steady state values appear to be larger when scale factors are included. However, as both instances of $\sigma_{max}(\bar{Q}_k)$ appear to be bounded, the values of $\sigma_{max}(\Lambda_k)$ and $\sigma_{max}(\bar{Q}_k)$ imply that the system is stochastically observable for both cases of scale factor inclusion.

5.3.8 Low Inclination-orbit, Spin Stabilized Angular Velocity

Table 5.10 Simulation 8 Parameters

Parameter	Value	Description
$\bar{\omega}_0^{SE}$	$[0 \quad 0 \quad 0.57]^T \, °/s$	Initial Angular Velocity
i	$2°$	Orbital Inclination
Ψ_{321}	$[0° \quad 80° \quad 0°]^T$	Initial 3-2-1 Euler Angles
$q_{SE,0}$	$[0.667 \quad 0 \quad -0.745 \quad 0]^T$	True Initial Attitude Quaternion
$\bar{b}_0$	$-0.4°/s \leq b_0 \leq 0.4°/s$	Constant Bias Error
$\overline{sf}$	$-50000 \, ppm \leq \overline{sf} \leq 50000 \, ppm$	Scale Factor Errors

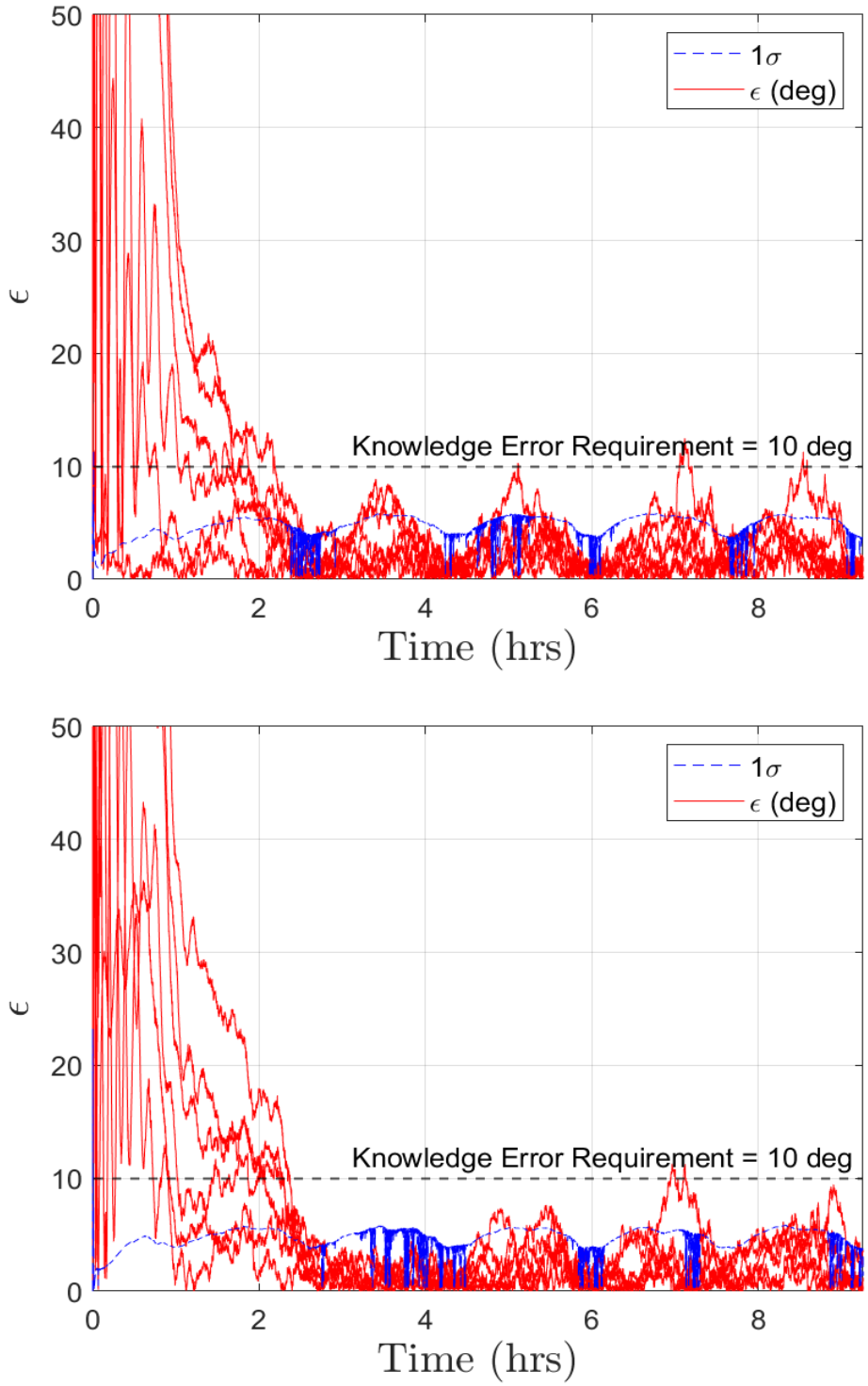

Figure 5.37 Pointing error ϵ history for low inclination, spin $\bar{\omega}$ with no scale factor errors (top) and with scale factor errors (bottom).

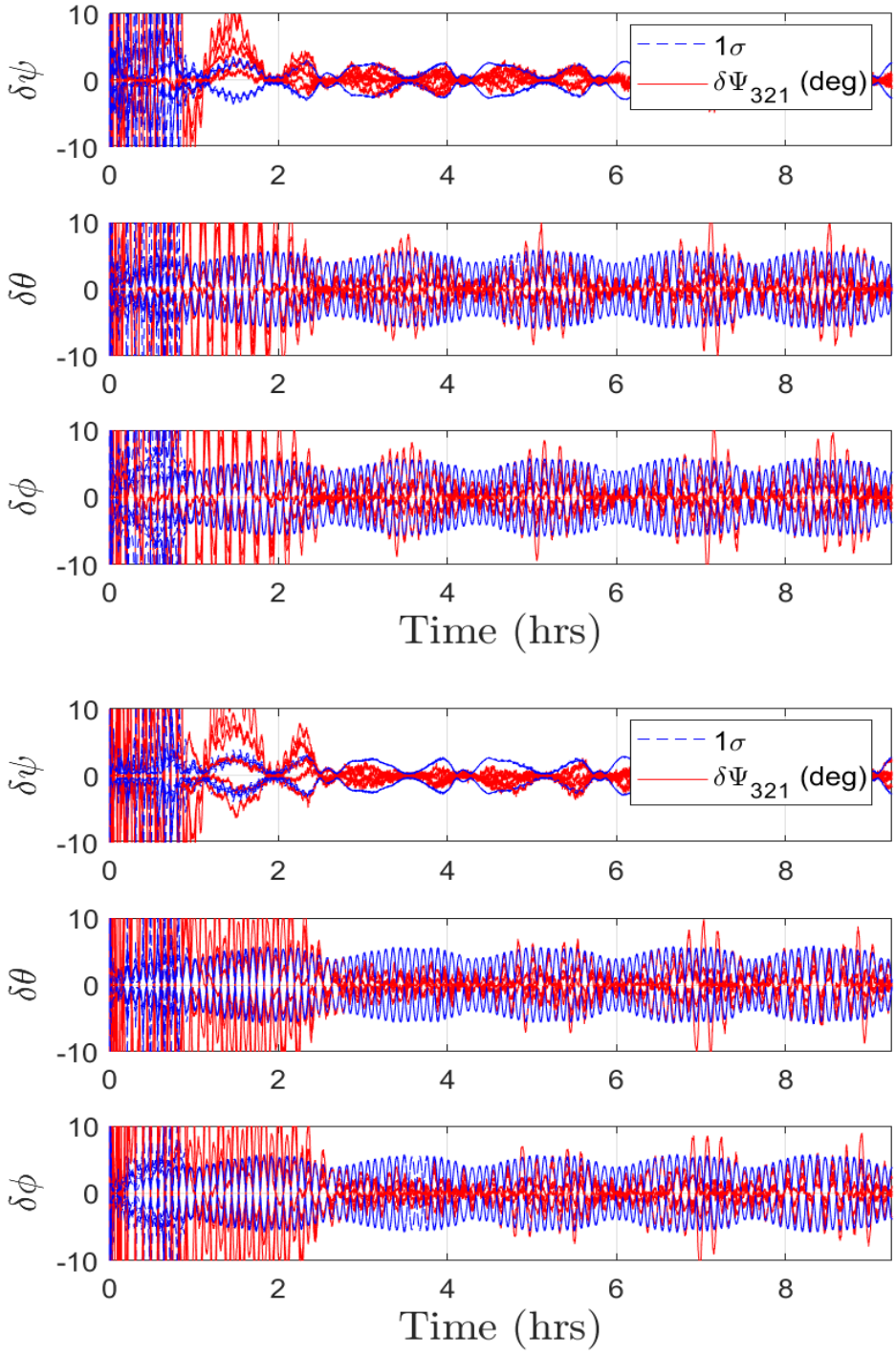

Figure 5.38 Euler angle error $\delta\Psi_{321}$ history for low inclination, spin $\bar{\omega}$ with no scale factor errors (top) and with scale factor errors (bottom).

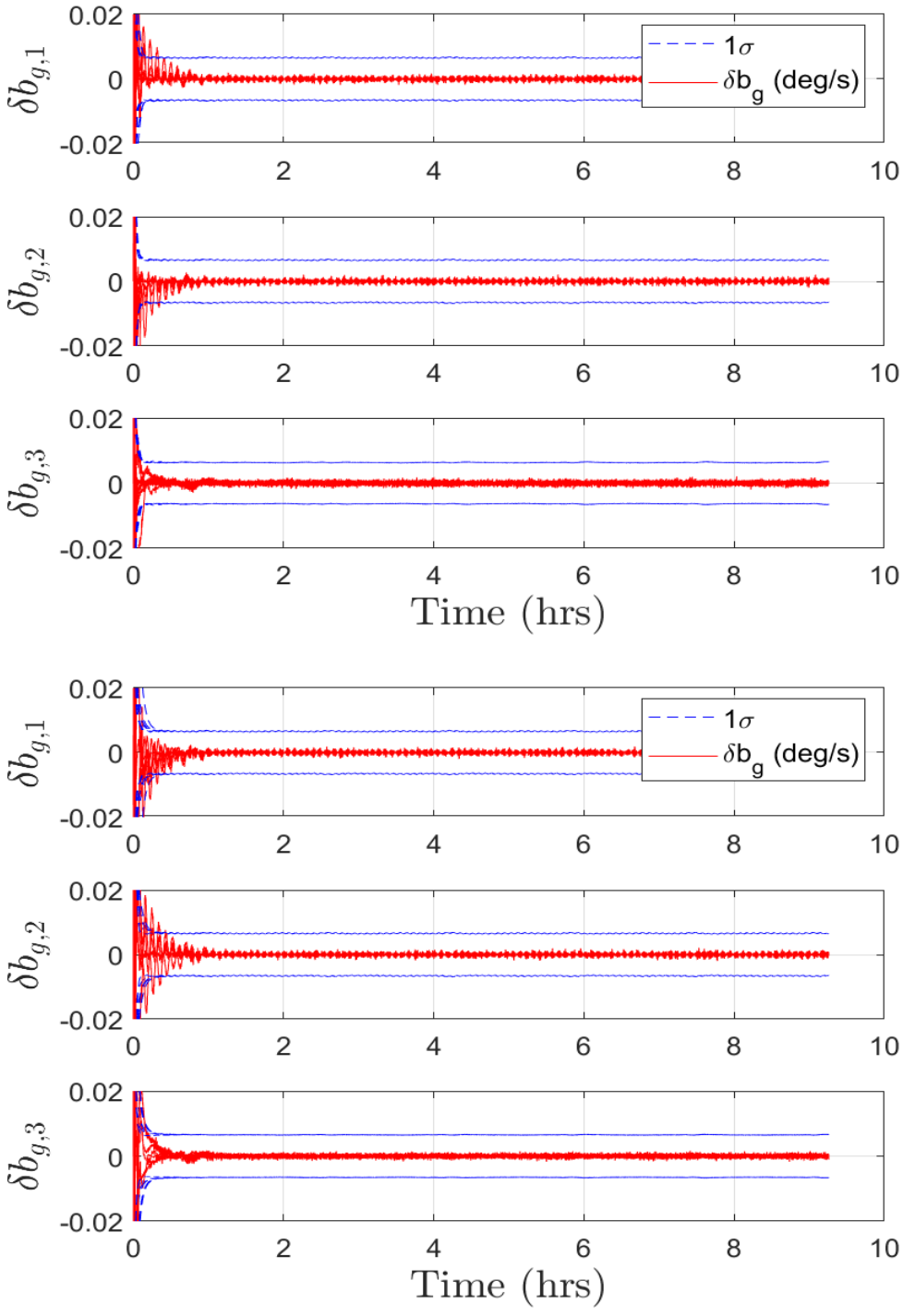

Figure 5.39 IMU bias error δb_g history for low inclination, spin $\bar{\omega}$ with no scale factor errors (top) and with scale factor errors (bottom).

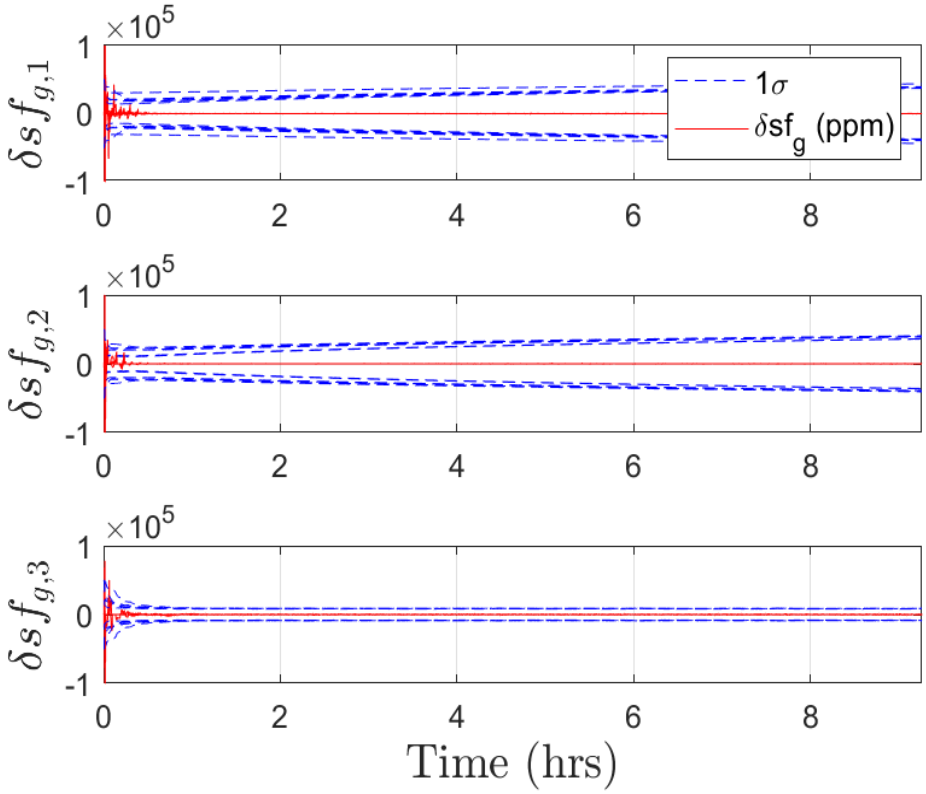

Figure 5.40 IMU scale factor error δsf_g for low inclination, spin $\bar{\omega}$ for cases where scale factors are included.

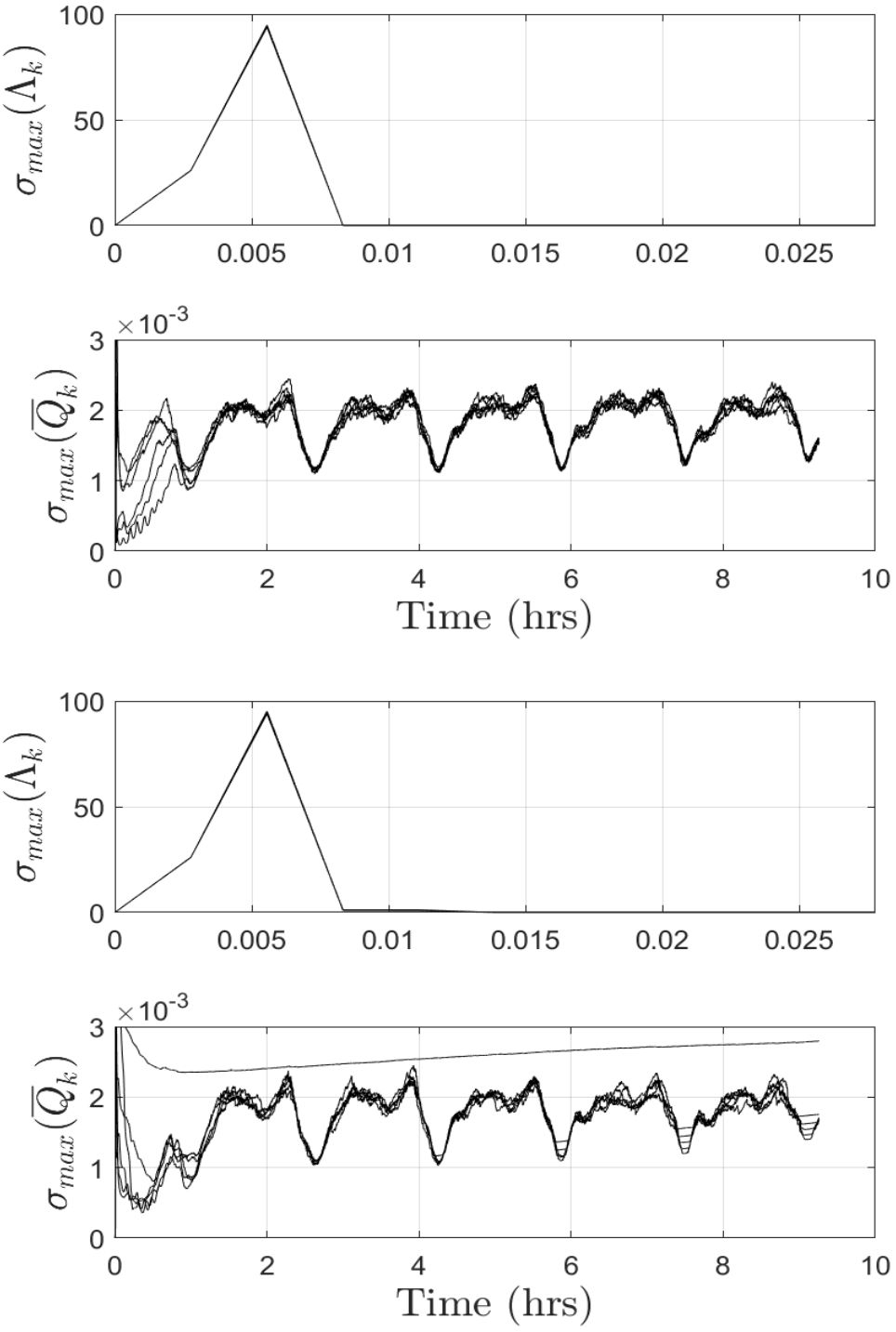

Figure 5.41 Stochastic observability metrics for low inclination, spin $\overline{\omega}$ with no scale factor errors (top) and with scale factor errors (bottom).

In Figure 5.37 the angular error ϵ is given for a spin stabilized $\bar{\omega}^{SE}$ scenario at an orbital inclination of $i = 2°$. In both cases of scale factor inclusion, the ϵ estimate converges to below or near a 1σ of $6°$ in a little over two hours. A similar phenomenon is shown in the Euler angle plots of Figure 5.38. In this figure, it is clearly seen that the covariance on the $\delta\psi$ estimates have less oscillation frequency than those of $\delta\phi$ and $\delta\theta$. In all cases of the attitude being estimated, at least one out of the six Monte Carlo runs has its steady state value exceed the covariance bound given by the blue lines, similar to the high $\bar{\omega}^{SE}$ case. This implies that the state estimates are less accurate at this orbital inclination.

In Figure 5.39, the bias state estimation errors are presented. Similar to the high $\bar{\omega}^{SE}$ case, the 1σ bound on the bias errors are approximately $0.006°/s$, with estimates converging to below that bound in less than a half hour of initialization. In each case of scale factor inclusion, the bias estimates maintain relatively similar convergence trend, converging to relatively steady values in about one hour.

In the instance of the scale factor estimation errors seen in Figure 5.40, we see each axis estimate converging to a steady state value within half an hour. However, in the S^1 and S^2 axes, the covariance appears to be noticeably different for each run. Moreover, some covariance bounds appear to be growing throughout time in these axes. This is due to the lack of angular velocity in the S^1 and S^2 axes, causing the respective scale factors to be unobservable. The S^3 axis of the scale factor estimates has a lower covariance bound that appears to be constant. In the S^1 and S^2 axis, the upper bounds on the covariance appear to be nearing $40000\,ppm$, whereas the covariance on the S^3 is bounded near $8500\,ppm$.

The results of a stochastic observability test of the system are presented in Figure 5.41. Similar to the high $\bar{\omega}^{SE}$ case, the values of $\sigma_{max}(\Lambda_k)$ for both scale factor cases peak at the 2nd measurement update, and then begin to reduce to 0 in the following measurements, with slightly different rates, implying that the state covariance is no longer a function of the initial state covariance, P_0.

The value of $\sigma_{max}(\bar{Q}_k)$ can be seen in the lower sub-plots of Figure 5.41. When no scale factors are included, the value of $\sigma_{max}(\bar{Q}_k)$ converges to an oscillatory behavior in about one hours. Noticeable peaks and troughs in the value of $\sigma_{max}(\bar{Q}_k)$ are present throughout the simulation time frame, implying stochastic observability. Contrary to the higher inclination spin cases, peaks do not seem to be increasing throughout the simulation run, with peaks and troughs staying at a relatively consistent level. Additionally, there seems to be larger difference between the steady state values of $\sigma_{max}(\bar{Q}_k)$ when compared to the higher inclination cases.

In the instance where scale factors are included, the plot of $\sigma_{max}(\bar{Q}_k)$ has slight differences from the no scale factor case. The general value of $\sigma_{max}(\bar{Q}_k)$ seem to be of similar size to the no scale factor case. Moreover, individual trends seem similarly sporadic, with the lone exception of a single trend line that remains flat at the top of the $\sigma_{max}(\bar{Q}_k)$ plot. After four hours, some troughs of the plot begin to disappear and are replaced by a growing trend line. This can be attributed to the growing covariance on the scale factor estimates in the S^1 and S^2 axes. As the peaks of the plot appear to follow the same pattern as the no scale factor instance, we treat this linear growth as failure to the stochastic observability test, indicating this simulation scenario is stochastically unobservable.

5.3.9 Low Inclination-orbit, Low Angular Velocity

Table 5.11 Simulation 9 Parameters

Parameter	Value	Description
$\bar{\omega}_0^{SE}$	$[0 \quad 0 \quad 0.057]^T \, °/s$	Initial Angular Velocity
i	$2°$	Orbital Inclination
Ψ_{321}	$[0° \quad 80° \quad 0°]^T$	Initial 3-2-1 Euler Angles
$q_{SE,0}$	$[0.667 \quad 0 \quad -0.745 \quad 0]^T$	True Initial Attitude Quaternion
$\bar{b}_0$	$-0.4°/s \leq b_0 \leq 0.4°/s$	Constant Bias Error
$\overline{sf}$	$-50000 \, ppm \leq \overline{sf} \leq 50000 \, ppm$	Scale Factor Errors

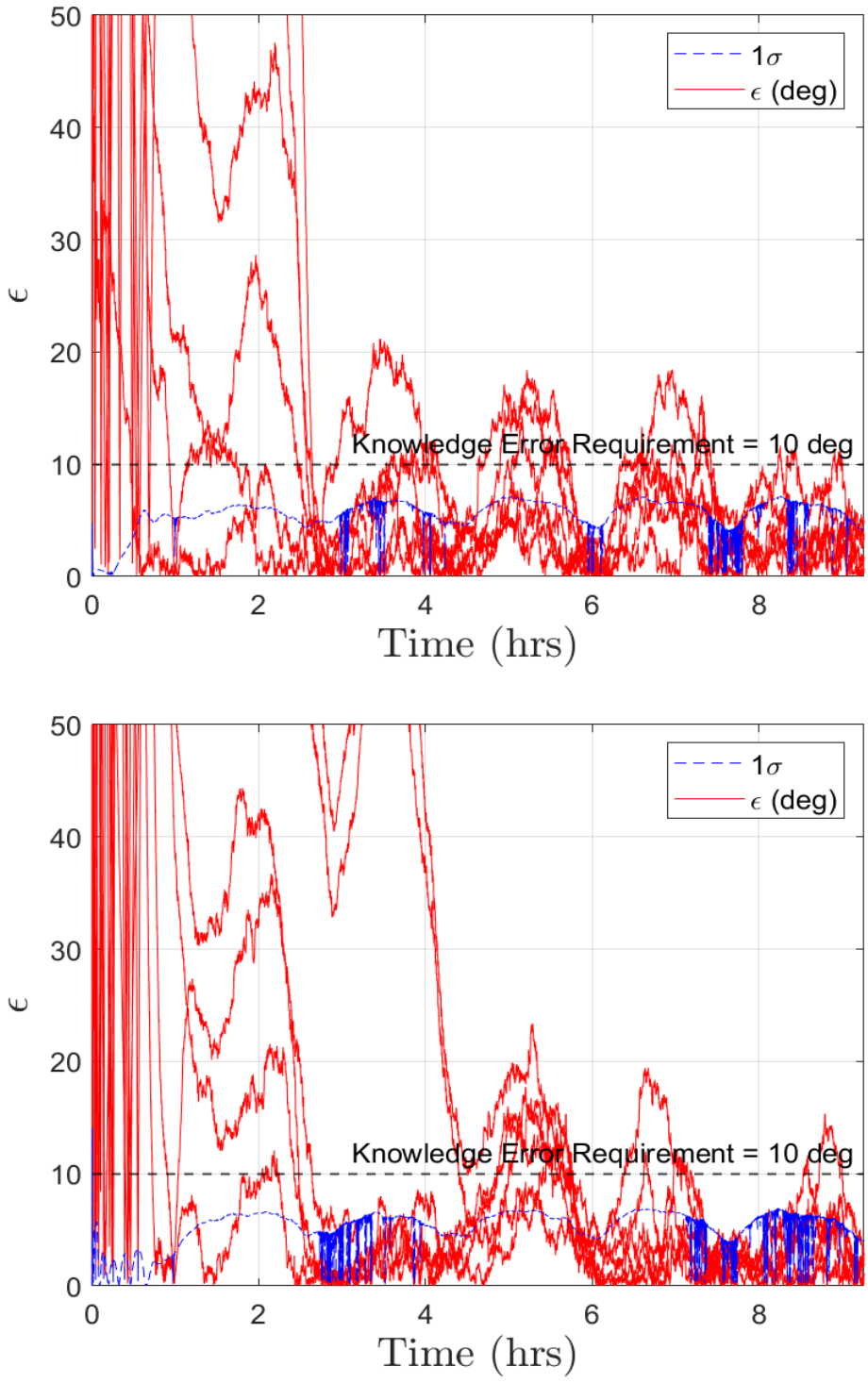

Figure 5.42 Pointing error ϵ history for low inclination, low $\overline{\omega}$ with no scale factor errors (top) and with scale factor errors (bottom).

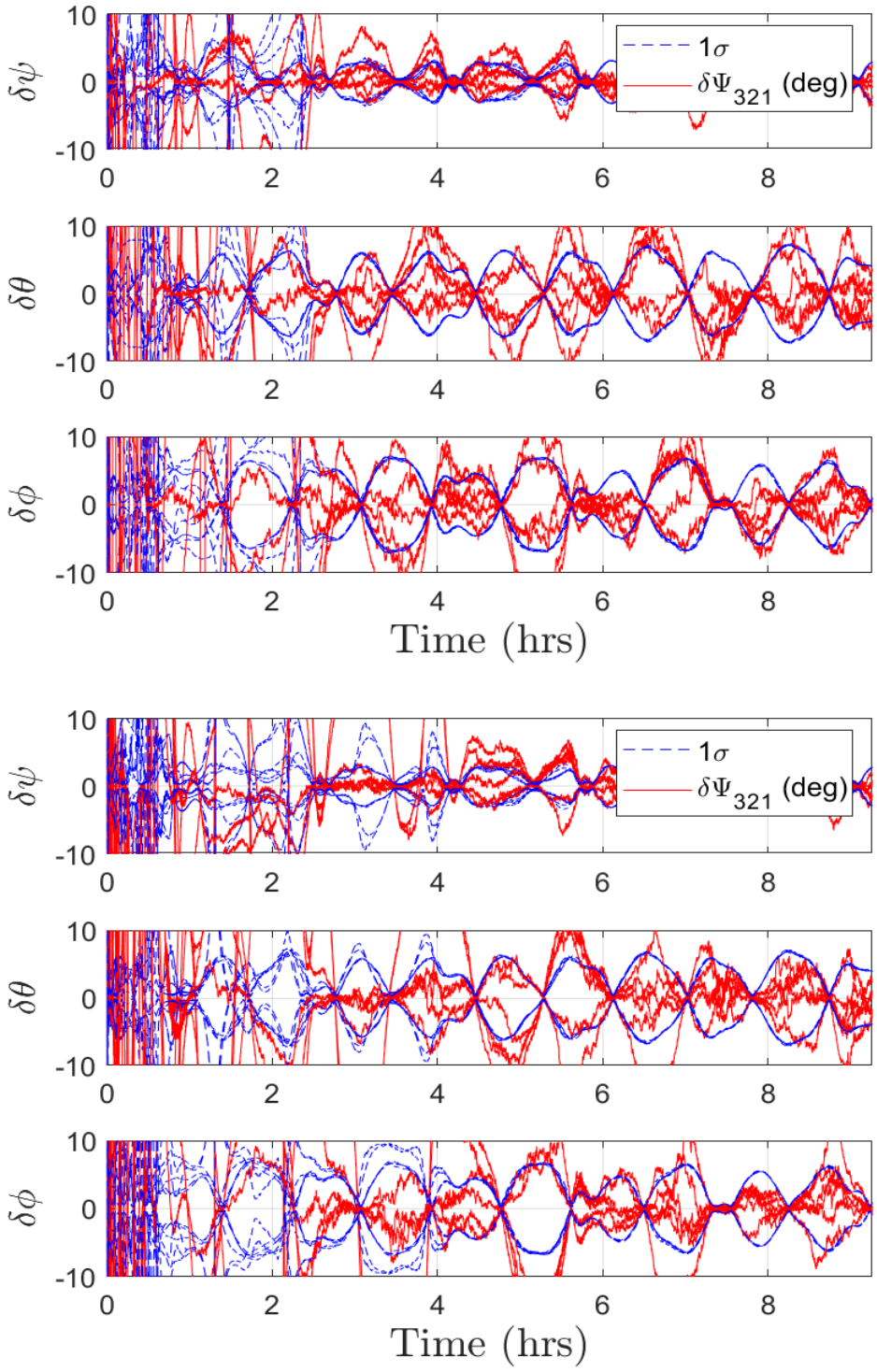

Figure 5.43 Euler angle error $\delta\Psi_{321}$ history for low inclination, low $\bar{\omega}$ with no scale factor errors (top) and with scale factor errors (bottom).

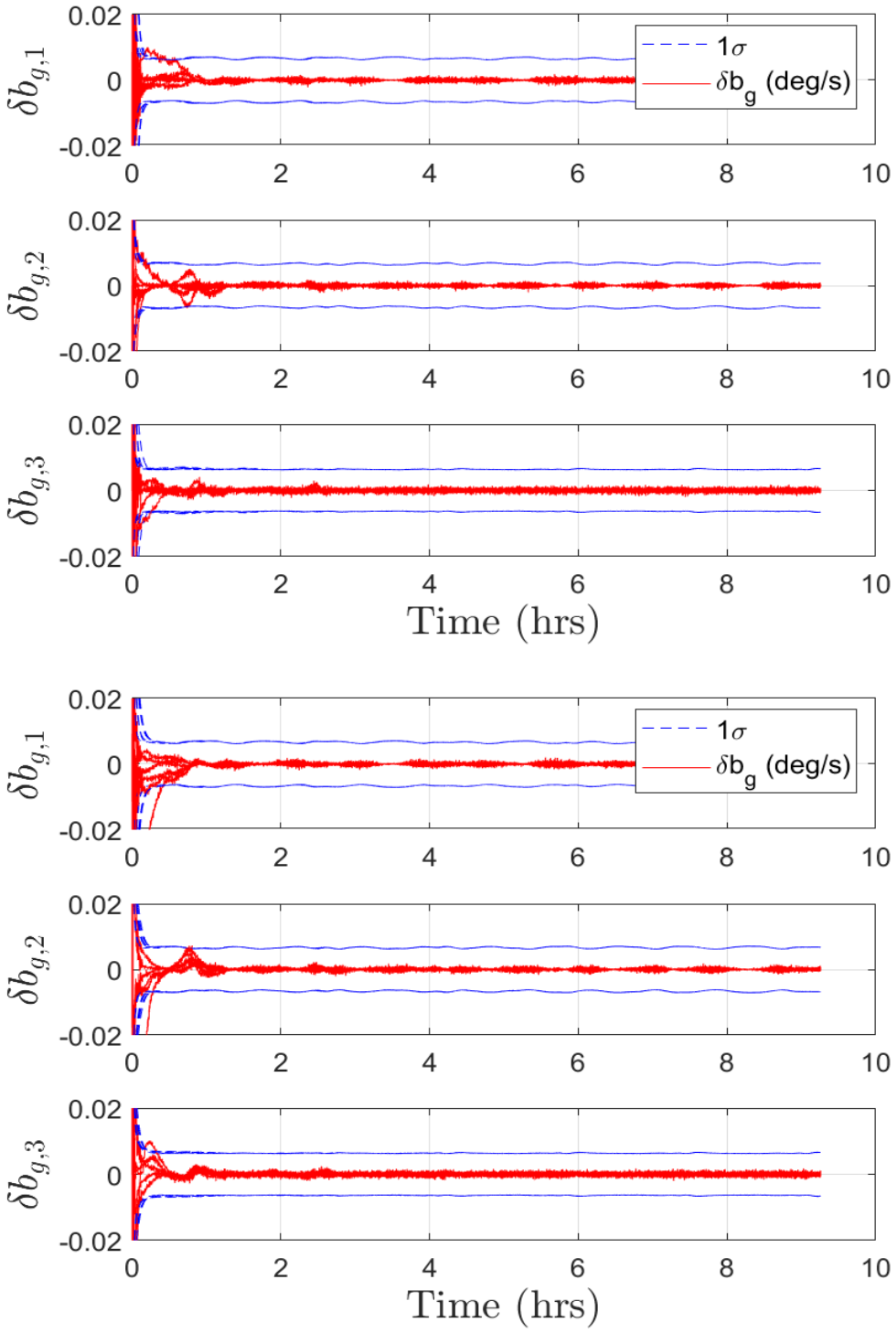

Figure 5.44 IMU bias error δb_g history for low inclination, low $\bar{\omega}$ with no scale factor errors (top) and with scale factor errors (bottom).

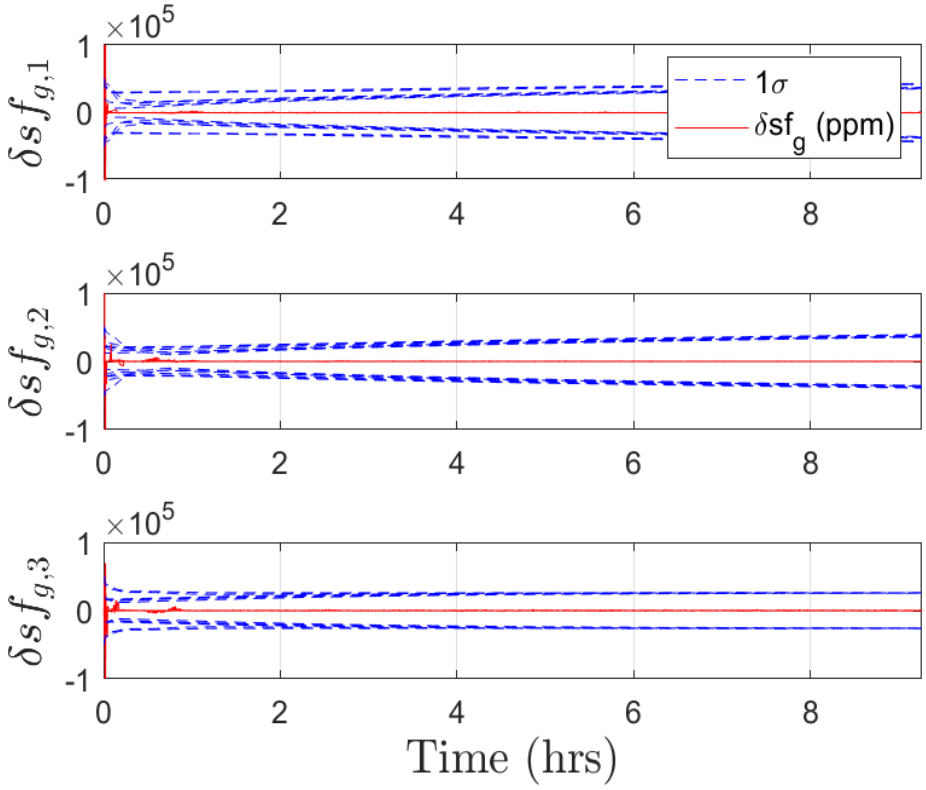

Figure 5.45 IMU scale factor error δsf_g for low inclination, low $\bar{\omega}$ for cases where scale factors are included.

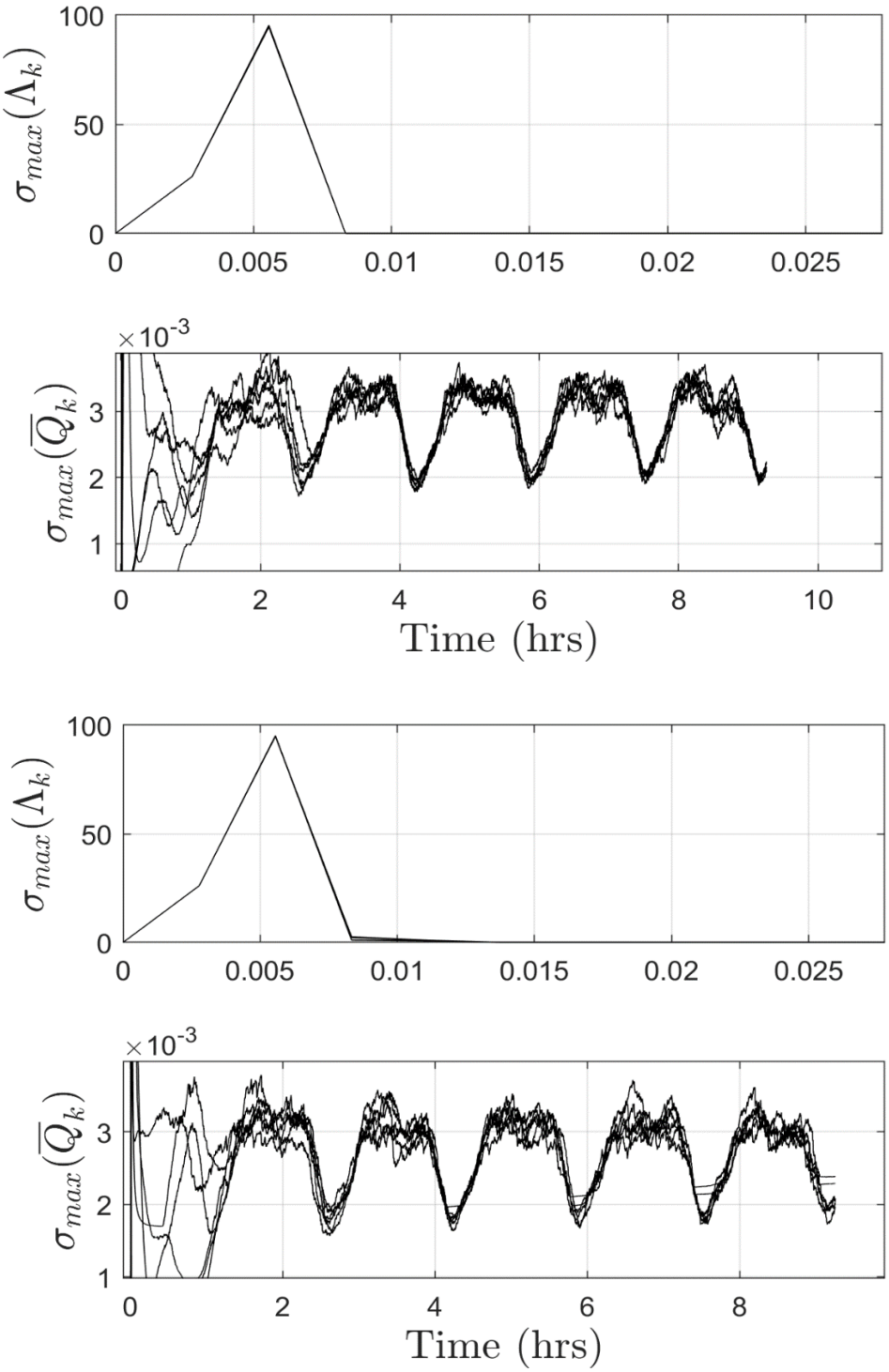

Figure 5.46 Stochastic observability metrics for low inclination, low $\overline{\omega}$ with no scale factor errors (top) and with scale factor errors (bottom).

Figure 5.42 showcases the VMA convergence for the low $\bar{\omega}^{SE}$ case. When no scale factor errors are present within the noise of the system, all runs seemingly converge within two and a half hours, but with the majority of attitude estimates not bounded by the covariance. Additionally, the 1σ state covariance bounds are relatively consistent with max amplitude near $7°$. When scale factor estimates are included, all runs converge within four hours, similarly with large state estimate errors. The covariance bound is also similarly near $7°$. Similar phenomena is shown in the Euler angle plots of Figure 5.43.

The bias estimation errors are shown in Figure 5.44. Similar to both the high and spin stabilized $\bar{\omega}^{SE}$ cases, the 1σ bound on the bias errors are approximately $0.007°/s$, with estimates converging to below that bound in less than a half hour of initialization. A noticeable difference is that the bias covariance in Figure 5.44 appears slightly oscillatory when compared to higher $\bar{\omega}^{SE}$ cases. In both instances of scale factor inclusion, the bias estimates seem to converge to a steady estimate after about two hours.

In the instance of the scale factor estimation errors of Figure 5.45, we see each axis estimate converging below the 1σ bounds almost immediately. Covariance estimates on the S^1 and S^2 axes are climbing throughout the simulation time, while the covariance estimate in the S^3 axis converges to a steady bound of 20000 ppm. This is a noticeable increase when compared to the covariance in the S^3 axis as seen by Figure 5.40.

The stochastic observability is given in Figure 5.46. Similar to both the high and spin stabilized $\bar{\omega}^{SE}$ cases, the value of $\sigma_{max}(\Lambda_k)$ peaks at 20 seconds, and then begins to limit to zero afterwards. The value of $\sigma_{max}(\bar{Q}_k)$ appears to have a lower

frequency of oscillation than the higher $\bar{\omega}^{SE}$ cases, and matches the values presented in Figure 5.41. In the case where scale factor errors are included, the values of $\sigma_{max}(\bar{Q}_k)$ begin to have a linear slope near the troughs of the trend after 4 hours, similar to the cases of scale factor inclusion for the spin stabilized $\bar{\omega}^{SE}$ case. Due to this trend, we treat this simulation scenario as stochastically unobservable.

5.3.10 General Observations

For each simulation scenario above, the state covariance on the Euler angles was seen to be relatively oscillatory, with peak amplitudes ranging from 3° to 7°, depending on the case tested. Firstly, this oscillation is due to the varying dynamics of the spacecraft when measuring the EMF vector throughout time, in addition to the orbital position. When the EMF vector aligns with a TAM 3-axis, the covariance in the spacecraft 3-axis decreases, while it increases in the 2 and 1 axes. Conversely, as the EMF vector decreases in magnitude along the 3-axis, the covariance increases in the spacecraft 3-axis and decreases in the 2 and 1 axes. This phenomenon is shown in the high inclination spin stabilized Euler angle scenario of Figure 5.8 where troughs in the covariance of $\delta\psi$ align with peaks in $\delta\theta$ and $\delta\pi$, and vice versa. Additionally, this phenomenon is also prevalent within [41].

The frequency of the covariance oscillation varied with orbital inclination and spacecraft angular rate, suggesting a dependence on the rate of change of the EMF vector, or more specifically, how the magnitude changes with respect to each of the TAM axes. Consider the low angular velocity cases of Figure 5.43, Figure 5.28, and Figure 5.13. In each of these scenarios, the angular velocity is given as $\bar{\omega}^{SE} = [0 \quad 0 \quad 0.057]^T\ °/s$. It can be seen that the covariance bounds maintain a periodic oscillatory behavior but have a much lower frequency than the higher

angular velocity cases. However, as i increases, the frequency of the covariance also increases slightly, implying a slight dependence on-orbital inclination. Now consider the spin stabilized scenarios of Figure 5.38, Figure 5.23, and Figure 5.8 where the angular velocity vector is given as $\bar{\omega}^{SE} = [0\ 0\ 0.57]^T\ °/s$, and remains constant throughout the 5 orbits in each axis. Within these plots, the covariance on the $\delta\phi$ and $\delta\theta$ appear more oscillatory than that of $\delta\psi$. This matches with intuition, as we are spinning about the S^3 axis and are in a roll condition, allowing the magnitude and direction of the EMF vector along the 2 and 1 axes to changes more rapidly. Additionally, as we change inclination, the amplitude and general shape of the covariance changes. For example, in the low inclination scenario of Figure 5.43, the covariances on $\delta\phi$ and $\delta\theta$ have maximum amplitudes that are maintained near $7°$ and low frequency oscillations. As we move up in inclination, the amplitude on $\delta\phi$ and $\delta\theta$ decrease, while the amplitude on $\delta\psi$ increases. This is because the local EMF has a higher rate of change in its magnitude and direction as we move up through higher latitudes.

The state covariance of the attitude estimates was also affected by the inclusion of scale factor errors into the measurements of the system. In the high angular velocity cases, scale factor inclusion increased the covariances on the ϵ estimates, most notably seen in Figure 5.17. This can be simply attributed to the fact that there is more noise in the system. However, it can also be noticed in the scale factor case of Figure 5.17 that the covariance bound on $\delta\phi$ and $\delta\theta$ have sharper peaks with higher magnitude than those of $\delta\psi$. This can be attributed to the estimation of the scale factor in the 2 and 1 axes, which correlate to estimates on θ and ϕ. Additionally, consider the gyro measurement equation given by Equation (3.1)

$$C_{Sg}\bar{\omega}_m^{gE}(t) = \left(1_3 + SF(t)\right)\left(\bar{\omega}^{SE}(t)\right) + C_{Sg}\left(\bar{b}_g(t) + \bar{n}_g(t)\right) \tag{3.1}$$

In the instance of constant angular velocity vector, Equation (3.1) can be modified to be

$$C_{Sg}\bar{\omega}_m^{gE}(t) = \bar{\omega}^{SE} + SF(t)\bar{\omega}^{SE} + C_{Sg}\bar{b}_g(t) + C_{Sg}\bar{n}_g(t)$$

$$C_{Sg}\bar{\omega}_m^{gE}(t) = \bar{\omega}^{SE} + \bar{B} + C_{Sg}\bar{n}_g(t) \tag{5.6}$$

where a new bias is defined by $\bar{B}$. As the rates of change of both the scale factor errors and the bias errors are relatively small, $\bar{B}$ is effectively constant over time. Due to this, the combined effect of the scale factor and bias errors are observable as a "virtual bias" [49], whereas the individual contributions are unobservable. Additionally, when $\bar{\omega}^{SE} = 0$, the SF estimate will also be unobservable, however this is a more limiting case than the one discussed above.

In our system, the angular velocity along the 3-axis is constant for all simulations, implying that the scale factors and bias in the 3-axis are unobservable and cannot be modified individually. Additionally, in the spin stabilized conditions, the scale factors in all three axes can no longer be resolved. Consider the high angular velocity cases given in Figure 5.33, Figure 5.18, and Figure 5.3. While the filter cannot estimate the individual scale factor or bias in the 3-axis, it can estimate the combined effect of these errors in addition to their variance. This provides a solution; however, it is a less accurate one. Additionally, this method treats the scale factor in the 3-axis as a larger bias, allowing for the covariance on that axis to not capture the effects of the scale factor itself. This causes lower covariances to be reported on the ψ estimates as opposed to the sharper covariances on the θ and ϕ estimates. Now consider the spin stabilized cases of Figure 5.38, Figure 5.23, and Figure 5.8. The scale factors in the 2 and 1 axes are not being estimated, and their

covariances appear to be growing unbounded in each case. However, as the measured angular velocity in these axes is primarily due to noise, scale factor estimates do not largely affect the output, allowing for the filter to still converge.

In some instances of the high $\bar{\omega}^{SE}$, it was found that the virtual bias in the 3-axis could also cause the combined value of $(1_3 + SF)$ to be less than 0 in the 2 and 1 axes, which is highly unlikely. While this proved to not be an issue in the 3-axis estimate, it affected the 2 and 1 axes estimates at high $\bar{\omega}^{SE}$ and often caused a non-nominal state convergence. As such, a state constraint was used in the format of Equation (3.56) and the QP discussed in the beginning of this chapter. The effect of this constraint, especially in the covariance of the system, was not investigated, but would be an interesting and beneficial case of future work.

In most scenarios, the attitude estimate converged no matter the inclusion of scale factors. However, in the high inclination cases of Figure 5.2 and Figure 5.3, the inclusion of scale factors caused the attitude estimate to diverge in half of the Monte Carlo runs. As this only occurs for the high inclination, high angular velocity case, it seems to imply that this specific combination of the EMF measurement, scale factor, and bias estimates caused divergence. If attention is turned to the state estimation errors of Figure 5.4 and Figure 5.5, it can be seen that the bias and scale factor state error estimates oscillate throughout time, ultimately resulting in the bias and scale factor estimates themselves to oscillate through time. It is believed that this behavior leads to a divergence in the estimates of ϵ to be highly oscillatory as seen in Figure 5.2. While the direct cause of this behavior is unknown, it is assumed that the tuning parameters used are only valid for the lower inclination cases. As such, future works should investigate the design of more robust and potentially dynamic tuning parameters.

State observability tests showed two primary results: (1) the state covariance of the system, no matter the inclusion of scale factor errors, is no longer a function of the initial covariance after 5 measurement updates at $0.1\,Hz$, and (2) the state covariance is bounded when no scale factors are included, and unbounded in instances when scale factors are unobservable. Specifically, in the instances where scale factors were not included, the value of $\sigma_{max}(\bar{Q}_k)$ maintained a small steady state value for all Monte Carlo runs. When scale factors were included, spin stabilized and low angular velocity scenarios resulted in a growth of $\sigma_{max}(\bar{Q}_k)$. As shown previously with Equation (5.6), this result matches with the intuition stated that the individual scale factor estimates will always be unobservable in instances where the angular velocity is 0. This also matches with intuition based upon the scale factor covariances in the 2 and 1 axes that seemed to grow unbounded, indicating stochastic unobservability.

While the stochastic observability seemed to provide an interesting and valuable metric, there are some areas for concern. In cases where scale factor was estimated, not every Monte Carlo run resulted in a similar value of $\sigma_{max}(\bar{Q}_k)$. This can be seen by the case shown in Figure 5.26. In one run, we see a relatively flat and constant value of $\sigma_{max}(\bar{Q}_k)$ at the top of the plot. If this was plotted by itself, it would indicate to us that the system is stochastically observable based on our current metrics. However, we chose to label the system as stochastically unobservable based upon the majority of the other runs that were plotted with a continuous upward trend. The difference in trends of $\sigma_{max}(\bar{Q}_k)$ indicates that we may need to be careful about how we define the stochastic observability. Perhaps the trends would have leveled out had we run the simulations for longer timespans.

The variation of $\sigma_{max}(\bar{Q}_k)$ can be attributed to the random noise within the system matrix of Φ_k. Specifically, this noise is due to the fact that we choose to linearize our system about the estimated trajectory at each time step (see Equation (3.36)), and thus use estimated noisy values of angular velocity and attitude. If we were to instead linearize our system about the truth, then we can create a common value of Φ_k from run to run. While we do not know the truth trajectory in practice, it can be beneficial in simulation to verify the stochastic observability. Future work should verify state stochastic observability by analyzing the system when linearized about the truth trajectory.

Based on the results of each simulation scenario, VMA convergence seems to be dependent on two factors: (1) the angular velocity of the spacecraft, and (2) the orbital inclination. In a more general sense, these factors seem to point to a requirement that the local EMF vector must change sufficiently through time, as posited in the beginning of Chapter 3. However, it can be seen in Figure 5.42, Figure 5.27, and Figure 5.12 that the VMA either did not converge or converged slowly and with higher state errors when the angular velocity vector was $\bar{\omega}^{SE} = [0\ 0\ 0.057]^T\ °/s$. When angular velocity was increased to be either $\bar{\omega}^{SE} = [0\ 0\ 0.57]^T\ °/s$ or $\bar{\omega}^{SE} = [1.15, -2.86, 1.71]^T\ °/s$, the VMA converged in varying amounts of time. This suggests that general convergence is primarily dependent on the angular velocity of the spacecraft, $\bar{\omega}^{SE}$, with convergence rate dependent on the orbital inclination i. This also suggests that the EMF vector changes sufficiently in the inertial frame to be generally used as a sole aiding sensor for AD.

5.4 Summary

Within this chapter, we showcased the performance of the VMA over multiple CubeSat flight conditions. We discussed mission performance metrics, in the form of the angular error between the estimate 3-axis $\hat{S}^3$ and the true 3-axis S^3, denoted by ϵ, and the stochastic observability of the system. Specifically, we investigated these parameters over multiple scenarios ranging from low to high orbital inclinations, with varying angular velocities. Moreover, we included simulations in which scale factor errors were included within the noise of the system and estimated for each of the flight conditions.

Based upon the results of the VMA simulations, we made conclusions about the effectiveness of the EMF vector as an aiding measurement within an EKF architecture. Namely, we showed that VMA convergence is highly dependent upon the angular rates of a CubeSat, showing that the VMA did not converge or converged slowly in low angular velocity ($\omega^{SE} < 0.57\,°/s$) conditions. In instances where the angular velocity vector was sufficiently large, it was shown that the VMA convergence rate depended on-orbital inclination, with convergence occurring within 2 hours for inclinations of $i \geq 50°$. The system was shown to be stochastically observable in every instance where scale factors were not included, and stochastically unobservable in most cases of scale factor inclusion.

6 Conclusions

6.1 Summary of Results

This thesis investigated the problem of attitude determination on small CubeSats by fusing the information from an IMU and magnetometer triad. A MATLAB simulation environment was developed which accounted for the effects of orbital inclination, CubeSat angular velocity, and IMU noise characteristics. The attitude determination algorithm was a VMA EKF in many ways similar to the algorithm in [41]. We developed an updated gyroscope measurement model to include scale factor errors and modified the state error vector equations to include an estimate of the errors. We simulated multiple scenarios, varying orbital inclination, angular velocity, and scale factor estimation to determine the conditions in which the VMA effectively and ineffectively estimated the attitude of a CubeSat. Additionally, we modified the stochastic observability test derived in [47] for implementation in the VMA architecture.

It was found that general VMA convergence was highly dependent on the angular velocity of the CubeSat itself. Moreover, convergence speed was dependent on the orbital inclination of the vehicle. In spin stabilized velocity conditions above an inclination of $i = 50°$, it was seen that the VMA converged to acceptable error levels within one and half to two hours of initialization, starting from random initial state conditions. For inclinations close to zero, it was found that convergence occurred within five hours of initialization. When angular velocity of the system was below a given threshold of $\bar{\omega}^{SE} < [0\ 0\ 0.57]^T\ °/s$, it was found that convergence was not guaranteed within the 5 orbit simulation timeframe.

When scale factor errors were added to the system, it was shown that they were adequately calibrated out in most test conditions. However, it was also shown that in every scenario tested, at least one scale factor was unobservable due to the angular velocity of the system. In conditions where angular velocity was constant, scale factors could not be differentiated from the gyro bias, causing a "virtual bias" to be estimated. In conditions where the angular velocity was zero, the scale factors in those axes were also be unobservable. While this proved not to be an issue in many cases, it was posited as a potential problem within the high angular velocity, high inclination test of Figure 5.3. In this instance, state estimates appeared to oscillate throughout the simulation time frame, causing a lack of convergence. Another potential contributing factor was suggested to be tuning parameters of the system.

When testing the stochastic observability of the system, it was determined that the system was stochastically observable in all instances where scale factors were not included. When scale factors were included, the system was shown to be stochastically unobservable in most cases. Specifically, the stochastic observability criteria of $\sigma_{max}(\Lambda_k) = 0$ was met in every simulation run, whereas the criteria of $\sigma_{max}(\bar{Q}_k) < T_v$ was not met in instances where at least one component of the angular velocity vector was 0, indicating that the state covariance of the system would grow unbounded through time.

In general, two high-level results obtained from the VMA simulations can be made: (1) VMA convergence appears to be highly dependent on angular velocity of the vehicle, and (2) scale factor additions within the model require angular acceleration in each axis to be fully observable. Based on these results, further investigation of the VMA should incorporate active control to create angular

acceleration in each axis. Additionally, more dynamic, and potentially robust tuning parameters should be utilized in future analysis.

6.2 Effect of IMU Grade on Attitude Estimates

The vector matching algorithm (VMA) is used to correct the inherent attitude drift that arises from integration of a noisy rate gyroscope. In cases where the noise content on the gyros is high (consumer grade IMUs), frequent application of an external aiding measurement (and thus the use of the VMA) is required to correct the gyro attitude estimate. However, in higher grade IMUs, the noise content is lower, and inertial attitude estimates may not require as frequent aiding vector corrections.

In an effort to explore the effect of gyro grade on attitude estimates, this section describes simulations on the attitude drift for three different IMU grades: Consumer, tactical, and navigational. Moreover, we perform analysis on these IMUs by simulating a scenario in which only inertial based attitude determination is applicable; HyCUBE (Hypersonic Configurable Unit Ballistic Experiment). HyCUBE is 3U CubeSat with a multi-sensor payload used to help characterize high-speed aerothermodynamics associated with orbital reentry, currently being developed by the UMN's Small Satellite Research Lab.

A CONOPS for HyCUBE is given in Figure 6.1. The primary scientific mission begins with a controlled deorbit from a given nominal attitude condition ((1) in Figure 6.1). Scientific flow field measurements begin during a period of radio blackout as reentry begins ((2) in Figure 6.1). During this time HyCUBE will be in a passively stabilized state After data collection has completed, data downlink will begin ((3) in Figure 6.1) followed by a hardware burnup ((4) in Figure 6.1).

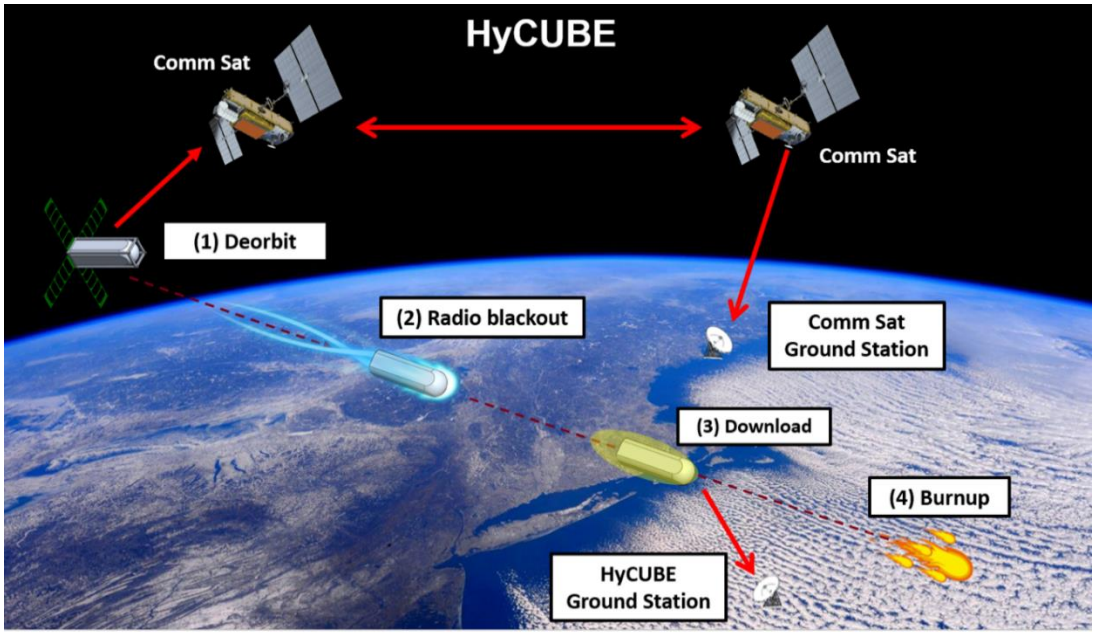

Figure 6.1 HyCUBE CONOPS.

The ADCS of HyCUBE can be split into two functionalities: A station keeping functionality used while on-orbit about the Earth, and an active pointing functionality used during atmospheric reentry. The focus of the station keeping functionality will be to place HyCUBE into a stable attitude configuration conducive to flow-field science prior to reentry. The pointing functionality will be used to maintain stability during HyCUBE reentry. Initial analysis suggests that the knowledge error must be below $\epsilon \leq 2°$ throughout mission duration.

As the primary focus of HyCUBE is to collect data on the hypersonic flow fields, typical ADCS schemes prove challenging to implement due to the intense heat and plasma distribution. Many common sensors and actuators (see Table 1.1) cannot be effectively used in this regime, requiring the use of pure inertial based AD with high-grade gyros.

6.2.1 HyCUBE Reentry Simulations

For HyCUBE, accurate pointing during orbital reentry is a key factor for effective data collection. However, reentry prohibits the use of the EMF as a measurement (and thus the VMA), due to the intense heat and plasma distribution around the exterior of the vehicle. As such, HyCUBE will need to rely solely on the use of an IMU and inertial navigation throughout its reentry mission. Based on this requirement, simulations were run to determine the inertial drift rate (as discussed in Chapter 2) dependent upon the grade of gyro used. Specifically, simulations were run based upon external angular velocity and attitude data simulated for the reentry conditions of HyCUBE. This data was then corrupted with consumer, tactical, and navigational gyro noise characteristics (see Appendix C). The noisy IMU data had its covariance and estimated attitude propagated over the entirety of the reentry time to determine the amount of drift possible.

Reentry simulations were run over a period of $1200\,s$ and assumed perfect knowledge of the attitude at the beginning of reentry, with an initial state given by the initial quaternion. It was also assumed that any scale factor or null-shift bias errors were calibrated out during the orbital portion of the HyCUBE mission. Initial state covariance, P_0, was obtained by running the VMA architecture to completion with the gyro noise characteristics used in the below tables to obtain a steady state covariance matrix at the end of the 5 orbits. This covariance matrix was then used as the initial starting covariance at the beginning of orbital reentry. The plots below show 30 Monte Carlo runs in which the gyro measurements are corrupted by the white noise and in-run biases given in the tables below.

6.2.2 Consumer Grade IMU

Table 6.1 HyCUBE Consumer Grade Gyro Sim Parameters

Parameter	Value	Description
σ_{IRB}	$180\ °/hr$	In-Run Bias Stability, STD
τ_{GM}	$300\ s$	Correlation Time of Gauss-Markov Process
σ_g	$0.05\ °/s$	Output Noise, STD
$\delta q_{S\hat{S}}$	$[1\ 0\ 0\ 0]^T$	Initial Attitude Error Quaternion

$$P_0 = \begin{bmatrix} 0.0019 & 0.0014 & -0.0049 & 0 & 0 & 0 \\ 0.0014 & 0.0016 & -0.0045 & 0 & 0 & 0 \\ -0.0049 & -0.0045 & 0.0159 & 0 & 0 & -0.0001 \\ 0 & 0 & 0 & 0 & 0 & 0 \\ 0 & 0 & 0 & 0 & 0 & 0 \\ 0 & 0 & -0.0001 & 0 & 0 & 0 \end{bmatrix} \tag{6.1}$$

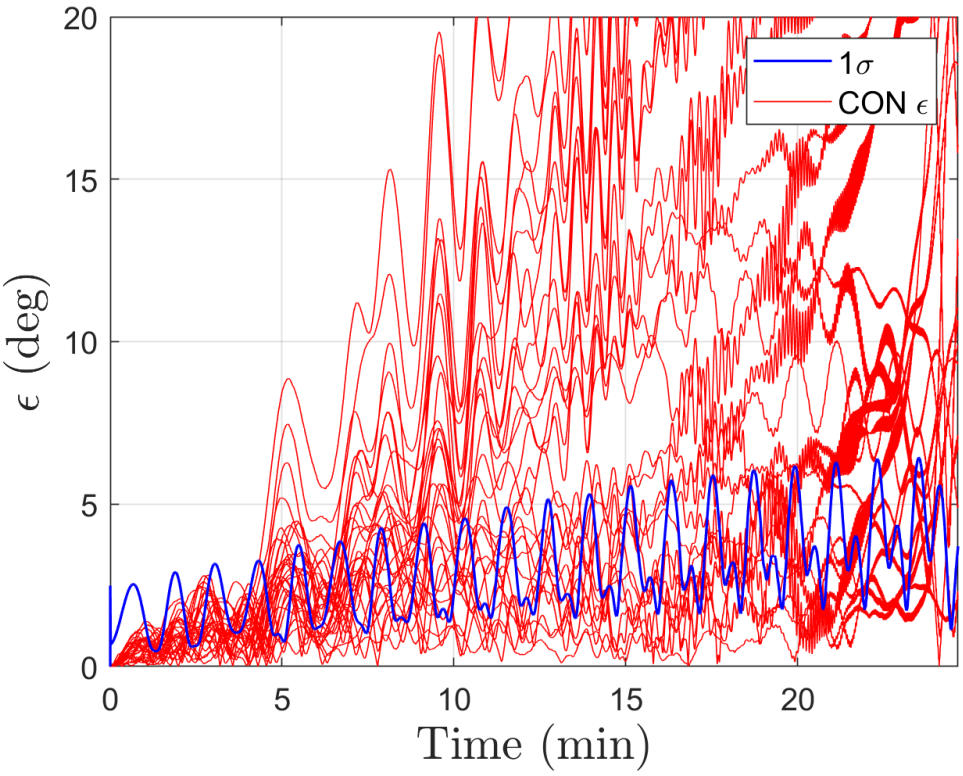

Figure 6.2 Consumer grade gyro drift rate.

Figure 6.2 above shows the attitude estimate divergence as a function of time for a consumer grade gyro with noise parameters given in Table 6.1. Specifically, the plot showcases ϵ as defined in Equation (5.2). It can be seen that the state attitude estimate begins to diverge immediately, with large divergences occurring after about 5 minutes from simulation start. By 6-7 minutes, the value of ϵ is increasing to $10°$, limiting past the covariance bounds specified by the blue lines on each plot.

6.2.3 Tactical Grade IMU

Table 6.2 HyCUBE Tactical Grade Gyro Sim Parameters

Parameter	Value	Description
σ_{IRB}	$0.35\,°/hr$	In-Run Bias Stability, STD
τ_{GM}	$1000\,s$	Correlation Time of Gauss-Markov Process
σ_g	$0.0017°/s$	Output Noise, STD
$\delta q_{S\hat{S}}$	$[1\ 0\ 0\ 0]^T$	Initial Attitude Error Quaternion

$$P_0 = 1E^{-3} * \begin{bmatrix} 0.1117 & -0.0328 & -0.0881 & 0 & 0 & 0 \\ -0.0328 & 0.1281 & 0.1127 & 0 & 0 & 0 \\ -0.0881 & 0.1127 & 0.3885 & 0 & 0 & 0 \\ 0 & 0 & 0 & 0 & 0 & 0 \\ 0 & 0 & 0 & 0 & 0 & 0 \\ 0 & 0 & 0 & 0 & 0 & 0 \end{bmatrix} \tag{6.2}$$

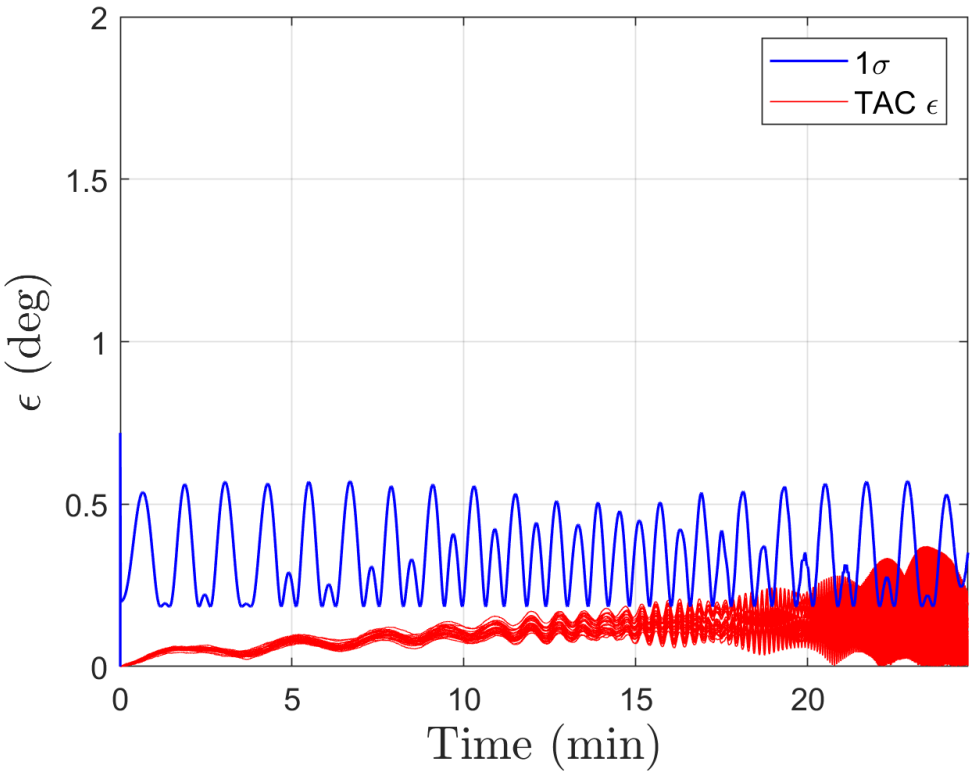

Figure 6.3 Tactical grade gyro drift rate.

Figure 6.3 above shows the attitude estimate divergence as a function of time for a tactical grade gyro with noise parameters given in Table 6.2. Specifically, the plot showcases ϵ as defined in Equation (5.2). It can be seen that the state attitude estimate stays within the covariance bounds throughout the entire simulation run, with ϵ falling below a 1σ bound of $0.6°$.

6.2.4 Navigation Grade IMU

Table 6.3 HyCUBE Navigational Grade Gyro Sim Parameters

Parameter	Value	Description
σ_{IRB}	$0.0030\,°/hr$	In-Run Bias Stability, STD
τ_{GM}	$3600\,s$	Correlation Time of Gauss-Markov Process
σ_g	$8.0E^{-4}\,°/s$	Output Noise, STD
$\delta q_{S\hat{S}}$	$[1\ 0\ 0\ 0]^T$	Initial Attitude Error Quaternion

$$P_0 = 1E^{-3} * \begin{bmatrix} 0.1568 & 0.0764 & -0.2038 & 0 & 0 & 0 \\ 0.0764 & 0.1685 & -0.2201 & 0 & 0 & 0 \\ -0.2038 & -0.2201 & 0.6735 & 0 & 0 & 0 \\ 0 & 0 & 0 & 0 & 0 & 0 \\ 0 & 0 & 0 & 0 & 0 & 0 \\ 0 & 0 & 0 & 0 & 0 & 0 \end{bmatrix} \tag{6.3}$$

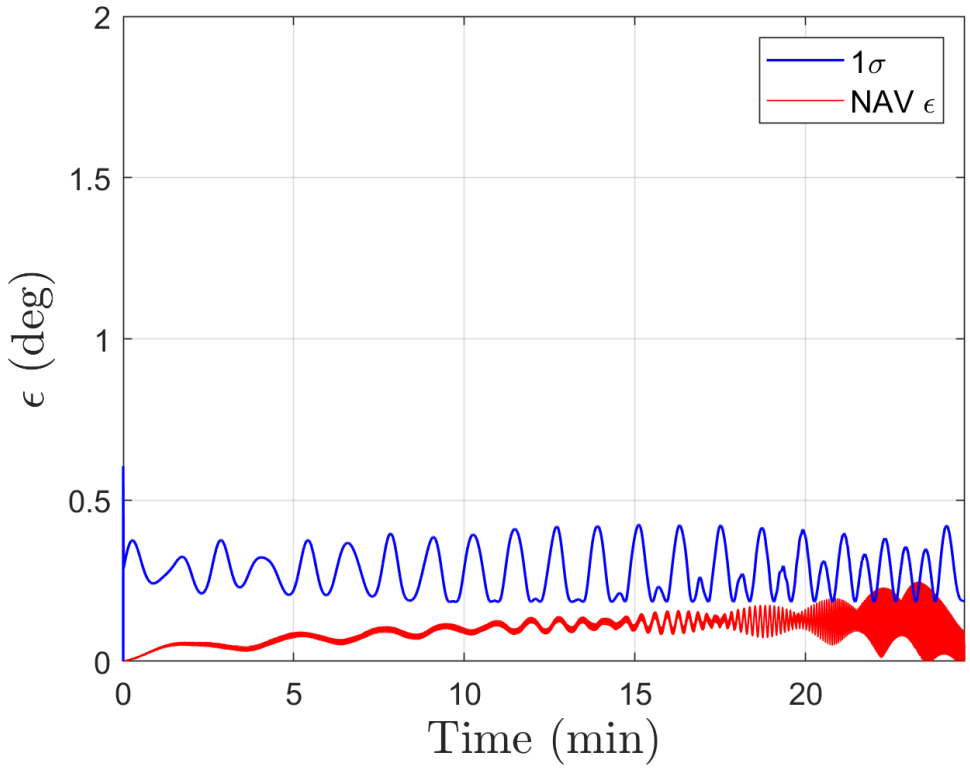

Figure 6.4 Navigational grade gyro drift rate.

Figure 6.4 above shows the attitude estimate divergence as a function of time for a tactical grade gyro with noise parameters given in Table 6.3. Specifically, the plot showcases ϵ as defined in Equation (5.2). It can be seen that the state attitude estimate stays within the covariance bounds throughout the entire simulation run, with ϵ falling below a 1σ bound of $0.4°$. This is similar to the tactical grade gyroscope scenario.

6.2.5 General Analysis of the HyCUBE Simulations

The covariance bounds seen in Figure 6.4, Figure 6.3, and Figure 6.2 highlight a similar oscillatory nature to the one seen in the VMA simulations. While there are no EMF measurements occurring in the HyCUBE case, this oscillation can be described as remnants of the state covariance obtained during the on-orbit period of HyCUBE's mission. Specifically, as the initial covariance was calculated from running the VMA and taking the final state covariance after 8 hours, an oscillatory behavior remains. As the inertial measurements begin to drift due to noise, this covariance bounds also begin to increase.

Accurate hypersonic data collection requires that the value of ϵ remain below $2°$ over the data collection period occurring between 10 and 15 minutes after orbital reentry begins. Based upon the drift rates seen in Figure 6.4, Figure 6.3, and Figure 6.2, this limits the choice of IMU to be of tactical grade or higher. With cost also playing a role in the decision, the most economic choice that meets HyCUBE requirements would be a tactical grade IMU.

If we extend these results to the VMA, we can extrapolate that the use of higher grade IMUs would reduce the frequency of EMF measurements required, in addition to the general covariance bounds on the attitude estimates. However,

tactical and navigational grade IMUs typically cost on the order of $\$5{,}000 - \$100{,}000$, which is beyond the cost limitations of CubeSats. As such, these IMUs are better suited for missions in which typical aiding schemes cannot be employed, such as HyCUBE.

6.3 IMPRESS and EXACT ADCS Structure

As the results of Chapter 5 show, the VMA AD solution converges to below the knowledge requirement of $\epsilon = 10°$ in most cases and converges within 2 hours. As the phenomena of interest for both IMPRESS and EXACT occur over the periods of days or weeks, AD convergence time is not a constricting factor. As such, the VMA developed can be used as the AD solution for both IMPRESS and EXACT on-orbit. With this in mind, the following section will describe a high-level overview of the currently planned ADCS of each CubeSat.

6.3.1 IMPRESS & EXACT ADCS

As the operational slew rates of the missions are not significantly large, the length of time required to operate the ADCS is not heavily constrained. In terms of the AD, this means that VMA convergence times of 2 hours are acceptable for mission science. While this is acceptable, we would also like to ensure VMA convergence occurs as fast as possible on-orbit, necessitating the use of a relatively high inclination-orbital condition with a spin stabilized angular velocity. As an aside, science objectives limit the spin stabilized angular velocity to be $\bar{\omega}^{SE,3} < 5°/s$. Thus, the choice of an ISS orbit is conducive to both cost and VMA convergence, as many CubeSat missions use the P-POD deployers on board the ISS at an inclination of $i \approx 50°$. Additionally, a spin stabilized condition of $\bar{\omega}^{SE} =$

$[0\ 0\ 0.57]^T\ °/s$ is shown to aid VMA convergence and also meets the science requirement.

While the control system (CS) is not the focus of this work, we will discuss it briefly here as motivation for some of the selected parameters. Firstly, as ADCS time is not greatly constrained, the use of low-bandwidth actuation techniques is allowable. Specifically, based on UMN heritage and cost-effectiveness, current actuation plans include the use of tri-axial magnetorquers as the sole control technique. While this provides cost and mass effectiveness, it also requires that determination and control be performed separately, as any change in the local EMF vector due to the magnetorquers would interfere with accurate VMA performance. Due to this, the sampling rate of the TAM was selected to be $0.1\ Hz$, allowing for 10 second intervals between magnetometer sampling, leaving ample room in between magnetometer samples for the magnetorquers to actuate. This determination/control duty cycle is discussed in detail within [50].

With regards to IMU quality, simulations run within Chapter 5 utilize noise characteristics from the Analog Devices ADIS16488A IMU, which is considered a high-end consumer grade IMU. The ADIS IMU chosen as it allowed for an acceptable 1σ covariance bound on ϵ estimates, falling below the requirement of $\epsilon = 10°$. Additionally, the ADIS IMU contains a TAM within it, minimizing hardware complexities of the AD. For future missions, the simulations of Chapter 5 should be run again with varying IMU characteristics based upon mission needs.

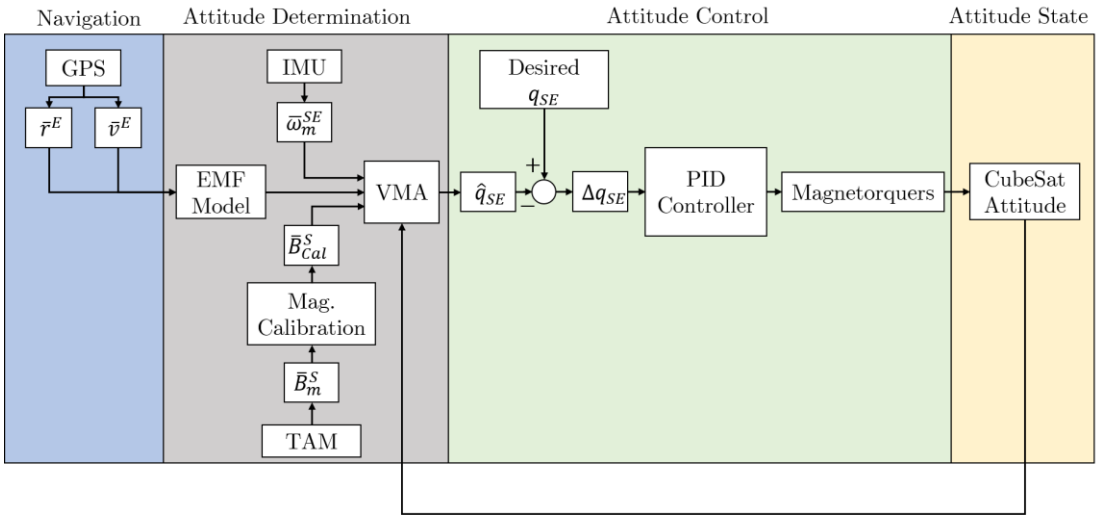

Figure 6.5 IMPRESS & EXACT ADCS Block Diagram

Figure 6.5 is a block diagram of the planned ADCS for both IMPRESS & EXACT. On-orbit, a Global Positioning System (GPS) will give local position, velocity, and timing information at a given frequency throughout the mission. This data is used to determine the modeled EMF vector throughout time. This vector, coupled with angular velocities measured from the IMU and calibrated EMF measurements from a TAM, are the inputs to the VMA developed in Chapter 3. The output of the VMA in the form of the estimate attitude quaternion $\hat{q}_{SE}$ is then compared with the desired quaternion q_{SE}. The difference between these two quaternions, parameterized by Δq_{SE}, is then given as the input into a PID controller. This PID controller calculates the magnetorquer actuation required to bring Δq_{SE} to zero, and then performs the actuation giving a new attitude in orbit. This new attitude is then input into the VMA, coupled with the most recent sensor measurements, to obtain the newest estimate of the state. This cycle continuously operates as we propagate through time.

6.4 Future Work

There are many additional paths that can be pursued in an effort to increase the validity and accuracy of the VMA developed and extended upon within this work. A key grouping of these paths, in the opinion of the author, are listed and discussed below.

6.4.1 Updated Scale Factor Models

The scale factor model developed within this work assumed that scale factors vary slowly with time due to Gaussian white noise. However, scale factors and other gyro noise parameters, are often considered to be functions of temperature, with set characteristics within a given temperature range. While the incorporation of temperature could prove to be a challenging non-linear inclusion, further work could utilize a higher order scale factor propagation model to increase accuracy. Specifically, a 1st order Gauss-Markov process could be used, similar to the in-run bias stability, such that

$$\dot{\overline{sf}}(t) = -\frac{1}{\tau_{sf}} sf(t) + \bar{n}_{sf}^{sf}(t) \tag{6.4}$$

where τ_{sf} represents a correlation time associated with the scale factor random process $sf(t)$, and $\bar{n}_{sf}^{sf}(t)$ is the additive wideband noise to the scale factor propagation. While this may increase the validity of the scale factor model, it also brings about the addition of τ_{sf} that must be selected. As a first approximation, this value could be assumed to be large such that $\tau_{sf} > 1000\,s$, implying the propagation of the scale factor is predominantly attributed to the additive wideband noise.

6.4.2 Real-Time Magnetometer Calibration

The noisy EMF data used within this work assumed that noise was purely white and Gaussian throughout all time. In reality, the TAM on-orbit is subject to many variations, as discussed in Section 2.5.1.1. To remove these external sources of noise, the TAM must either be placed far away from the electrical components of the satellite or must be calibrated in flight. As we are already constrained in size and volume, a real-time magnetometer calibration must occur on-orbit to ensure TAM measurements are valid for use within the VMA. A potential first approach may be to investigate the real-time magnetometer calibration discussed within [51] [52], which does not require any attitude information and uses an iterative approach to determine any present biases.

6.4.3 Increased "Truth" Data Fidelity

Truth data used within the VMA simulations is created by using ODE45 to propagate the satellite attitude dynamics throughout time. While the equations used are accurate, they do not include the effects of external torques. Namely, any gravity gradient torques, residual magnetic moments, aerodynamic torques, and solar radiation torques are not included within the simulation. Further work could include these additional torques by modifying the angular velocity propagation equation such that

$$\dot{\bar{\omega}}^{SE} = I_S(-\bar{\omega}^{SE,\times} I_S \bar{\omega}^{SE} + \tau_{external})^{-1} \tag{6.5}$$

where I_S is the 3×3 moment of inertia tensor and $\tau_{external}$ is the sum of any external torques within the system.

Additionally, rudimentary control torques could also be incorporated into the system to allow the controlled variation of the angular velocity vector $\bar{\omega}^{SE}$,

which would allow the investigation of certain calibration maneuvers required for accurate scale factor observability.

6.4.4 Inclusion of Spacecraft Dynamics in VMA

In [41], the angular momentum vector was an estimated parameter included in the state vector. This allowed for a mathematical constraint to be placed upon the vehicles attitude throughout time. However, this required that the angular momentum vector change throughout time to be meaningful. While the work in [41] derived the accurate state error equations to estimate the angular momentum, the Stanford Gravity Probe B (in which the data was collected from) had its angular momentum vector relatively fixed in space.

To determine the validity of including the attitude dynamics, additional rotation maneuvers must take place throughout the VMA timeframe. Further work could rederive the attitude dynamics equations seen in [41] with the inclusion of scale factor errors, and then run further simulations to verify the effectiveness of including the attitude dynamics equations.

6.4.5 Covariance Pre-Conditioning

As discussed within Chapter 3, the accurate selection of noise covariance parameters is often a challenging task. Generally, the size and scaling of the covariance matrices, can change the convergence characteristics of EKF. A common parameter that often affects EKF convergence and accuracy is the condition number, κ, of the matrix Q_w. When this number is sufficiently large, EKF convergence tends to deteriorate. From a theoretical viewpoint, the EKF should not be dependent at all on the condition number. However, numerically, high condition numbers on matrices can often lead to poor or slow iterative results. A

common work around to this challenge is to incorporate tuning parameters into the system. By manipulating the tuning parameters as discussed in Section 3.3.4.2, we effectively vary the condition number of the state transition matrices of the system and change the rate of convergence.

While this is a solution to the problem at hand, it removes the physical interpretation of the EKF that we formulate by using the covariance matrices. Namely, we no longer have a clear mapping between how the noise of the system affects the convergence and accuracy of the EKF itself. As such, it may be beneficial to find another approach to tuning that does not change the state matrices. A potential solution to this could be formed by utilizing matrix pre-conditioning. The process of pre-conditioning effectively applies a transformation to a matrix that places it into a form more suitable for numeric solvers. While we still have some form of transformation, the use of pre-conditioners provides a reverse mapping from the transformed state back to the original state matrices. In practice, a pre-conditioner could be used to transform the EKF state matrices, perform our updates, and then transform results back to allow for better numerical solving.

6.4.6 VMA Failure Criteria

The VMA as designed converged in most cases but had issues when being implemented in a low angular velocity environments. While this may align with the intuitive idea that the EMF vector has not varied sufficiently between measurements, no failure criteria that state this observation have been defined. Additionally, no qualitative metric for why the VMA has not converged is developed or utilized. Future work could develop a numerical metric that is a function of the EMF vector model and the angular rate of the spacecraft to provide

a “yes/no” criteria for VMA convergence over time. This may require additional investigation into the EMF and a determination of what parameters are satisfied in VMA convergence, and what parameters are not satisfied in VMA divergence.

6.4.7 AD Testing Environment

While the VMA results shown within this work suggest that the EMF vector can be used as a sole aiding measurement, the simulation environment contains inaccuracies and may not represent reality. As such, adequate physical testing of the AD system developed is required. To this end, a comprehensive testing procedure based upon the hardware used, expected noise parameters, and expected operational scenarios on-orbit must be developed. Additionally, the environment in which to perform these tests must be created or identified. Further work could attempt to build a testing environment within the UMN SmallSat lab to ensure accurate AD testing. In general, the testing of the VMA described here would require a form a magnetic isolation (i.e. Helmholtz Cage). This could be utilized to create an artificial EMF vector that could be measured by a hardware-in-the-loop test environment. With these measurements, the VMA could be run on hardware and tested to ensure accurate convergence, while removing the need to create physical rotations of the CubeSat hardware. As a starting point, an initial VMA hardware test plan is included within Appendix D.

7 Bibliography

[1] NASA, "What are SmallSats and CubeSats?," 7 August 2017. [Online]. Available: https://www.nasa.gov/content/what-are-smallsats-and-cubesats.

[2] NASA, "NASA Technical Reports Server," 2014. [Online]. Available: https://ntrs.nasa.gov/archive/nasa/casi.ntrs.nasa.gov/20140013242.pdf. [Accessed 15 April 2020].

[3] T. Scholz, P. Rambaud and C. Asma, "Design of and aerodynamic stability and de-orbiting system for cubesats," in *2013 6th International Conference on Recent Advances in Space Technologies (RAST)*, 2013.

[4] NASA, "What is AzTechSat-1?," NASA, 14 February 2020. [Online]. Available: https://www.nasa.gov/ames/aztechsat-1. [Accessed 15 April 2020].

[5] C. Nagarajan, R. G. D'souza, S. Karumuri and K. Kinger, "Design of a Cubesat Computer Architecture using COTS Hardware for Terrestrial Thermal Imaging," in *2014 IEEE International Conference on Aerospace Electronics and Remote Sensing Technology (ICARES)*, 2014.

[6] J. A. Larsen and K. Vinther, "Inexpensive CubeSat Attitude Estimation Using COTS Components and Unsencted Kalman FIltering," in *Proceedings of 5th International Conference on Recent Advances in Space Technologies - RAST2011*, 2011.

[7] S. Song, H. Kim, Y.-K. Chang and J. Straub, "Design and Implementation of 3U CubeSat Platform Architecture," *International Journal of Aerospace Engineering,* vol. Vol.2018, no. 2018, p. 17, 2018.

[8] F. L. Markley and J. L. Crassidis, Fundamentals of Spacecraft Attitude Determination and Control, New York: Springer, 2014, pp. 147-166.

[9] G. Wahba, "Problem 65-1: A Least Squares Estimate of Satellite Attitude," *SIAM Review,* vol. 7, no. 3, p. 409, 1965.

[10] M. D. Shuster and S. D. Oh, "Attitude determination from vector observations," *Journal of Guidance and Control,* vol. 4, no. 1, pp. 70-77, 1981.

[11] J. L. Farrell, "Attitude Determination by Kalman Filtering, Contractor Report," NASA Goddard Space Flight Center, Washington, DC, 1964.

[12] D. E. Gaylor and E. G. Lightsey, "GPS/INS Kalman Filter Design for Spacecraft Operating in the Proximity of the International Space Station," in *AIAA Guidance, Navigation, and Control Conference and Exhibit*, Austin, 2003.

[13] K. S. Yoon, S. Y. Kim and Y. J. Choi, "Ultrasonic Satellite System Moving Object Positioning by Extended Kalman Filter," *International Journal of Precision Engineering and Manufacturing,* vol. 12, no. 5, pp. 783-790, 2011.

[14] Y. Shen, "Adaptive Extended Kalman Filter Based State of Charge Determination for Lithium-Ion Batteries," *Electrochimica Acta,* vol. 283, pp. 1432-1440, 2018.

[15] H. N. Mocan and K. Topyan, "Illicit Drug Use and Health Analysis and Projections of New York City Birth Outcomes Using a Kalman Filter Model," National Bureau of Economic Research, Cambridge, 1993.

[16] S. F. Kvamsdal and S. M. Stohs, "Estimating Endangered Species Interaction Risk With the Kalman Filter," *American Journal of Agricultural Economics,* vol. 96, no. 2, pp. 458-468, 2014.

[17] B. D. Tapley, G. H. Born and B. E. Schutz, "2.2.3 Basic Coordinate Systems," in *Statistical Orbit Determination*, Burlington, Elsevier Academic Press, 2004, pp. 29-32.

[18] Y. Dong, "Chapter 8: MEMS Inertial Navigation Systems for Aircraft," in *MEMS for Automotive and Aerospace Applications*, Woodhead Publishing, 2013.

[19] G. Slabaugh, "Computing euler angles from a rotation matrix," [Online]. Available: www.gregslabaugh.net/publications/euler.pdf. [Accessed 21 April 2020].

[20] E. Hemingway and O. O'Reilly, "Perspectives on Euler angle singularities, gimbal lock, and the orthogonality of applied forces and applied moments," *Multibody System Dynamics,* vol. 44, no. 1, pp. 31-56, 2018.

[21] J. Sola, *Quaternion Kinematics for the Error-State Kalman Filter,* 2017.

[22] NovAtel, *IMU Errors and Their Effects,* NovAtel, 2014.

[23] G. A. Quinchia, G. Falco, E. Falletti, F. Dovis and C. Ferrer, "A Comparison between Different Error Modeling of MEMS Applied to GPS/INS Integrated Systems," *Sensors,* vol. 13, no. 8, pp. 9549-88, 2013.

[24] NOAA, "International Geomagnetic Reference Field," NOAA, 19 December 2019. [Online]. Available: https://www.ngdc.noaa.gov/IAGA/vmod/igrf.html. [Accessed 27 4 2020].

[25] NOAA, "The World Magnetic Model," NOAA, 10 12 2019. [Online]. Available: https://www.ngdc.noaa.gov/geomag/WMM/. [Accessed 27 4 2020].

[26] D. Simon, Optimal State Estimation, Hoboken: John Wiley & Sons, 2006.

[27] Yole Developpement, "High-end Gyroscopes, Accelerometers and IMUs for Defense, Aerospace & Industrial," Yole Developpement, 2015.

[28] C. Hajiyev and H. E. Soken, State Estimation and Control for Low-cost Unmanned Aerial Vehicles, New York: Springer, 2015.

[29] D. Martinez, J. M. Quero, J. Garcia, L. Leon, P. Castro and C. Nieto, "Attitude determination module for CubeSat," in *2015 IEEE International Conference on Industrial Technology (ICIT)*, Seville, 2015.

[30] A. Cortiella, D. Vidal, J. Jane, E. Juan, R. Olive, A. Amezaga, J. F. Munoz, P. V. Hugo Carreno-Luengo and A. Camps, "CAT-2: Attitude Determination and Control System for a GNSS-R Earth Observation 6U

CubeSat Mission," *European Journal of Remote Sensing,* vol. 49, no. 1, pp. 759-776, 2017.

[31] C. Hajiyev, D. Cilden and Y. Somov, "Gyro-free attitude and rate estimation for a small satellite using SVD and EKF," *Aerospace Science and Technology,* vol. 55, pp. 324-331, 2016.

[32] C. Hajiyev and D. C. Guler, "Review on gyroless attitude determination methods for small satellites," *Progress in Aerospace Sciences,* vol. 90, pp. 54-66, 2017.

[33] L. Baroni, "Kalman filter for attitude determination of a CubeSat using low-cost sensors," *Computational and Applied Mathematics,* vol. 37, no. 1, pp. 72-83, 2018.

[34] D. Y. Lee, H. Park, M. Romano and J. Cutler, "Development and experimental validation of a multi-algorithmic hybrid attitude determination and control system for a small satellite," *Aerospace Science and Technology,* vol. 78, pp. 494-509, 2018.

[35] V. Carrara, R. B. Januzi, D. H. Makita, L. F. d. P. Santos and L. S. Sato, "The ITASAT CubeSat Development and Design," *Journal of Aerospace Technology and Management,* vol. 9, no. 2, pp. 147-156, 2017.

[36] A. C. Chiella, B. O. Teixeira and G. A. Pereira, "Quaternion-Based Robust Attitude Estimation Using an Adaptive Unscented Kalman Filter," *Sensors,* vol. 19, no. 10, 2019.

[37] S. K. Biswas, B. Southwell and A. G. Dempster, "Performance analysis of Fast Unscented Kalman Filters for Attitude Determination," *IFAC-PapersOnLine,* vol. 51, no. 1, pp. 697-701, 2018.

[38] J. Wang, R. Zhang, J. Yuan and J. Luo, "Multi-CubeSat Relative Position and Attitude Determination Based on Array Signal Detection in Formation Flying," *IEEE Transactions on Aerospace and Electronic Systems ,* vol. 55, no. 6, pp. 3378-3393, 2019.

[39] F. Santoni, P. Seitzer, T. Cardona, G. Locatelli, N. Marmo, S. Masillo, D. Morfei and F. Piergentili, "Optical tracking and orbit determination performance of self-illuminated small spacecraft: LEDSAT (LED-based SATellite)," *Advances in Space Research,* vol. 62, no. 12, pp. 3318-3334, 2018.

[40] T. M. Roberts, K. A. Lynch, R. E. Clayton, M. E. Disbrow and C. J. Hansen, "Magnetometer-Based Attitude Determination for Deployed Spin-Stabilized Spacecraft," *Journal of Guidance, Control, and Dynamics,* vol. 40, no. 11, pp. 2940-2946, 2017.

[41] V. L. Bageshwar, D. Gebre-Egziabher and W. L. Garrard, "Inertially-Aided Vector Matching Algorithm for Attitude Determination of Spin Stabilized Satellites," in *AIAA Guidance, Navigation and Control Conference and Exhibit*, Honolulu, 2008.

[42] D. Gebre-Egziabher, G. H. Elkaim, J. D. Powell and B. W. Parkinson, "A gyro-free quaternion-based attitude determination system suitable for implementation using low cost sensors," in *IEEE 2000 Position Location and Navigation Symposium*, 2000.

[43] D. Gebre-Egziabher, G. H. Elkaim, J. D. Powell and B. W. Parkinson, "Calibration of Strapdown Magnetometers in the Magnetic Field Domain," *Journal of Aerospace Engineering,* vol. 19, no. 2, pp. 87-102, 2006.

[44] A. B. Younes and D. Mortari, "Derivation of All Attitude Error Governing Equations for Attitude Filtering and Control," *Sensors,* 28 October 2019.

[45] D. Simon and D. Simon, "Aircraft Turbofan Engine Health Estimation Using Constrained Kalman Filtering," NASA Glenn Research Center, Atlanta, 2003.

[46] L. D. Le, *Constraint-Based Networked Inertial Navigation, Dissertation,* Minneapolis: University of Minnesota - Twin Cities, 2018.

[47] V. L. Bageshwar, D. Gebre-Egziabher, W. L. Garrard and T. T. Georgiou, "Stochastic Observability Test for Discrete-Time Kalman Filters," *Journal of Guidance, Control, and Dynamics,* vol. 32, no. 4, pp. 1356-1370, 2009.

[48] J. B. Schleppe, *Development of a Real-Time Attitude System Using a Quaternion Parameterization and Non-Dedicated GPS Receivers , Thesis,* Calgary: University of Calgary, 1996.

[49] S. Winkler and F. Schiemenz, "On-Board Real-Time Gyro Calibration for Fast High-Precision Repointing Spacecraft: Challenges and Solutions," in *ESA GNC*, Salzburg, 2017.

[50] T. Kukowski, *Attitude Control Development for a 3U CubeSat, Thesis,* Minneapolis: University of Minnesota, 2019.

[51] Z. Zhen, X. Jianping and J. Jin, "On-Orbit Real-Time Magnetometer Bias Determination for Micro-Satellites Without Attitude Information," *Chinese Journal of Aeronautics,* vol. 28, no. 5, pp. 1503-1509, 2015.

[52] R. Alonso and M. D. Shuster, "A new algorithm for attitude-independent magnetometer calibration," in *NASA Goddard Space Flight Center, Flight Mechanics (Estimation Theory Symposium, 1994)*, Greenbelt, 1994.

[53] E. Delgado and A. Barreiro, "Discrete-time EKF convergence analysis. Application to sonar navigation," *IFAC Proceedings Volumes,* vol. 37, no. 8, pp. 334-339, 2004.

[54] O. Gonzales and A. Rosales, "Robust MPS Tuning by Quadratic Weights Online Estimation of the Cost Function through Extended Kalman Filter," in *2018 International Conference on Information Systems and Computer Science*, 2018.

[55] Analog Devices, "ADIS16488A," [Online]. Available: https://www.analog.com/en/products/adis16488a.html#product-overview. [Accessed 27 4 2020].

[56] T. Delabie, B. Vandoren, W. De Munter, G. Raskin, B. Vandenbussche and D. Vandepitte, "Testing and Calibrating an Advanced CubeSat Attitude

Determination and Control System," in *Space Telescopes and Instrumentation 2018: Optical, Infrared, and Millimeter Wave*, 2018.

[57] L. Chuanjun, L. Jiang and W. Long, "Magnetometer-Based Attitude Determination for Spinning Flight Vehicles," in *2015 8th International Conference on Intelligent Computation Technology and Automation (ICICTA)*, Nanchang, 2015.

[58] J. A. Larsen and K. Vinther, "Inexpensive CubeSat attitude estimation using COTS components and Unscented Kalman Filtering," in *Proceedings of 5th International Conference on Recent Advances in Space Technologies - RAST2011*, 2011.

Appendix A

Noise and Random Variables

It may seem as though the AD problem has been solved; all we need is to measure the angular rates in the body frame (commonly done with a rate gyroscope in an IMU) and the numerically integrate Equations (2.23) or (2.25) over time to obtain the attitude throughout the mission. However, there is one major challenge: no measurement is perfect (i.e. without noise). Sensor noise causes the solutions obtained by integration of Equations (2.23) or (2.25) to be erroneous. In Appendix A, we describe how noise within a system is characterized. As a note, much of the resulting discussion is adapted from Chapter 2 of [26].

A.1 Random Variables

Noise is often considered to be a continuous random variable (RV). An RV, as defined by [26], is a mapping from a set of experimental outcomes to a set of real numbers. An example of an RV is the roll of a die. The roll of the die can take the value of any number in the range of 1 through 6, and the process of rolling the die is an RV. The outcome of the roll of the die is known as a realization of the RV and is certain. Additionally, the chance that a realization of a RV will be equivalent to some value in the designated range is known as the probability. For example, the probability that a roll of a dice will result in 2 is 1/6, meaning there is a 1 out of 6 chance that the die will land on 2.

A.2 Probability Distribution Function (PDF)

Consider an RV, X. An RV X has the property of a probability distribution function (PDF) given by $F_X(X)$ and is defined as

$$F_X(X) = P(X \leq x) \tag{A.1}$$

where $P(X \leq x)$ is the probability that a realization of X will be less than or equivalent to a constant non-random value x. The PDF itself provides the probabilities of all different outcomes of a given experiment.

A.3 Probability Density Function (pdf)

The derivative of Equation (A.1) with respect to x is known as the probability density function (pdf), which specifies the likelihood a realization of X will be equivalent to x and is given by

$$f_X(x) = \frac{dF_X(x)}{dx} \tag{A.2}$$

Based on this definition, useful properties of the pdf can be defined. Namely, the pdf is always larger or equivalent to 0, the integral of the pdf from $-\infty$ to ∞ is equivalent to 1, and the probability of a value x being within the range $[a, b]$ is given by the integral of the pdf from a to b. These properties are defined mathematically below as

$$f_X(x) \geq 0 \tag{A.3a}$$

$$\int_{-\infty}^{\infty} f_X(x)dx = 1 \tag{A.3b}$$

$$P(a < x \leq b) = \int_a^b f_X(x)dx \tag{A.3c}$$

The definitions provided by Equation (A.3) allows a useful interpretation; The probability that a constant value x will be an outcome of an experiment over all possible values from $-\infty$ to ∞ is 1 or 100% probable. Given a pdf for a certain random process, the probabilities of certain outcomes of the process can be easily determined.

A.4 Expected Value

The expected value of an RV X can be defined as the average outcome over many experiments. This is also known as the mean or average of the RV. The expected value is defined as

$$E\{X\} = \boldsymbol{X} = \frac{1}{number\ of\ outcomes} * (sum\ of\ all\ outcomes) \qquad (A.4)$$

where $\boldsymbol{X}$ is another definition for the mean. The expectation can also be described for functions of random variables. Consider the function of a random variable $g(X)$. The expectation of this can be given as

$$E\{g(X)\} = \int_{-\infty}^{\infty} g(X) f_X(x) dx \qquad (A.5)$$

where $f_X(x)$ is the pdf of X.

A.5 Variance and Covariance

The variance of an RV is a measure of how much an RV is expected to vary from its mean, which in turn is a measure of how uncertain an RV is. Typically, a lower variance implies realizations of the RV will be closer to its mean or expected value. The variance is given as

$$\sigma_X^2 = E\{(X - \boldsymbol{X})^2\}$$

$$= \int_{-\infty}^{\infty} (X - \boldsymbol{X})^2 f_X(x) dx \qquad (A.6)$$

where σ_X^2 is the variance of the RV X and $\boldsymbol{X}$ is the mean of the RV X.

For a vector of multiple random variables denoted as $\bar{X} = [X_1\ X_2\ \dots X_n]^T$, the variance of each RV within $\bar{X}$ is placed in a covariance matrix, R, defined as

$$R = E\{(\bar{X} - \bar{\boldsymbol{X}})(\bar{X} - \bar{\boldsymbol{X}})^T\}$$

$$= \int_{-\infty}^{\infty} (\bar{X} - \bar{\boldsymbol{X}})(\bar{X} - \bar{\boldsymbol{X}})^T f_{\bar{X}}(x) dx$$

$$= \begin{bmatrix} \sigma_{11}^2 & \cdots & \sigma_{1n}^2 \\ \vdots & \ddots & \vdots \\ \sigma_{n1}^2 & \cdots & \sigma_{nn}^2 \end{bmatrix} \tag{A.7}$$

where $\bar{\boldsymbol{X}} = [\bar{\boldsymbol{X}}_1 \, \bar{\boldsymbol{X}}_2 \ldots \bar{\boldsymbol{X}}_n]^T$ denotes the vector containing the mean of each RV. The matrix R will contain the variance of each individual RV within its diagonals and correlated variances between each RV within $\bar{X}$ given by σ_{ij}^2 in the off diagonals. If the RVs within the RV vector $\bar{X}$ are independent [26], then the off-diagonal variances in R will go to zero such that

$$R = \begin{bmatrix} \sigma_{11}^2 & \cdots & 0 \\ \vdots & \ddots & \vdots \\ 0 & \cdots & \sigma_{nn}^2 \end{bmatrix} \tag{A.8}$$

The covariance matrix is a positive semidefinite matrix.

A.6 Standard Deviation

The standard deviation of an RV X is given by σ_X and is the square root of the variance σ_X^2. In general, we use the notation of

$$X \sim (\boldsymbol{X}, \sigma_X^2) \tag{A.9}$$

to indicate that X is a RV with a mean denoted by $\boldsymbol{X}$ and variance given by σ_X^2.

A.7 Gaussian/Normal RVs

If the pdf of an RV can be described by the function

$$f_X(x) = \frac{1}{\sigma_X \sqrt{2\pi}} \exp\left[-\frac{(x - \boldsymbol{X})^2}{2\sigma_X^2} \right] \tag{A.10}$$

then it is said to be a Gaussian or Normal RV. This is notated by

$$X \sim N(\boldsymbol{X}, \sigma_X^2) \tag{A.11}$$

which is similar to Equation (A.9). The pdf of a Gaussian or normal RV is known as a "bell curve" and is shown in Figure A.1. This figure is the pdf of a Gaussian RV with mean of $\boldsymbol{X} = 0$ and $\sigma_X^2 = 1$.

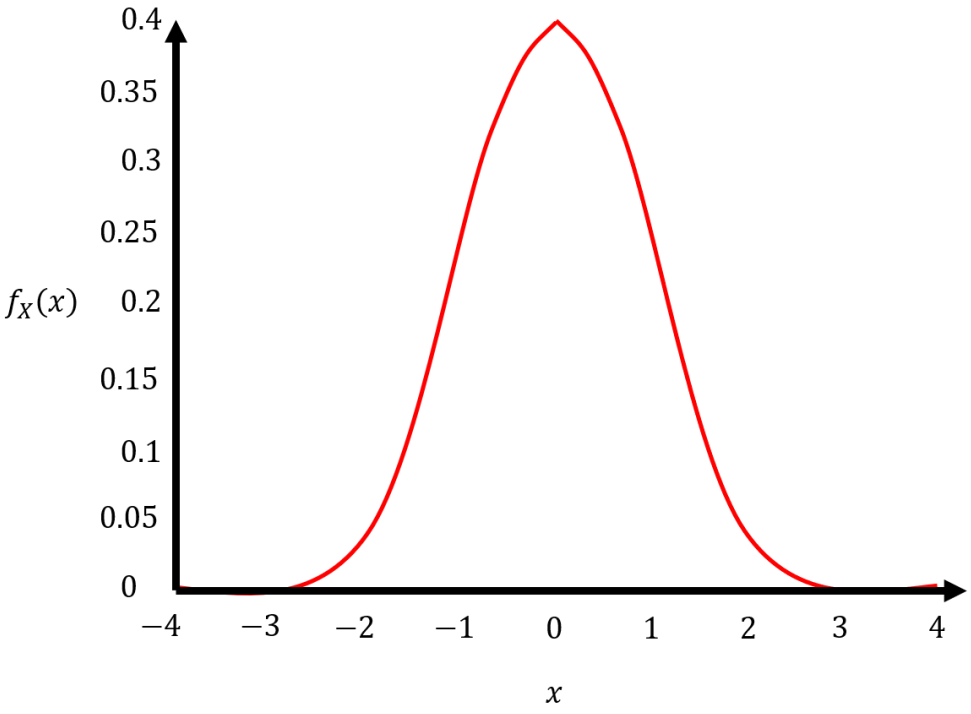

Figure A.1 Gaussian distribution of RV X.

A.8 Stochastic Processes and White Noise

A stochastic or random process is a RV $X(t)$ that is a function of time. The definitions found in the prior parts of this section can also be extended to stochastic processes, with the PDF, pdf, expectation, and covariance now being functions of time.

If it is assumed that an RV $X(t_1)$ is independent from the RV $X(t_2)$ for all $t_1 \neq t_2$, then the stochastic process $X(t)$ is called white noise. While it is possible that the stochastic process is correlated throughout time (known as colored noise),

we will restrict discussion to white noise. For further description of these phenomenon, see Chapter 2 of [26].

Throughout this thesis, the term "noise" will be used frequently. Unless otherwise stated, we assume any noise discussed will be Gaussian white noise as defined by Equation (A.11). Moreover, we assume the noise is a stochastic process with zero-mean and variance denoted by σ^2. Additional notation will be applied based upon what sensor or system noise is attributed to.

Appendix B

Kalman Filtering

B.1 The Kalman Filter (KF)

The system that the KF operates on can be broken up into two components: a dynamic "time-update" model that encompasses how the dynamics of the system change throughout time, and a measurement model that encompasses how a sensor measures the states of interest. The noise within the system can be modelled as some process noise that is attributed to inaccuracies within the dynamic model, and some measurement noise attributed to noise found in the sensors. Given these models and characteristics on the noise, the goal of the KF is to determine an estimate of the state vector $\hat{\bar{x}}_k$ at each timestep.

Suppose a linear discrete-time system in state space form is given as

$$\bar{x}_k = F_{k-1}\bar{x}_{k-1} + L_{k-1}\bar{u}_{k-1} + \bar{w}_{k-1} \tag{B.1a}$$

$$\bar{y}_k = H_k\bar{x}_k + \bar{v}_k \tag{B.1b}$$

where $\bar{x}_k$ and $\bar{y}_k$ are the $n \times 1$ state vector and $n \times 1$ measurement of the state vector at timestep k, respectively. Additionally, $\bar{x}_{k-1}$ is the state vector at timestep $k-1$, $\bar{u}_{k-1}$ is the vector of inputs to the system at $k-1$, w_{k-1} is the noise associated with the dynamic process of $\bar{x}_k$ at $k-1$, F_{k-1} and L_{k-1} are the discrete time state space matrices that map the state and the inputs at timestep $k-1$ to time k, respectively, H_k is the measurement matrix that maps the state vector at time k to a measurement made at time k, and $\bar{v}_k$ is the measurement noise associated with the measurement process. As the filter will be ultimately

implemented on hardware, a discrete time system is used as opposed to a continuous time system.

The discrete equations of Equation (B.1) break the system into the dynamics and measurement components, respectively. However, the noise vectors $\bar{w}_{k-1}$ and $\bar{v}_{k-1}$ are generally unknown. Fortunately, the characteristics of the noise can be assumed based upon discussion seen in Appendix A. Assume that both noise vectors can be modeled as stochastic processes such that

$$\bar{w}_k \sim (0, Q_k) \tag{B.2a}$$

$$Q_k = E\{\bar{w}_k \bar{w}_k^T\} \tag{B.2b}$$

$$\bar{v}_k \sim (0, R_k) \tag{B.2c}$$

$$R_k = E\{\bar{v}_k \bar{v}_k^T\} \tag{B.2d}$$

$$E\{\bar{v}_k \bar{w}_k^T\} = 0 \tag{B.2e}$$

where Q_k and R_k are the $n \times n$ covariance matrices attributed to the process and measurement noise, respectively.

Knowing the information contained in Equations (B.1) and (B.2), the KF utilizes a weighted linear least squares approach [26] to obtain an optimal estimate of the state vector such that

$$\hat{\bar{x}}_k = E\{\bar{x}_k\} = \bar{\boldsymbol{x}}_{\boldsymbol{k}} \tag{B.3}$$

where $\hat{\bar{x}}_k$ is the KF optimal estimate and is equivalent to the mean of the state vector. Different filtering techniques can have different definitions for optimal. It

will be assumed that any further discussion of "optimal" will refer to the definition of Equation (B.3).

This estimate can be split into two different types: *a priori* and *a posteriori*. The *a priori* estimate is defined as

$$\hat{\bar{x}}_k^- = E\{\bar{x}_k | \bar{y}_1, \bar{y}_2, \dots, \bar{y}_{k-1}\} \tag{B.4}$$

where the "-" sign in the superscript implies that the estimate was conditioned on all measurements before, but not including, time k. The *a posteriori* estimate is defined by

$$\hat{\bar{x}}_k^+ = E\{\bar{x}_k | \bar{y}_1, \bar{y}_2, \dots, \bar{y}_k\} \tag{B.5}$$

where the "+" sign in the superscript implies that the estimate was conditioned on all measurements up to the current time k.

Both $\hat{\bar{x}}_k^-$ and $\hat{\bar{x}}_k^+$ are estimates of the same quantity, but are dependent on if the estimate was formed by a propagating the state dynamics ($\hat{\bar{x}}_k^-$) or by using a sensor measurement ($\hat{\bar{x}}_k^+$). Generally, the time update portion of the KF will calculate a less accurate *a priori* estimate of the state, where measurement updates will calculate a more accurate *a posteriori* estimate. This is on the assumption that the noise content of measurement sensors is less than that of the dynamic process of the system. The general structure of the KF is discussed below.

B.2 KF Initialization

We assume that we have access to some initial state vector, $\bar{x}_0^+$, and initial state covariance, P_0^+, at $k = 0$. While no measurements have yet occurred, we assume that the initial estimate and covariance are as accurate as possible and are

a posteriori, hence the "+" superscript. Thus, the initial *a posteriori* state estimate and covariance are given by

$$\hat{\bar{x}}_0^+ = E\{\bar{x}_0\} \tag{B.6a}$$

$$P_0^+ = E\{(\bar{x}_0 - \hat{\bar{x}}_0^+)(\bar{x}_0 - \hat{\bar{x}}_0^+)^T\} \tag{B.6b}$$

where the covariance is on the estimation error between the estimate $\hat{\bar{x}}_0^+$ and the truth state $\bar{x}_0$. Note that the placement of $\hat{\bar{x}}_0^+$ in Equation (B.6b) implies that we assume our initial estimate is equivalent to the mean of the state vector such that $\hat{\bar{x}}_0^+ = \bar{\boldsymbol{x}}_{\boldsymbol{0}}$. In the KF, the covariance is directly used as a metric to quantify the estimation error.

B.3 KF Time Update

The time update portion of the KF propagates the state estimate and covariance using the dynamic model for the system. The state evolution of the estimate can be determined by taking the expected value of the true state evolution given by Equation (B.1a) such that

$$\hat{\bar{x}}_1^- = E\{\bar{x}_1\} = E\{F_0\bar{x}_0 + L_0\bar{u}_0 + \bar{w}_0\}$$

$$= E\{F_0\bar{x}_0\} + E\{L_0\bar{u}_0\} + E\{\bar{w}_0\}$$

$$\hat{\bar{x}}_1^- = F_0\hat{\bar{x}}_0^+ + L_0\bar{u}_0 \tag{B.7}$$

where $E\{\bar{w}_0\} = 0$ as it is assumed to be zero-mean. Note that the input vector $\bar{u}_0$ is not an estimate as it is assumed that we always know the inputs to system. The covariance can be propagated by substituting Equation (B.1a) evaluated at $k = 0$ into Equation (B.6) and taking the expected value

$$P_1^- = E\{(\bar{x}_1 - \hat{\bar{x}}_1^-)(\bar{x}_1 - \hat{\bar{x}}_1^-)^T\}$$

$$= E\{(F_0\bar{x}_0 + L_0\bar{u}_0 - \bar{w}_0 - F_0\hat{\bar{x}}_0^+ - L_0\bar{u}_0)(F_0\bar{x}_0 + L_0\bar{u}_0 - \bar{w}_0 - F_0\hat{\bar{x}}_0^+ - L_0\bar{u}_0)^T\}$$

$$= E\{(F_0(\bar{x}_0 - \hat{\bar{x}}_0^+) - \bar{w}_0)(F_0(\bar{x}_0 - \hat{\bar{x}}_0^+) - \bar{w}_0)^T\}$$

$$= E\{F_0(\bar{x}_0 - \hat{\bar{x}}_0^+)(\bar{x}_0 - \hat{\bar{x}}_0^+)^T F_0^T + \bar{w}_0\bar{w}_0^T + F_0(\bar{x}_0 - \hat{\bar{x}}_0^+)\bar{w}_0^T + \bar{w}_0(\bar{x}_0 - \hat{\bar{x}}_0^+)F_0^T$$

$$= E\{F_0(\bar{x}_0 - \hat{\bar{x}}_0^+)(\bar{x}_0 - \hat{\bar{x}}_0^+)^T F_0^T\} + E\{\bar{w}_0\bar{w}_0^T\}$$

$$P_1^- = F_0 P_0^+ F_0^T + Q_0 \qquad (B.8)$$

Where the covariance updates as a function of the process noise at the previous timestep Q_0 and the mapping matrix F_0. While Equations (B.7) and (B.8) are specific for the first time update, they can be extended to include all time updates such that

$$\hat{\bar{x}}_k^- = F_{k-1}\hat{\bar{x}}_{k-1}^- + L_{k-1}\bar{u}_{k-1} \qquad (B.9)$$

$$P_k^- = F_{k-1}P_{k-1}^- F_{k-1}^T + Q_k \qquad (B.10)$$

where $\hat{\bar{x}}_k^-$ and P_k^- are the *a priori* state estimate and state covariance. Note that the prior estimate is no longer *a posteriori* and it is assumed that multiple time updates have occurred since the last measurement update.

B.4 KF Measurement Update

The measurements are incorporated by utilizing a recursive least squares approach. Consider a measurement that occurs immediately after the time updates given by Equations (B.7) and (B.8) at $k = 1$ such that

$$\bar{y}_1 = H_1\bar{x}_1 + \bar{v}_1 \qquad (B.11)$$

Where $\bar{y}_1$ is the measurement at $k = 1$. Note that while we may know the measurement matrix H_1, we do not know the true state $\bar{x}_1$ nor the noise vector $\bar{v}_1$. A Kalman gain K_1, is then calculated by

$$K_1 = P_1^- H_1^T (H_1 P_1^- H_1^T + R_1)^{-1} \tag{B.12}$$

where P_1^- is the *a priori* covariance update seen in Equation (B.8) and R_1 is the measurement noise covariance matrix for the given measurement. The state estimate and covariance are updated to create the *a posteriori* values via

$$\hat{\bar{x}}_1^+ = \hat{\bar{x}}_1^- + K_1(\bar{y}_1 - H_1 \hat{\bar{x}}_1^-) \tag{B.13}$$

$$P_1^+ = (1_n - K_1 H_1) P_1^- \tag{B.14}$$

where 1_n is the $n \times n$ identity matrix. Extending Equations (B.12) - (B.14) through all time, we have

$$K_k = P_k^- H_k^T (H_k P_k^- H_k^T + R_k)^{-1} \tag{B.15}$$

$$\hat{\bar{x}}_k^+ = \hat{\bar{x}}_k^- + K_k(\bar{y}_k - H_k \hat{\bar{x}}_k^-) \tag{B.16}$$

$$P_k^+ = (1_n - K_k H_k) P_k^- \tag{B.17}$$

At this point, the *a priori* state estimate has been "corrected" by the measurement update via the Kalman gain. Generally, the KF decides how much weight to place on the measurement by looking at the measurement covariance matrix R_1. For example, if R_1 is large, the value of K_1 will be small (by inspection of Equation (B.13)), and the measurement will not change the *a priori* estimate $\hat{\bar{x}}_1^-$ by much. Conversely, if R_1 is small, then K_1 will be large and the measurement will "correct" the *a priori* estimate by a noticeable amount. It is this phenomenon that highlights

the value of the KF, as it weights the measurement and dynamics against each other continuously based upon the covariances Q_k and R_k.

B.5 KF "Timeline"

The KF equations are summarized here for clarity.

Time Update:

$$\hat{\bar{x}}_k^- = F_{k-1}\hat{\bar{x}}_{k-1}^- + L_{k-1}\bar{u}_{k-1} \tag{B.9}$$

$$P_k^- = F_{k-1}P_{k-1}^- F_{k-1}^T + Q_k \tag{B.10}$$

Measurement Update:

$$K_k = P_k^- H_k^T (H_k P_k^- H_k^T + R_k)^{-1} \tag{B.15}$$

$$\hat{\bar{x}}_k^+ = \hat{\bar{x}}_k^- + K_k(\bar{y}_k - H_k\hat{\bar{x}}_k^-) \tag{B.16}$$

$$P_k^+ = (1_n - K_k H_k)P_k^- \tag{B.17}$$

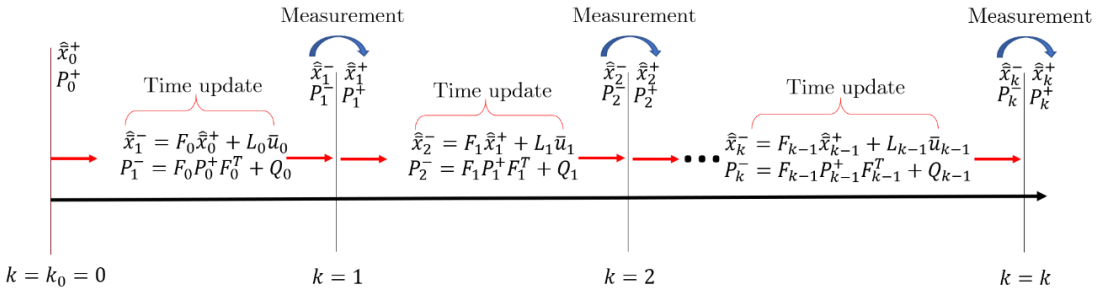

Figure B.1 KF timeline.

In general, there can be multiple time updates that occur before a measurement update does. The frequency of the time updates and the measurement

updates is dependent on the problem and the sensors used. A KF "timeline" detailing the KF algorithm as it propagates the state and covariance through time with one measurement update per time update is given by Figure B.1.

B.6 The Extended Kalman Filter (EKF)

While the KF is an extremely useful tool, it has made some assumptions about the linearity of the system. Namely, the KF assumes that a linear state space representation can be formed as seen in Equation (B.1), and that the stochastic noise of the system maintains its form as it is propagated through the time and measurement update equations. While these assumptions hold for some systems, there are arguably more systems in which these assumptions are invalid.

Consider the simple, scalar, discrete time non-linear system denoted by the following

$$x_k = x_{k-1}^2 + w_{k-1} = f(x_{k-1}, w_{k-1}) \qquad (B.18a)$$

$$y_k = h(x_{k-1}, v_{k-1}) \qquad (B.18b)$$

$$w_k \sim N(0, \sigma_w^2) \qquad (B.18c)$$

$$v_k \sim N(0, \sigma_v^2) \qquad (B.18d)$$

where x_k is the scalar state, y_k is the scalar measurement of the state, w_{k-1} is the stochastic process noise attributed to the dynamics, and v_{k-1} is the stochastic process noise attributed to the measurement itself. It is assumed that the noise of the system is gaussian with zero mean and variances given by σ_w^2 and σ_v^2.

Now, consider the gaussian process noise of w_k. In the instance of the KF, the process noise is updated by passing the pdf of the noise through the linear state dynamics of the system. The output of this is another gaussian pdf. However, a

gaussian pdf input into non-linear state dynamics *will not* result in another gaussian pdf being output. Figure B.2 highlights this phenomenon, with the left plot resembling linear system dynamics denoted by F_k and the right plot resembling non-linear dynamics modeled by $f(x_{k-1}, w_{k-1})$. As seen on the left, the resultant pdf is still gaussian with some new mean denoted by the black dashed line. However, on the right plot, the non-linear dynamics have now changed the pdf to no longer be gaussian and have caused the estimated mean to longer be the truth. It is this phenomenon that highlights that the KF must be modified.

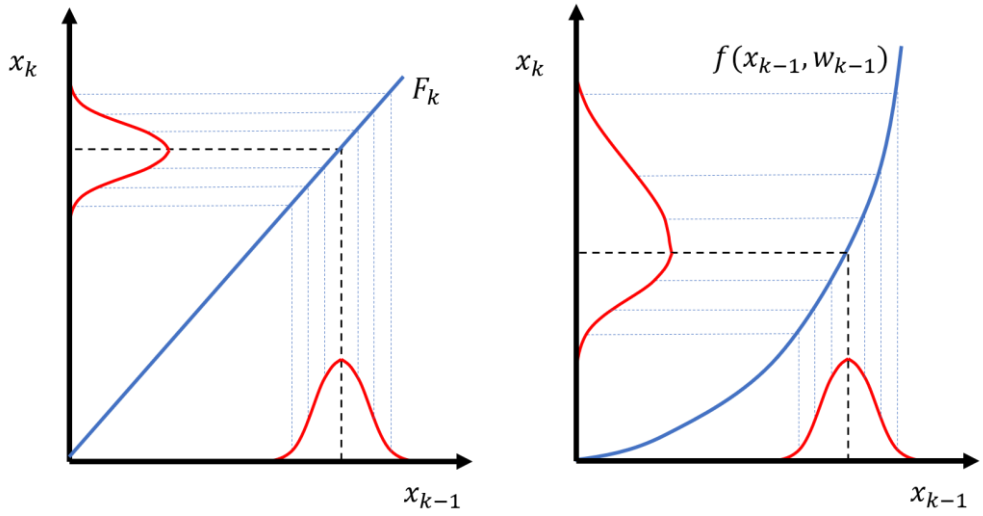

Figure B.2 A pdf propagated through a linear system (left) vs. nonlinear system (right).

Enter the extended Kalman filter (EKF). The EKF handles the non-linear system dynamics by linearizing the state dynamics about a nominal state trajectory or operating condition. Generally, this nominal state trajectory is unknown, but the EKF uses its own estimate as the nominal state trajectory. Specifically, the EKF linearizes the non-linear system about its *previous* estimate at each time step.

The linearization is a Taylor series expansion about the state estimate as time goes on and is elaborated on below.

Let the true, non-linear, discrete time state dynamics be modeled by

$$\bar{x}_k = f_{k-1}(\bar{x}_{k-1}, \bar{u}_{k-1}, \bar{w}_{k-1}) \tag{B.19a}$$

$$\bar{y}_k = h_k(\bar{x}_k, \bar{v}_k) \tag{B.19b}$$

$$\bar{w}_k \sim (0, Q_k) \tag{B.19c}$$

$$\bar{v}_k \sim (0, R_k) \tag{B.19d}$$

where $f_{k-1}(.)$ and $h_k(.)$ are non-linear functions of the state and measurement dynamics. Like the KF definition, we assume the noise on the system is zero-mean with variance modeled by covariance matrices Q_k and R_k. A Taylor series expansion on Equation (B.19a) is performed around the operating condition of $\bar{x}_{k-1} = \hat{\bar{x}}_{k-1}^{+}$ and $\bar{w}_{k-1} = 0$ to obtain

$$\bar{x}_k = f_{k-1}(\hat{\bar{x}}_{k-1}, \bar{u}_{k-1}, 0) + \frac{\partial f_{k-1}}{\partial \bar{x}} \Big|_{\hat{\bar{x}}_{k-1}} (\bar{x}_{k-1} - \hat{\bar{x}}_{k-1}^{+}) + \frac{\partial f_{k-1}}{\partial \bar{w}} \Big|_{\hat{\bar{x}}_{k-1}} \bar{w}_{k-1}$$

$$= f_{k-1}(\hat{\bar{x}}_{k-1}, \bar{u}_{k-1}, 0) + F_{k-1}(\bar{x}_{k-1} - \hat{\bar{x}}_{k-1}^{+}) + L_{k-1}\bar{w}_{k-1}$$

$$= F_{k-1}\bar{x}_{k-1} + [f_{k-1}(\hat{\bar{x}}_{k-1}^{+}, \bar{u}_{k-1}, 0) - F_{k-1}\hat{\bar{x}}_{k-1}^{+}] + L_{k-1}\bar{w}_{k-1}$$

$$\bar{x}_k = F_{k-1}\bar{x}_{k-1} + \tilde{u}_{k-1} + \tilde{w}_{k-1} \tag{B.20}$$

where we have neglected 2nd order and higher terms in the assumption that they are small and negligible. Note that Equation (B.20) is very similar to the KF equation for the state dynamics given by Equation (B.1a). In the EKF instance, the state mapping matrices F_{k-1} and L_{k-1} are formed by computing the Jacobian of the non-linear state matrices with respect to the state and noise vectors at each

timestep. These matrices, along with the noise signal and known input signal are defined below as

$$F_{k-1} = \frac{\partial f_{k-1}}{\partial \bar{x}} \Big|_{\hat{\bar{x}}_{k-1}} \tag{B.21a}$$

$$L_{k-1} = \frac{\partial f_{k-1}}{\partial \bar{w}} \Big|_{\hat{\bar{x}}_{k-1}} \tag{B.21b}$$

$$\tilde{u}_k = f_k(\hat{\bar{x}}_k^+, \bar{u}_k 0) - F_k \hat{\bar{x}}_k^+ \tag{B.21c}$$

$$\tilde{w}_k \sim (0, L_k Q_k L_k^T) \tag{B.21d}$$

where the process noise covariance has now been modified by matrix L_k. The measurement equation is also linearized via Taylor series approximation around $\bar{x}_k = \hat{\bar{x}}_k^-$ and $\bar{v}_k = 0$

$$\bar{y}_k = h_k(\hat{\bar{x}}_k^-, 0) + \frac{\partial h_k}{\partial \bar{x}} \Big|_{\hat{\bar{x}}_k^-} (\bar{x}_k - \hat{\bar{x}}_k^-) + \frac{\partial h_k}{\partial \bar{v}} \Big|_{\hat{\bar{x}}_k^-} \bar{v}_k$$

$$= h_k(\hat{\bar{x}}_k, 0) + H_k(\bar{x}_k - \hat{\bar{x}}_k^-) + M_k \bar{v}_k$$

$$= H_k \bar{x}_k + [h_k(\hat{\bar{x}}_k^-, 0) - H_k \hat{\bar{x}}_k^-] + M_k \bar{v}_k$$

$$\bar{y}_k = H_k \bar{x}_k + \bar{z}_k + \tilde{v}_k \tag{B.22}$$

again neglecting 2nd order and higher terms. Similar to Equation (B.20), H_k and M_k are Jacobians computed at each timestep. These, along with the noise and known signal $\bar{z}_k$ are defined below as

$$H_k = \frac{\partial h_k}{\partial \bar{x}} \Big|_{\hat{\bar{x}}_k^-} \tag{B.23a}$$

$$M_k = \frac{\partial h_k}{\partial \bar{v}} \Big|_{\hat{\bar{x}}_k^-} \tag{B.23b}$$

$$\bar{z}_k = h_k(\hat{\bar{x}}_k^-, 0) - H_k \hat{\bar{x}}_k^- \tag{B.23c}$$

$$\bar{v}_k \sim (0, M_k R_k M_k^T) \tag{B.23d}$$

where the measurement noise covariance has now been modified by matrix M_k. Now, Equations (B.20) and (B.22) are linear state space realizations of Equation (B.19), which means that the KF formulation and equations can be used.

B.7 EKF Initialization

It is again assumed that we have access to some initial state vector, $\bar{x}_0$ and initial state covariance, P_0^+, at $k = 0$. The initial *a posteriori* state estimate and covariance are given by

$$\hat{\bar{x}}_0^+ = E\{\bar{x}_0\} \tag{B.6a}$$

$$P_0^+ = E\{(\bar{x}_0 - \hat{\bar{x}}_0^+)(\bar{x}_0 - \hat{\bar{x}}_0^+)^T\} \tag{B.6b}$$

which is the identical initialization to the KF.

B.8 EKF Time Update

At the time update, we update the state by pushing our estimate through the non-linear dynamics such that

$$\hat{\bar{x}}_k = f_{k-1}(\hat{\bar{x}}_{k-1}^-, \bar{u}_{k-1}, 0) \tag{B.24}$$

where it is assumed that the inputs to the system are known. This expression can be found similarly to how (2.50) was calculated. After the *a priori* state estimate has been determined, the partial derivative matrices F_{k-1} and L_{k-1} are computed such that

$$F_{k-1} = \frac{\partial f_{k-1}}{\partial \bar{x}} \Big|_{\hat{\bar{x}}_{k-1}^-} \tag{B.21a}$$

$$L_{k-1} = \frac{\partial f_{k-1}}{\partial \bar{w}} \Big|_{\hat{\bar{x}}_{k-1}^-} \tag{B.21b}$$

The $a\ priori$ covariance is computed by

$$P_k^- = F_{k-1}P_{k-1}^- F_{k-1}^T + L_{k-1}Q_{k-1}L_{k-1}^T \quad (B.25)$$

where it is assumed that multiple time updates have occurred since the last measurement update. If one measurement update occurs for every time update, the covariance in Equation (B.25) would be replaced by P_{k-1}^+.

B.9 EKF Measurement Update

The EKF measurement update begins by calculating the partial derivative matrices of Equation (B.23) such that

$$H_k = \frac{\partial h_k}{\partial \bar{x}} \Big|_{\hat{\bar{x}}_k^-} \quad (B.23a)$$

$$M_k = \frac{\partial h_k}{\partial \bar{v}} \Big|_{\hat{\bar{x}}_k^-} \quad (B.23b)$$

where the matrices are calculated based upon the *a priori* state estimate determined in Equation (B.24). The measurement update occurs by then calculating the Kalman gain, *a posteriori* state estimate, and updated covariance such that

$$K_k = P_k^- H_k^T (H_k P_k^- H_k^T + M_k R_k M_k^T)^{-1} \quad (B.26)$$

$$\hat{\bar{x}}_k^+ = \bar{x}_k^- + K_k[\bar{y}_k - h_k(\hat{\bar{x}}_k^-, 0)] \quad (B.27)$$

$$P_k^+ = (1_n - K_k H_k)P_k^- \quad (B.28)$$

where 1_n is the $n \times n$ identity matrix. As is seen by the time and measurement update equations, they are similar to the KF with slight modifications made to the noise covariance matrices of the system.

B.10 EKF "Timeline"

The EKF equations are summarized here for clarity.

Time Update:

$$F_{k-1} = \frac{\partial f_{k-1}}{\partial \bar{x}} \Big|_{\hat{\bar{x}}_{k-1}} \tag{B.21a}$$

$$L_{k-1} = \frac{\partial f_{k-1}}{\partial \bar{w}} \Big|_{\hat{\bar{x}}_{k-1}} \tag{B.21b}$$

$$\hat{\bar{x}}_k = f_{k-1}(\hat{\bar{x}}_{k-1}^-, \bar{u}_{k-1}, 0) \tag{B.24}$$

$$P_k^- = F_{k-1} P_{k-1}^- F_{k-1}^T + L_{k-1} Q_{k-1} L_{k-1}^T \tag{B.25}$$

Measurement Update:

$$H_k = \frac{\partial h_k}{\partial \bar{x}} \Big|_{\hat{\bar{x}}_k^-} \tag{B.23a}$$

$$M_k = \frac{\partial h_k}{\partial \bar{v}} \Big|_{\hat{\bar{x}}_k^-} \tag{B.23b}$$

$$K_k = P_k^- H_k^T (H_k P_k^- H_k^T + M_k R_k M_k^T)^{-1} \tag{B.26}$$

$$\hat{\bar{x}}_k^+ = \bar{x}_k^- + K_k[\bar{y}_k - h_k(\hat{\bar{x}}_k^-, 0)] \tag{B.27}$$

$$P_k^+ = (1_n - K_k H_k) P_k^- \tag{B.28}$$

Like the KF, there can be multiple time updates that occur before a measurement update does. The frequency of the time updates and the measurement updates is dependent on the problem and the sensors used. An EKF "timeline" detailing the EKF algorithm as it propagates the state and covariance through time with one measurement update per time update is given by Figure B.3.

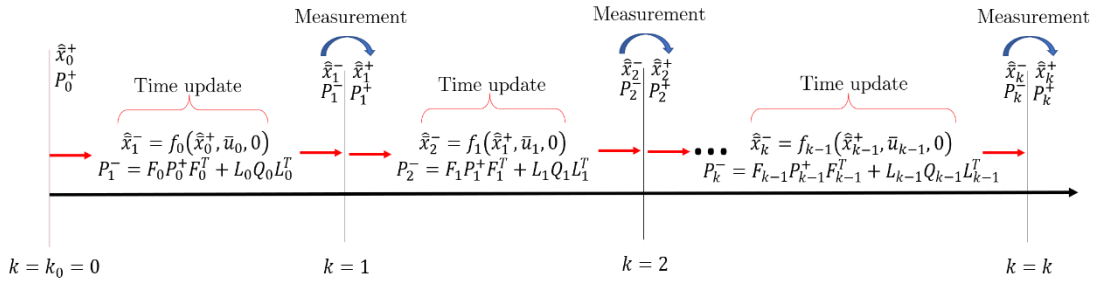

Figure B.3 EKF timeline.

B.11 Notes on the KF and EKF

Assuming that the goal of the KF and EKF is to minimize the error between the true state and the estimate, a few notable results are present.

- The KF is the best linear solution, assuming system noise is Gaussian, zero-mean, and white [26].
- If the system is observable, the KF has guaranteed convergence results.
- The EKF has wide applicability but is not necessarily the most optimal solution.
- EKF convergence is highly dependent on initial conditions (i.e. state covariance, noise).
    - EKF convergence is a highly researched topic [53] [54].
- The EKF is one type of non-linear estimator and may not be applicable depending on the problem (See UKFs, EnKFs).
- In some cases, noise is considered to be an input to the systems of Equations (B.1a) and (B.20). In these scenarios, the input vector $\bar{u}$ is replaced by the noise vectors of the system $\bar{n}$.

Appendix C

IMU/Gyro Specification Sheets & IMU Classification

Specific noise characteristics like those listed in Section 2.4.3 can be found within IMU specification sheets. However, in the experience of the author, reading IMU specification or "spec" sheets has proved challenging and frustrating at times, as there are no standards for what should and should not be reported. Additionally, the testing parameters used to determine gyro specifications are often lacking within the spec sheets themselves. To enlighten readers as to how to navigate these documents, this appendix will attempt to describe the common parameters found on spec sheets along with their general naming conventions. Section C.1 discusses how to read IMU spec sheets and how to obtain useful parameters. Section C.2 introduces the use of these parameters in the essence of filtering. Section C.3 briefly describes IMU grades. The types of noise listed within this appendix are also organized in Table C.1 for brevity. A general caveat is that this information is based off the experience of the author.

C.1 Reading IMU Spec Sheets

In general, spec sheets provide numerical values on the standard deviation (STD) of the important parameters. These are generally created by obtaining multiple, long-timescale, measurements of the sensor outputs and then performing statistical analysis on those measurements. As a rule of thumb, spec sheet parameters can be used in filter development and trade studies but should be determined experimentally by the user after hardware has been obtained.

Table C.1 Common Gyroscope Parameters

Parameter, STD	Units	Common Naming
sf, σ_{sf}	$\%, ppm$	Gyro Scale Factor, Scale Factor
b_0, σ_{b_0}	$°/s, °/hr$	Bias Repeatability, Null-shift, Turn-on Bias
b_1, σ_{b_1}	$°/hr$	In-Run Bias, Bias Stability, Gauss-Markov Noise
ARW, σ_{ARW}	$°/\sqrt{hr}$	Angle Random Walk, Random Walk
W, σ_g	$°/s\ rms$	Output noise, Wideband noise
N, σ_N	$°/sec/\sqrt{Hz}$	Noise Density, Rate Noise Density

Take for example the spec sheet for an Analog Devices ADIS16488A IMU given in [55]. Page 4 of the spec sheet includes specifications on the gyroscopes, accelerometers, and magnetometer found within the IMU itself, along with the testing conditions used in obtaining the values. Within the gyroscope section of Table 1, there are multiple parameters listed. While all of them are relevant, the primary ones for general AD filter design are the bias repeatability, the in-run bias stability, angular random walk (ARW), and output noise. Unfortunately, there is no value listed on scale factors. This parameter is typically lacking and must be determined by user calibration.

Both the bias repeatability and in-run bias stability values are listed as one standard deviation values (given as "1σ" in the second column of the spec sheet), with values of $\pm\ 0.2°/sec$ and $5.1°/hr$, respectively. This implies that the constant

turn-on bias is *repeatable* to within $\pm 0.2°/s$ and that the in-run bias will be $5.1°/hr$ approximately 66% of time. If the STD value listed was instead "2σ", then the constant turn-on bias is repeatable to within $\pm 0.2°/s$ and the in-run bias will be $5.1°/hr$ approximately 95% of the time. The sigma values essentially indicate a bound on the expected measurements. If no sigma value is listed along with the parameter, it is safe and conservative to assume it is a 1σ value.

C.2 Using Spec Sheet Information

Often, spec sheet information can be utilized within an AD simulation to help model the expected noise characteristics within a system. To effectively perform this modeling, the parameters seen within Table C.1 are typically required.

If the in-run bias is modeled as a 1st order Gauss-Markov process, a correlation time constant τ_{GM} will be required for accurate modeling. However, most specification sheets do not provide this value. In general, this value can be approximated based upon experience or can be calculated using autocorrelation techniques as seen in [23]. Additionally, a grouping of approximate τ_{GM} values is shown in Table C.3.

The ARW and output noise values are slightly more dubious, as they are sometimes used interchangeably. Some spec sheets will list one or the other, both, or neither. In the instance of neither being on a spec sheet, "Noise Density" will typically be the value that is closest in similarity, with units being $°/s/\sqrt{Hz}$. ARW typically has units of $°/\sqrt{hr}$, and output noise will have units of $°/sec\ rms$.

ARW is a measure of how much the sensor output randomly deviates throughout time and is representative of the expected white noise on a gyro output.

Similar to the bias, this value is often listed as a 1σ STD. This phenomenon is prevalent in all gyros and is a function of the gyro's internal sampling rate, which is why there are $\sqrt{hr}$ units attached to it. To make use of this value, the ARW term must be divided by 60 to place it into the units of $°/\sqrt{sec}$. Due to the nature of how the ARW term is obtained (see IEEE Std. 952-1997 C.1.1), the units of $°/\sqrt{sec}$ are actually equivalent to $°/sec$, allowing for the use of the ARW as the driving white noise term in filter design. In the experience of the Author, both the ARW metric (with proper unit conversions) and the output noise metric can be used to simulate white noise within the EKF system. However, the use of output noise can cause the covariance to overbound the estimates (as seen by the results of Chapter 5). For a more accurate and less noisy solution, the ARW metric should be used to drive the gyro white noise.

In general, all the parameters listed above can vary drastically with temperature. While this may not initially seem as a troublesome issue, it can have lasting effects on the AD system depending on the flight environment that the IMU will see (For example, Earth reentry vehicles). To this end, it is important to know the temperature range in which the bias values are accurately modeled. In the instance of the ADIS16488A, the temperature range is listed as $-40°C \leq T \leq 85°C$, meaning that the parameters listed within the spec sheet should be accurate for environmental temperatures within this operating range. Temperatures exceeding this range will need to be further tested and calibrated to determine their noise characteristics.

C.3 IMU Grades

IMUs can be classified in three groups: Consumer (industrial), tactical, and navigational grade IMUs [27]. Specifically, depending on the in-run bias stability, an IMU will fall into one of the three categories. This is shown in Table C.2, which shows that the gyroscope quality typically sought in CubeSat applications is given by consumer grade IMUs. Additional information on the typical noise characteristics for each grade (based on author experience), is given in Table C.3.

Table C.2 IMU Grades

Gyroscope Grade	Uses	Cost
Consumer	Small UAVs, CubeSats	$< \$2{,}000$
Tactical	Commercial UAVs, Robotics	$\$2{,}000 - \$100{,}000$
Navigational	Ships, Commercial Aircraft, Cruise Missiles	$\geq \$100{,}000$

Table C.3 Common IMU Parameter Values

Gyroscope Grade	ARW	In-Run Bias, τ_{GM}	Scale Factor
Consumer	$> 0.5\ °/\sqrt{hr}$	$> 10°/hr, 100\ s$	$5\% - 10\%$
Tactical	$0.2°/\sqrt{hr}\ - 0.05°/\sqrt{hr}$	$10°/hr - 0.1°/hr$, $300\ s$	$2\% - 5\%$
Navigational	$< 0.05\ °/\sqrt{hr}$	$< 0.1°/hr$, $1200\ s$	$< 2\%$

Appendix D

AD Testing Environment & Plan

To utilize the VMA developed in [41] and expanded upon within this thesis, additional hardware testing and validation must be performed. The goal of this appendix is to provide a baseline test plan for any implementation of the VMA on-board a CubeSat. Note that the testing of an active control system will not be discussed here.

Section D.1 will discuss the general requirements for testing an AD algorithm based on magnetic field measurements. Section D.2 will cover the objectives of specific VMA testing, with a brief discussion of testing facilities that meet these objectives. Section D.3 will provide an initial test plan format, with specific test cases and test expectations.

D.1 CubeSat AD Testing

To effectively test the AD on-board a CubeSat, the AD hardware must be placed in an environment that represents the orbital conditions (low friction, varying EMF vector) as accurately as possible. Additionally, the phenomena that the AD sensors measure must be accurately represented within the environment itself. In the case of the VMA, the phenomena required would be the local EMF vector as seen by the CubeSat and spacecraft rotational rates.

To simulate these phenomena, a Helmholtz cage and air bearing table can be used in union, as seen in Figure D.1 Diagram of Helmholtz cage & air bearing table.. A Helmholtz cage is a large structure that applies electric current through its structure to create a uniform magnetic field in a defined space, while the air bearing table is a low-friction platform used to apply kinematic rotation to the

vehicle. The coupling of these two devices can be used to emulate the CubeSat's kinematics and orbital environment. Specifically, the Helmholtz cage can be used to simulate the local EMF vector in an inertial frame $\boldsymbol{\mathcal{F}_E}$ seen by a CubeSat on-orbit, while the air bearing simulates the rotational rates $\bar{\omega}^{SE}$ of the CubeSat itself.

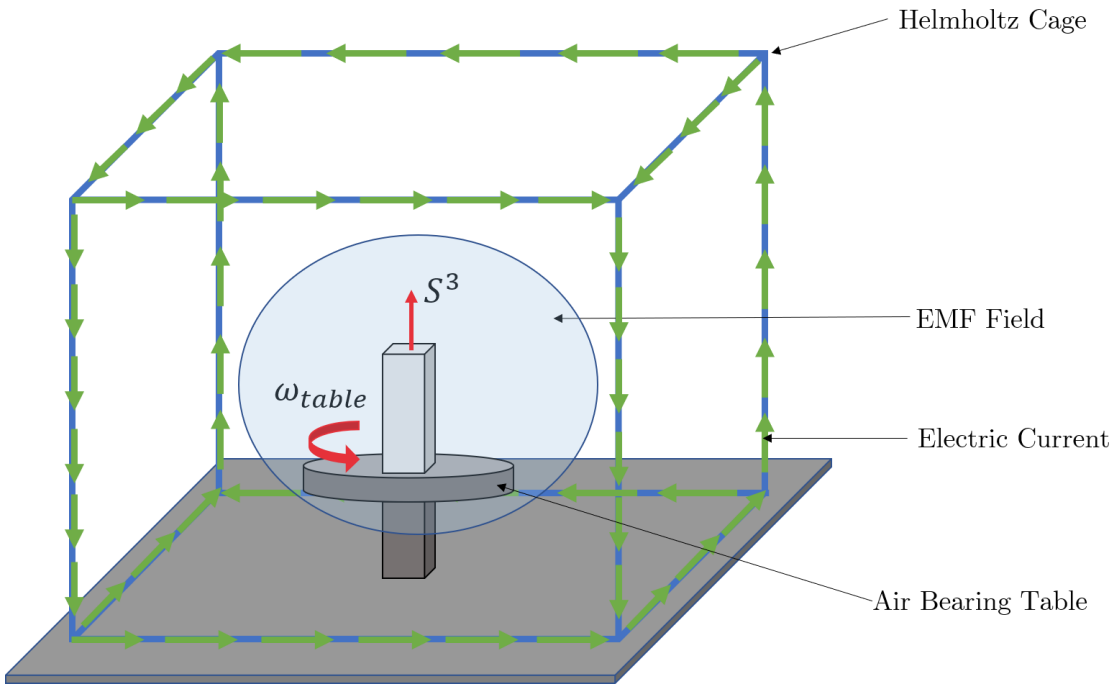

Figure D.1 Diagram of Helmholtz cage & air bearing table.

While the use of both a Helmholtz cage and air bearing table provide an adequate testing environment, there are limitations with respect to vehicle kinematics. For example, only rotations about a single axis are handled by the air bearing table. Moreover, air bearing tables do not negate any aerodynamic friction seen by the vehicle while rotating. In practice, AD tests utilizing this setup typically verify single-axis rotational dynamics by aligning the CubeSat's principal axis with the air bearing table's rotation axis, and then compile these individual results to try to understand 3 degree of freedom behavior.

There are two types of tests present when testing the VMA: Tests in which the CubeSat rotates within the EMF by use of an air bearing table, and tests where the EMF rotates about the CubeSat (due to lack of air bearing table). In the first type, an air bearing table can provide single axis kinematic rotations which can be measured with the IMU, while the magnetic field vector in the inertial ECI frame $\boldsymbol{\mathcal{F}_E}$ is emulated with the Helmholtz cage. The combination of this data provides the full set of measurements required for the VMA.

In the second type of test, no air bearing table is present, requiring the magnetic field vector to account for the angular velocities of the CubeSat. Specifically, the magnetic field vector supplied by the Helmholtz cage must be the magnetic field vector in the spacecraft frame $\boldsymbol{\mathcal{F}_S}$ to account for the simulated rotation of the CubeSat. Additionally, simulated IMU data must also be utilized to propagate time dynamics of the system and to determine expected TAM measurements within the body frame. Before this type of test is performed, it should be verified that the Helmholtz cage used can sufficiently vary the output EMF vector in a way that emulates rotational rates of the CubeSat.

While the first testing scenario provides actual measurement data for both sensors, it does not allow for 3 degree of freedom motion, limiting tests to single axis rotation cases. This is not an issue with the second testing type, however the test fidelity is lower than that of the air bearing case, as simulated IMU data is used as opposed to measured data. To validate the VMA robustly, it is advised that a combination of the two test types is used.

D.2 AD Testing Objectives

The primary objective of testing the AD is to validate the use of the EMF vector as the sole aiding measurement within the VMA architecture. To adequately meet this objective, 4 sub-objectives must be met:

1. Characterize the noise parameters on selected IMU hardware
2. Characterize the noise parameters on selected TAM hardware
3. Verify the use of real-time magnetometer calibration software
4. Validate the simulation test cases shown within this thesis

Sub-objectives 1 and 2 must be performed to determine the standard deviations of noise parameters seen on the chosen IMU and TAM, including any scale factor and bias errors. By performing these characterizations, updated and more realistic noise values can be utilized within the VMA simulations as opposed to the values taken from spec sheets. Sub-objective 3 must be performed to ensure that any external magnetic field variations due to the CubeSat hardware or solar phenomena are effectively removed before use within the AD algorithm. Sub-objective 4 is broader and is meant to validate the success and failure criteria given within Chapter 5 of this thesis. Specifically, sub-objective 4 should be met by validating each simulation condition presented within a varying EMF and angular velocity environment.

While the concept of testing the AD in the above cases is relatively simple, some institutions do not have an adequate testing environment. Moreover, the development of this testing environment is not trivial. As such, it may be beneficial to leverage external testing facilities. A list of these potential facilities is given below:

- Space Dynamics Laboratory (SDL), Utah State University

- Georgia Tech Space Systems Design Lab
- Michigan eXploration Lab, University of Michigan
- Laboratory for Advanced Space Systems at Illinois (LASSI), University of Illinois
- Spacecraft Development Laboratory, Moorhead State University

The SDL is directly tied to the University Nanosatellite Program (UNP), which is a stakeholder in many CubeSat projects. Due to this, the use of the SDL facilities may be the easiest and most cost-effective choice for testing.

D.3 Initial AD Testing Plan

The remainder of this appendix will overview an initial test plan for the AD of a CubeSat utilizing the VMA shown within this thesis. This section lays out the advised AD tests, along with their objectives and requirements. It should be noted that the plan presented serves as a testing baseline, and the user is advised to adapt these tests as they see fit. Additionally, the amount and length of data collected may be modified as well. Before testing occurs, the analysis techniques should be validated.

Test #1: Characterize IMU noise

As detailed within Chapter 2 and Appendix C of this thesis, the IMU noise characteristics are comprised of 4 errors: turn-on bias or null-shift, in-run bias, scale factors, and white noise. While the noise characteristics for these values may be given on a specification sheet for the hardware, it is wise to verify them through additional testing.

Test Objectives:

- Obtain standard deviations on the values $\bar{b}_0, \bar{b}_g(t), \overline{sf}, \bar{n}_g(t)$
- Obtain a value on the Gauss-Markov correlation time for the in-run bias, τ_{GM}

Test Requirements:

- IMU hardware containing rate gyroscope
- IMU specification sheet and user manual
- Electrostatic discharge protection (ESD) equipment
- Data collection device (i.e. laptop)
- Connection between IMU and data collection device

Test Procedure:

Ensure testing environment is free from external vibrations or low frequency noise (i.e. fans, loud equipment, etc.). Equip ESD apparel and connect self to ground to assure hardware safety. Turn on and connect IMU hardware to data collection device as recommended by the hardware manufacturer. With the IMU static (non-rotating) collect output data over a span of at least 1 hour. Perform this data collection 3-5 times. The sampling frequency of the IMU should resemble the frequency anticipated on-orbit (i.e. 10 Hz for work presented in this thesis). After a sufficient amount of data is collected, begin data collection on non-static cases. Specifically, perform angular rotations of the IMU through fixed angles. This link (Analog Devices "A Simple Calibration for MEMS Gyroscopes") gives a thorough description of a simple test bench for these fixed rotations. This process should be repeated at least 10 times.

With static data, look at the first few seconds. Take the mean of this data to obtain bias offset. This should be collected for each run. Perform standard deviation

and mean analysis of the turn-on bias over each run to determine the average value and standard deviation of the turn on bias, $\bar{b}_0$ and σ_{b_0}. Over the entire time length of data, take the standard deviation to determine σ_g. Perform Allan variance and autocorrelation processes, as shown in [23], on the static data to determine the values of σ_{IRB} and τ_{GM}. As a note, these analyses are not necessarily trivial, and should be developed in detail before actual testing implementation. With non-static data, perform the analysis given in the above link on each case. This should result in the scale factor seen in each axis.

Test #2: Characterize TAM noise

While the TAM may be susceptible to multiple errors similar to the IMU, we assume that these errors can be adequately removed through the real-time calibration software. With this assumption, an initial baseline test can simply determine the relative output noise of the sensor and any turn on biases present. Note that additional tests on the other errors may be required depending on the quality of the selected calibration software.

Test Objectives:

- Obtain standard deviations on the values of $\bar{b}_{mag}, \bar{n}_{mag}(t)$

Test Requirements:

- TAM hardware
- TAM specification sheet and user manual
- Secondary magnetic field measurement device
    - Note: this device should be calibrated and have higher resolution than the TAM, if possible

- Electrostatic discharge protection (ESD) equipment
- Data collection device (i.e. laptop)
- Connection between TAM and data collection device
- Helmholtz Cage and Operation Information

Test Procedure:

NOTE: Additional testing steps and procedures may be in place depending on the testing facility.

Ensure testing environment is free from external vibrations or low frequency noise (i.e. fans, loud equipment, etc.). Equip ESD apparel and connect self to ground to assure hardware safety. Remove any electronics or devices that may interfere with the magnetic field measurements before proceeding. Place the TAM within the Helmholtz cage. With the Helmholtz cage and TAM turned off, measure the ambient magnetic field at the TAM location with the secondary magnetic measurement device. Turn on the Helmholtz cage and zero the ambient magnetic field. Ensure this magnetic field is as close to zero as possible. Turn on and connect the TAM hardware to data collection device as recommended by the hardware manufacturer. With the TAM static (non-rotating) collect output data over a span of at least 1 hour (this is arbitrarily picked and may be modified). Perform this data collection 3-5 times. The output frequency of the TAM should resemble the frequency anticipated on-orbit (i.e. 0.1 Hz for work performed in this thesis).

With static data, look at the first few seconds. Take the mean of this data to obtain bias offset. This should be collected for each run. Perform standard deviation and mean analysis of the turn on biases to determine the average value and standard deviation of the turn on bias, $\bar{b}_{mag}$ and $\sigma_{b_0,mag}$. Take the standard

deviation of the entire time length of data to obtain the output noise standard deviation σ_{mag}.

Test #3: Verify Helmholtz cage can vary magnetic field sufficiently

To accurately test the VMA, it must be ensured that the Helmholtz cage can vary the magnetic field at a sufficient enough rate to capture any satellite kinematics. This can be tested by verifying a desired, sufficiently time varying EMF vector can be input to the Helmholtz cage infrastructure.

Test Objectives:

- Measure the time history of the Helmholtz cage's output EMF vector and verify it matches the input time history

Test Requirements:

- TAM hardware
- TAM specification sheet and user manual
- Secondary magnetic field measurement device
    - Note: this device should be calibrated and have higher resolution than the TAM, if possible
- Electrostatic discharge protection (ESD) equipment
- Data collection device (i.e. laptop)
- Connection between IMU and data collection device
- Helmholtz Cage and Operation Information

Test Procedure:

NOTE: Additional testing steps and procedures may be in place depending on the testing facility.

Ensure testing environment is free from external vibrations or low frequency noise (i.e. fans, loud equipment, etc.). Equip ESD apparel and connect self to ground to assure hardware safety. Remove any electronics or devices that may interfere with the magnetic field measurements before proceeding. Place the TAM within the Helmholtz cage. With the Helmholtz cage and TAM turned off, measure the ambient magnetic field at the TAM location with the secondary magnetic measurement device. Turn on the Helmholtz cage and zero the ambient magnetic field. Ensure this magnetic field is as close to zero as possible. Turn on and connect the TAM hardware to data collection device as recommended by the hardware manufacturer. Input a time varying desired EMF vector over the course of approximately 10 minutes. This input EMF vector should resemble the changing EMF vector seen in the body frame of the spacecraft. Compare the output measurements collected by the TAM or secondary measurement device to the input EMF vector. Verify that they resemble each other within case-specific tolerance.

Test #4: Verify real-time TAM calibration

Before magnetic field measurements can be used within the VMA, they must be calibrated to remove any hard iron and soft iron biases present. This can be done via a real-time calibration technique that occurs on-orbit. The methodology of the calibration technique is not discussed here and must be determined before the VMA is used on-orbit. Instead, a potential testing technique for the calibration is discussed. Note that this test may vary greatly depending on the calibration used.

The time required for calibration will be dependent on the calibration technique used. In some cases, calibration may require multiple orbits of data collection, which could take up to 3 hours. As this time is a variable, it will be

referred to as t_{cal} for the remainder of this section. Accordingly, tests will need to occur over the length of time dictated by t_{cal}, which can be roughly determined through simulation.

Test Objectives:

- Ensure the calibration technique used adequately removes external noise on the EMF measurements
- Determine experimental t_{cal} required to have EMF measurements

Test Requirements:

- TAM hardware within completed engineering flight unit of CubeSat
- TAM specification sheet and user manual
- Secondary magnetic field measurement device
    - Note: this device should be calibrated and have higher resolution than the TAM, if possible
- Electrostatic discharge (ESD) equipment
- Data collection device (i.e. laptop)
- Connection between IMU and TAM and data collection device
- Helmholtz Cage and Operation Information

Test Procedure:

NOTE: Additional testing steps and procedures may be in place depending on the testing facility.

Ensure testing environment is free from external vibrations or low frequency noise (i.e. fans, loud equipment, etc.). Equip ESD apparel and connect self to ground to assure hardware safety. Remove any electronics or devices that may

interfere with the magnetic field measurements before proceeding. Place the CubeSat engineering flight unit (with TAM included, referred to as EFU from here) within the Helmholtz cage. With the Helmholtz cage and EFU unpowered, measure the ambient magnetic field at the EFU location with the secondary magnetic measurement device. Turn on the Helmholtz cage and zero the ambient magnetic field. Ensure this magnetic field is as close to zero as possible. Turn on and connect the EFU to the data collection device. Input a time varying desired EMF vector over the course of approximately $t_{cal} + 10\ minutes$. This input EMF vector should resemble the changing EMF vector seen in the body frame of the spacecraft and should allow enough time for calibration to occur. Compare the TAM output after calibration to the magnetic field output by the Helmholtz cage (via measurements from the secondary measurement device). Verify they resemble each other. Compare the output of the calibration to the desired EMF vector input into the Helmholtz cage.

Test #5: Validate AD performance

To validate the VMA performance, tests should occur for each simulation condition presented within this thesis, in addition to any further conditions the user may formulate. Note that if the sensor characterization Tests #1 and #2 were not performed within a few days prior to Test #5, they should be reperformed to ensure sensor characterization has remained relatively constant. For each condition, a set of data containing the EMF vector represented in both the inertial and spacecraft frames, $\boldsymbol{\mathcal{F}_E}$ and $\boldsymbol{\mathcal{F}_S}$, along with the noisy angular velocity data, should be provided so as to allow desired kinematic and EMF time histories. This data can be obtained by running the simulation environment used within this thesis (see Appendix E). The structure of the tests will depend on whether or not an air

bearing table is present. In the event that one is not present, the air bearing tests described within this section should simply be neglected. As a note, the procedures listed below should be completed for each condition presented within Chapter 5.

Test Objectives:

- Verify VMA performance

Test Requirements:

- TAM hardware within completed EFU of CubeSat
- TAM specification sheet and user manual
- IMU hardware within completed EFU of CubeSat
- IMU specification sheet and user manual
- Secondary magnetic field measurement device
    - Note: this device should be calibrated and have higher resolution than the TAM, if possible
- Electrostatic discharge (ESD) equipment
- Data collection device (i.e. laptop, RF transmitter, etc.)
- Connection between IMU and data collection device
- Helmholtz Cage and Operation Information
- Air bearing table (optional)

Test Procedure, No Air Bearing Table:

NOTE: Additional testing steps and procedures may be in place depending on the testing facility.

Ensure testing environment is free from external vibrations or low frequency noise (i.e. fans, loud equipment, etc.). Equip ESD apparel and connect self to ground to assure hardware safety. Remove any electronics or devices that may interfere with the magnetic field measurements before proceeding. Place the CubeSat EFU within the Helmholtz cage. With the Helmholtz cage and EFU unpowered, measure the ambient magnetic field at the EFU location with the secondary magnetic measurement device. Turn on the Helmholtz cage and zero the ambient magnetic field. Ensure this magnetic field is as close to zero as possible. Connect and turn on the EFU to the data collection device. Input a time varying desired EMF vector (as represented in the spacecraft frame $\boldsymbol{\mathcal{F}_S}$) over the course of approximately $t_{cal} + 2\ hours$. Note that this time may vary depending on the simulation case tested.

The input EMF vector should resemble the changing EMF vector seen in the body frame of the spacecraft, $\boldsymbol{\mathcal{F}_S}$, and should allow enough time for calibration to occur. Additionally, the IMU simulated data should be used as kinematic inputs to the VMA during the test. After the test is completed, validate the VMA performance by looking at the time history of state error covariance, P, and states themselves, $\delta\bar{x}$.

Test Procedure, With Air Bearing Table:

NOTE: Additional testing steps and procedures may be in place depending on the testing facility.

Ensure testing environment is free from external vibrations or low frequency noise (i.e. fans, loud equipment, etc.). Equip ESD apparel and connect self to ground to assure hardware safety. Remove any electronics or devices that may

interfere with the magnetic field measurements before proceeding. Attach the CubeSat EFU to the air bearing table within the Helmholtz cage. Ensure the desired EFU axis of spin is parallel to the air bearing table's spin axis, in addition to having the centroid of the EFU aligned with the table's spin axis. Moreover, it is important to ensure the TAM has as little translational motion as possible within the Helmholtz cage. With the Helmholtz cage, air bearing table, and EFU unpowered, measure the ambient magnetic field at the EFU location with the secondary magnetic measurement device. Turn on the Helmholtz cage and zero the ambient magnetic field. Ensure this magnetic field is as close to zero as possible. Connect and turn on the EFU to the data collection device. Input a time varying desired EMF vector (represented in the ECI frame $\boldsymbol{\mathcal{F}_E}$) over the course of approximately $t_{cal} + 2\ hours$ and begin rotational kinematics by powering on air bearing table. Note that this time may vary depending on the simulation case tested.

The input EMF vector should resemble the changing EMF vector seen in the ECI frame, $\boldsymbol{\mathcal{F}_E}$, and should allow enough time for calibration to occur. The IMU should be measuring rotational rates provided by the air bearing table. After the test is completed, validate the VMA performance by looking at the time history of state error covariance, P, and states themselves, $\delta\bar{x}$.

Additionally, the user may want to verify performance via the knowledge error ϵ. While this is possible, it should be noted that a form of "truth" attitude data is required to obtain this metric. In the instance where an air bearing table is included, the truth attitude would need to be obtained by propagating the rotational rates reported by the air bearing table itself. Note that these values are not exact, and in this instance the ϵ metric may be of lower fidelity.

Appendix E

VMA Simulation Environment Operation

This appendix details the operation and flow of the MATLAB simulation environment used to obtain the results presented within this thesis. Code is located within the UMN GitHub repository https://github.umn.edu/laugh055/KPL_EKF and the author's personal GitHub repository https://github.com/Kail-L/Vector-Matching-Algorithm. For specific questions, please direct them to the UMN Small Satellite Research Lab at smallsat@umn.edu.

Note that much of the simulation software presented here utilizes MATLAB's Aerospace toolbox. While this appendix details the high-level approach of the code, there should also be adequate comments on all functions seen in the above link.

E.1 Simulation Flow

Figure E.1 depicts the general flow of the simulation environment. The right side of the diagram showcases the main MATLAB scripts and functions used. The left side describes the high-level overview of the scripts and functions themselves. Before simulations begin, the user must define the parameters of importance for the simulation, namely the sensor noise characteristics, spacecraft parameters, and simulation timespan. These are all found within the `constants_struct.m` script, which serves to define the important constants and parameters used within the simulation environment. These values are placed within a structure labeled `const` that is called periodically throughout the simulation.

To run the simulation, the user needs to go to the `SatAttEst.m` script and hit "Run" within the MATLAB Editor toolbar. At this point, nothing else is

required from the user. A general overview of sim parameters (orbit, noise characteristics, sim run time, etc.) are printed on the command line after the simulation has started. Simulation runtime is dependent upon the number of orbits simulated and whether or not Monte Carlo runs are being implemented. For the results presented in this thesis, simulation took on average 45-60 minutes for 30 Monte Carlo runs. For single runs, the time frame is typically 2-3 minutes.

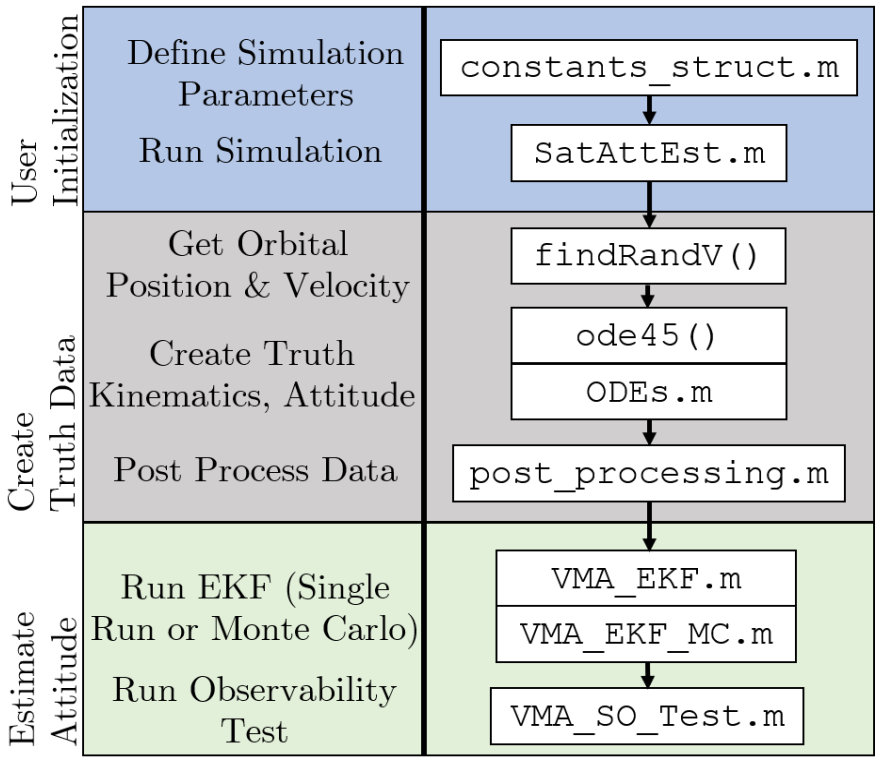

Figure E.1 Simulation Flow Diagram

While it was not shown within this thesis, the simulation environment has the capability to run the VMA using both a TAM and sun sensor as two separate measurements. To perform this, simply change the `const.UseSun` flag within the `constants_struct.m` structure.

E.1.1 User Initialization

The user initializes the simulation by modifying parameters within the `constants_struct.m` script and by running `SatAttEst.m`. The `constants_struct.m` script is split into 6 sections:

- Orbital Parameters
- Spacecraft Parameters
- Sim Initialization Parameters
- EKF Initialization Parameters
- Sensor Parameters
- Plotting & Visualizer Parameters

The orbital parameters section defines all relevant orbital parameters used within the sim, such as initial position, gravitational constants, inclination, eccentricity, and others.

The spacecraft parameters section covers the general mass, inertia, and size of the CubeSat, along with whether or not to use Stanford Gravity Probe B data. Note, the data that this functionality requires is not included within the Github repository and is only available through communication with Dr. Demoz Gebre-Egziabher.

Sim initialization parameters defines the number of orbits to simulate as well as the number of Monte Carlo runs to perform, in addition to simulation start time in UTC. Other parameters of importance are flags that set what EMF model to use in simulating truth data, in addition to starting angular velocity and attitude in terms of Euler angles.

EKF initialization parameters set the EKF's initial estimate, in addition to how that estimate is created via a set of initial quaternion flags. The quaternion can be initialized in 4 ways: By using the true attitude quaternion at time zero, using a randomized quaternion that is below a maximum ϵ error threshold, using a completely random quaternion that places ϵ between $0°$ and $180°$, or using a set of error Euler angles. Additionally, this section specifies the tuning parameters used within the sim, in addition to whether or not to constrain scale factor estimates, or to even estimate them at all.

Sensor parameters defines the sampling frequencies on all sensors used. It is advised that the magnetometer sample rate and sun sensor sample rate are set to be equivalent if sun sensor is included in simulation, as there are potential timing bugs within the code.

This section also defines the noise characteristics of the system. In the opinion of the author, this section is arguably the one that is modified the most. Note that there are flags that determine what types of noise are added to the system for both the TAM and IMU.

The plotting and visualizer parameters section allows for the user to define the size of the σ bounds plotted, as well as where to save plots. Additionally, a flag to create a video of the EKF is also present, however the user is advised that this functionality takes long amounts of time create.

E.1.2 Create Truth Data

After the user has initialized the simulation and ran `SatAttEst.m`, the simulation truth data is created. This is started by defining the initial states to be

integrated by MATLAB's `ode45()` function. In the instance of this simulation, the integration initial state vector is given as

$$IC = \begin{bmatrix} \bar{r}_0^{SE} & \bar{v}_0^{SE} & q_{0,0} & \bar{q}_0 & \bar{\omega}_0^{SE} \end{bmatrix}^T \tag{E.1}$$

where $\bar{r}_0^{SE}$ and $\bar{v}_0^{SE}$ define the initial position and velocity that are output from `findRandV()`, $q_{0,0}$ and $\bar{q}_0$ define the initial quaternion defined by the user, and $\bar{\omega}_0^{SE}$ defines the initial angular velocity also defined by the user. This state vector is then integrated through time using `ode45()` and a function handle that contains the differential equations for each state given in Equation (E.1). Within this sim, the differential equations are contained within `ODEs.m`. If it is desired to increase the simulation fidelity (i.e. modify equations of motion for the satellite to include disturbance torques), then this script would be the one to modify.

Based upon the simulation timeframe, `ode45()` will output a time history of the state vector described by Equation (E.1) that is interpreted as the truth data for the simulation. After the integrator is run, we parse the truth data into a manageable format through the use of the `post_processing.m` script. This script places the angular rate and quaternion data into a useable format, in addition to obtaining the truth EMF and sun position vectors in the spacecraft frame based upon MATLAB's WMM and solar ephemeris data. As a note to the user, MATLAB's ephemeris data is not included in the base package and must be downloaded to the simulation's file path from MATLAB's website.

The required data to run the EKF should be stored in the workspace after the post processing script is run, however it can also be saved by uncommenting a block of code at the end of `post_processing.m`.

E.1.3 Estimate Attitude

After `post_processing.m` is run, the script `VMA_EKF.m` or `VMA_EKF_MC.m` is run, depending on if Monte Carlo is desired or not. Both functions run the EKF developed in Chapter 3 and are close to identical, other than modifications made to implement variation in parameters from run to run. At the beginning of the script, parameters are taken from the constants structure and redefined with shorter variable names. Additionally, empty storage matrices for parameters of interest are created to aid in computational speed.

Based upon the noise characteristics specified by the user, in addition to the types of noise expected, both truth angular rates and EMF values are corrupted through the individual functions `emulateGyro()` and `emulateMag()`. Any updates to the measurement models for the IMU or the TAM should also be made to the code within these functions. While it is missing in this work, a magnetometer calibration scheme should also be implemented in the same area of code that these functions are called. After the EKF is run for the desired timespan, the observability test detailed in Chapter 4 is run via `VMA_SO_Test.m`.

After the majority of `VMA_EKF.m` or `VMA_EKF_MC.m` is run, figures detailing the VMA performance are created. Many of these are the same as the ones presented within Chapter 5, however there are additional figures depending on whether or not Monte Carlo analysis is taking place. To modify the plotting parameters, change the code at the end of the script as desired.